Efficient and Spatially Controlled Functionalization of SBA-15

Von der Fakultät Chemie der Universität Stuttgart zur Erlangung der Würde eines Doktors der Naturwissenschaften (Dr. rer. nat.) genehmigte Abhandlung

Vorgelegt von

Ann-Katrin Beurer

aus Bietigheim-Bissingen

Hauptberichter: Apl.-Prof. Dr. Yvonne Traa
Mitberichter: Apl.-Prof. Dr. Thomas Sottmann

Tag der mündlichen Prüfung: 11.10.2023

Institut für Technische Chemie der Universität Stuttgart
2023

Erklärung über die Eigenständigkeit der Dissertation

Ich versichere, dass ich die vorliegende Arbeit mit dem Titel *Efficient and spatially controlled functionalization of SBA-15* selbständig verfasst und keine anderen als die angegebenen Quellen und Hilfsmittel benutzt habe; aus fremden Quellen entnommene Passagen und Gedanken sind als solche kenntlich gemacht.

Declaration of authorship

I hereby certify that the dissertation entitled *Efficient and spatially controlled functionalization of SBA-15* is entirely my own work except where otherwise indicated. Passages and ideas from other sources have been clearly indicated.

Ludwigsburg, 11.10.2023   _____

                                        Ann-Katrin Beurer

Acknowledgments

List of publications directly relevant to my cumulative dissertation:

A.-K. Beurer, S. Dieterich, H. Solodenko, E. Kaya, N. Merdanoğlu, G. Schmitz, Y. Traa, and J. R. Bruckner, "Comparative Study of Lattice Parameter and Pore Size of Ordered Mesoporous Silica Materials Using Physisorption, SAXS Measurements and Transmission Electron Microscopy", *Microporous Mesoporous Materials* **2023**, *354*, 1387-1811, DOI 10.1016/j.micromeso.2023.112508.

A.-K. Beurer, J. R. Bruckner, and Y Traa, "Influence of the template removal method on the mechanical stability of SBA-15", *Chemistry Open* **2021**, *10*, 1123-1128, DOI 10.1002/open.202100225.

A.-K. Beurer, M. Kirchhof, J. R. Bruckner, W. Frey, A. Baro, M. Dyballa, F. Giesselmann, S. Laschat, and Y. Traa, "Efficient and spatially controlled functionalization of SBA-15 and initial results in asymmetric Rh-catalyzed 1,2-additions under confinement", *ChemCatChem* **2021**, *13*, 2407-2419, DOI 10.1002/cctc.202100229.

In addition, the results of this work contributed to publishing the following publications:

M. Kirchhof, K. Gugeler, A.-K. Beurer, F. R. Fischer, D. Batman, S. Bauch, S. Kolin, E. Nicholas, R. Schoch, C. Vogler, S. R. Kousik, A. Zens, B. Plietker, P. Atanasova, S. Naumann, M. Bauer, J. R. Bruckner, Y. Traa, J. Kästner and S. Laschat, "Tethering chiral Rh diene complexes inside mesoporous solids: experimental and theoretical study of substituent, pore and linker effects on asymmetric catalysis", *Catalysis Science & Technology* **2023**, *13*, 3709-3724, DOI 10.1039/d3cy00381g.

C. Rieg, M. Kirchhof, K. Gugeler, A.-K. Beurer, L. Stein, K. Dirnberger, W. Frey, J. R. Bruckner, Y. Traa, J. Kästner, S. Ludwigs, S. Laschat, and M. Dyballa, "Determination of accessibility

and spatial distribution of chiral Rh diene complexes immobilized on SBA-15 *via* phosphine-based solid-state NMR probe molecules", *Catalysis Science & Technology* **2023**, *2*, 410-425, DOI 10.1039/D2CY01578A.

E. L. Goldstein, F. Ziegler, A.-K. Beurer, Y. Traa, J. R. Bruckner, and M. R. Buchmeiser, "Cationic molybdenum imido alkylidene *N*-heterocyclic carbene complexes confined in mesoporous silica: Tuning transition states towards *Z*-selective ring-opening cross-metathesis", *ChemCatChem* **2022**, *14*, DOI 10.1002/cctc.202201008.

Z. Li, C. Rieg, A.-K. Beurer, M. Benz, J. Bender, C. Schneck, Y. Traa, M. Dyballa, and M. Hunger, "Effect of aluminum and sodium on the sorption of water and methanol in microporous MFI-type zeolites and mesoporous SBA-15 materials", *Adsorption* **2021**, *27*, 49-68, DOI 10.1007/s10450-020-00275-8.

Z. Li, M. Benz, C. Rieg, D. Dittmann, A.-K. Beurer, D. Häussermann, B. Arstad, and M. Dyballa, "The alumination mechanism of porous silica materials and properties of derived ion exchangers and acid catalysts", *Materials Chemistry Frontiers* **2021**, *5*, 4254-4271, DOI 10.1039/D1QM00282A.

J. R. Bruckner, J. Bauhof, J. Gebhardt, A.-K. Beurer, Y. Traa, and F. Giesselmann, "Mechanisms and intermediates in the true liquid crystal templating synthesis of mesoporous silica materials", *The Journal of Physical Chemistry B* **2021**, *125*, 3197-3207, DOI 10.1021/acs.jpcb.0c11005.

Table of Contents

List of Abbreviations and Symbols

Abbreviations

as	as-synthesized
Au-NP	gold nanoparticle
AzPTES	3-azidopropyltriethoxysilane
BET	Brunnauer-Emmett-Teller
BJH	Barrett, Joyner, and Halenda
calc	calcined
CP	cross polarization
DFT	density functional theory
DRIFT	diffuse infrared reflectance Fourier transform
e.g.	Latin *exempli gratia*; English *for example*
E	Soxhlet extraction with ethanol
EO	ethylene oxide
ex	external
FFT	fast Fourier transformation
FTIR	Fourier-transform infrared spectroscopy
HMDS	1,1,1-trimethyl-*N*-(trimethylsilyl)silanamine

List of Abbreviations and Symbols

HPLC	high-performance liquid chromatography
i.e.	Latin *id est*; meaning *that is to say*
I	precursor molecule
in	pore walls
IR	infrared
ISEC	inverse size exclusion chromatography
IUPAC	International Union of Pure and Applied Chemistry
MAS	magic angle spinning
MC	molecular simulation
MCF	mesostructured cellular foam
MCM	mobile composition of matter
MOF	metal-organic framework
MS	mass spectroscopy
NLDFT	non localized density functional theory
NMR	nuclear magnetic resonance
OMS	ordered mesoporous silica
p	thermal treatment
PHTS	plugged hexagonal templated silica
PO	propylene oxide
re	refilled
S	surfactant
SAXS	small angle X-ray scattering
SBA	Santa Barbara amorphous
SEM	scanning electron microscopy
SiOH	silanol groups

STP		standard temperature and pressure
TEM		transmission electron microscopy
TLCT		true liquid crystal templating
TMOS		tetramethyl orthosilicate
X		counter ion
XRD		X-ray diffractometry

Latin Letters

a	nm	lattice parameter
d	nm	a) distance; b) diameter
g		dimensionless packing parameter
q	nm	scattering vector
S	m^2	surface area
V	m^3	volume

Indices - superscript

+		positively charged
-		negatively charged
0		nonionic

Indices - subscript

100/110/200	Miller *hkl* indices
ads	adsorption branch
des	desorption branch
m	repeat units of EO in block copolymers $EO_mPO_nEO_m$
meso	mesoporous
micro	microporous
n	repeat units of PO in block copolymers $EO_mPO_nEO_m$
tot	total

Abstract

Mimicking enzymes is one of the biggest goals of current catalysis research. They have defined micro environments that enable high enantioselectivities and thus can produce targeted products. With organometallic catalysts, especially when immobilized on solid supports, often low enantioselectivities are achieved compared to enzymes. In addition, the costs of producing and recovering dissolved catalysts are often high. Considering environmental issues and resource scarcity, it is important to develop catalysts for enantioselective and efficient chemical reactions. The combination of the advantages of homogeneous catalysis, with similarly high enantioselectivities as well as productivities as enzymes show, with the positive aspects of heterogeneous catalysis is a promising concept. Behind this approach is the immobilization of highly selective complex catalysts on porous support materials like mesoporous silica materials. By confining the reaction space in the pore and channel structure of the support material, shape selectivity can be achieved in desired product configurations. To enable shape selectivity through confinement, it is necessary to ensure that the immobilized metal complexes are located exclusively in the mesopores and channels of the support material. Therefore, the efficient and spatially controlled functionalization of mesoporous silica materials as support materials for catalytically active metal complexes is very important and can significantly advance heterogeneous catalysis.

Precise knowledge of properties of the support material is required to ensure efficient and spatially controlled functionalization to mimic the functioning of enzymes. Various methods are available for determining characteristic properties such as the lattice parameter and pore size of mesoporous silica materials. In this work, four different mesoporous silica materials with an average pore size of 3 to 11 nm were used to compare commonly used characterization methods with alternative methods. Determination of lattice parameters by small angle X-ray (SAXS) measurements and from images from the transmission electron microscope yields similar values. Considering that errors during the evaluation of transmission electron microscopy (TEM) images may occur due to pore orientation, the determination of lattice parameters from TEM images is an alternative method that provides equivalent results. The pore size of various mesoporous silica materials was

Abstract

determined using physisorption measurements and SAXS studies. In addition, a new method was presented in which electron density maps were generated from SAXS data and used to determine pore sizes. Since it is difficult to determine the transition between the pore wall and the pore when viewing small pores in TEM images due to the different gray levels, the tractability of the open pore network was investigated in proof of principle experiments using gold nanoparticles (Au-NPs) as probe particles. The values for the pore size determined by different characterization methods agree well, although it should be noted that Au-NPs can only determine a range of pore sizes and not an exact value. Nevertheless, the comparison shows that the two new characterization methods - generation of electron density maps and use of Au-NPs as probe particles to determine the pore size - have the potential to become alternatives to the established methods. [1]

The characterization of possible carrier materials is followed by functionalization, the most important step for mimicking enzymes. In order to ensure that catalytically active species are located exclusively in the mesopores, all freely accessible silanol groups on the external surface of the support material must be inertized before the functionalization of the pore walls. Various methods for controlled functionalization of porous silica have been reported in literature, but do not unequivocally demonstrate that selective functionalization of pore walls was achieved while the external surface was left inert. The procedure used in this work for selective functionalization of SBA-15 develop the selective functionalization procedures described in literature further. The introduction of a separate and independent control step ensures that the functionalization procedure results in a material in which the organic groups - in this case azide groups - are located exclusively on the pore walls. Click chemistry can then be used to attach linkers and noble metal complexes to the azide groups and provide the actual catalysts. Before the control step, the external surface of SBA-15 was previously functionalized with 1,1,1-trimethyl-*N*-(trimethylsilyl)silanamine (HMDS). In the following independent and separate control step, this material is treated with 3-azidopropyltriethoxysilane (AzPTES). When silanol groups on the external surface are accessible to the AzPTES molecules on the putatively fully functionalized external surface of SBA-15, they react with them. The azide groups on the external surface are then detectable by IR spectroscopy and elemental analysis after the control step. If all freely accessible silanol groups are indeed inert after functionalization of the external surface with HMDS, treatment with AzPTES has no effect. Both the infrared (IR) spectrum and the elemental analysis results show that SBA-15 functionalized with HMDS has a completely inert external surface. This ensures that only the silanol groups on the pore walls of SBA-15 are functionalized with AzPTES. [2]

Another important aspect in the preparation of selectively functionalized catalysts is their preparation and use in reactors. Since mesoporous silica materials are often produced as powders, they must be shaped e.g. by tableting or extrusion. In addition, pressures act on catalysts when reactors are loaded and reactions take place. For example, pressures of up to 40 MPa prevail in laboratory-scale reactors and ultra-fast high-performance liquid chromatography (HPLC) systems. With this in mind, calcined SBA-15 and SBA-15, whose pores were opened by Soxhlet extraction with ethanol and subsequent heating in nitrogen were subjected to a pressure of 39 MPa for 10 min.

Results of different surface areas and pore volumes obtained from nitrogen physisorption measurements showed that both materials were stable up to this pressure. At higher pressure of 156 MPa, both samples lose parts of their porosity, as shown by the nitrogen physisorption measurements. The broadening of the characteristic SAXS reflections as well as the decrease in intensity confirm a partial destruction of the nanostructure of the samples pressed at 156 MPa.[3]

Thus, the three publications of this cumulative dissertation are the basis for an efficient use of mesoporous silica materials as support for the immobilization complex catalysts and an unambiguous determination of confinement effects.

Zusammenfassung

Die Nachbildung von Enzymen ist eines der wichtigsten Ziele der aktuellen Katalyseforschung. Denn Enzyme verfügen über definierte Mikroumgebungen, die hohe Enantioselektivitäten ermöglichen. Somit ist es ihnen möglich gezielt Produkte herzustellen. Mit metallorganischen Katalysatoren, insbesondere wenn sie auf festen Trägern immobilisiert sind, werden im Vergleich zu Enzymen oft geringe Enantioselektivitäten erreicht. Darüber hinaus sind die Kosten für die Herstellung und Rückgewinnung gelöster Katalysatoren hoch. In Anbetracht von Umweltproblemen und Ressourcenknappheit ist es wichtig, Katalysatoren für enantioselektive und effiziente chemische Reaktionen zu entwickeln. Die Kombination der Vorteile der homogenen Katalyse, mit ähnlich hohen Enantioselektivitäten sowie Produktivitäten, wie sie Enzyme aufweisen, mit den positiven Aspekten der heterogenen Katalyse ist ein vielversprechendes Konzept, um gezielt enantiomerenreine Produkte kostengünstiger und umweltschonender herzustellen. Hinter diesem Ansatz steht unter anderem die Immobilisierung von hochselektiven Katalysatoren auf porösen Trägermaterialien wie mesoporösem Siliziumdioxid. Durch die räumliche Eingrenzung der Reaktion in der Poren- und Kanalstruktur des Trägermaterials kann eine formselektive Reaktion zu gewünschten Produktkonfigurationen erreicht werden. Um Formselektivität zu ermöglichen, muss sichergestellt sein, dass sich die immobilisierten Katalysatoren wie beispielsweise Metallkomplexe ausschließlich in den Mesoporen und Kanälen des Trägermaterials befinden. Daher ist die selektive und räumlich kontrollierte Funktionalisierung von mesoporösem Siliziumdioxid als Trägermaterial für katalytisch aktive Metallkomplexe sehr wichtig und kann die heterogene Katalyse erheblich voranbringen.

Um eine selektive und räumlich kontrollierte Funktionalisierung zur Nachbildung der Funktionsweise von Enzymen zu gewährleisten, ist die genaue Kenntnis der Eigenschaften des Trägermaterials erforderlich. Für die Bestimmung charakteristischer Materialeigenschaften wie des Gitterparameters und der Porengröße mesoporöser Siliziumdioxide stehen verschiedene Methoden zur Verfügung. In dieser Arbeit wurden vier mesoporöse Siliziumdioxide mit durchschnittlichen Porengrößen von 3 bis 11 nm verwendet, um gängige Charakterisierungsmethoden mit alternativen

Methoden zu vergleichen. Die Bestimmung der Gitterparameter durch Röntgenkleinwinkelmessungen (SAXS) und aus Bildern des Transmissionselektronenmikroskops ergab ähnliche Werte. Unter Berücksichtigung der Tatsache, dass bei der Auswertung von Aufnahmen mit dem Transmissionselektronenmikroskop (TEM) durch die Porenorientierung Fehler auftreten können, liefert die Charakterisierungsmethode gleichwertige Ergebnisse. Die Porengröße verschiedener mesoporöser Siliziumdioxide wurde klassisch mit Hilfe von Physisorptionsmessungen und aus den Daten von SAXS-Messungen bestimmt. Darüber hinaus wurde eine neue Methode vorgestellt, bei der Elektronendichtekarten aus SAXS-Daten erstellt und zur Bestimmung der Porengrößen verwendet werden. Da es bei der Betrachtung kleiner Poren in TEM-Aufnahmen aufgrund der unterschiedlichen Graustufen schwierig ist, den Übergang zwischen Porenwand und Pore zu bestimmen, wurde in Proof-of-Principle-Experimenten unter Verwendung von Gold-Nanopartikeln (Au-NPs) als Sondenpartikel untersucht, ob die Siliziumdioxide als offene Porennetzwerke vorliegen. Die mit den verschiedenen Charakterisierungsmethoden ermittelten Werte für die Porengröße stimmen gut überein, obwohl zu beachten ist, dass Au-NPs nur einen Bereich von Porengrößen und keinen exakten Wert bestimmen können. Dennoch zeigt der Vergleich, dass die beiden neuen Charakterisierungsmethoden - die Erstellung von Elektronendichtekarten und die Verwendung von Au-NPs als Sondenpartikel zur Bestimmung der Porengröße - das Potenzial haben, Alternativen zu den etablierten Methoden zu werden.[1]

Nach der Charakterisierung der möglichen Trägermaterialien folgt deren selektive und räumlich kontrollierte Funktionalisierung, der wichtigste Schritt bei der Nachbildung von Enzymen. Um sicherzustellen, dass sich die katalytisch aktive Spezies ausschließlich in den Mesoporen befindet, müssen vor deren Aufbringen auf das Trägermaterial alle frei zugänglichen Silanolgruppen auf der Partikeloberfläche des Trägermaterials inertisiert werden. Verschiedene Methoden zur slektiven und räumlich kontrollierten Funktionalisierung von porösem Siliziumdioxid sind in der Literatur beschrieben, zeigen aber nicht eindeutig, dass eine selektive und räumlich kontrollierte Funktionalisierung der Porenwände erreicht wurde, während die äußere Oberfläche inert blieb. Das in dieser Arbeit verwendete Verfahren zur selektiven und räumlich kontrollierten Funktionalisierung von SBA-15 als Trägermaterial entwickelt die in der Literatur beschriebenen Verfahren weiter. Es unterscheidet sich durch die Einführung eines separaten und unabhängigen Kontrollschritts, der sicherstellt, dass das Funktionalisierungsverfahren zu einem Material führt bei dem sich die organischen Gruppen - in diesem Fall Azidgruppen - ausschließlich an den Porenwänden befinden. Mittels Klick-Chemie können im Anschluss Linker und Edelmetallkomplexe an die Azidgruppen gebunden werden, um eine spezifische katalytisch aktive Spezies bereitzustellen. Vor dem Kontrollschritt wurde die äußere Oberfläche, bestehend aus Partikeloberfläche und den Poreneingängen von SBA-15 zuvor mit 1,1,1-Trimethyl-N-(trimethylsilyl)silanamin (HMDS) funktionalisiert. In dem folgenden, unabhängigen und separaten Kontrollschritt wird dieses Material mit 3-Azidopropyltriethoxysilan (AzPTES) behandelt. Sind noch Silanolgruppen auf der vermeintlich voll funktionalisierten äußeren Oberfläche von SBA-15 zugänglich, reagieren sie mit dem AzPTES. Die Azidgruppen auf der äußeren Oberfläche sind nach dem Kontrollschritt durch

IR-Spektroskopie (IR) und Elementanalyse nachweisbar. Wenn alle frei zugänglichen Silanolgruppen nach der Funktionalisierung der äußeren Oberfläche mit HMDS tatsächlich inert sind, hat die Behandlung mit AzPTES keine Auswirkungen. Sowohl das IR-Spektrum als auch die Ergebnisse der Elementanalyse zeigen, dass das mit HMDS funktionalisierte SBA-15 eine völlig inerte äußere Oberfläche aufweist. Dies gewährleistet, dass in einem nachfolgenden Schritt nur die Silanolgruppen an den Porenwänden von SBA-15 funktionalisiert werden. Im Rahmen dieser Arbeit wurden die Silanolgruppen der Porenwände mit AzPTES funktionalisiert, um im Anschluss mittels Klick-Chemie katalytisch aktive Metallkomplexe in das Porensystem einzubringen.[2]

Ein weiterer wichtiger Aspekt bei der Herstellung von selektiv funktionalisierten Katalysatoren ist die Herstellung und Verwendung in Reaktoren. Da mesoporöse Siliziumdioxide häufig als Pulver hergestellt werden, müssen sie beispielsweise durch Tablettierung oder Extrusion in Form gebracht werden. Außerdem wirken bei der Beladung der Reaktoren sowie bei der Durchführung von Reaktionen darin Drücke auf die Katalysatoren ein. So herrschen beispielsweise in Reaktoren im Labormaßstab und in ultraschnellen Hochleistungsflüssigkeitschromatographiesystemen (HPLC) Drücke von bis zu 40 MPa. Vor diesem Hintergrund wurden kalziniertes SBA-15 und SBA-15, deren Poren durch Soxhlet Extraktion mit Ethanol und anschließendem Erhitzen in Stickstoff geöffnet wurden, einem Druck von 39 MPa für 10 min ausgesetzt. Die Ergebnisse der verschiedenen Oberflächen und Porenvolumina, die aus Stickstoffphysisorptionsmessungen ermittelt wurden, ergaben, dass beide Materialien bis zu diesem Druck stabil sind. Bei höherem Druck von 156 MPa verlieren beide Proben einen Teil ihrer Porosität, wie die Ergebnisse der Stickstoffphysisorptionsmessungen zeigen. Die Verbreiterung der charakteristischen SAXS-Reflexe sowie die Abnahme der Intensität bestätigen eine teilweise Zerstörung der Nanostruktur der bei 156 MPa gepressten Proben.[3]

Somit bilden die drei Publikationen dieser kumulativen Dissertation die Grundlage für eine effiziente Nutzung von mesoporösem Siliziumdioxid als Trägermaterial für die Immobilisierung komplexer Katalysatoren zur eindeutigen Durchführung formselektiver Reaktionen.

Introduction

1.1 Porous Materials

Porous materials are solids with cavities or channels, which are deeper than wide.[4;5] Since their introduction, various porous materials have been developed, differing in pore size, properties and applications. In everyday life, porous materials can be found almost everywhere. For example, foams with pores in millimeter range are used for heat[6;7] and sound insulation[8]. The remarkable properties of GoreTex® membranes for clothing are based on micropores.[9] A further application for nanoporous silica gels as desiccants are the small pouches included with many electronic devices and clothing.[10] In addition, mesoporous silica materials are used in separation processes or as sensors, as well as in other electro-optical technologies.[11;12] Common materials with even smaller pore sizes are zeolites. Zeolites are used in detergents as ion exchangers.[13] The wide range of properties complicates the classification of porous materials.[10] According to the IUPAC technical report, porous materials are classified by their pore size. Porous materials are divided into microporous materials with a pore size <2 nm, mesoporous materials with a pore size between 2 nm and 50 nm and macroporous materials with pore sizes >50 nm.[14] This work deals with mesoporous silica materials.

1.2 Mesoporous Silica Materials

In 1971, literature described the synthesis of mesoporous silica for the first time. The generation of mesoporous silica materials was achieved by using self-assembled molecules.[15;16] The lack of analytical capabilities for characterization meant that remarkable properties of these materials initially remained undiscovered during this time.[17;18] Later on, with advanced analytical techniques, the essential properties were recognized. Today, it is possible to prepare a variety of mesoporous silica materials with the use of triblock copolymers as structure-directing template. In this context, mesoporous silica with pore sizes ranging from 5 nm to 30 nm are feasible.[19] Due to their large surface area, silica materials have a large number of surface-active centers. The

functionalization of these surface-active centers leads to a change and multiplication of physical and chemical properties. Consequently, porous silica materials are not only used as catalytically active materials, but their function as support materials is also of great interest.

1.2.1 Mobil Composition of Matter Materials

The Mobil Oil Corporation described the first mesoporous silica material with an ordered pore structure in 1992 under the name M41S.[20;21] For the production of these materials, a self-assembling template was surrounded by silica precursor molecules. The silica precursor molecules react with each other via condensation reactions and build the structure of the mesoporous silica material. In general, M41S materials are prepared in an alkaline environment using a quaternary ammonium salt or gemini surfactants.[18] Quaternary ammonium salts behave like a classical surfactant in solution. Predictions about the morphology of an M41S material prepared with a quaternary ammonium salt can therefore be made via the dimensionless packing parameter g. The packing parameter is calculated from the quotient of the effective volume of the hydrophobic chain, the surface area of the hydrophilic head group and the critical hydrophobic chain length. Spherical micelles are formed when $g < 0.\overline{3}$, rod-shaped micelles when $g = 0.5$ and lamellar micelles when $g = 1$.[22] The surface area of the head groups of the ammonium salt can also influence the morphology. If the surface area is large, spherical structures are preferentially formed, while rod-like and lamellar structures are formed when the head groups can be densely packed and have a high aggregation number. Different reaction conditions can affect the packing parameters and thus the order of M41S materials. M41S materials can be synthesized as powders, thin film layers on various substrates or as monoliths.[18;23;24] The M41S family groups together all porous materials with uniformly defined and highly ordered pores. The different Mobile Composition of Matter (MCM) materials are assigned by a sequential number after their respective acronym.[21] The best known materials of the M41S family are MCM-41[22;25–30], MCM-48[30–34] and MCM-50[35–37]. MCM-41, with the space group *p6mm*, is a well-known material and is used within this work. The pores of MCM-41 are arranged in a honeycomb shape and separated by amorphous pore walls, yielding to a large surface area and high pore volume. Figure 1.1 shows the characteristic particle shape and pore structure of MCM-41. The uniform pores can be tuned to a diameter between 1.5 nm and 20 nm during the synthesis and exhibit a narrow pore size distribution.[18] To obtain large pores, swelling agents must be added during synthesis. The pore walls are 1 nm to 1.5 nm thick which is relatively thin compared to other mesoporous silica materials resulting in low chemical and hydrothermal stability.[18;38;39]

1.2.2 Santa Barbara Amorphous Materials

Santa Barbara amorphous (SBA) materials are mesoporous silica materials with various pore sizes, which can be prepared by using the nonionic triblock copolymer consisting of blocks of poly(ethylene oxide) (EO) and poly(propylene oxide) (PO). Depending on the block sizes *n*

(a)

(b)
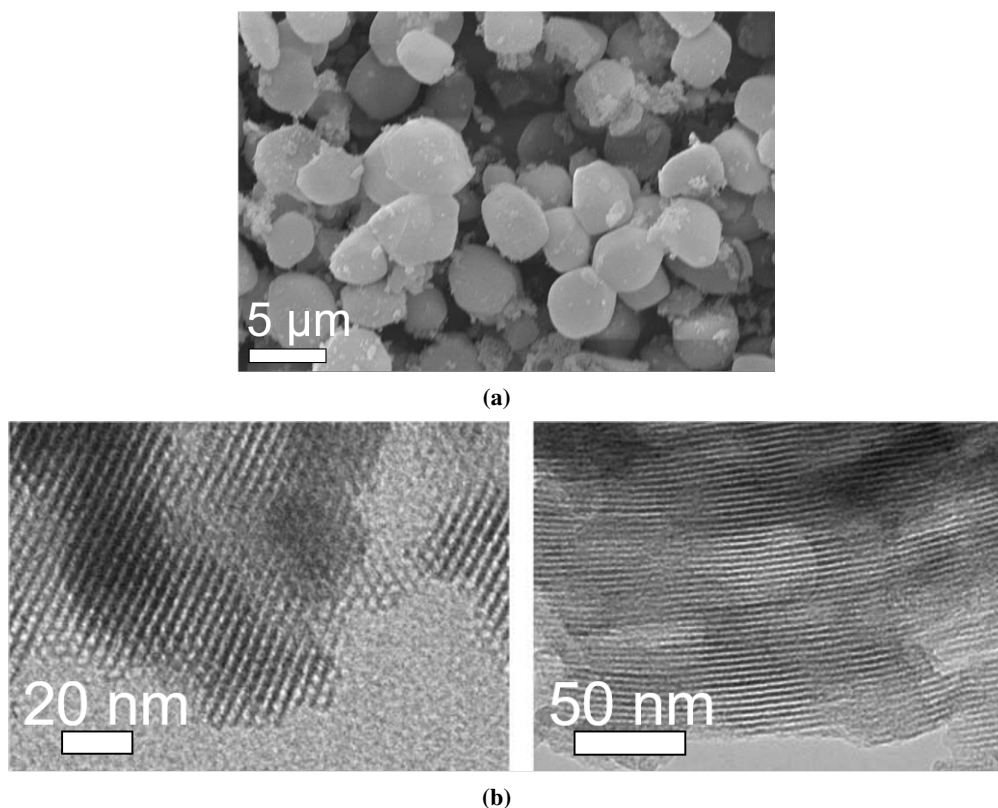
Figure 1.1: (a) Image from the scanning electron microscope of the MCM-41 particles as well as (b) TEM images of the honeycomb pore structure of MCM-41.[18]

and *m*, different triblock copolymers poly(ethylene oxide)$_m$-poly(propylene oxide)$_n$-poly(ethylene oxide)$_m$ (EO$_m$PO$_n$EO$_m$) are known.[40;41] These kind of silica materials find use as support for metals in nanowire shape[42–46], as template for the synthesis of (inverse) carbon replicas[47–51], for immobilization of enzymes[52;53] and in lithium batteries[54]. SBA materials are used as catalysts in reactions[17;55–64], for the controlled release of active ingredients or antioxidants from support materials[65;66] and for recovery of heavy metals[67]. In general, SBA materials are classified as relatively neutral structures since the interactions between structure-directing template and silica lattice are very weak.[11] The different SBA materials are distinguished from each other by structural properties. These properties can be adjusted by varying the number of polypropylene oxide and polyethylene oxide blocks in the triblock copolymer. This allows the control of the morphology, the pore structure and size during the production process. Accordingly, the actual structure in each SBA material is determined by the composition of the structure-directing template or more specifically by the quotient of the number of polyethylene oxide blocks and polypropylene oxide blocks in the triblock copolymer. This results in SBA materials with lamellar, hexagonal or cubic mesophase structure.[18]

A well-known SBA material is SBA-15, whose mesopores are hexagonally arranged, indicating the space group *p6mm*.[18] The worm-like particles of SBA-15 can be seen in Figure 1.2 as well

(a)

(b)

Figure 1.2: (a) Images of the worm-like particle structure of SBA-15 from the scanning electron microscopy (SEM) as well as (b) TEM images of the parallel channels within the particles and the hexagonal pore structure of SBA-15.[18]
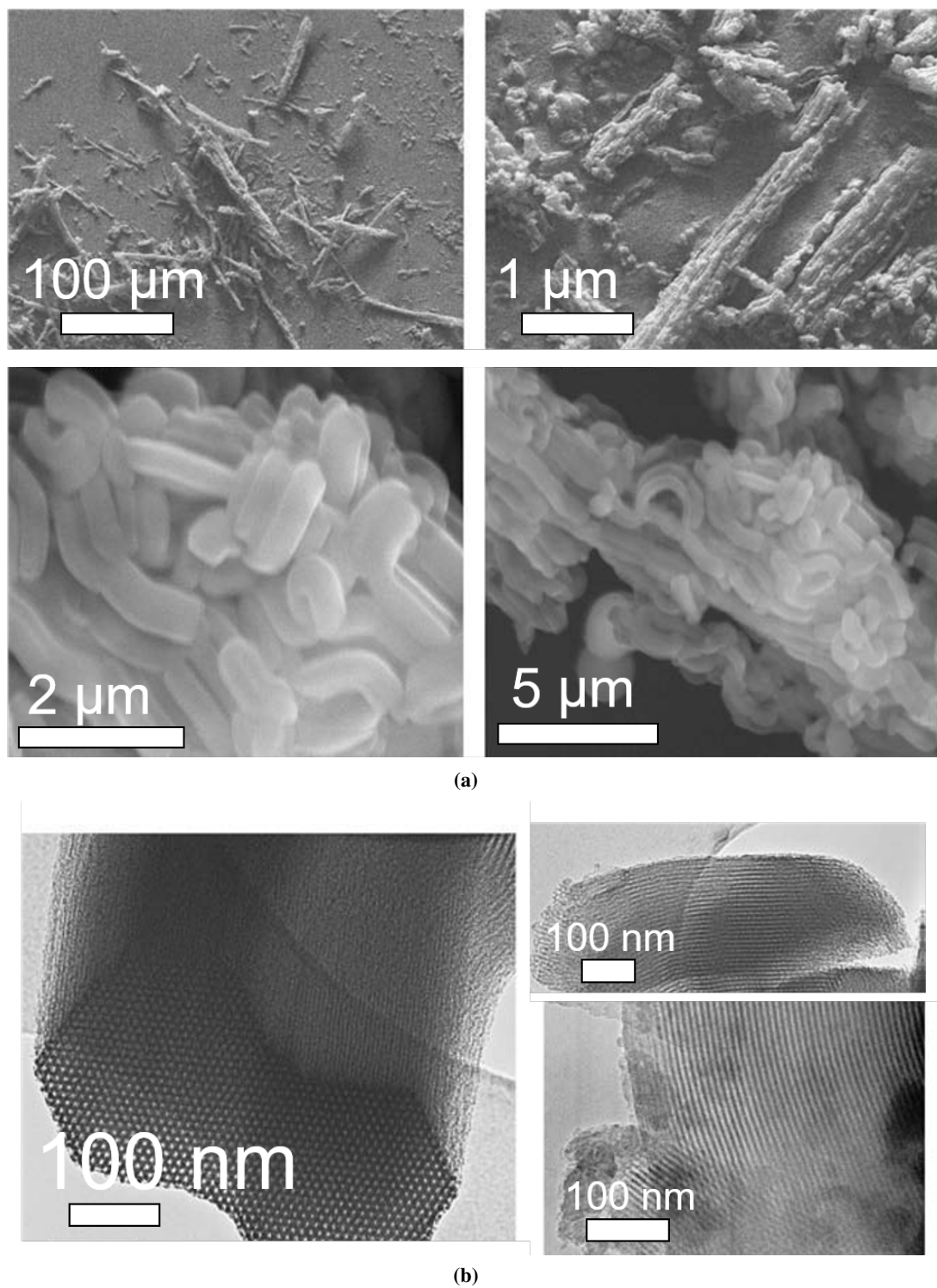
as the typical pore and channel structure. The pore walls, which are 3 nm to 6 nm thick, consist of micropores, which are responsible for the hydrothermal stability.[68] Varying the number of polyethylene oxide blocks causes a change in the number and proportion of micropores in the pore walls, as well as the pore wall thickness.[51;69–73] The smaller the polyethylene block m, the smaller the micropores are.[69–71] By shortening or lengthening the polypropylene blocks n in the triblock copolymer, the size of the mesopores can be controlled by their hydrophobic properties. Concluding from this, it is possible to influence the size of mesopores as well as the microporosity of pore walls by varying the ratio of polyethylene and polypropylene blocks of the triblock copolymer. This is attributed to the fact that polypropylene blocks form agglomerates in solution and represent the negative of the later mesoporous tunnel structure.[40;69;70;72;74] The larger the polypropylene oxide block, the larger the agglomerates in the aqueous phase leading to larger pores.[69;71] In addition to the template and the inorganic precursor molecules, reaction conditions such as temperature[68;69;75], pH value[76], and additives influence the material.[18;77] Solvents, swelling agents such as alkanes and organic compounds like mesitylene or electrolytes can be used as additives.[78–84] Depending on the additive, different functionalities of the additives are incorporated into the material. In the case of short-chain alkanes, literature describes that molecules attach themselves between the tails of the template molecules. For longer-chain alkanes, such as decane, a core-shell structure is formed with molecules of the additive as the core and an enclosed layer of the template molecules as shell.[85;86]

Another SBA material is SBA-16, which has hydrothermal properties similar to the ones of SBA-15. The difference between SBA-15 and SBA-16 is the use of different templates during synthesis. For example, triblock copolymers with large polyethylene oxide blocks such as $EO_{106}PO_{70}EO_{106}$ are used for synthesis of SBA-16.[87] SBA-16 has a three-dimensional cubic cage structure consisting of two non-intersecting three-dimensional channel systems with the space group *Im3m*.[87;88] The intersections of both channel systems form spherical cavities.[18] The nature of the hysteresis loop within the sorption isotherms suggests bottle-shaped pores.[88;89] In general, as with SBA-15, changes in the morphology of SBA-16 are controllable by the reaction conditions.[90–97]

1.2.3 Plugged Hexagonal Templated Silica Material

An analog to SBA-15 is plugged hexagonal templated silica (PHTS) material. Compared to SBA-15, the ratio of silicon source to structure-directing template is higher for PHTS.[51;98–100] The difference between both materials is the fact that amorphous nanoparticles are in the mesoporous channels of PHTS. The nanoparticles in the pore channels have a positive effect on the stability of PHTS through their support function.[101;102] Despite the nanoparticles in the channel system, the hexagonal pore structure of PHTS as well as the pore size remains similar to SBA-15 (Figure 1.3). Just like SBA-15, the pore walls are interspersed with micropores. The amount of grafted pores can be adjusted by varying the synthesis conditions from only open to only grafted pores.[98;103;104] Moreover, by changing reaction conditions, size and stability of the nanoparticles located in the

(a)

(b)
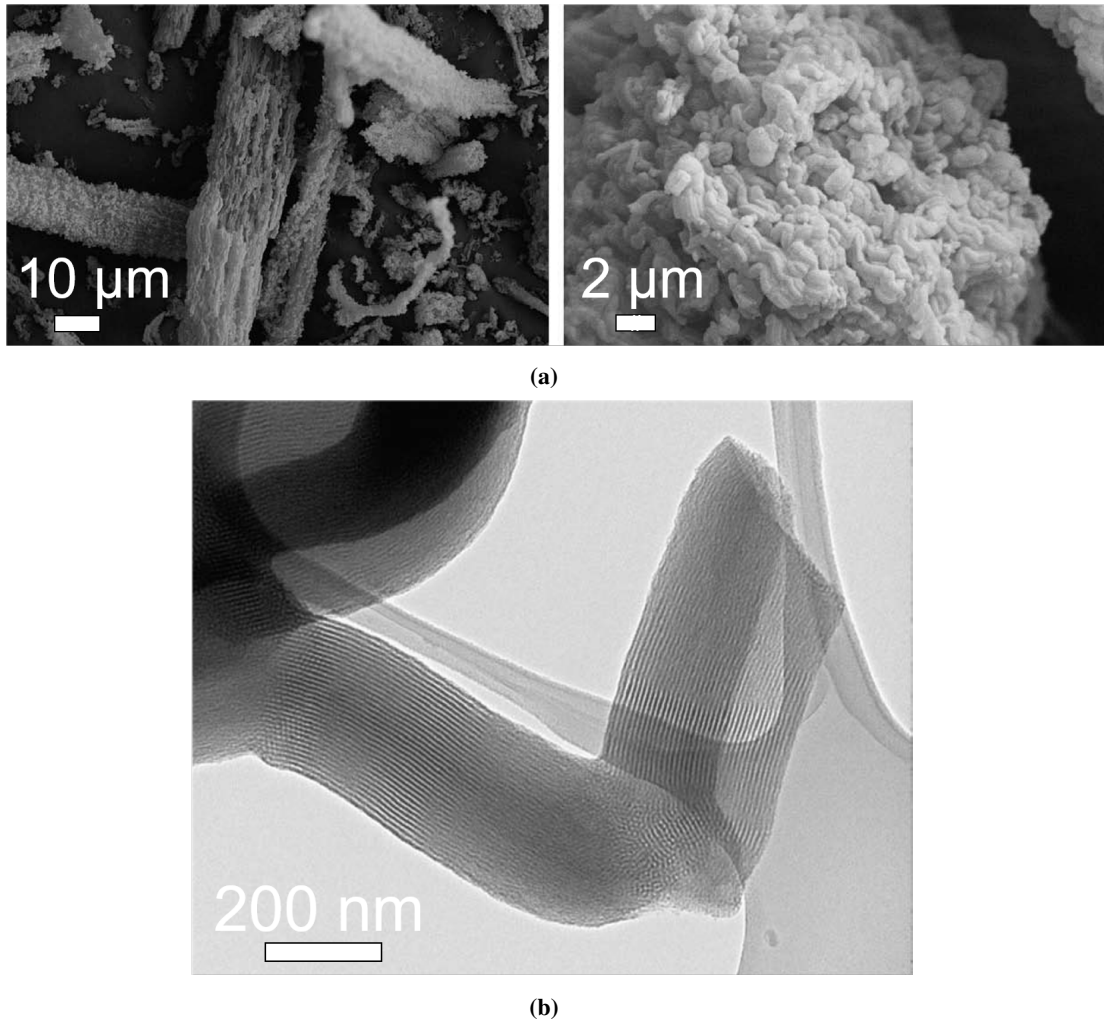
Figure 1.3: (a) SEM images of the worm-like particle structure of PHTS as well as (b) a TEM image of the channels within the particles and the hexagonal pore structure of PHTS.[18]

pore channels can be varied.[102;105] The pore size and the size of the nanoparticles can be adjusted, for example, via the synthesis temperature, means the higher the temperature, the larger the pore size and nanoparticles. Another difference of PHTS compared to SBA-15 is the larger micropore volume. This is because the micropores in the nanoparticles increase the total micropore volume of PHTS.[99] Furthermore, the morphology of PHTS can be influenced by the proportion of the silica precursor and by different reaction temperatures. Possible morphologies are smooth fibers, rough fibers, and spherical particles. At low temperatures and low silica precursor concentrations, smooth PHTS fibers are formed, while high temperatures form spherical particles. The relationship between reaction temperature and morphology can be found in the cloud point of the template. The cloud point is the temperature at which a clear liquid becomes turbid by crystallization under defined conditions. Other factors why there could be different morphologies for PHTS

are the degree of polymerization of the silica matrix and the amount of mesoporous silica material already formed.[100]

1.2.4 Mesostructured Cellular Foam

Another mesoporous silica material is the mesostructured cellular foam (MCF). This material has a sponge-like structure (Figure 1.4) with thick pore walls responsible for its hydrothermal stability.[18] The pores of MCF are bottle-shaped and are accessible through 5 nm to 20 nm wide openings.[18] By adding ammonium fluoride during the synthesis, the openings can be selectively enlarged by 50 % to 80 %.[106;107] As a result of the large pores, rapid kinetic mass transport is possible to transport large molecules such as polymers or enzymes.[108–111] Other structural properties can be influenced during the production of MCF by changing the reaction conditions such as temperature, reaction time, adjusted pH value, as well as additives and swelling agents such as mesitylene.[18;106–108;112–116] The swelling agent causes the micelles to expand, creating larger micelle radii in the sponge-like foam structure. MCF can be produced as a powder or monolith.[117–119] The material can be modified to find use in biocatalysis, catalysis, sorption, and controlled release of sorbed substances.[83;109–111;120–124]

(a) **(b)**
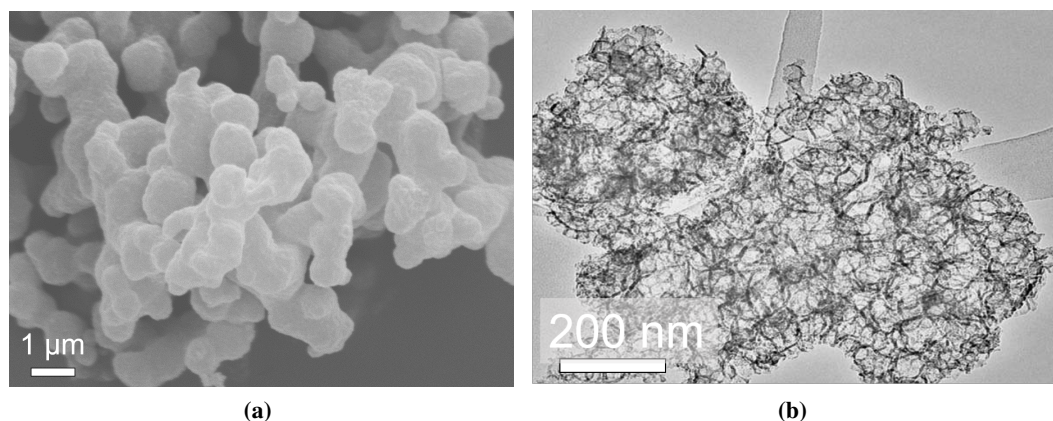
Figure 1.4: (a) SEM and (b) TEM images of the sponge-like structure of MCF.[18]

1.3 Process for the Preparation of Mesoporous Silica Materials

1.3.1 Synthesis of Mesoporous Silica Materials

In general, preparation of most inorganic mesoporous materials is based on the use of organic template molecules. These are brought into solution and form micelles due to their composition. The subsequently added inorganic precursor molecules enclose the template micelles. During hydrothermal treatment, condensation reactions take place to build a lattice around the micelles of the structure-directing template (Figure 1.5).[18] In the literature, simple oligomers or liquid crys-
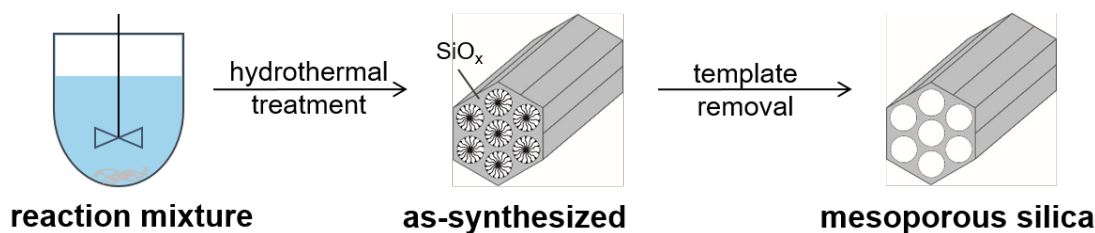
Figure 1.5: Schematic representation of the synthesis route of mesoporous silica materials according to the cooperative self-assembly mechanism.

talline phases are used as templates for the preparation of mesoporous silica materials. Using such liquid crystalline phases consisting of neutral, cationic and anionic diblock copolymers, mesoporous silica materials with large spherical pores[125], hexagonally arranged cylindrical pores[126] and lamellar vesicular pores[127] are successfully prepared in acidic environment. Besides diblock copolymers, triblock copolymers are suitable for producing mesoporous silica materials in acidic environment.[41;87;128–130] One of the most useful groups of surfactants are triblock copolymers of poly(ethylene oxide)$_m$-poly(propylene oxide)$_n$-poly(ethylene oxide)$_m$ ($EO_mPO_nEO_m$). These triblock copolymers consisting of polyethylene oxide and polypropylene oxide blocks arrange micelles in aqueous reaction solutions and have the ability to form liquid crystal structures. In the case of micelle formation, the interior of the micelles consist of polypropylene oxide blocks, while the shell of the micelles consist of polyethylene oxide blocks.[17;18] Depending on the template, the structural properties of mesoporous silica materials can be influenced by the number of repeat units of individual polymer blocks.[18] When the structure of the formed mesoporous silica materials is sufficiently built up by condensation reactions of the precursor molecules, the pores are filled with structure-directing template (Figure 1.5, as-synthesized). The structure-directing template molecules are no longer needed and can be removed in a further step. As a result, the pores are open and a porous structure is built (Figure 1.5, mesoporous silica material).[11;131] The mechanistic consideration of the pore structure formation of mesoporous materials bases on different pathways. In the following, the mechanism of cooperative self-assembly, true liquid crystal templating (TLCT) and nanocoasting are considered.[131]

In the mechanism of cooperative self-assembly, the lyotropic liquid crystalline phase is already present but at low surfactant concentrations. This is possible if there is cooperative self-assembly of the structure-directing template and the already added inorganic precursor. As with the TLCT mechanism, liquid crystalline phases with hexagonal, cubic or lamellar arrangement can be formed in the cooperative self-assembly process.[132;133] The cooperative self-assembly formation mechanism was first observed under basic reaction conditions, but can also occur in acidic environments as in the synthesis of SBA-15. Regardless of the pH value during preparation of mesoporous silica materials, this formation mechanism requires the occurrence of attractive interactions between molecules of the structure-directing template and the silica precursor molecules. Inclusion of the structure-directing template is only guaranteed without phase separation in this case.[131] The pos-

sible interactions between inorganic precursor molecule (I) and structure-directing template, the surfactant (S), are shown in Figure 1.6.[131;134;135]

The direct co-condensation of mesoporous materials takes place in an alkaline environment. The quaternary ammonium surfactant molecules used as structure-directing template are present as cations (S^+), while the silica precursor molecules are in their anionic form (I^-). This formation mechanism is referred to as the S^+I^- pathway.[131;135]

The formation mechanism according to the S^+I^- pathway can be carried out in acidic reaction solutions. This means that the pH value is below the isoelectric point of the silanol groups of the silica precursor. In this case, the silica precursor molecules are positively charged (I^+). Since the structure-directing template molecules are positively charged by the acidic environment (S^+), negatively charged counter ions (X^-) are required to ensure interactions between surfactant and inorganic species. This formation mechanism is referred to the $S^+X^-I^+$ pathway.[131;135]

Another possible formation mechanism is the S^-I^+ pathway. In this case, the formation of mesoporous materials takes place in acidic environment, which is why the structure-directing template molecules are negatively charged (S^-). In contrast, the silanol groups of the silica precursor are positively charged (I^+). A counterion is not necessary in this formation mechanism.[131;135]

In the $S^-X^+I^-$ pathway, both the structure-directing template and the silica precursor molecules are present in their anionic form in an alkaline environment ((S^-) and (I^-)). Thus, a positively charged counter ion (X^+) is required during this formation mechanism.[131;135]

In addition to the ionic formation mechanisms, non-ionic mechanisms are also known. In this case, the interactions are hydrogen bond interactions instead of electrostatic interactions between the structure-directing template and the silica precursor molecules, as it is the case with ionic formation mechanisms. Hydrogen bond interactions occur when nonionic surfactants (S^0) are used. The silanol groups of the silica precursor molecules are neutral (I^0), so this formation mechanism is called the S^0I^0 pathway. If the silanol groups of the silica precursor molecules are positively charged, charge equalization must occur via a free electron pair. As a result, an ion pair is present and the formation mechanism is called the $S^0(XI)^0$ pathway.[131;135]

Another process for the preparation of mesoporous silica materials is the true liquid crystal templating (TLCT) process. In the TLCT mechanism, the template concentration is so high that an ordered lyotropic liquid crystal phase is formed as a function of temperature and pH value. During the formation process, the structure-directing template molecules form spherical micelles initially. Afterwards, the micelles agglomerate into rod-shaped micelles. In the next step, template rods aggregate to form a lyotropic liquid crystal phase, which determines the structure of the mesoporous silica material. The precursor molecules for the inorganic silica material are added to the surface-active liquid crystalline phase and condensate to the silica matrix during the hydrothermal treatment. The formation process following the TLCT mechanism was proposed in the early 1990s as a possible mechanism for the formation of MCM-41.[20] Later, the mechanism was confirmed by the hydrolysis of tetramethyl orthosilicate (TMOS) within a liquid crystalline phase.[136] It was shown that the lyotropic liquid crystal phase was destroyed when methanol was formed as side

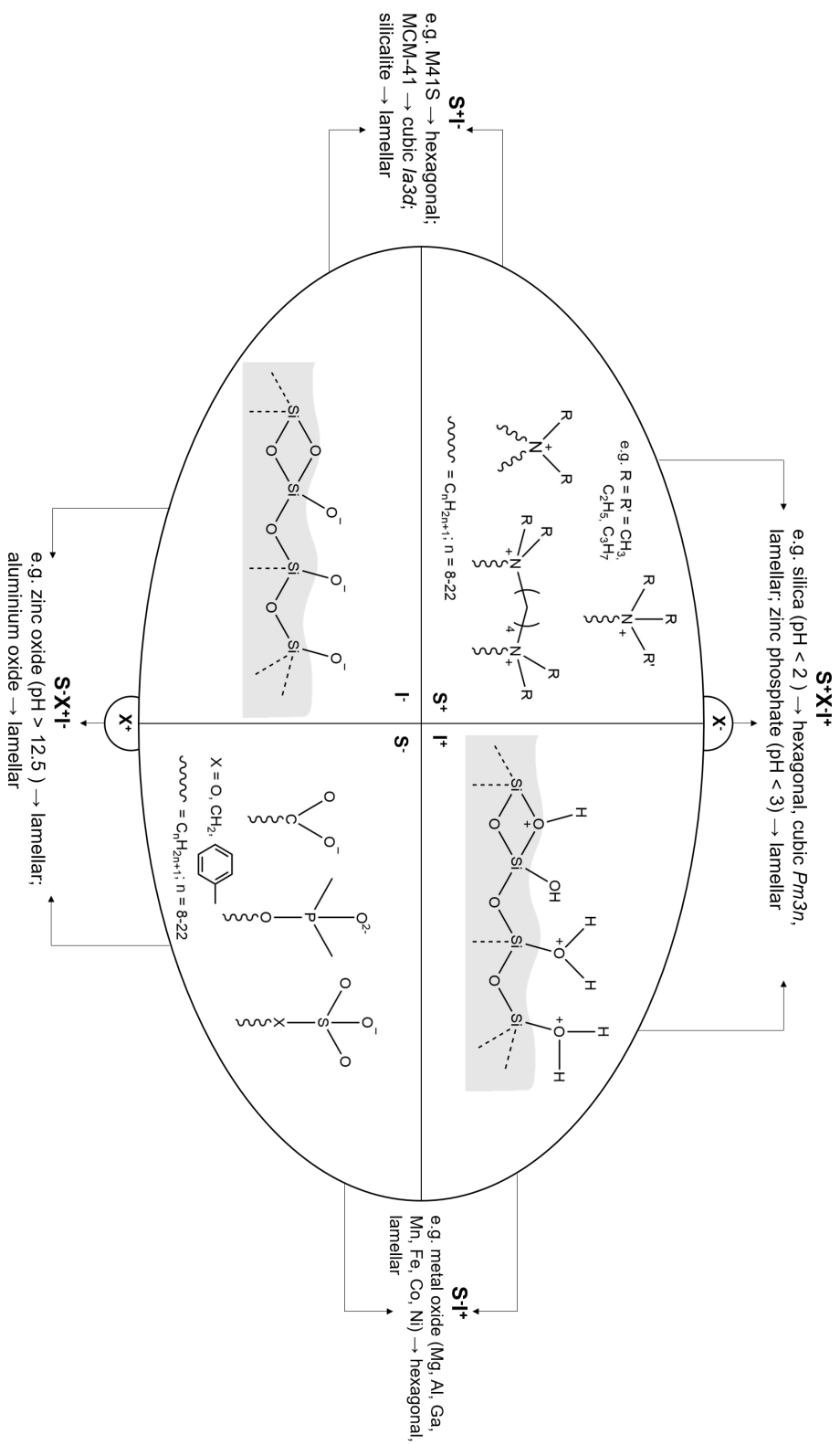*Figure 1.6:* Schematic representation of the possible interactions between the inorganic precursor molecule (I) and the structure-directing template, the surfactant (S) during the synthesis of mesoporous materials via the self-assembly formation mechanism. In two cases, counter ions (X) are required to ensure interactions between surfactant and inorganic species. The schema was created according to the literature. [131;134;135]

product. After the evaporation of alcohol, the lyotropic liquid crystal phase was reformed. There-fore, it is difficult to make a sharp distinction from the mechanism of cooperative self-assembly.[17] In contrast to the TLCT mechanism, the cooperative self-assembly mechanism described above relies on cooperative interactions between the surfactant and the inorganic species, yielding an organic-inorganic mesostructured composite.[131]

Overall, various synthetic routes for mesoporous silica materials are known and it is quite pos-sible that a material can be produced via several synthetic routes. However, independent of the production process of mesoporous silica materials, the cavities and channels must be opened by removing the template (Chapter 1.3.2).

1.3.2 Template Removal

Organic template molecules are usually used as structure-directing template to produce meso-porous silica materials (Chapter 1.3.1). They are often dissolved in an acidic solution before in-organic precursor molecules are added. Inorganic precursor molecules arrange themselves around the micelles, formed by the structure-directing template. During hydrothermal treatment, conden-sation reactions of the precursor molecules take place and build a negative of the micelles.[18] After formation of the inorganic matrix of the mesoporous silica material, the structure-directing tem-plate is no longer needed and must be removed to make the pores accessible.[11] Template removal from the inorganic matrix is not trivial, because it is possible that characteristic properties of the mesoporous silica material will change significantly as a result of the template removal method.[11] Various methods are available in the literature describing how to remove the structure-directing template from pores and channels.[19;103;137;138] Depending on the interactions between template molecules and the embedded matrix and the adaptation of the template to the matrix, different approaches are suitable for an efficient and gentle removal of the template molecules. Ideally, the organic template molecules are removed without changing the properties of the host structure. This means that the inorganic precursor remains as a negative of the template micelles structure and the surface properties of the mesoporous silica material are still preserved. It is important to ensure the removal of the entire structure-directing template.[137] As described in the literature, the amount of removed template as well as the change of the mesoporous silica structure depends on the cho-sen method.[11;18;139] It should be noted that the removal of the structure-directing template is not always the same owing to the structural properties of different mesoporous silica materials.[11]

The most commonly used method to open the pores of as-synthesized mesoporous silica materials is calcination. In this process, the as-synthesized mesoporous silica materials are heated up to temperatures of $550\,°C$ in a stream of oxygen or air, and the temperature is maintained for $4\,h$ to $8\,h$.[11] At these temperatures, organic structure-directing template molecules burn and make the pores of the mesoporous silica material accessible. However, if the combustion is not complete, carbon species can be formed. These can block pores and channels. The multistage decomposition process of the structure-directing template of as-synthesized SBA-15 can be illustrated by thermo-

analytical investigations. At temperatures below 150 °C, the physisorbed water molecules firstly desorb in an endothermic process from the surface of SBA-15. Between 150 °C and 280 °C, thermal decomposition of the template molecules occurs in an exothermic step. All fragments detected by the mass spectrometer during the exothermic process can be assigned to the structure-directing template.[11;140] The mass loss of this decomposition step is more than 40 % and is assigned to carbon dioxide and water. At temperatures above 280 °C, a further mass loss of 10 % is observable, which is attributable to the removal of water and residues of the carbon species. This leads to a total mass loss of more than 50 %.[11;19;68;87]

Temperature-dependent X-ray analytical studies show structural changes of SBA-15 during calcination. When as-synthesized SBA-15 is heated up to 200 °C, an increase in the intensity of the scattering reflections can be observed. This means that no changes in the hexagonal structure are observed up to this temperature. Between 200 °C and 250 °C, the intensities of the scattering reflections are initially weaker than at temperatures below 200 °C. The intensities again become stronger when the temperature increases above 250 °C. At temperatures above 250 °C, additionally a shift of the scattering reflections to smaller angles can be observed. Shifts of the scattering reflections to smaller angles are equivalent to the shrinkage of the silica lattice compared to the as-synthesized SBA-15.[11;141–143] Accordingly, calcined SBA-15 shrinks by about 13 % after cooling to room temperature.[11]

Shrinkage means the decrease of the lattice parameter of the mesoporous silica material. The effect can be explained by the restructuring of the silica lattice during the thermal treatment. The rearrangement of the silica lattice is possible as not all possible condensation reactions take place during the synthesis of mesoporous silica materials, causing structural defects. The high temperature during the calcination enables restructuring and quenching of defects within the silica lattice.[141–143] Since the structure shrinkage differs between various mesoporous silica materials such as SBA and MCM materials, it is assumed that silica materials catalyze the thermal decomposition and oxidation of the template molecules in presence of the oxygen, even at low temperatures.[11;68] Carbon species and water formed in these reactions are removed from the pores and channels only at higher temperatures. In this process, condensation reactions are still possible, which shrink the structure further.[11]

Another template removal method is extraction of the structure-directing template with an extracting agent. In the literature, solvents such as ethanol or propanol are used for this purpose. The use of sulfuric acid or hydrochloric ethanol solutions and the use of neutral salts in ethanol are also described to remove the structure-directing template from the pores and channels of mesoporous silica materials.[139;144–146] Regardless of the extraction agent, mesoporous silica materials are treated under reflux or by Soxhlet extraction to make the pores and channels accessible.[11]

When as-synthesized mesoporous silica materials are treated with up to 60 wt % sulfuric acid in ethanol, polypropylene oxide blocks are removed. Due to the treatment with sulfuric acid, ether groups are cleaved. The built fragments are removed by diffusion from the channel and pore structure, resulting in opened mesopores whereas the micropores remain closed.[147] The influ-

ence of acid concentration during the extraction process as well as the extraction time were investigated.[139] The X-ray analytical studies show that the hexagonal structure shrinks at a concentration of 60 wt% sulfuric acid solution in the same way as during the calcination process. At the same time, it should be noted that high concentrations are not necessary, as a concentration of 48 wt% sulfuric acid solution is sufficient to remove the polypropylene oxide blocks completely. The micropores sealed after the treatment with sulfuric acid can be accessed by a subsequent temperature treatment.[147]

Compared to the calcined samples, the samples treated with sulfuric acid have larger cell constants and larger pore sizes, but thinner pore walls. Reaction time studies showed that both the amount of removed template and the structural properties of SBA-15 are affected. Regardless of the concentration and reaction time, the micropores remain closed and can only be opened by thermal treatment. The micropore volume of mesoporous silica materials treated with sulfuric acid and then calcined at 200 °C is about twice that of silica materials, which are calcined at 540 °C. Even when sulfuric acid treated mesoporous silica materials are additionally calcined at 540 °C, the micropore volume is significantly larger than that of a mesoporous silica material calcined exclusively at 540 °C. The gradual removal of the structure-directing template is confirmed by nitrogen physisorption measurements of the silica material treated with 60 wt% sulfuric acid solution.[139]

Another alternative for removing the structure-directing template from the pores of silica materials is microwave digestion. Microwave digestion has the same effect as calcination, but shortens the reaction time for template removal significantly compared to the calcination process.[148] Major advantages of this method are the smaller structural shrinkage and the retention of a higher degree of freely accessible silanol groups. Furthermore, higher surface areas and pore volumes are obtained by removing the structure-directing template with microwave digestion. This is clearly demonstrated by nitrogen physisorption measurements. At the same time, elemental analysis shows that more than 99.5 % of the template is removed by microwave digestion.[137]

In summary, it is shown that the calcination process removes the structure-directing template completely but at the expense of the mesopore structure. Extraction of structure-directing template with sulfuric acid showed that the sulfuric acid concentration and the treatment time influence the degradation of the structure-directing template and thus the structural properties of SBA-15. The comparison of silica materials that are exclusively calcined with those, whose structure-directing template is removed by extraction in a first step and then thermally treated, shows that template removal via extraction is a good alternative. Further advantages of extraction arise from an ecological and economic point of view when the triblock copolymer used as a template and the solvents used for extraction are recycled. A big disadvantage of extraction of the template molecules is that during the extraction often not the entire structure-directing template from the channel-pore system is removed.[18]

1.4 Properties of Mesoporous Silica Materials

1.4.1 Silanol Groups on Surfaces of Mesoporous Silica Materials

When the structure-directing template is removed from the as-synthesized mesoporous silica material, silanol groups (SiOH) are on the whole surface. These are either isolated silanol groups or silanol groups interacting via hydrogen bridges with each other or geminal silanol groups (Figure 1.7).[140] Type and number of accessible silanol groups on the surface of mesoporous silica materials are of enormous importance for various fields of applications. For example, the number of accessible silanol groups decide how many catalyst complexes can be anchored to the surface.
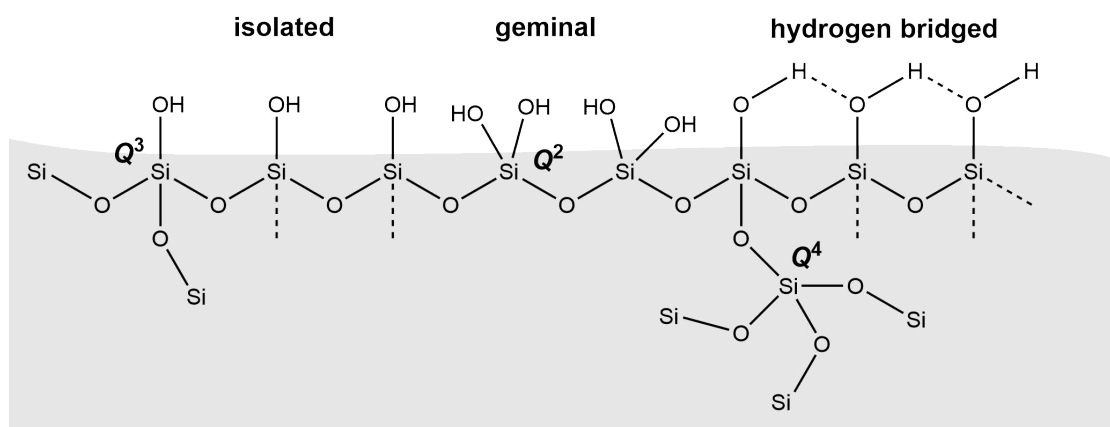

Figure 1.7: Schematic representation of the single, geminal and hydrogen bridged silanol groups on silica surfaces[140] and the assignment of Q^2, Q^3 and Q^4 sites in ^{29}Si MAS NMR spectra of MCM and SBA materials[149].

Acidic properties introduced via silanol groups depend, among other things, on the nature of the accessible silanol groups on the silica surface.[150;151] Isolated or geminal silanol groups have higher acid strength compared to silanol groups connected by hydrogen bridges, which exhibit a non-acidic character.[150;152] For this reason, only isolated and geminal silanol groups can be functionalized, whereas the non-acidic silanol groups do not react with the molecules of the functionalization reagents.[140] Therefore, knowledge about the nature of accessible silanol groups on the surface of silica materials is important depending on the application. Various analytical methods are known to investigate the nature of silanol groups on the silica surface.[92;149–151;153]

Among other methods, the ^{29}Si magic angle spinning (MAS) nuclear magnetic resonance (NMR) measurement is one of them.[149;153] The ^{29}Si MAS NMR measurement is a bulk method. This means that the ^{29}Si MAS NMR measurement examines not only the silanol groups on the surface of the silica materials, but also silicon atoms of the SiO_4 tetrahedra in the lattice structure of the silica material.[149] The ^{29}Si MAS NMR spectrum shows signals for isolated and geminal silanol groups as well as for silanol groups, which are connected by hydrogen bridges. Accordingly, the spectrum of a silica material exhibits the signal of Q^4 groups at -110 ppm. The signal is charac-

teristic for four bonded SiO_4 tetrahedra in the lattice structure of silica materials (Figure 1.7). The silanol groups on the silica surface are observed at -101 ppm and -92 ppm. They are assigned to the silicon atoms to which one silanol group SiOH (Q^3 groups) or two isolated silanol groups $Si(OH)_2$ (Q^2 groups) are bound.[149;151;153] In the ^{29}Si MAS NMR spectrum of as-synthesized MCM-41, the signal from Q^3 groups has the highest intensity compared to the signals for Q^2 and Q^4 groups.

Calcination, which removes the structure-directing template from the pores, alters the ^{29}Si MAS NMR spectrum. Corresponding to this aspect, the ^{29}Si MAS NMR spectrum no longer shows a splitting of the individual signals. Rather, a broad, fuzzy signal is observed exclusively at a chemical shift of -107 ppm.[153] A possible reason for this is that free silanol groups in the pore walls of mesoporous silica materials of the M41S family combine by condensation reactions.[154] Broadening and shifting of signals occur from changes in Si-O bond length and Si-O-Si angle. When calcined mesoporous silica materials of the M41S family are treated hydrothermally, the signals of Q^2 and Q^3 groups reappear in the ^{29}Si MAS NMR spectrum instead of the broadened signal.[153] The ^{29}Si MAS NMR spectrum of calcined SBA-15 shows a different distribution of signal intensities of Q^2, Q^3, and Q^4 groups compared to the ^{29}Si MAS NMR spectrum of calcined MCM-41. The signal from Q^4 groups exhibits the highest intensity. If the ^{29}Si cross polarization (CP) MAS NMR spectra are considered, it can be seen that most of the silicon atoms are surrounded by O-Si units. This indicates that most of the silicon atoms are in the pore walls rather than on the surface of SBA-15.[155] The ratio of the signals from Q^3 and Q^4 groups is 1 : 3 for MCM-41 and 1 : 4 for SBA-15. Differences in the ratios can be attributed to various pore sizes and pore wall thicknesses. The Q^3:Q^4 ratio confirms that SBA-15 has thicker pore walls compared to MCM-41.[156]

In addition to the investigations of silanol groups by ^{29}Si MAS NMR measurements, it is possible to distinguish them by IR spectroscopy.[149;150;153] Overlaps of the individual bands sometimes make assignment difficult. This complicates the quantitative determination of different types of silanol groups.[157] The presence of isolated and geminal silanol groups can be evidenced by the band between 3760 cm^{-1} and 3735 cm^{-1}. The band between 3620 cm^{-1} and 3200 cm^{-1} is assigned to interacting silanol groups. This band often overlaps with bands of isolated silanol groups and Si-O bonds in the silica lattice.[157] It is described that silanol groups connected by hydrogen bridges appear as a shoulder of the band of isolated silanol groups at 3710 cm^{-1}.[149]

Besides the knowledge of the nature of silanol groups, it is important to characterize the number of accessible silanol groups on the silica surfaces in terms of the chemical properties of silica materials. Quantification is difficult because water from air is easily adsorbed onto the silanol groups. Accurate quantification by MAS NMR, Fourier-transform infrared spectroscopy (FTIR), selective chemisorption, deuterium exchange, or mass spectroscopy (MS) is usually hampered by the need of very controlled conditions for sample preparation and the measurement itself.[149] It is impossible to localize silanol groups on different surfaces using these methods.[151] Another problem is the comparability of data known from the literature about the silanol group density on silica surfaces. Table 1.1 lists exemplary silanol group densities from literature. The silanol

Table 1.1: Silanol group densities on surfaces of MCM- and SBA-type materials reported in the literature.

reference	silanol group density of MCM-type materials [$SiOH/nm^2$]	silanol group density of SBA-type materials [$SiOH/nm^2$]
ZHAO ET AL. [140]	2.5 - 3	6 - 8
RAMÍREZ ET AL. [150]	not investigated	3.4 - 6.5
KOZLOVA AND KIRIK [158]	3 - 4	5 - 6

group density on surfaces of MCM-41 reported by ZHAO ET AL. ranges from $2.5\,SiOH/nm^2$ to $3\,SiOH/nm^2$, while the silanol group density on surfaces of SBA-15 ranges from $6\,SiOH/nm^2$ to $8\,SiOH/nm^2$.[140] For comparison, KOZLOVA AND KIRIK indicated a silanol group density on surfaces of MCM-41 ranging from $3\,SiOH/nm^2$ to $4\,SiOH/nm^2$ and a silanol group density on the surface of SBA-15 ranging from $5\,SiOH/nm^2$ to $6\,SiOH/nm^2$.[158] Differences in the data can be explained by various reaction conditions and parameters used during the determination of the silanol group density.[149] For example, an influence on the quantification is the temperature dependency of silanol groups. With increasing temperature, a decrease of the silanol group condensation is visible as result of random condensation reactions. Silanol groups, which interact via hydrogen bridges convert into free silanol groups. At temperatures above $600\,°C$, the number of free silanol groups decreases. This is due to the formation of siloxane bridges by further condensation reactions. The formation of these siloxane bridges can lead to the collapse of surface and pore structure.[92;159] Various approaches for determining silanol group densities on silica surfaces and their accessibility are discussed in the literature. One possibility is the determination based on hydrated and dehydrated silica and the investigation with IR spectroscopy. According to this, the bands of water in the IR spectrum occur at $1630\,cm^{-1}$ and $5260\,cm^{-1}$, while the ones for silanol groups occur in the ranges of $3800\,cm^{-1}$ to $3000\,cm^{-1}$ and of $4800\,cm^{-1}$ to $4200\,cm^{-1}$.[160]

The quantification of silanol groups using diffuse infrared reflectance Fourier transform (DRIFT) spectroscopy is possible. DRIFT measurements using pyridine as probe molecules are suitable for this purpose.[150] The band appearing in the DRIFT spectrum at $1595\,cm^{-1}$ can be attributed to pyridine molecules interacting with silanol groups via hydrogen bridges. In contrast, the band at $1446\,cm^{-1}$ is characteristic for weaker interactions between isolated silanol groups and pyridine molecules.[92;161] The broad band at $3050\,cm^{-1}$ in the DRIFT spectrum masks the vibrational bands of isolated and hydrogen bridged silanol groups interacting with pyridine molecules.[150] For determining the number of isolated silicon groups and via hydrogen bridges connected ones, the peak areas of pyridine bands, the surface area of the silica material from nitrogen physisorption measurements, and the amount of desorbed pyridine are needed. The amount of desorbed pyridine is determined by thermogravimetric measurements. In the literature, silanol group densities between $3.4\,SiOH/nm^2$ and $6.5\,SiOH/nm^2$ are indicated for SBA-3.[150] Another discussed way to determine silanol group densities is treating silica materials with benzylamine. Afterwards,

the amount of benzylamine adsorbed by the silica material is determined spectroscopically. As for nitrogen physisorption measurements, the adsorption isotherms show the typical behavior of forming a monolayer before reaching a plateau at higher benzylamine concentrations (1.7 μmol benzylamine per m^2 for SBA-15). Thus, the estimated silanol group density is approximately equal to 1 SiOH/nm^2. It should be noted that a considerable part of the surface determined by nitrogen physisorption measurements is inaccessible to benzylamine molecules. The microporous wall of SBA-15 is the reason for this. The micropores are accessible for nitrogen molecules, but not for benzylamine molecules, which is why no conclusions can be drawn about the proportions of various silanol groups. [151]

It is also possible to determine silanol group densities by thermogravimetric measurements. As with IR spectroscopic investigations, the silica material is loaded with pyridine. Depending on the interaction of pyridine molecules with various silanol groups, thermogravimetric measurements yield expected peaks between 50 °C and 100 °C and between 120 °C and 170 °C. The desorption features ranging between 50 °C and 100 °C are attributed to desorption of pyridine molecules interacting with hydrogen bridged silanol groups. [150] Pyridine desorbing from isolated silanol groups is classified within the peak between 120 °C and 170 °C. [162] However, thermogravimetric studies identify three peaks rather than just two. The first two peaks at 50 °C and 100 °C are also assigned to desorption processes of pyridine molecules interacting with hydrogen bridged and isolated silanol groups during the study. In contrast, the peak in the temperature range between 140 °C and 150 °C is assigned to desorption of pyridine molecules from both isolated silanol groups and silanol groups connected by hydrogen bridges in small cavities. Depending on how small the cavities or their entries are, the penetration of pyridine is hindered, giving rise to a broad band. Determining the number of silanol groups, one pyridine molecule is assumed to interact with each pair of silanol groups connected by hydrogen bridges. Using the findings of thermogravimetric measurements, silanol group densities between 3 SiOH/nm^2 and 5 SiOH/nm^2 are observed as a function of calcination temperature and duration. Most of the identified silanol groups are silanol groups linked by hydrogen bridges. [150]

The comparison of silanol group densities determined from IR spectroscopic and thermogravimetric investigations reveals that silanol group densities determined by IR spectroscopy are higher than these determined by thermogravimetric measurements. The pyridine loss of the third peak is assigned to free silanol groups and, therefore, only one pyridine molecule is counted per silanol group, which might be the reason for the observed discrepancy. [150]

In summary, it can be stated that especially the quantification of the silanol group density of silica materials poses a challenge. Overlaps of the individual bands sometimes make assignment difficult. Since the density of silanol groups depends on many factors, literature values can only be used as estimates.

1.4.2 Characterization of the Pore Size of Mesoporous Silica Materials

After the synthesis of mesoporous silica materials, the structure-directing template must be removed. The hexagonal structure of mesoporous silica materials remains, whereby the thickness of the pore walls depends on the material itself and the conditions during the synthesis. The structure of mesoporous silica materials is of great interest in determining the most suitable material for various applications. Mesoporous silica materials consist of voids, i.e. pores or channels, separated by the silica matrix. Depending on the pore sizes and the associated pore walls of different thicknesses, the hydrothermal, mechanical, and chemical stabilities of the materials differ (Chapter 1.4.3).[163] Various methods are known for determining pore sizes as well as pore wall thicknesses of silica materials.

Based on nitrogen physisorption measurements, the detection of micro- and mesopores is possible using various methods.[14] For sorption studies, gases such as nitrogen, carbon monoxide, and argon, or vapors like water vapor are used as adsorptives.[164] Depending on the pore size and the surface properties, the appropriate adsorptive must be selected. In physisorption measurements, the micropores are initially filled with the adsorptive at low relative pressures. The exact range of the relative pressure depends on the shape and size of the micropores as well as on the size of the adsorptive molecules and the interactions between the molecules of the adsorptive and between adsorbent and adsorptive.

When filling, a distinction is made between ultra micropores, which are no more than two or three molecular diameters in size, depending on the pore geometry and larger micropores. After filling the ultra micropores, which is called "primary micropore filling", the larger micropores are filled in a secondary process at higher relative pressures. In this process, the interactions between adsorptive and adsorbent decrease, while the cooperative interactions between adsorptive and adsorbate increase in a confined space. Thus, the choice of adsorptive is important. Nitrogen is frequently used for the analysis of micropores and mesopores in the standard measurement at 77 K. However, due to the quadrupolar properties nitrogen is not optimal, since it leads to specific interactions with a variety of surface functional groups and exposed ions. This affects the orientation of the adsorbed nitrogen molecules on the surface of the adsorbent and strongly influences the filling pressure of the micropores, which is why extremely low relative pressures are required. In this pressure range, the diffusion rate is slow, which makes it difficult to measure equilibrium adsorption isotherms. It must be considered that nitrogen molecules can be adsorbed at the entrances of narrow micropores and close them. As a result, the pore filling pressure does not correlate uniquely with pore size and structure. Despite the potential difficulties, the literature mainly contains data on nitrogen physisorption measurements.

Aside from nitrogen, argon is a relatively common adsorptive. It does not have quadrupolar properties and therefore does not exhibit specific interactions with surface functional groups. When argon physisorption measurements are performed at a temperature of 77 K, the analysis of the isotherms is difficult, while the cryogenic temperature is 87 K.[14] One reason why the advantages

of argon in determining pore size and surface area do not yield the expected benefits is that argon physisorption measurements at 77 K make it impossible to characterize the pores in the microporous and mesoporous regions. At 77 K, the measurement temperature is about 6.5 K below the triple point temperature of bulk argon. Therefore, only pores with a pore size of less than 12 nm can be characterized. This can be avoided by performing argon physisorption measurements at 87 K.[165] Another reason why argon physisorption measurements at 77 K are not optimal is that although the argon adsorption isotherms at 77 K are shifted to higher relative pressures compared to those of nitrogen physisorption measurements, the shift is not large enough compared to argon physisorption measurements at 87 K. Accordingly, adsorption in the narrow micropores occurs at relative pressures lower than 10^{-5}. At these pressures, the adsorption kinetics are very slow, so the supercooled state of argon in the micropores should be assumed.[166] For these reasons, argon physisorption measurements are performed usually at 87 K.[5;166;167] The higher temperature allows the narrow micropores to be filled with argon at much higher relative pressures. This accelerates equilibration and enables the measurement of adsorption isotherms with high resolution. Furthermore, it leads to measurements with a more direct correlation between the pore filling pressure and the confinement effect (despite the dependence on pore size and shape). For zeolitic materials, metal-organic frameworks (MOFs), and some oxides, as well as for activated carbon, this is particularly important.

Another adsorptive that is used rather infrequently is carbon dioxide. Kinetic limitations at cryogenic temperatures (87 K, 77 K) limit the adsorption of argon and nitrogen for the characterization of very narrow micropores. This can be circumvented by using carbon dioxide as adsorptive at 277 K.[14] With the correct choice of the adsorptive, the determination of the micropore volume from type I physisorption isotherms is relatively straightforward. This is caused by the horizontal plateau of the isotherm which corresponds to the limited uptake for the micropores. Thus, the capacity can be considered as the adsorption of the gas at the corresponding measurement temperature as the micropore volume. For the conversion of the capacity to the micropore volume, the pores are assumed to be filled with the condensed adsorptive in the normal liquid state (Gurvich rule).[5;167] The problem is that the plateau of the adsorption isotherm is rarely horizontal, most microporous materials having a large external surface area and additional mesopores. This means that the Gurvich rule for determining the micropore volume is not always applicable. Several proposed solutions are known to circumvent this problem. For example, an empirical comparison of an isotherm with a suitable standard is performed. The standard must be a non-porous reference material with a similar chemical composition.

The t-plot method is a standard multilayer thickness curve and depends on the application of the Brunnauer-Emmett-Teller (BET) method, which cannot be always applied. This problem can be circumvented with the α_s-plot method. It does not require evaluation of monolayer capacitance and is more adaptable compared to the t-plot method.[5;167] Effects of micropore size and shape on molecular packing are not considered in this method.

In many cases, it is useful to apply methods related to molecular simulation (MC) and density functional theory (DFT) to determine the micropore volume. These methods describe the configuration of the adsorbed phase at molecular level and are superior to empirical and semi-empirical methods. They offer a more reliable approach to pore size analysis over the entire nanopore range. The basic principle of these methods is to describe the distribution of adsorbed molecules in the pores at the molecular level. This provides detailed information about the local fluid structure near the adsorbent surface. A pore model depends on the interaction potential between liquid and solid, so various pore shape models (e.g., slot, cylindrical, spherical, and hybrid geometries) have been developed for different classes of materials such as carbons, silicas, and zeolites. For this reason, the application of methods relying on MC and DFT is only useful if a given nanoporous system is compatible with the chosen MC/DFT kernel.[14]

Besides the micropores, the pore volume and pore size of mesopores can be derived from physisorption measurements. If the material is free of macropores, a type IV isotherm is obtained that is nearly horizontal at high relative pressures. The pore volume can then be derived from the amount of adsorbent at a relative pressure close to the relative pressure of one. The pores are assumed to be filled with the adsorbent in the liquid state.[5;167] The analysis of the mesopores is based on the modified Kelvin equation (Barrett, Joyner, and Halenda (BJH) and Broeckhoff and de Boer). It should be noted that these methods significantly underestimate the pore size for narrow mesopores.[14;168] By adding MC or DFT, these inaccuracies can be corrected, and a more reliable assessment of the pore size distribution over the entire domain is obtained.[14] With the pore sizes determined from physisorption measurements and the lattice parameters determined from X-ray analytical studies, the pore wall thickness of mesoporous silica materials can be estimated.[25;169;170]

The standard method for characterizing macropores is mercury porosimetry. Mercury porosimetry can also be used to study small mesopores ($d_{\text{pore,DFT}}$ >3 nm). In addition, mercury porosimetry is used to obtain information on pore shape as well as network effects.[171;172] The main assumption of mercury porosimetry is a cylindrical pore shape of the porous materials. This assumption is used to describe the relationship between pressure difference at the curved mercury interface and the corresponding pore size using the surface tension of the mercury and the contact angle between solid and mercury. The relationship is known as the Washburn equation. If the pore shape of the material is not cylindrical, there may be large differences between the pore size determined from mercury porosimetry and the actual pore size. During the analysis process, mercury is pressed into the pores, which is why pressure is one of the most important measured variables. This is explained by the fact that an incorrect pressure measurement automatically means an incorrect pore size. The capacitance measurement is almost always made between a metal shield on the outside of a measuring cell and the length of the mercury column inside, so the pore volume is another important parameter. This is because if the inside or the outside of the measuring cell is not uniform or some other external factors affect the capacitance, this will lead to inaccurate values.[173] The unique feature of mercury porosimetry is the non-wetting characteristic. This means that the

contact angle between mercury and the sample surface is >90°. For this reason, the mercury must be forced into the pores with pressure. With increasing pressure, the mercury can penetrate pores with decreasing pore size. Accordingly, there is an inverse relationship between pressure and pore size, thus the pore size distribution can be determined.[4] Although the contact angle is a parameter that significantly affects the results, a fixed value is usually chosen, regardless of the sample material.[173]

As an alternative technique for determining pore size distributions, thermogravimetric analysis was described in the early 1990s. In this method, the porous materials are first loaded with an adsorbate. Then, thermogravimetric analysis is performed and the pore size is determined indirectly by mass loss. At the beginning of the measurement, the desorption of liquid outside the pores is detected. The second stage of mass loss corresponds to the capillary condensed liquid inside the pores together with the adsorbed film on the pore walls. This corresponds to the measurement of the total pore volume. The inflection point of the step in the desorption curve corresponds to the maximum of the pore size distribution. With the Kelvin equation, it is possible to convert the pore size distribution from sample mass loss as a function of temperature to the volume loss as a function of the pore radius.[174] Various publications discuss the optimization of the technique for determining the pore size distribution with respect to the conditions during the desorption process and the choice of adsorptive for different samples.[175–178] Benzenes[175;177], alcohols such as n-butanol[176;178], acetone, diethyl ketone[177] and aliphatic hydrocarbons such as n-heptane[177;178] were used as adsorptive. It was found that it made a difference whether the program was a heating program (constant heating rate) or a quasi-isothermal program (no constant heating rate). Depending on the adsorptive, the optimum desorption conditions must be selected. The optimum desorption conditions are determined by the heating rate where the shape of the distribution curve approximates those of the nitrogen physisorption measurement. Thereby, the changes in heating coefficients in the quasi-isothermal program only slightly affect the maximum of the distribution curves.[176;178] With the selection of the appropriate adsorbate, it is possible to determine the total pore volume as well as the pore size distributions from the thermogravimetric studies.[175;177] However, corrections must be made owing to surface film effects. The degree of interference depends on the choice of adsorptive.[177] Overall, the differences from the values determined from nitrogen physisorption measurements as well as from mercury porosimetry are large.[178]

Another technique for determining the pore size distribution is nuclear magnetic resonance (NMR) spectroscopy. The ^{1}H NMR measurement is proving particularly useful for in situ experiments. The reason is that characterization of porous materials with standard methods requires dry samples during the measurement. For low-field spin-lattice NMR relaxation measurements, dry samples are not required.[179] The relaxation time of water molecules is faster or slower depending on where they are located in the porous material. Enhanced interactions of water molecules at liquid-solid interface that disrupt molecular motion are one reason for the different behavior. Due to the externally applied high-frequency voltage, water molecules, in the pores relax faster than water

molecules in the bulk phase. This leads to a decrease in the decay constant of the relaxation rate, which is directly related to the pore volume to surface area ratio.[180;181]

An alternative to characterize pores by means of nitrogen physisorption measurements as well as X-ray analytical examinations is the measurement of the pore size by taking TEM images. Determination in this manner should be used with caution, as the measurement is error prone. Inaccuracies can occur in the measurement of pore size and wall thickness and during the acquisition of the TEM images. This is because it cannot be guaranteed that the frontal view on the pore entrances of the porous silica particle is always available for measurement. A non-frontal view creates an incorrect determination. Similar to the determination of the pore size, the lattice parameter and the pore wall thickness can be detected with the help of TEM images. The procedure is not or only little explained in the literature.[103;170;182]

In addition to the methods already described for determining pore size, inverse size exclusion chromatography (ISEC) is another option.[183] This method has been used to characterize various materials to determine pore size and pore size distribution.[184–187] In ISEC, the material to be characterized is often packed as a monolith into a column, which is then treated with solutes of different particle sizes.[188;189] It is important that the mobile phase and solvent do not interact with the stationary phase, i.e., the material under study. If the solute is chosen correctly, the corresponding chemical interactions between the stationary and mobile phases are suppressed, so that exclusion is based on a physical sieving process. Information about the pore size as well as its distribution can then be obtained from the resulting retention time.[189;190] ISEC is usually performed using standard monodisperse solutions. However, there are also studies showing that the same information about pore structure can be obtained with polydisperse suspensions. In this case, care must be taken to minimize dispersive mass transfer effects.[191]

1.4.3 Stability of Mesoporous Silica Materials

Mesoporous silica materials modified with different functionalities can be used in heterogeneous catalysis.[192;193] For the study of confinement effects in catalytic applications, spatially controlled functionalization of mesoporous silica materials is necessary. At the same time, it is important that the developed catalysts can be used in larger reactors and synthesized on a larger scale. Therefore, the catalysts, which are often prepared as powder, must be formed, e.g., by tableting or extrusion. For this reason, mechanical stability of the catalysts is of interest.

The mechanical stability of calcined SBA-15 as a function of pressures between 16 MPa and 260 MPa was investigated.[194;195] The X-ray diffractograms showed a loss of intensity of the characteristic reflections d_{100}, d_{110}, and d_{200} for the calcined and pressed SBA-15. The decrease of the intensities was attributed to loss of long-range order within the mesoporous silica material. The lattice parameters and the main pore size of the SBA-15 treated with pressures between 16 MPa and 260 MPa did not change compared to the unpressed sample. However, the pore size distribution widened with increasing pressure. The widening of the pore size distribution is ex-

plained by a deformation of the pores under pressure. The change in the pores reduced surface area and mesopore volume.[194;195] Literature has dealt with the difference of various silica materials with regard to their mechanical stability. The findings regarding the mechanical stability in air of MCM-41 and MCM-48 are similar to those of SBA-15. When the investigations were done in nitrogen, the samples are more stable against pressure having removed physisorbed water molecules prior to mechanical testing. This results in fewer Si-O-Si bonds being hydrolyzed during compression. ^{29}Si MAS NMR spectroscopic measurements show that the unpressed materials have Q^2, Q^3 and Q^4 species, while the Q^2 and Q^3 species increase at the expanse of the Q^4 for the samples pressed in air (compare Chapter 1.4.1). This effect is not visible for the samples pressed in nitrogen.[163;196]

Investigations done by GALARNEAU ET AL. [197] suggest, that mechanical and thermal degradation follow different mechanisms. A decrease in surface area and pore volume is visible by both influences, but a change in intergranular porosity is observed only under pressure. Considering thermal stability of mesoporous silica materials, pore wall thickness has an important influence onto their mechanical stability. Results from nitrogen physisorption measurements suggest that the thicker the pore walls the more stable the mesoporous silica material is against high temperatures.[197]

Studies on the stability against hydrothermal treatment show that surface areas and pore volume decrease while the pore size distribution for MCM-41 broadened. X-ray analysis shows a deterioration of the structure after the hydrothermal treatment. The reason for these observations is the partial hydrolysis of Si-O-Si bonds within the silica matrix caused by the hydrothermal treatment. Owing to the thicker pore walls of SBA-15 compared to MCM-41, the structural loss of SBA-15 is lower as more Si-O-Si bonds need to be hydrolyzed to destroy the porous structure. The higher the temperature during the hydrothermal treatment, the greater the destruction of the mesoporous silica structure.[163]

Since mesoporous silica materials are stable in aqueous solutions with a pH value of seven or less, the chemical stability studies are conducted in an alkaline environment.[198] For the chemical stability studies, the mesoporous silica materials were treated with 0.5 mol sodium hydroxide solution. This treatment completely hydrolyzed the silica lattice of MCM-41 and SBA-15 within one hour. Not even the change from a hydrophilic to a hydrophobic surface makes the mesoporous silica material more stable. After two hours, the sample has dissolved to such an extent that the particles are too small for characterization.[163]

It is shown that various mesoporous silica materials are stable to different influences. Structural properties such as pore wall thickness or surface properties play an important role and enable the stability of the materials to be influenced during production and subsequent modification.

1.5 Functionalization of Mesoporous Silica Materials

In general, surfaces of mesoporous silica materials are functionalized in many cases to multiply their catalytic properties. Functionalization of porous materials describes the modification of surface properties and thus their activity. This makes materials suitable for a wider range of applications, because functionalization with specific groups improves the range of properties of the porous materials without deteriorating the already existing positive properties such as porosity or large surface areas.[12;199;200] Porous materials with a large surface area are particularly suitable as support materials. In principle, it is possible to introduce active sites directly during the synthesis of the support materials or to add them in a further step after preparation.[17;201–203] X-ray analytical studies show that the insertion and anchoring of active sites do not significantly affect the structure of the material.[12;201] However, functionalization of porous materials leads to a reduction in surface area.[201] Porous silica materials like SBA-15 are particularly suitable as support material for surface modifications thanks to their large pore sizes and thick walls resulting in a high hydrothermal stability.[204]

1.5.1 Catalytically Active Species

Depending on the field of application, the surface silanol groups can be active species. But compared to zeolites, silanol groups of mesoporous silica materials as active centers are no that defined due to the relatively thick pore walls. However, with the functionalization of mesoporous silica materials, active centers are generally introduced into the lattice structure or on the surface of a support material.

In many cases, metals in form of ions, particles or oxides are introduced into a support materials as active centers.[17] By introducing heteroatoms such as aluminum, boron, fluorine, titanium, gallium, or oxide groups, silicon atoms are replaced in the lattice structure of the support material.[17;205] When this creates a charge imbalance, cations must be introduced into the pores for charge balancing. Replaced ions, which are introduced, act as acidic or redox active centers on the pore walls of the support material. The concentration of heteroelements in the structure is significantly lower, when they have been introduced into an as-synthesized support material.[17] Rather, different centers are present in various local environments and are more similar to metal-substituted amorphous silica materials. When the lattice atoms are replaced during the synthesis, relatively homogeneous incorporation and uniform distribution of heteroatoms in the support material are achieved.[17;205] Furthermore, it is possible to exchange heteroatoms after the synthesis of support materials, but mainly the pore walls are then functionalized.[17]

Another method for the introduction of catalytic active centers is the deposition of nanoparticles on surfaces of support materials. The introduction of active species in form of nanoparticles is possible in various ways. On the one hand, nanoparticles can already be introduced into the gel during the synthesis.[146;206–211] On the other hand, it is possible to apply active species to support

materials by impregnation or vacuum evaporation.[146;209;211–214] The advantage of the deposition of nanoparticles is the large catalytically active surface area, which is introduced by the high surfaces of nanoparticles.[215] A disadvantage is the risk of pore blocking if, e.g., agglomerates of the nanoparticles are formed due to their high loading.[17;205]

A third way to modify porous materials is to anchor molecular catalysts on surfaces of a support material.[17] The simplest method is to physically adsorb the molecular catalyst on the surface.[216;217] However, the interactions between the catalytically active component and the support material are relatively weak. Leaching of the active species in the presence of solvents is thus possible.[17] An alternative to the adsorption of catalyst complexes on surface-active groups of the support material is the attachment by forming chemical bonds. The introduction of functional groups bound to the surface of the silica material via a chemical bond is possible in various ways. One of them is the possibility to introduce functional groups as active centers into a lattice structure already during the synthesis of the mesoporous silica material used as a support material by adding an organosilane.[204] The advantage of this method is to achieve a relatively homogeneous distribution of the functional groups on the surface.[17] Alternatively, anchoring the functional groups on the surface of the support material after synthesis can also be realized.[17] In this case, the functional groups are subsequently applied to the surface via covalent bonds.[204] Afterwards, catalyst complexes can be attached to the functional groups, which are then called anchor groups, applied to the surface of the support material, regardless of the type of modification. In this way, molecular catalysts are immobilized onto the surface of the support material.[218] Literature-known organosilanes serve as anchor groups.[200;219]

1.5.2 Introduction of Functional Groups

The introduction of functional groups into the structure of mesoporous silica materials is possible already during the preparation.[220] In this approach, referred to co-condensation approach or one-pot synthesis, hydrolysis and co-condensation of tetraalkoxysilanes with one or more organoalkoxysilane take place in a single reaction mixture in presence of the structure-directing template. Organic residues introduced in this way are mainly located on the silica surface or protrude from the walls into the pores. There are two reasons for this. Firstly, incompatibility of the hydrophobic organic residues with the polar silica lattice results in a large portion of the organosilane being enclosed in the pore walls. Secondly, lower hydrolysis and condensation rate of the organosilane component in a basic environment compared to pure mesoporous silica materials plays an important role. This leads to a slower polycondensation process.[221] By integrating functional groups during the synthesis of mesoporous silica materials, they are relatively homogeneously distributed without affecting the pore size.[17;221] A major disadvantage of the co-condensation method is the limitation on the functional groups density. The reason for the limitation is that with increasing organosilane concentration in the reaction mixture, the arrangement of template molecules providing the structure is hampered.[221] In addition, high organosi-

lane concentrations can cause an inhomogeneous distribution of functional groups.[221;222] Functional groups installed by contributed co-condensation can be used to anchor various synthetic catalysts, biomolecules, and polymers to create new functional materials.[204] Both structure and morphology of the functionalized materials can be highly dependent on the amount and type of the organosilane used.[206] For example, azide-containing nanoparticles with particle size between 50 nm and 80 nm were found to agglomerate more easily.[223]

An alternative to the surface modification of mesoporous silica materials with organosilanes via co-condensation is the functionalization after synthesis. Insertion of organosilanes on silica surface areas is typically used to bind organic residues as functional groups onto silica surfaces via Si-C bonds. Organosilanes typically used for the modification of mesoporous silica materials are chloro-, methoxy- and ethoxysilanes.[224] A major advantage is the preservation of mesoporous silica materials as support material, whose preparation can be well controlled.[202] Further processing of mesoporous silica materials such as MCM-41 or SBA-15 into a catalytic material while retaining large surface areas, pore sizes and their arrangement is relatively straightforward. Modifications with moisture-sensitive trichlorosilyl groups release hydrogen chloride, which is harmful to many catalyst systems. Consequently, it is useful to utilize other organosilanes for the functionalization of mesoporous silica materials. Instead of using organosilanes with trichlorosilyl groups, it is possible to use organosilanes with trialkoxysilyl groups. During the functionalization process, the corresponding alcohols are released. Even with this method, there is a risk of altering sensitive organic molecules.[222] As such, it is necessary to adjust reaction conditions, so that the mesoporous silica materials can be modified at low temperatures in a short reaction time with moisture-insensitive reagents without affecting the actual functionalization.[202] Subsequent introduction of functional groups onto the surface areas of mesoporous silica materials has the advantage of preserving the mesoporous structure. A disadvantage is that the lining of the pore walls influences porosity[221] as well as pore volume of the mesoporous silica material.[203] At the same time, the reaction conditions, such as the choice of solvent during the functionalization, play an important role. This can be explained by the solubility parameters of the different solvents. The solubility parameter is related to the polarity of the solvent. Thereby, the polarity parameter increases with the increase of the solubility parameter. The solubility parameter is subdivided into the various intermolecular interactions (e.g., for dispersion interactions, dipole interactions, and hydrogen bridges). These parameters can be used to determine the appropriate solvent for the solubility of certain substances.[201] Another difficult point is the achievement of the homogeneous distribution of functional groups on the silica surface. While at the beginning of the functionalization, organosilane molecules react preferentially with silanol groups at the pore entrances of the mesoporous silica material, diffusion problems can occur with progress of the functionalization process. In extreme cases, i.e. with very bulky molecules, a complete closure of the pores can occur.[221]

Silylation of support materials like mesoporous silica materials offers possibilities of imparting catalytic properties to support materials.[225] The reaction conditions, such as the choice of solvent, play an important role in surface functionalization with silanes.[200;201]

1.5.3 Selective Functionalization

The functionalization of enzymes for the production of stereoselective products is a miracle of the nature. Until now, it is difficult to copy the function of enzymes. A possibility to copy the function of enzymes is the use of complex, organic catalysts. Often these are expensive and difficult to regenerate, so the use of solid catalysts, whose catalytic active component is located exclusively in the pores, is of great interest. The porosity of the porous support material helps to obtain the desired configuration of the products. In order to take advantage of the porosity, it is necessary to ensure that the catalytic active sites are located exclusively in the pores of the porous support material. Only then, it is possible to carry out the reactions under confinement. Therefore, selective functionalization plays an important role for these catalysts. It enables the controlled immobilization of highly selective catalyst complexes on the pore walls of porous support materials and allows reactions to be carried out under confinement. Selective functionalization of mesoporous silica materials is challenging as it has been impossible to determine the precise localization of the introduced functional groups.[192] For selective functionalization, it is important to recognize that the surface of porous materials is divided into two areas. One is the particle surface and the other one is the surface area of the pore walls. In most cases, the particle surface of mesoporous materials is the smaller part of the total surface area compared to the surface area of the pore walls, but it is easily accessible. For the surface area of the pore walls, it is the other way around: It is the larger part of the total surface area, but the surface area of the pore walls is difficult to access.[192] As explained earlier, for selective functionalization it is of great importance to know where the functional groups are located on the surface of the porous support material.

There are two different methods for selective functionalization:[192]

The diffusion-controlled method is one of them. Starting material of this method is a porous material, whose pores are opened (through extraction with ethanol or calcination of the as-synthesized material for example). The functionalization process consists of two steps. First, the particle surface of the porous material is functionalized and in a further step the pore walls. This method of selective functionalization is suitable only for porous materials with small mesoporous (d_{pore} <3 nm) and microporous. The reason is that for the functionalization of the particle surface, functionalization reagents must be used whose molecular diameter is larger than the pore size.[11;12;205;226]

The other approach for selective functionalization of porous materials is the pore protection method. This approach is suitable for selective functionalization of all porous materials,[205;227;228] because the pores of the starting material are closed and thus inaccessible to the functionalization reagent, which is used for the modification of the particle surface. Accordingly, either as-synthesized materials[192;229] or calcined materials whose pores have been closed again[224] are used.

Since initially, only the particle surface is accessible through the closed pores, it can be functionalized without considering the functionalization reagent. It should be considered that besides the particle surface, the pore entrances or parts of the pore walls are functionalized. A reason for this is that the pores are not filled to the edge with structure-directing template. As a result, more

silanol groups are accessible than are present on the particle surface that can be reached by the functionalization reagent. Another reason is that organosilanes with chloro or ethoxy groups can dissolve parts of the template due to the amphiphilic character of the structure-directing Pluronic® P123. After functionalization of the particle surface and the pore entrances, summarized as the external surface, the template is removed from the pores. For this purpose, Soxhlet extraction with ethanol is usually performed. In the final step, the pore walls can be functionalized since the particle surface is passivated.[192;229]

Various approaches for the selective functionalization of porous silica materials have been described in the literature. For example, the selective functionalization of micropores of SBA-15 with trivinylchlorosilane and subsequent introduction of palladium complexes has been described. In this case, it was suspected that the silanol groups on the particle surface as well as on the pore walls were made inaccessible to the metal complexes by functionalization with trimethylsilyl chloride.[230] Another example is the stepwise functionalization of as-synthesized MCM-41. In this case, the pore protection process was executed. The particle surface was modified with mercaptopropyl moieties before the structure-directing template was removed from the pores by Soxhlet extraction. Then the pore walls were functionalized with aminopropyl moieties. It was assumed that all freely accessible silanol groups on the particle surface reacted with the functionalization reagent.[229] The putative selective functionalization of calcined silica materials was performed by WEBB ET AL. [192] and ZIEGLER ET AL. [231] by refilling the pores before functionalization of the particle surface. In both approaches, the particle surface was modified with 1,1,1-trimethyl-*N*-(trimethylsilyl)silanamine and the pores were opened by Soxhlet extraction. Subsequently, the pore walls were functionalized with mercaptopropyltrimethoxy[192] or immobilized with a ruthenium complex[231], respectively. As with other works, it was assumed that selective functionalization was performed. However, none of the studies have actually shown whether this is true.

2
Motivation and Objectives

The function of enzymes for the production of stereoselective products is unique. Therefore, mimicking of enzymes for the production of enantioselective products is an important topic. Immobilization of highly selective complex noble metal catalysts in the pores of mesoporous silica materials is one approach to obtain the high enantioselectivity and productivity of enzymes. This is because the confinement effect resulting from the porous structure of the support material can be exploited by utilizing the pore and channel structure of mesoporous silica materials. However, this requires the immobilized metal complexes to be located exclusively on the mesopore walls of the support material. Therefore, the efficient and spatially controlled functionalization of mesoporous silica materials as support materials is very important to be able to immobilize catalytically active metal complexes and to proceed with heterogeneous catalysis in a shape-selective way. To ensure that the catalytically active species are located exclusively in the mesopores, all freely accessible silanol groups on the particle surface and at the pore entrances of the support material must be passivated prior to the functionalization of the pore walls. Various methods for the controlled functionalization of mesoporous silica materials have been described in literature, but these do not clearly demonstrate that selective functionalization of the inner pore walls has been achieved.

Knowledge of the material properties is of enormous importance in order to exploit the advantages and eliminate any weaknesses in the corresponding field of application. Among other properties, the lattice parameter and pore size are important for the determination of appropriate functionalization reagents for subsequent modification steps. In this work, it was the task to determine the lattice parameter and pore size of mesoporous silica materials in the pore range between 3 nm and 11 nm using physisorption and SAXS measurements as well as TEM investigations and probe particles. The results of the different characterization methods were compared and evaluated in Chapter 3.1. Reason for this comparison is that not all characterization methods are available at all times and knowledge of the material properties is still required.

With knowledge of the material properties, selective functionalization can be tackled in the next step. Since spatially controlled functionalization and precise analytical detection are still a challenge, it was the goal of this work to develop a method for selective functionalization of meso-

porous silica materials (Chapter 3.2). For this purpose, the silanol groups on the particle surface as well as at the pore entrances summarized as external surface were first functionalized. In a separate and independent control step, the complete inertization of the external surface was demonstrated. With the knowledge of the complete functionalization of the external surface and after removal of the structure-directing template, finally the pore walls were functionalized. The control step was used to demonstrate that the functional groups were located exclusively on the pore walls.

Furthermore, this work dealt with the influence of template removal method on the mechanical stability of SBA-15 (Chapter 3.3). Background is that there are different approaches depending on the procedure of the functionalization of mesoporous silica materials. Regardless of the functionalization method, the catalysts are subjected to stresses, e.g., during reactor loading and during reactor performance, so the mechanical stability of the catalysts is important. To investigate the influence of the template removal method, the different intermediate materials of the functionalization process were pressed and the change of the samples was investigated.

Results and Discussion

3.1 Mesoporous Silica Materials

As described in Chapter 1.2, there are many different mesoporous silica materials known. In this work, SBA-15 was mainly used, but also a material prepared by the true liquid crystal templating mechanism. In addition, SBA-15, whose pores were expanded with a swelling agent, and MCM-41 were utilized. The synthesis procedure of the individual mesoporous silica materials are described in the publications on which this work is based.[1–3] After the preparation of the different mesoporous silica materials and before the selective functionalization of them, it is necessary to characterize them in order to obtain knowledge about the characteristic properties such as the lattice parameter or the pore size. Only if the structural properties are known, it is possible to optimize the material properties, e.g., by changing the synthesis conditions (Chapter 1.3.1) or additional functionalization of the surface areas (Chapter 1.5). An overview of common methods for material characterization is described in Chapter 1.4.2.

3.1.1 Characterization of Mesoporous Silica with Common Methods

The most common method for the determination of the lattice parameter is SAXS measurement. The resulting diffractograms of OMS_TLCT, MCM-41, SBA-15 and SBA-15_sa show the characteristic reflexes d_{100}, d_{110}, and d_{200}, which confirm the hexagonal structure *p6mm* of SBA-15 (Figure 3.1 (a)).[1] Using the maxima from the diffractograms, the lattice parameter a_{SAXS} was determined from the measured SAXS data (Table 3.1).

In addition to the lattice parameters, knowledge of the pore size and the pore size distribution is important in order to use porous materials as a catalyst or support material. A common method for the characterization of the pore size is to perform physisorption measurements with nitrogen as adsorptive gas. In the literature, nitrogen is cited as the most commonly used adsorptive gas. This is due to historical reasons, as liquid nitrogen used to be readily available, while liquid argon was not. The shape of the resulting isotherms and hystereses obtained by the physisorption measurements for calcined OMS_TLCT, MCM-41, SBA-15 and SBA-15_sa are as expected and show the
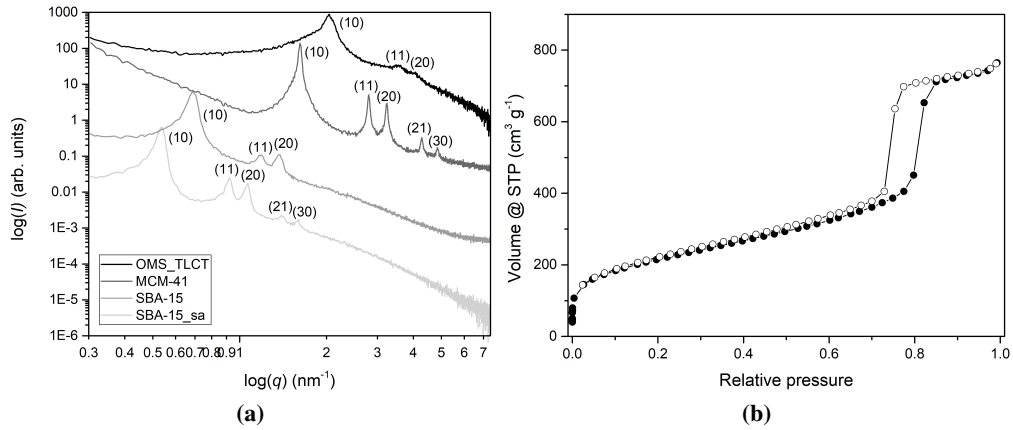
Figure 3.1: (a) Double logarithmic plot of the scattered intensity *I* versus the scattering vector *q*. The intensities of the scattering curves were normalized and stacked for better visualization. All four mesoporous silica materials exhibit a 2D hexagonal order, as revealed by the characteristic reflexes d_{100}, d_{110}, and d_{200}. Further maxima in the scattering curves of MCM-41 and SBA-15_sa hinting at an improved mesopore ordering. (b) In addition, an exemplary adsorption (●) and desorption (○) isotherm of SBA-15_sa resulting from nitrogen physisorption measurements.[1]

Table 3.1: Mean lattice parameters calculated from the SAXS data (a_{SAXS}) and determined from TEM images with the top view of the pores ($a_{TEM,FFT}$) and with the side view of the pore channels ($a_{TEM,line}$). The number of particles and pores examined on the basis of TEM images are given in parentheses.[1]

Sample	a_{SAXS} nm	$a_{TEM,FFT}$ nm	$a_{TEM,line}$ nm
OMS_TLCT	3.567 ± 0.008	4.3 ± 0.1 (2/292)	4.3 ± 0.4 (5/542)
MCM-41	4.502 ± 0.004	4.2 ± 0.2 (5/3320)	4.3 ± 0.9 (5/265)
SBA-15	10.37 ± 0.05	9.9 ± 0.3 (4/570)	9.7 ± 0.9 (7/241)
SBA-15_sa	13.74 ± 0.07	13.3 ± 0.3 (6/5870)	13.3 ± 2.5 (6/220)

characteristic properties for mesoporous materials with hexagonal pore structure and corresponding pore size (Figure 3.1 (b)). The same applies to the determined surface areas and pore volumes, whose values are in the range of the literature data.[1] For the determination of the pore size, the branch of the isotherm describing the thermodynamic equilibrium must be used. For MCM-41, SBA-15 and SBA-15_sa, the hysteresis closes at relative pressures >0.4, therefore the desorption branch describes the thermodynamic equilibrium state. Hence, the desorption branch is evaluated. For OMS_TLCT, the steep increase of the isotherms can be seen at a relative pressure <0.2. The adsorption and desorption branches of the physisorption measurements of OMS_TLCT do not

show large differences. Thus, the desorption branch was used to determine the pore size distribution for all materials in this work. The pore size distributions resulting from the desorption branch of the nitrogen physisorption measurements show mostly sharp and narrow distributions for all materials (Figure 3.2).[1] For historical reasons, the pore size is usually determined by the BJH method in the literature.[14] The pore sizes and distributions calculated by the BJH method obtained from the desorption branch of the nitrogen physisorption measurements are listed in Table 3.2 and shown in Figure 3.2, respectively. For OMS_TLCT and MCM-41, no pore size could be determined from the nitrogen physisorption measurement using the BJH method due to their small mesopores (Figure 3.2 (a) and (b)). The reason why the determination of the pore size distributions with the BJH method is unsuitable for materials with small mesopores is due to the software Quantachrome® ASiQwin version 3.01 used for the evaluation. By default, the software neglects the pressure points below 0.3 when evaluating the isotherms with the BJH method. Consequently, pores with a pore size <3 nm are not considered. In contrast, the DFT method gives more accurate results because it takes into account the hexagonal pore structure and the conditions during the physisorption measurement.[14;232;233] In this work, the non-localized density functional theory
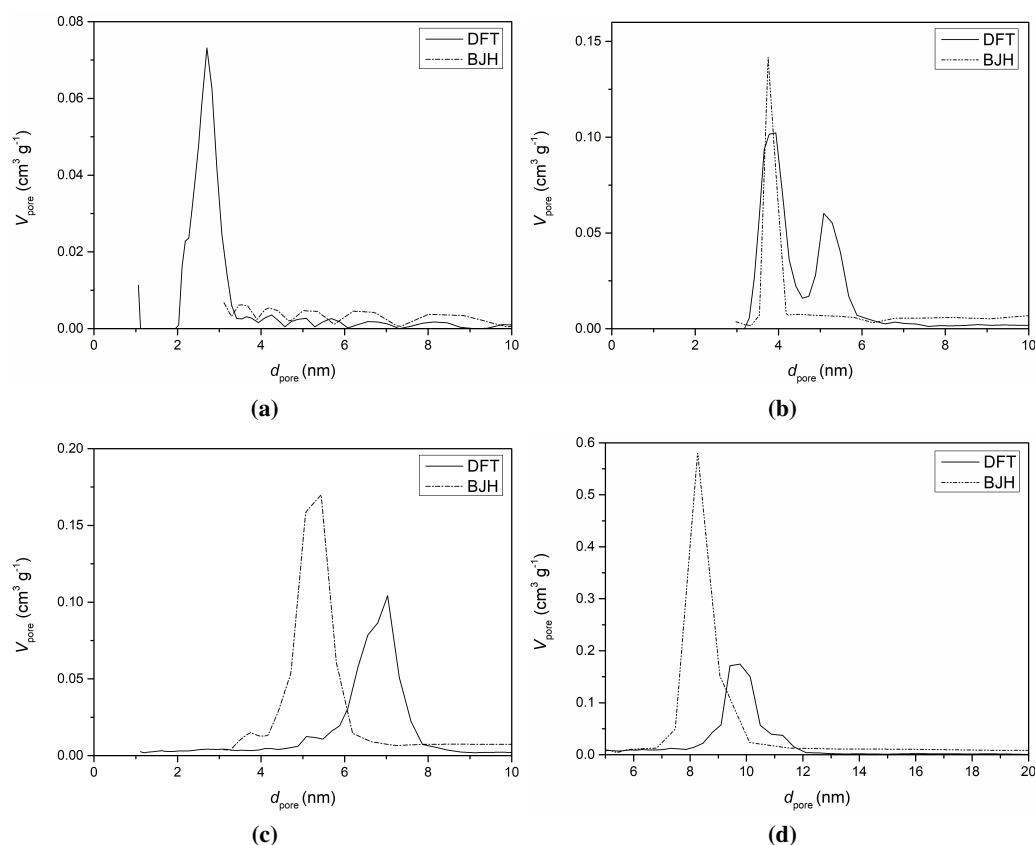
Figure 3.2: Pore size distributions ascertained with the BJH and the NLDFT method from the desorption branch of nitrogen physisorption measurements of (a) OMS_TLCT, (b) MCM-41, (c) SBA-15 and (d) SBA-15_sa.[1]

Table 3.2: Mean pore sizes determined from the desorption branch of nitrogen physisorption measurement by the BJH ($d_{\text{BJH,des}}$) and the NLDFT ($d_{\text{NLDFT,des}}$) method. The standard deviations are given where available. [1]

Sample	$d_{\text{BJH,des}}$ nm	$d_{\text{NLDFT,des}}$ nm	$d_{\text{form factor}}$ nm	$d_{\text{electron density}}$ nm
OMS_TLCT	-*	2.7 ± 0.6	2.6 ± 0.5	2.6
MCM-41	-*	3.9 ± 0.6	3.6 ± 0.4	3.3
SBA-15	5.4 ± 0.7	7.0 ± 1.0	7.4 ± 0.7	7.1
SBA-15_sa	8.3 ± 0.8	10.1 ± 1.1	10.7 ± 0.8	10.1

* The pore size cannot be determined due to the settings in the software, which is used for the evaluation with the BJH method. Details are explained in the supporting information. [1]

(NLDFT) kernel was used for silica materials with cylindrical pores. When using the NLFDT kernel for the determination of the pore size distribution from the desorption branch for MCM-41, the two-step isotherm of the nitrogen physisorption measurement must be used. The reason for the occurrence of two steps is the forced hysteresis closure, which is causal for the step at higher relative pressures and thus, also for the pore size distribution resulting from these pressure points. From this point of view, the pore size distribution around the main pore size of 3.9 nm describes the pores actually present in MCM-41 and the pore size distribution at higher relative pressures is negligible. The evaluation of the desorption branch of the nitrogen physisorption measurement of MCM-41 by the BJH method shows a monomodal pore size distribution (Figure 3.2 (b)). The absence of the bimodal pore size distribution can be explained by the used software version (see above). The comparison of the mean pore sizes determined with the BJH and the NLDFT method shows relative deviations of up to 23 % for the nitrogen physisorption measurements. This is consistent with other findings in the literature that the pore size of mesopores with a diameter of less than 10 nm is underestimated by up to 30 % using the BJH method. [14]

3.1.2 Alternative Characterization Methods

Since not every research group has access to all characterization methods, e.g., to obtain information about the lattice parameter or the pore size, deviations for the same material may be conceivable. At the same time, comparison of the most common methods for the determination of the lattice parameter and pore size over a larger pore size range of mesoporous silica materials has been lacking. In the publication "Comparative Study of Lattice Parameter and Pore Size of Ordered Mesoporous Silica Materials Using Physisorption, SAXS Measurements and Transmission Electron Microscopy" such a comparison, as well as an evaluation of the general interchangeability of the different characterization methods, was made for ordered mesoporous silica synthesized via true liquid crystal templating (OMS_TLCT), MCM-41, SBA-15 and SBA-15 with bigger pores

resulting from the use of the swelling agent *n*-decane during the synthesis (SBA-15_sa).[1] The experimental section of the work is described in the context of the publication, which is located in the appendix.

3.1.2.1 Determination of the Lattice Parameter

An alternative characterization method to SAXS measurements (Chapter 3.1.1) for the determination of the lattice parameter is the evaluation from TEM images. The approach is known from the literature, but the procedure is not described in detail.[68] For this reason, different approaches were investigated in this work.[1] The aim was to obtain an uncomplicated method for determining the lattice parameter as quickly and reproducibly as possible. Furthermore, it was considered if the pore orientation under TEM influences the results. To be distinguished are the orientations of the pores in top view, as well as the side view of the pore channels (Figure 3.3 (a)). Looking at the pores in top view, the (100) distance d_{100} of the investigated mesoporous silica material can be determined using the fast Fourier transformation (FFT) method. With the determined (100) distance d_{100} and the following equation

$$a = \frac{d_{100}}{\sin(60°)}$$
(3.1)

the lattice parameter $a_{\text{TEM,FFT}}$ was calculated (Figure 3.3 (b)). A possible negative influence due to the oblique view of the pore orientation was considered when determining the lattice parameter using the FFT method. Evidence that the particles are well aligned is obtained by analyzing different particles and comparing the results. If the values agree well, it indicates that the respective particles are aligned in the correct direction. In addition, a low inclination of the particles would only lead to minimal errors in the determined lattice parameters. Since the orientation of the top view of the pore entrances is relatively rare, it is useful to also consider the side view of the pore channels to determine a representative value for the lattice parameter. For the evaluation of the side view of the pore channels, the gray values are plotted along a line perpendicular to the course of the pore channels (Figure 3.3 (c)). The distance between two maxima is equal to the (100) distance d_{100}, so equation 3.1 is used to calculate the lattice parameter $a_{\text{TEM,line}}$. In Table 3.1, the values for $a_{\text{TEM,FFT}}$ and $a_{\text{TEM,line}}$ for all materials are listed.

The relative deviation of the two lattice parameters $a_{\text{TEM,FFT}}$ and $a_{\text{TEM,line}}$ determined from the TEM images is at most 2 %. At the same time, the determined lattice parameters are within the range of the lattice parameters a_{SAXS} determined from the SAXS data. However, when evaluating the TEM images, care must be taken to align the pores in top view so that the hexagonal arrangement of the pores is not distorted. Distortion would result in an erroneous lattice parameter. Since such distortions are relatively easy to detect, these particles can be neglected. When looking at the side view of the pore channels, attention must be paid to the orientation in the (100) direction d_{100}. Deviations in this regard are difficult to detect with the naked eye. Difficulties that may arise dur-
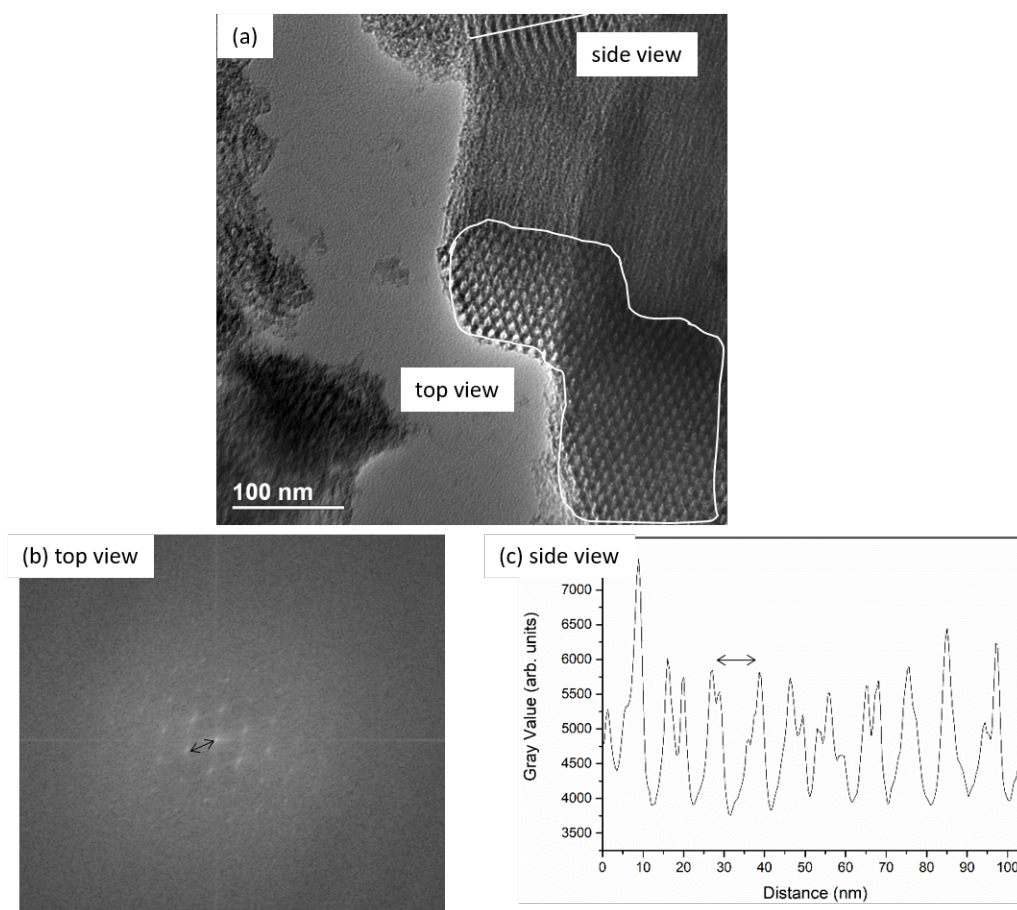
Figure 3.3: Exemplary TEM image showing the pores of SBA-15 in the top view and the parallel pore channels (side view, (a)). The area showing the pores in the top view was obtained using the fast Fourier transform method, from which the (100) distance was determined (b). For the pore channels in the side view, the gray values were plotted along the white line (c). The distance between two maxima is equal to the (100) distance, so that the lattice parameter for both viewing angles $a_{\text{TEM,FFT}}$ and $a_{\text{TEM,line}}$ can be calculated using the equation 3.1.[1]

ing the evaluation of the lattice parameter using TEM images and the implications are described and discussed in detail in the publication's supporting information. Nevertheless, it is possible to obtain consistent values if sufficiently many different particles and pores are considered. When these requirements are fulfilled, the determination of the lattice parameter from TEM images is a suitable alternative characterization method to the usual SAXS investigations.

3.1.2.2 Determination of the Pore Size

An alternative method for the determination of the pore size from physisorption measurements (Chapter 3.1.1) is the extraction of the pore sizes from SAXS measurements.[70;234;235] The SAXS measurements considered for the publication as well as their interpretation were performed by Dr.

Johanna R. Bruckner as well as Dr. Sonja Dieterich. The obtained diffractograms can generally be described quite well by the theory. It is shown that the contributions of the form factor of the cylindrical pores and the structure factor of the hexagonal order from the diffractograms curves have to be multiplied and not added. Therefore, small changes in the pore size lead to different results. The resulting pore sizes $d_{\text{form factor}}$ are listed in Table 3.2. Comparison with values obtained from the nitrogen physisorption measurements using the NLDT method ($d_{\text{NLDFT,des}}$) gives the best agreement. For OMS_TLCT and MCM-41, the values of the $d_{\text{form factor}}$ are at most 8 % smaller, while the values for SBA-15 and SBA-15_sa are at most 6 % larger.

For the two established methods, i.e., the physisorption measurements and the fitting of the SAXS data, the pore size distribution was also investigated. For this purpose, the standard deviations were calculated assuming a normal distribution of the pore size (Table 3.2).[1] In general, an increase in the standard deviation with increasing mean pore size can be observed. In most cases, there is fairly good agreement between the standard deviations determined by both methods.

In addition to the well-known method for extracting pore size from SAXS data, a new method for the determination of the pore size was proposed by Dr. Johanna R. Bruckner. This method is based on the reconstruction of the electron density distribution of the ordered mesoporous silica materials. Electron density maps were constructed from the determined electron densities. Assuming that in inverse Fourier synthesis the decrease in electron density representing the mesopores corresponds to a sinusoidal function and the wall-mesopore interface is characterized by the fastest increase in the electron density distribution, the second derivative of the electron density distribution can be used to measure the distance between the two most distant inflection points. The pore sizes $d_{\text{electron density}}$ calculated by this method are also shown in the Table 3.2. Comparison with the values obtained by fitting the diffractograms to the form factor $d_{\text{form factor}}$ shows good agreement. Therefore, the determination of pore size using electron density calculations is a good alternative for mesoporous silica materials. Both methods are described in detail in BEURER ET AL. .[1]

In the following, the principle of a new method for the determination of the minimum opening of the pore network is explained. The basic idea is a mixture of TEM investigations and inverse size exclusion chromatography (ISEC) using probe particles of different sizes. Similar to ISEC, it is exploited that only a portion of the probe particles can fit into the pores. During the experiment, SBA-15 is treated with a suspension of gold nanoparticles (Au-NPs), which are defined as probe particles. Depending on the diameter, the Au-NPs may or may not diffuse into the pores and adsorb onto the silanol groups. The sample is then examined by TEM. If Au-NPs are detectable in the pores, the pore entrances of the pore network must be at least as large as the particle diameter or even larger. The accuracy of this method depends on the step size between the probe particle sizes and the width of the probe particle size distribution. To avoid interactions between the Au-NPs and the silanol groups on the external surface, the silanol groups were functionalized with HMDS. For the demonstration of the principle of using Au-NPs as probe particles to determine the minimum opening of the pore network, Au-NPs were chosen to be much smaller than the pore size (4.9 ± 0.2 nm), in the range of the pore size (9.0 ± 0.01 nm), and much larger than the pore

size of SBA-15 (11.3 ± 0.4 nm). SBA-15 treated with Au-NPs of different sizes (SBA-15_4.9nm, SBA-15_9.0nm, SBA-15_11.3nm) was examined in TEM (Figure 3.4). As expected, the TEM images of SBA-15_4.9nm (Figure 3.4 (a)) show particles in the pore channels. In the TEM images of SBA-15_9.0nm (Figure 3.4 (b)), it is not clear whether the Au-NPs are inside the pores or not. It appears that some of the Au-NPs are agglomerated on the external particle surface. In contrast, the TEM images of SBA-15_11.3nm show that there are no Au-NPs inside the pores, but that the Au-NPs are agglomerated both on the particle surface and at the pore entrances (Figure 3.4 (c)). The observations cautiously suggest that the openings of the open pore network of SBA-15 are larger than 4.9 ± 0.2 nm and smaller than 9.0 ± 0.01 nm. Overall, it must be considered that the present TEM images only show a few particles and thus only a fraction of the sample. Nevertheless, the first attempts to determine the openings of the pore network and the pore size with Au-NPs are promising. It is likely that with smaller differences between probe particle sizes, a narrower range for pore sizes can be achieved. In addition, probe particles with narrower particle size distributions would lead to more accurate results.

| (a) | (b) | (c) |
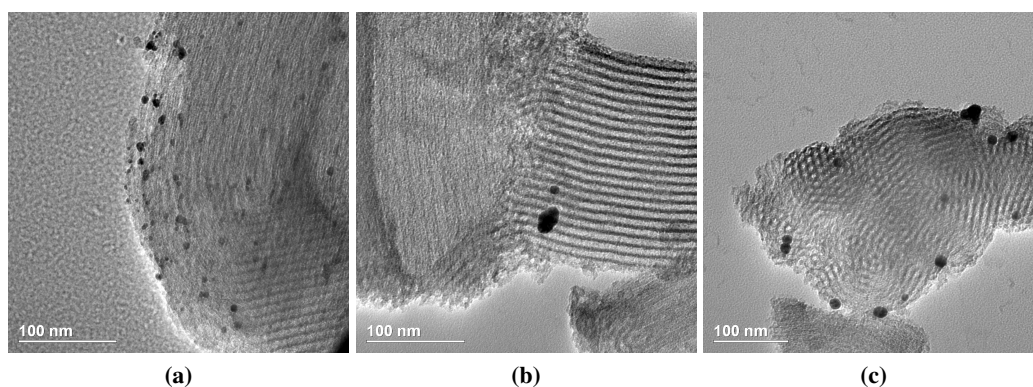
Figure 3.4: Exemplary TEM images of (a) SBA-15_4.9nm, (b) SBA-15_9.0nm and (c) SBA-15_11.3nm to investigate the access to the pore channels.

Regardless of the used characterization method, the comparison of the determined pore sizes shows quite good agreement for OMS_TLCT and MCM-41. Only the analysis of the data from the physisorption measurements with the BJH method is problematic for smaller mesopores, since the used software does not provide access to pore sizes <3 nm. For materials with larger mesopores, i.e., SBA-15 and SBA-15_as, good agreement is obtained between pore sizes from nitrogen physisorption measurements obtained with the NLDFT method and pore sizes from shape factor fitting and electron density distribution calculations.

3.1.3 Discussion of Common and Alternative Characterization Methods

Four mesoporous silica materials with an average pore size of about 3 to 11 nm were investigated using different characterization methods. For each mesoporous silica material, the hexagonal lattice parameter and the pore size of the cylindrical pores were determined and evaluated. It was

found that the averaged lattice parameters obtained from different particles of several TEM images agree well with the calculated lattice parameters from SAXS data. Since the SAXS measurement is a bulk method it averages over a layer of the sample whereby results obtained are statistically more meaningful. Since analysis is also significantly faster, SAXS remains the method of choice. However, if a SAXS instrument is not available, TEM is a reliable alternative method for the determination of the lattice parameter. When using TEM to determine the lattice parameter, it must be considered that there is a risk of larger errors due to the orientation of the pores.

Comparison of the pore sizes determined by different characterization methods shows a good agreement between the results of the established methods and the results of the new methods. Since the determined pore sizes provide values in the same size range, it is difficult to classify the methods, as each method has its advantages and disadvantages. Physisorption measurements are state of the art for the determination of the pore size. An advantage is that the amount of sample used for the measurement is relatively small and that the sample can be reused after the measurement. In addition, with physisorption measurements, more information about pore structure, surface area, and mesopores can be determined than the results from the TEM images. However, the measurement times for physisorption measurements are often very long and various assumptions are made when analyzing the data, which can affect the accuracy of the results.

As with physisorption measurements, SAXS measurements use small sample volumes that can be reused after the measurement. Fitting SAXS data is also a proven method from which further information can be derived. The short measurement times are another advantage of this characterization method. A disadvantage of SAXS instruments is that the technique is not so widely used due to high costs. When the pore size is determined from SAXS data by calculating electron density maps, the calculations are less complicated. This is because a relatively simple scattering theory is used. Furthermore, the results can be understandably visualized. It must be considered that this evaluation method is still in an early development stage, which makes a reliable evaluation difficult.

The determination of pore size using Au-NPs as probe particles is not based on a complex theory, so this method is not very error-prone if it is sure that the probe particles are in the pores. However, performing the experiments is very time consuming and depending on the width of the particle size distributions, only the range for the pore size can be determined instead of the exact value. Since only proof of principle experiments have been done so far, an exact evaluation is difficult.

3.1.4 Differences of Calcined and Extracted SBA-15

After the synthesis of mesoporous silica materials, pores are closed from the structure-giving template. To use the materials for example as catalysts or support materials, it is necessary to open the pores. Different possibilities for the template removal from pores are described in Chapter 1.3.2. The most commonly used procedures are calcination or extraction with an extracting agent of

structure-directing template. Depending on the application and function of the mesoporous silica material, not every template removal method is suitable. For example, when a calcined mesoporous SBA-15 (SBA-15-calc) silica material is to be functionalized, it is necessary to refill the pores with template to be able to modify the particle surface. In a further step, the template is removed by Soxhlet extraction (SBA-15-calc-re-E).[231] However, it is also possible to use the as-synthesized SBA-15 (SBA-15-as) as starting material for the selective functionalization, as described in Chapter 3.2. In this approach, the structure-directing template is removed by Soxhlet extraction with ethanol after the functionalization of the external surface (SBA-15-as-E). Another intermediate in this functionalization route is SBA-15-as-E, which is heated up to 400 °C (SBA-15-as-E-p400).[2] A temperature of 400 °C during the thermal treatment was chosen to protect the functional groups on the particle surface, to avoid shrinkage of the lattice structure as much as possible, and to activate the silanol groups on the pore walls. For better comparison with SBA-15-calc, SBA-15-as-E was additionally heated up to 550 °C (SBA-15-as-E-p550). Since the thermal treatment takes place in a nitrogen environment, the functional groups are protected and remain on the surface.[2] The properties of various samples and their differences are discussed in the following.

All investigated materials show the reflections d_{100}, d_{110}, and d_{200} in the respective SAXS curve, which are characteristic of a hexagonal structure with the space group *p6mm*.[3] The reflections of all thermally treated samples are shifted to larger q compared to those of the as-synthesized materials. This is explained by the restructuring of the silica lattice, which is discussed in detail in Chapter 1.3.2. Consequently, the lattice parameter of the corresponding samples shrinks as a result of thermal treatment.[141–143] However, it can be observed that the shift is smaller for SBA-15-as-E-p400 than for SBA-15-as-E-p550 and SBA-15-calc. Accordingly, the shrinkage of the silica lattice depends on the temperature during thermal treatment. In the diffractogram of SBA-15-as-E, a shift of the reflections to smaller q cannot be observed. Therefore, the extraction of the structural template may prevent the shrinkage of the lattice structure. This was expected since the conditions for Soxhlet extraction with ethanol are much gentler than those for thermal treatment. Based on the carbon content determined by elemental analysis, the amount of removed structure-directing template could be calculated. Calcination removed 97 % of the structure-directing template, while Soxhlet extraction with ethanol only removed 15 %. It is known from literature that especially micropores of SBA-15 remain closed.[147] With these results, it was expected that the reintroduced template into the pores of SBA-15-calc could not be completely removed by Soxhlet extraction with ethanol. The results of the elemental analysis of SBA-15-calc-re-E show that 62 % of the reintroduced template was removed. This suggests that not all pores are accessible. In contrast, thermal treatment of SBA-15-as-E was able to remove residues of the structure-directing template. The results of elemental analysis reveal that 99 % of the structure-directing template were removed from both SBA15-as-E-p400 and SBA-15-as-E-p550.

The adsorption and desorption isotherms of all samples obtained from the nitrogen physisorption measurement correspond to isotherms known from literature.[3] These are type IV isotherms with H1 hysteresis, which are known for mesoporous silica materials with pore sizes >4 nm.[14] The surface areas and pore volumes of SBA-15-calc, SBA-15-as-E-p400, and SBA-15-as-E-p550 determined from the nitrogen physisorption measurements differ not significantly from those of SBA-15 described in literature.[3] The two intermediates, whose pores were opened by Soxhlet extraction (SBA-15-as-E and SBA-15-calc-re-E) have a smaller total surface area compared to SBA-15-calc. Comparison of the pore volume for different materials shows similar results. It is found that the micropores of SBA-15-calc-re-E remain closed after extraction of the structure-directing template. Similar results are obtained for SBA-15-as-E. That the structure-directing template cannot be completely removed from the pores by Soxhlet extraction with ethanol is also reported in the literature.[144] The largest difference between the materials becomes apparent when comparing the pore size distributions obtained by DFT analysis.[3] While the pore size distribution of SBA-15-calc is relatively sharp with only a few small mesopores and micropores, the pore size distribution of SBA-15-calc-re-E shows no micropores but a broader distribution of mesopores. The pore size distribution of SBA-15-as-E is even broader and more uneven. The thermal treatment of SBA-15-as-E increases the amount of the mean pore size and the pore size distribution becomes sharper. Differences between the two materials, which were treated in nitrogen at 400 °C or 550 °C are observed in the microporous region of the pore size distribution. Obviously, the microporous fraction of SBA-15-as-E-p550 is larger than in SBA-15-as-E-p400 despite complete removal of the structure-directing template. This effect can be explained by shrinkage, which is more pronounced in SBA-15-as-E-p550. As a result of thermal treatment at 550 °C, the small mesopores shrink to such an extent that they become micropores and the overall pore size distribution shifts to smaller pore sizes.

In summary, all materials exhibit the characteristic properties of SBA-15. However, the results also show that the template removal method affects the properties of SBA-15. Accordingly, it can be expected that different materials respond differently to pressure and the template removal method affects the mechanical stability of SBA-15.

3.2 Efficient and Spatially Controlled Functionalization of SBA-15

Selective functionalization of porous materials allows highly selective and complex catalysts to be introduced into pores of support materials in a controlled manner to perform catalysis under confinement. However, it is challenging to ensure selective functionalization of mesoporous silica materials. As described in Chapter 1.5, the literature extensively addresses the functionalization of mesoporous silica materials. However, functionalization procedures described do not guarantee that these processes are indeed selective (Chapter 1.5.3). A method which proves the selective functionalization was presented in the publication entitled "Efficient and spatially controlled functionalization of SBA-15 and initial results in asymmetric Rh-catalyzed 1,2-additions under con-

finement".[2] The experimental section of the work is described in the context of the publication, which is located in the appendix.

3.2.1 Procedure of the Efficient and Spatially Controlled Functionalization

The method for the efficient and spatially controlled functionalization of mesoporous silica materials developed in this work follows the pore protection method (Chapter 1.5.3) and is shown in detail in Figure 3.5. In the procedure of selective functionalization, the first step is to functionalize particle surface and pore entrances, summarized as external surface (ex), of as-synthesized SBA-15 (SBA-15-as) with 1,1,1-trimethyl-*N*-(trimethylsilyl)silanamine (HMDS) (SBA-15-ex, Figure 3.5, step 1). Whether the functionalization of the particle surface was complete is tested in a separate and independent control step. The detailed methodology is described in the following chapters. After functionalization of the particle surface, the structure-directing template is removed from the pores by Soxhlet extraction with ethanol (E) leading to SBA-15-ex-E and then the material is heated up to 400 °C in nitrogen (p; SBA-15-ex-E-p; Figure 3.5, step 2). Finally, the pore walls (in) are functionalized with 3-azidopropyltriethoxysilane (AzPTES) (SBA-15-ex-E-p-in; Figure 3.5, step 3). Afterwards there is the possibility to attach linkers to the pore walls via click reactions to which the metal complexes can coordinate.[2]

3.2.2 Functionalization of the Particle Surface and the Pore Entrances

It is important to functionalize the support materials efficient and spatially controlled to ensure that the metal complexes used as catalysts are bound only to the pore walls, when reactions should work under confinement (Chapter 1.5.3). As described in Chapter 3.2.1, selective functionalization of as-synthesized SBA-15 (SBA-15-as) begins with modification of the particle surface with HMDS (Figure 3.5, step 1). The mesopore volume resulting from the nitrogen physisorption measurement of SBA-15-as (Table 3.3) shows that the pores of SBA-15-as are not completely filled after its synthesis. Therefore, the pore entrances are not closed with structure-directing template Pluronic® P123, which is why the silanol groups can be functionalized with HMDS in this area as well. This is not a problem, but rather an advantage. The advantage due to the functionalization of the silanol groups at the pore entrances is that it prevents the metal complexes, which are later introduced as catalysts, from being located directly at the pore entrances rather than penetrating deeper into the pores, so that the reaction can clearly proceed under confinement.

For the surface areas and pore volumes of SBA-15 determined from nitrogen physisorption measurements after the functionalization of the external surface with HMDS (SBA-15-ex), an increase is observed compared to the values of SBA-15-as. This was expected since organosilanes solubilize parts of the structure-directing template Pluronic® P123.[77;192;224;236–240]

Based on the results from nitrogen physisorption measurements, it is not possible to determine whether all freely accessible silanol groups on the particle surface as well as in the pore entrances were completely functionalized with HMDS. Therefore, additional IR spectroscopic studies were
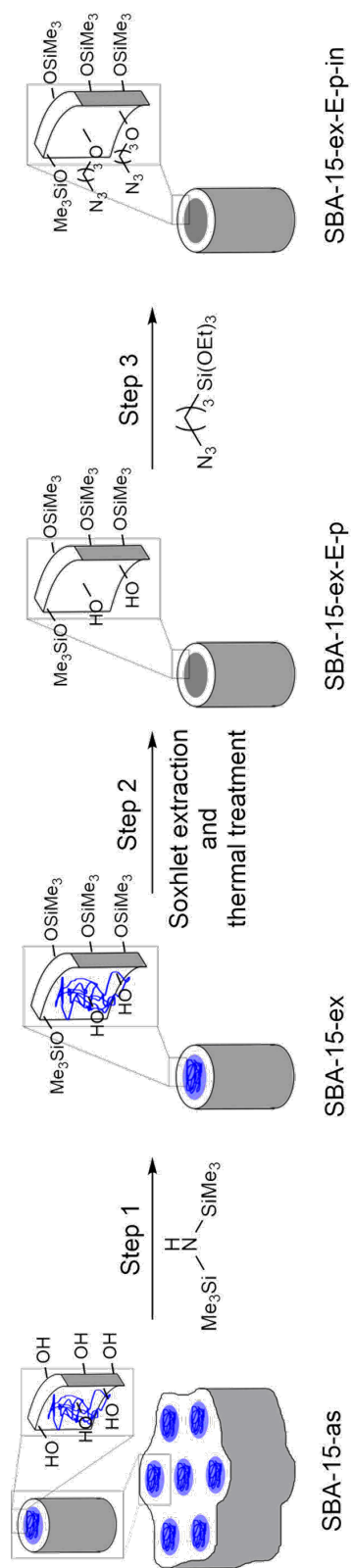
Figure 3.5: Schematic illustration of the efficient and spatially controlled functionalization procedure of SBA-15.[2]

Table 3.3: Total surface determined by the BET method (S_{BET}), external surface (S_{external}) and micropore surface (S_{micro}) determined by the V-t-method as well as the total volume (V_{tot}), the mesopore volume (V_{meso}) and the micropore volume (V_{micro}) of differently treated SBA-15. Furthermore, the pore diameters determined by the DFT method ($d_{\text{pore,DFT}}$) and the lattice parameter (a) from the SAXS measurements are listed. If SBA-15 is studied directly after the synthesis, it is named as-synthesized SBA-15 (as). As a reference material, SBA-15 with opened pores is used in this work. It is named calcined SBA-15 (calc). To obtain the selectively functionalized catalyst, the external surface of the SBA-15-as is functionalized in a first step (ex). In the next step, the triblock copolymer P123 used as a template is removed from the pores of the as-synthesized SBA-15 by Soxhlet extraction (ex-E). In a pretreatment step, the silanol groups on the pore walls are converted into freely accessible silanol groups (ex-E-p). To fix the metal complexes in the pores of SBA-15, the pore walls are modified (ex-E-p-in). Since the concentration of the functional groups on the pore walls is adjusted by the reaction time, the reaction time is also listed (ex-E-p-inX - X = 6, 24, 72 h). After the functionalization of the external surface, an independent control step is done to check if all accessible silanol groups on the external surface and at the pore entrances are completely functionalized (ex-control).[2]

SBA-15-*	S_{BET} $m^2\,g^{-1}$	S_{ex} $m^2\,g^{-1}$	S_{micro} $cm^3\,g^{-1}$	V_{tot} $cm^3\,g^{-1}$	V_{meso} $cm^3\,g^{-1}$	V_{micro} $cm^3\,g^{-1}$	$d_{\text{pore,DFT}}$ nm	a nm
as	80	80	0	0.270	0.207	0	7.0	12.4
calc	926	614	311	1.184	1.052	0.132	7.0	11.4
ex	281	281	0	0.789	0.789	0	7.6	12.6
ex-control	504	504	0	0.927	0.927	0	7.6	12.6
ex-E	518	518	0	0.885	0.885	0	7.6	12.6
ex-E-p	788	509	279	0.939	0.822	0.117	7.3	11.7
ex-E-p-in6	625	472	152	0.808	0.746	0.062	7.3	11.7
ex-E-p-in24	826	614	212	1.076	0.988	0.088	7.3	11.7
ex-E-p-in72	723	562	162	1.124	1.060	0.064	7.3	11.7

performed. The IR spectra of SBA-15-as and SBA-15-ex in Figure 3.6 (b) show bands between $1100\,cm^{-1}$ and $1000\,cm^{-1}$ and between $800\,cm^{-1}$ and $729\,cm^{-1}$, which are attributed to the silica lattice.[201;241] Characteristic for silanol groups are the bands between $3550\,cm^{-1}$ and $2700\,cm^{-1}$ and between $1010\,cm^{-1}$ and $832\,cm^{-1}$. However, it must be considered that the bands of silanol groups can overlap with the bands of adsorbed water molecules.

In addition to the typical bands for the silica lattice of SBA-15, bands due to CH_3 and CH-vibrations are detectable between $2970\,cm^{-1}$ and $2850\,cm^{-1}$, at $1475\,cm^{-1}$ and at $1375\,cm^{-1}$.[201;241] They are characteristic of the trimethoxy moieties on the external surface of SBA-15-ex. Since they are also found in the IR spectrum of SBA-15-as, it is clear that they can also be caused by the

structure-directing template Pluronic® P123 in the pores (Figure 3.6 (a)). Because the structure-directing template Pluronic® P123 is not completely removed during the functionalization of the external surface, no difference between the IR spectra of SBA-15-as and SBA-15-ex can be observed. Accordingly, it is impossible to assess the completeness of the functionalization with HMDS even by IR spectroscopic studies. Therefore, an independent and separate control step was added to the selective functionalization process of SBA-15.
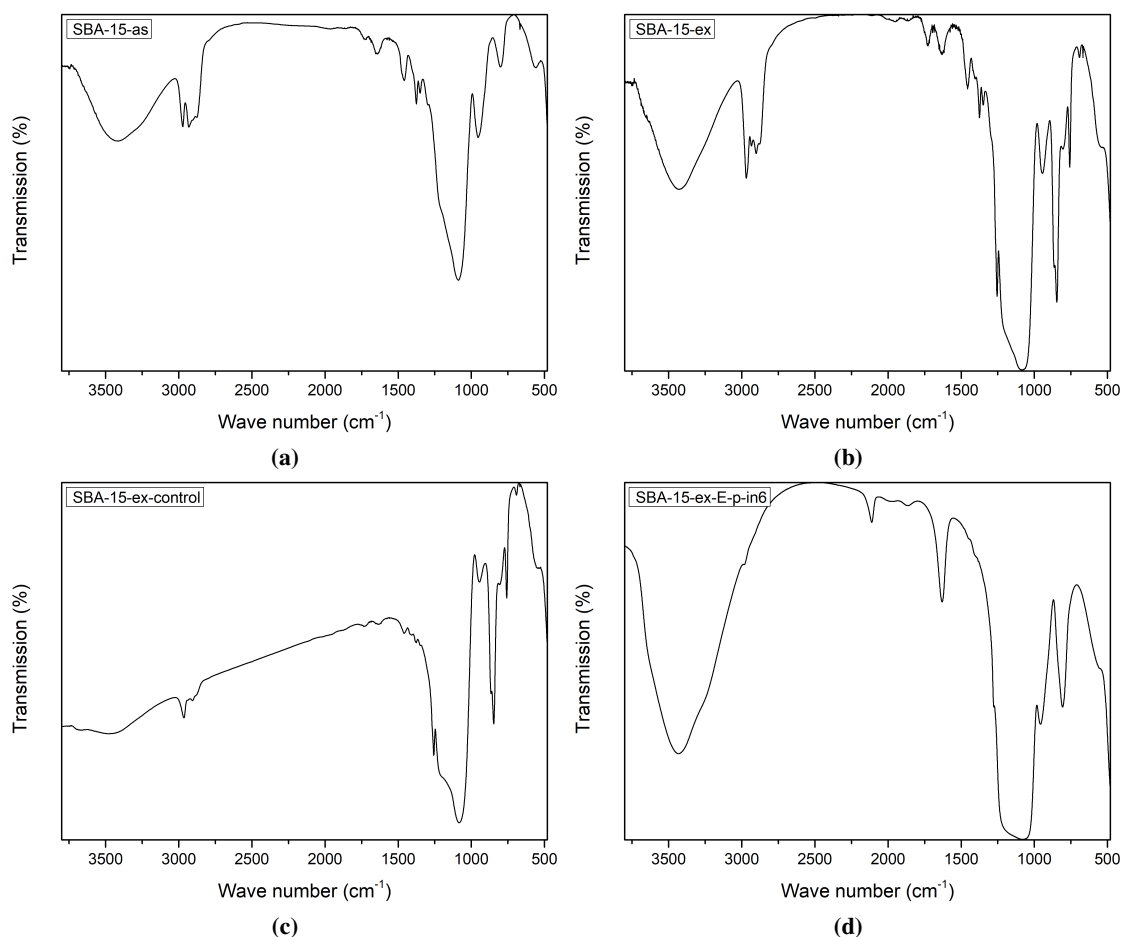
Figure 3.6: IR spectra of (a) as-synthesized SBA-15 (SBA-15-as), (b) SBA-15 with HMDS functionalized particle surface and pore entrances (SBA-15-ex), (c) SBA-15 with functionalized particle surface and pore entrances after the control step (SBA-15-ex-control) and (d) selectively functionalized SBA-15 (SBA-15-ex-E-p-in6), means SBA-15 with HMDS functionalized particle surface and pore entrances as well as with AzPTES functionalized pore walls. The duration of the functionalization of the pore walls was 6 h. Between the functionalization steps, the pores were opened by Soxhlet extraction with ethanol and the conversion of the silanol groups on the pore walls in freely accessible silanol groups.[2]

3.2.3 Control Step

After functionalization of the external surface, which is described in Chapter 3.2.2, it is necessary to check the completeness of the functionalization with HMDS even by IR spectroscopic studies. The independent and separate control step is schematically shown in Figure 3.7. It is a second functionalization after the initial functionalization step with HMDS (Figure 3.7 (a)). After the functionalization step, the putative fully functionalized SBA-15-ex is functionalized with AzPTES (Figure 3.7 (b)). If the external surface is fully functionalized, no silanol groups are freely accessible, and thus AzPTES cannot react (Figure 3.7, solid box). If not all silanol groups have been functionalized during the initial functionalization step with HMDS and there are silanol groups still freely accessible, they will react with AzPTES (Figure 3.7, dashed box). The azidopropyl moieties can be detected by IR spectroscopy and elemental analysis after the control step. If detected, the external surface was not inert after the functionalization step. As expected, the IR spectrum in Figure 3.6 (c) shows the previously described bands for the silica lattice, the silanol groups, the functional groups on the external surface and the structure-directing template Pluronic® P123. The characteristic azide band at $2100\,cm^{-1}$ [203;242;243] is not visible (Figure 3.6 (c)). According to this, the external surface, means the particle surface and the pore entrances, are inert after functionalization with HMDS. The results of the elemental analysis confirm this. [2]

3.2.4 Template Removal

After the functionalization of the external surface with HMDS (Chapter 3.2.2) and the check if the external surface is inert (Chapter 3.2.3), the pores of SBA-15-ex were opened by Soxhlet extraction with ethanol (SBA-15-ex-E, Figure 3.5, step 2). The surface areas and pore volume of SBA-15-ex and SBA-15-ex-E resulting from the nitrogen physisorption measurements do vary (Table 3.3). The increase in surface area as well as pore volume confirms the opening of the pores. However, the obtained surface areas are still smaller compared to these of SBA-15-calc. According to this, Soxhlet extraction with ethanol does not completely remove the structure-directing template Pluronic® P123. Contrary, the pore size of SBA-15-ex-E is larger because shrinkage of the pores is prevented by Soxhlet extraction with ethanol.

3.2.5 Thermal Treatment in Nitrogen

Before the pore walls of SBA-15-ex-E are functionalized in the last step, the silanol groups were activated by dehydroxylation and conversion of the silanol groups interacting via hydrogen bridges into isolated or geminal silanol groups. The reason for this is that the isolated and geminal silanol groups are reactive, while the groups interacting via hydrogen bridges are non-reactive (Chapter 1.4.1). [140] Activation of the silanol groups occurs at 400 °C in nitrogen (Figure 3.5, step 2). Gravimetric and elemental analysis confirm that heating up to 400 °C in nitrogen also removes residues of the structure-directing template Pluronic® P123 from the pores. [2] The comparison of
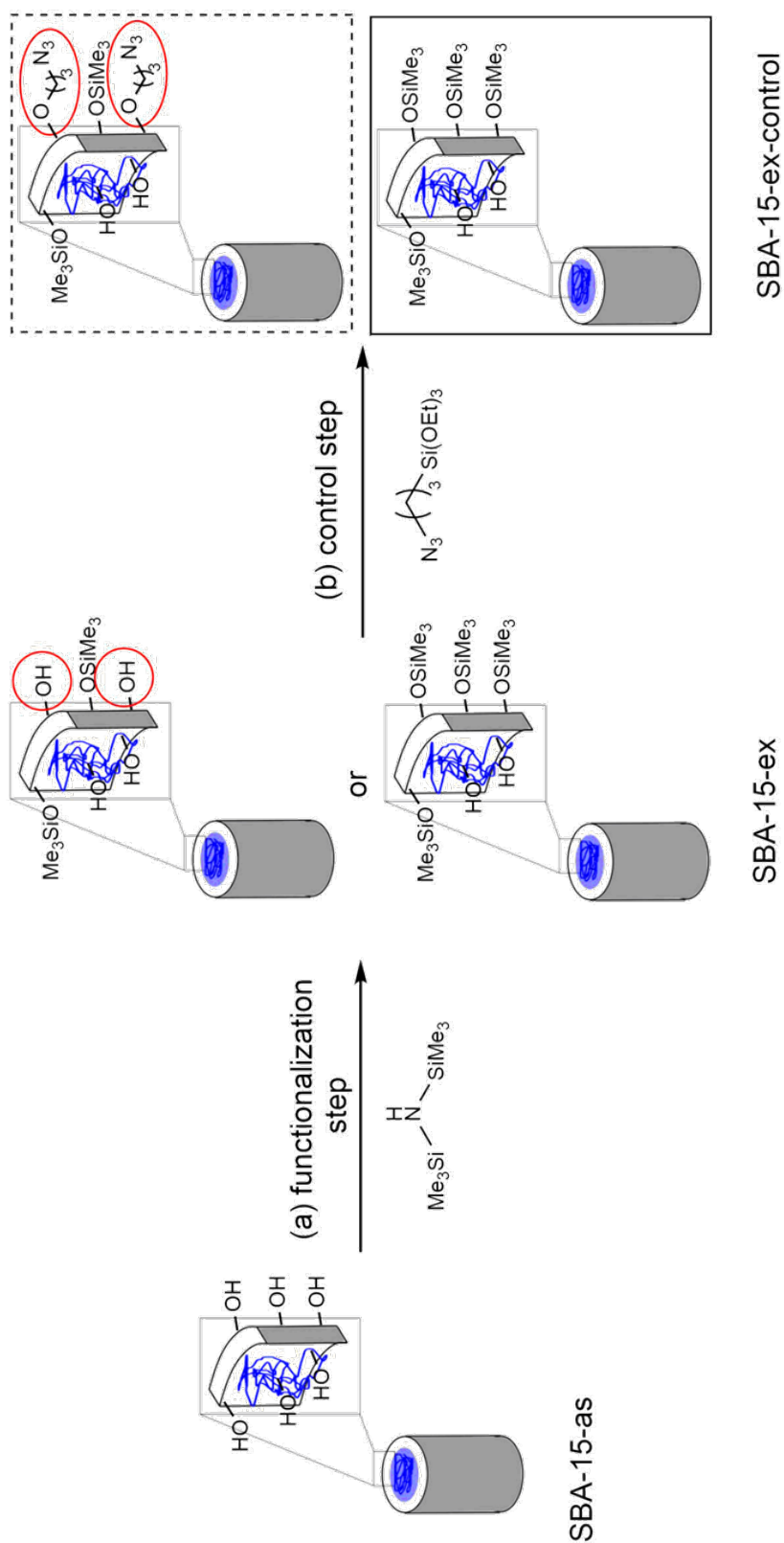
Figure 3.7: Schematic illustration for the investigation of the inertization of the external surface, means the particle surface and the pore entrances, consisting of (a) the functionalization step and (b) the separate and independent control step. [2]

results from elemental analysis of SBA-15, whose pore walls were functionalized with AzPTES, without (SBA-15-ex-E-in) and with (SBA-15-ex-E-p-in) prior activation of the silanol groups confirm the importance of the thermal treatment in nitrogen. [2] Results from nitrogen physisorption measurements for SBA-15-ex-E-p show the presence of micropores and thus a larger total surface area (Table 3.3). The external surface area (S_{ex}), consisting of particle surface and pore entrances, remains the same. However, thermal treatment shrinks the lattice parameter from 12.6 nm of SBA-15-ex-E to 11.7 nm of the SBA-15-ex-E-p. In addition, gravimetric studies were carried out to investigate the effects of thermal treatment in nitrogen on functional groups on the external surface. These studies showed that functional groups in nitrogen are stable up to 600 °C against the conditions during the thermal treatment in nitrogen. [2]

3.2.6 Functionalization of the Pore Walls

After activation (Chapter 3.2.5), the silanol groups on the pore walls of SBA-15-ex-E-p are functionalized with AzPTES (Figure 3.5, step 3). The number of azidopropyl moieties was adjusted by the reaction time (6 h, 24 h and 72 h). Knowledge of the azide concentration is important for the introduction of metal complexes. Since the azide concentration does not influence the subsequent selective functionalization, SBA-15, which was treated for 6 h (SBA-15-ex-E-p-in6), was used as an example. The control step after the functionalization of the external surface proves that the azidopropyl moieties must be located exclusively on the pore walls as discussed in Chapter 3.2.3. Only if the control step is positive, means the external surface is completely functionalized, the selective functionalization process is continued.

As for the previously described intermediates, a nitrogen physisorption measurement was performed for SBA-15-ex-E-p-in6. The resulting surfaces and pore volumes (Table 3.3) show that functionalization of the pore walls has no effect on the pore structure of SBA-15 and is within the error compared to SBA-15-ex-E-p. Also, the pore size does not change due to functionalization with AzPTES. TEM images confirm the retention of the hexagonal pore structure. [2] However, these studies do not prove the presence of azidopropyl moieties. For this purpose, an IR spectrum was recorded. In contrast to the IR spectra discussed so far, the spectrum of SBA-15-ex-E-p-in6 shows an additional band at 2100 nm^{-1} (Figure 3.6 (d)). This band is described in the literature as characteristic for azide groups. [244] The presence of nitrogen-containing moieties in SBA-15-ex-E-p-in6 is also confirmed by the results from elemental analysis. The azide concentration 3.41×10^{-2} mmol g^{-1} of SBA-15-ex-E-p-in6 was calculated from the detected nitrogen content. However, none of the discussed methods gives further information on the location of the azidopropyl moieties. Based on this, ^{13}C CP MAS NMR spectra of calcined SBA-15, whose external surface and pore walls were functionalized with AzPTES (SBA-15-calc-ex+in), and SBA-15-ex-E-p-in6 were recorded. [2] Both spectra show signals from the azidopropyl moiety, indicating that functionalization with AzPTES was successful. Additional signals are observable for the ethoxy moieties by incomplete reaction of the three ethoxy moieties of AzPTES. [140;245] The unreacted

ethoxy moieties remain in the sample and are thus detectable in the ^{13}C CP MAS NMR spectrum. The ^{13}C CP MAS NMR spectrum of SBA-15-ex-E-p-in6 additionally exhibits a strong signal, which can be attributed to the $(CH_3)_3-Si$ moieties on the external surface.[246] The obtained signals were expected based on the corresponding treatment of SBA-15, but the intensities are weak. Possible reasons for the weak signal intensities are the low concentrations of azidopropyl moieties $(1.23 \times 10^{-1}\,\mathrm{mmol\,g^{-1}}$ and $3.41 \times 10^{-2}\,\mathrm{mmol\,g^{-1}}$ sample). In addition, the conformation of the azidopropyl moieties on the pore walls cannot be affected. It is conceivable that the azidopropyl moiety protrudes into the pore at a 90° angle, but at the same time it is also possible that it interacts with the pore wall and lies on it. Since the intensity of the cross-polarization depends on the number of ^{1}H atoms in close proximity to ^{13}C atoms, the dynamics of the complexes and distances between the nuclei as well as different conformations on the surface can lead to different signal intensities in the CP spectra.[247] Therefore, it is not possible to make a quantitative statement about the azide concentration as well as its localization from NMR experiments.

In this chapter, the successful efficient and spatially controlled functionalization of SBA-15-as was shown. Functionalization of the particle surface and pore entrances prior to the removal of the structure-directing template Pluronic® P123 ensures that only the pore walls are decorated with azidopropyl moieties necessary for incorporation of metal complexes in the further functionalization process. To ensure that all free silanol groups on the particle surface and at the pore entrances reacted with HMDS, a separate and independent control step was introduced. The sample obtained from the control step can be used to verify spectroscopically and by elemental analysis whether all freely accessible silanol groups have reacted with the functionalization reagent. If the particle surface as well as the pore entrances are inert, the structure-directing template can be removed. In the final step, the pore walls can be modified, ensuring that the reactions later proceed under confinement. In summary, it can be stated that a efficient and spatially controlled catalyst system was successfully produced using this process.

3.3 Influence of the Template Removal Method on the Mechanical Stability of SBA-15

Since the selective functionalization of mesoporous silica materials is required for the study of reactions under confinement, it is important to be able to synthesize the developed catalysts on a larger scale in order to use them in larger reactors. The catalysts, which are often produced as powder, need to be shaped by tableting or extrusion, for example. With this in mind, the mechanical stability of mesoporous silica materials against pressure is of interest. As discussed in Chapter 1.5.3, the selective functionalization of mesoporous silica material can be achieved in different ways. Different approaches use different template removal methods.[19;103;137;138] As discussed in Chapter 1.4.3, the literature is concerned with the thermal, chemical and mechanical stability of mesoporous silica materials. The question of whether the template removal method

affects the mechanical stability of mesoporous silica materials was investigated in the publication entitled "Influence of the template removal method on the mechanical stability of SBA-15".[3] A detailed description of the experimental part is described in the context of the publication, which is located in the appendix.

3.3.1 Influence of the Template Removal Method on the Mechanical Stability of SBA-15 against a Pressure of 156 MPa

The mechanical stability of mesoporous silica material has been a topic in the literature for many years. So far, studies have been conducted on the influence of the calcination temperature[11;248] and the presence or absence of oxygen[75;249] during the template removal. Moreover, different silica structures have been compared from the point of view of mechanical stability.[194;196;197] The effects are considered in detail in Chapter 1.4.3. In addition to the calcination temperature, the mechanical stability of calcined SBA-15 as a function of pressures between 16 MPa and 260 MPa has also been investigated.[194;195] Following these studies, preliminary investigations on the mechanical stability of SBA-15-calc as a function of pressure were carried out. The results of X-ray analytical investigations and nitrogen physisorption measurements are in agreement with the literature.[3;194;195] Based on results of the preliminary investigations, the influence of the template removal method on the mechanical stability of SBA-15 was investigated further. Thermal treatment and Soxhlet extraction with ethanol were chosen as the template removal methods. The material properties of SBA-15-calc, SBA-15-calc-re, SBA-15-as-E, SBA-15-as-E-p400 and SBA-15-as-E-p550 are described in Chapter 3.1.4. For the mechanical stability studies, the samples were pressed at 156 MPa for 10 min.[3]

Just like the unpressed samples, the pressed samples were also subjected to X-ray analysis. The diffractograms show the reflexes d_{100}, d_{110}, and d_{200}, which are assigned to a hexagonal structure with the space group *p6mm*.[3] Compared to the diffractograms of the unpressed samples, the SAXS curves of SBA-15-calc-156MPa and SBA-15-calc-re-E-156MPa are almost identical and show no significant differences. The same is true for the positioning of the reflexes of SBA-15-as-E-156MPa, SBA-15-as-E-p400-156MPa, and SBA-15-as-E-p550-156MPa. It is therefore not surprising that the lattice parameters of the pressed samples correspond to those of the unpressed ones (Table 3.4). Thus, based on the lattice parameters, it is not possible to determine whether the template removal method affects the mechanical stability of SBA-15.

However, unlike the positions of the reflexes, differences can be observed in intensity. While the intensities of calcined samples are very similar, the intensities of the reflexes for SBA-15-as-E-156MPa, SBA-15-as-E-p400-156MPa, and SBA-15-as-E-p550-156MPa are significantly lower after pressure treatment. The decrease in intensity and broadening indicate partial destruction of the nanostructure. A direct correlation between the intensity decrease and structural integrity cannot be readily established. However, it is possible that width of the reflexes correlates with the degree of ordering of the two-dimensional hexagonal lattice. This correlation is described by the

Table 3.4: Total surface determined by the BET method (S_{BET}), micropore surface (S_{micro}) as well as the total volume (V_{tot}), the mesopore volume (V_{meso}) and the micropore volume (V_{micro}) of differently treated SBA-15. The as-synthesized SBA-15, whose pores were opened by Soxhlet extraction with ethanol is named SBA-15-as-E. Another investigated sample is SBA-15-as-E treated in nitrogen at 400 or 550 °C (as-E-p400/550). Instead of extraction the template from the pores the SBA-15-as could be calcined in air. The abbreviation for the sample is SBA-15-calc. And there is the possibility to combine both template removal methods in SBA-15-calc-re-E, where the pores of SBA-15-calc were refilled with template before the Soxhlet extraction with ethanol. The pressed samples are labeled at the end with the pressure with which they were treated Furthermore, the pore diameters determined by the DFT method ($d_{pore,DFT}$) and the lattice parameter (a) from the SAXS measurements are listed. [3]

SBA-15-	S_{BET} $m^2\,g^{-1}$	S_{micro} $m^2\,g^{-1}$	V_{tot} $cm^3\,g^{-1}$	V_{meso} $cm^3\,g^{-1}$	V_{micro} $cm^3\,g^{-1}$	$d_{pore,DFT}$ nm	a nm
as-E	727	134	1.094	1.042	0.052	7.6	12.2
as-E-156MPa	480	170	0.371	0.299	0.072	2.6	12.2
as-E-p400	1016	140	1.807	1.751	0.056	7.6	11.3
as-E-p400-156MPa	798	132	0.844	0.830	0.054	6.6	11.3
as-E-p550	869	236	1.148	1.053	0.095	7.0	11.1
as-E-p550-39MPa	819	222	0.995	0.902	0.093	6.8	11.0
as-E-p550-156MPa	720	209	0.697	0.610	0.087	6.8	10.8
calc	897	222	1.128	1.033	0.095	7.0	10.9
calc-39MPa	772	193	0.976	0.897	0.079	7.0	10.9
calc-156MPa	670	125	0.948	0.899	0.049	6.8	10.9
calc-re-E	510	0	1.345	1.345	0	6.8	10.8
calc-re-E-156MPa	409	7	0.699	0.699	0	6.6	10.8

paracrystal model. [250–252] When the increase in width of the reflex d_{100} of SBA-15-as-E-156MPa, SBA-15-as-E-p400-156MPa, and SBA-15-as-E-p550-156MPa is compared with those of the unpressed materials, the destruction of the structure is more pronounced for SBA-15-E-156MPa compared to the additionally thermally treated ones.

Since the results of the X-ray analysis do not allow a definitive statement on the influence of the template removal method on the mechanical stability, nitrogen physisorption measurements were also carried out. Examination of the obtained adsorption and desorption isotherms shows differences between the unpressed and pressed materials (Figure 3.8). The type IV isotherm from the nitrogen physisorption measurement of SBA-15-calc are still present for SBA-15-calc-156MPa, but with attenuated H1 hysteresis. This is an indication that the uniformity of the pores has been lost due to pressure. [11] The broadened pore size distribution obtained by DFT calculations and
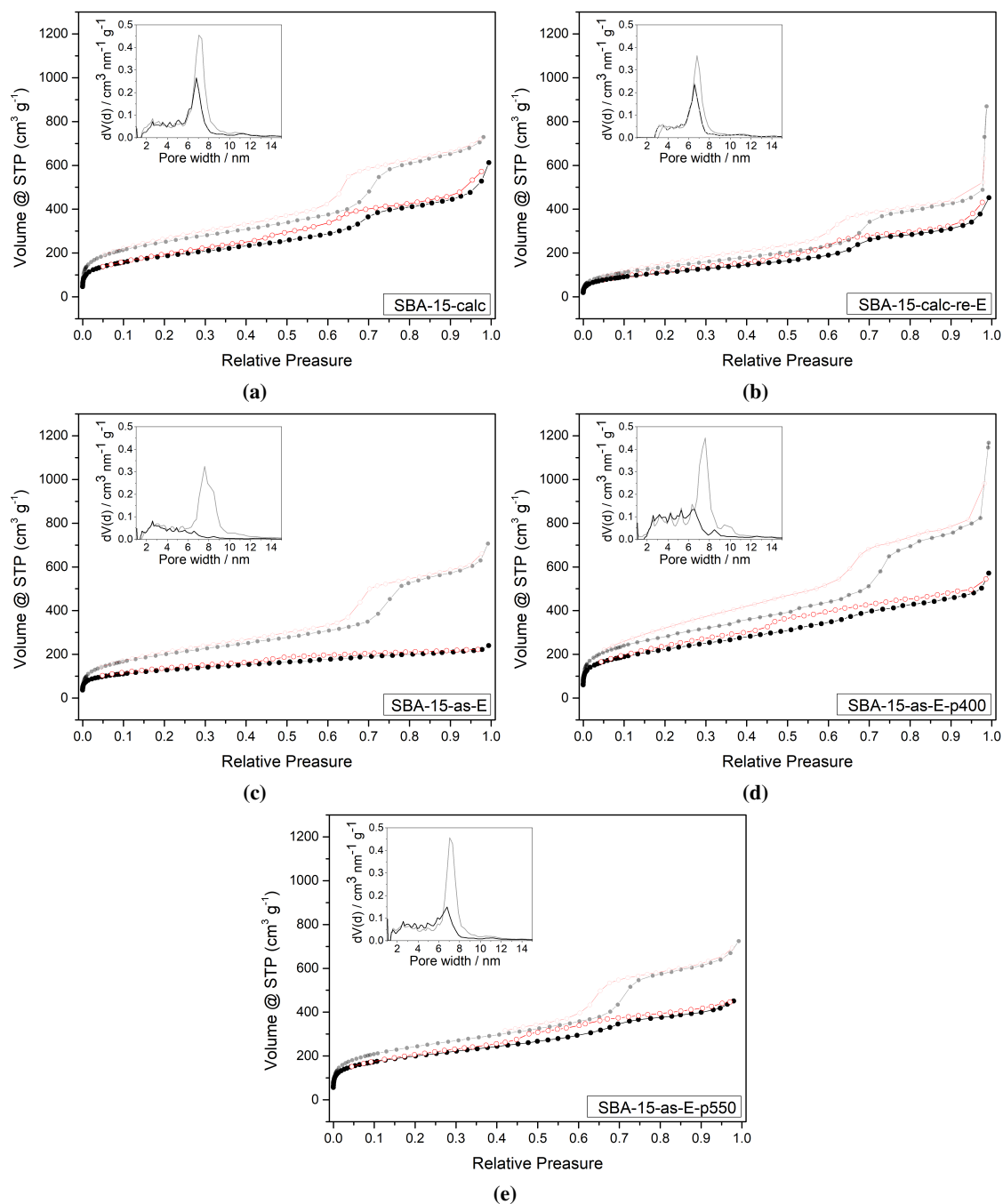
Figure 3.8: Adsorption (●) and desorption (○) isotherms and pore size distributions of (a) calcined SBA-15 (SBA-15-calc), (b) calcined SBA-15 with refilled pores after Soxhlet extraction with ethanol (SBA-15-calc-re-E), (c) as-synthesized SBA-15 after Soxhlet extraction with ethanol (SBA-15-as-E) and as-synthesized SBA-15 after Soxhlet extraction with ethanol and thermal treatment in nitrogen at (d) 400 °C (SBA-15-as-E-p400) or (e) 550 °C (SBA-15-as-E-p550) (light) and their analogues pressed with 156 MPa for 10 min (dark). [3]

the loss of pores with the original main pore diameter confirm the assumption of the partially destroyed structure as well as the decrease of the determined surface areas and pore volumes (Figure 3.8, Table 3.4). Similar results are observed for SBA-15-calc-re-E-156MPa, although residues of the template are still present in the pores of SBA-15-calc-re-E. Accordingly, the template residues have no supporting function and thus no positive influence on the mechanical stability of SBA-15 against pressure. As discussed in Chapter 1.3.2, imperfections in the lattice of SBA-15 could be repaired during calcination.[11]

For this reason, SBA-15-calc is expected to be more stable than SBA-15-as-E against pressure. The comparison of the adsorption and desorption isotherms of SBA-15-as-E-156MPa with the unpressed material shows that the hysteresis changed to an H4 hysteresis after pressing at 156 MPa. The H4 hysteresis indicates a complex pore structure,[14] which is confirmed by the determined pore size distribution, surface areas and pore volumes (Figure 3.8, Table 3.4). They show that the structure is in parts destroyed. Similarly results are obtained for SBA-15-as-E-p400-156MPa. This indicates that thermal treatment at $400\,°C$ in nitrogen is not sufficient to repair defects in the lattice structure which would increase stability. In contrast to the adsorption and desorption isotherms of SBA-15-as-E-p400, the isotherms and hysteresis of SBA-15-as-E-p550 are similar to those of SBA-15-calc-156MPa. At the same time, the hysteresis is much more pronounced compared to the isotherms of SBA-15-as-E-156MPa and SBA-15-as-E-p400-156MPa. An explanation for this is the increased temperature during thermal treatment in nitrogen, which leads to further condensation reactions in the silica lattice.[11] Examination of the pore size distribution shows a greater loss of pores with the mean pore diameter than for SBA-15-calc.

The discussed results show that the method of template removal affects the mechanical stability of SBA-15 as a function of the applied mechanical pressure. Comparison of the different template removal methods shows that residues of the structure-directing template have no supporting effect on the pore structure of SBA-15. In contrast, thermal treatment has a positive effect on the mechanical stability of SBA-15 against pressure. If the thermal treatment takes place in the presence of oxygen, the mesoporous silica material is slightly more stable to very high pressures. Moreover, the results show that the increase in mechanical stability correlates with the absolute value of the temperature. This may indicate that oxygen catalyzes the restructuring of the silica network into a more stable conformation.

3.3.2 Influence of the Template Removal Method on the Mechanical Stability of SBA-15 against a Pressure of 39 MPa

Studies on the influence of the template removal method discussed in Chapter 3.3.1 were carried out at 156 MPa. However, since laboratory-scale reactors and ultrafast HPLC systems are used at much lower pressures of up to 40 MPa[253–258], SBA-15-calc and SBA-15as-E-p550 were additionally studied under these conditions. For this purpose, they were pressed at 39 MPa for 10 min. The SAXS curves show the typical reflexes d_{100}, d_{110}, and d_{200} for SBA-15-calc-39MPa and

SBA-15-as-E-p550-39MPa.[3] As for SBA-15-calc-156MPa and SBA-15-as-E-p550-156MPa, the determined lattice parameters correspond to those of the unpressed samples (Table 3.4). The half-width of the d_{100} reflex increases only slightly compared to the respective unpressed samples, resulting in only minor damage to the structure of both samples.

In addition to the X-ray analytical studies, nitrogen physisorption measurements were performed for SBA-15-calc-39MPa and SBA-15-as-E-p550-39MPa. The recorded adsorption and desorption isotherms and the resulting pore size distribution of SBA-15-calc-press-39MPa and SBA-15-as-E-p550-39MPa differ only within the error range from those of the unpressed samples (Figure 3.9). The same is true for the surface areas and pore volumes (Table 3.4). Comparison of the results for SBA-15-calc-39MPa and SBA-15-as-E-p550-39MPa also shows only minor differences that are within the error range.

(a)   (b)
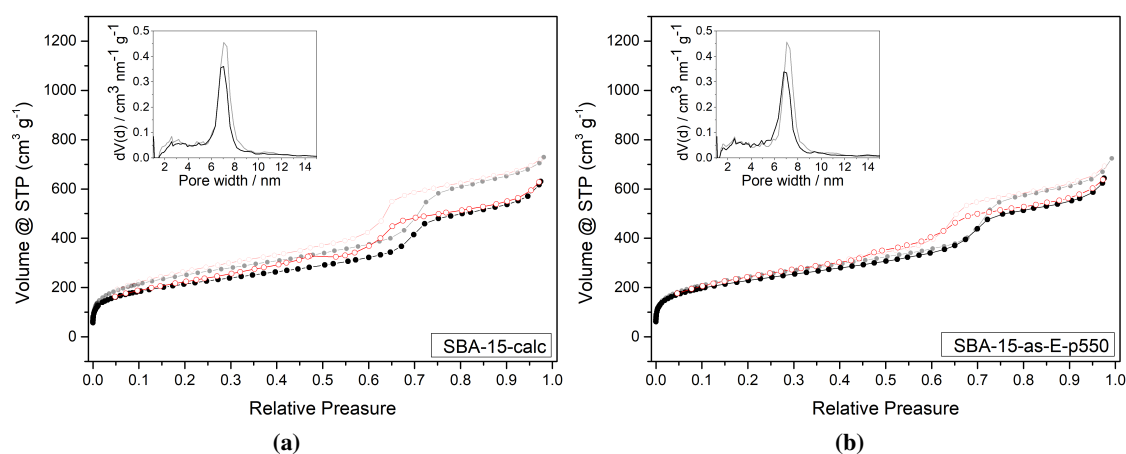
Figure 3.9: Adsorption (●) and desorption (○) isotherms as well as pore size distributions of (a) calcined SBA-15 (SBA-15-calc) and (b) as-synthesized SBA-15 which is Soxhlet extracted with ethanol and heated at 550 °C in nitrogen (SBA-15-as-E-p550) (light). Both samples were pressed with 39 MPa for 10 min (dark, abbreviated with "39MPa").[3]

In summary, the studies showed that the template removal method has no effect on the mechanical stability of SBA-15 against a pressure of 39 MPa. This means that our method for the efficient and spatially controlled functionalization of SBA-15 presented in Chapter 3.2, where no calcination is done, also delivers materials which are stable up to a pressure of at least 39 MPa.

4

Summary and Outlook

Mesoporous silica materials are used in a variety of research and industrial applications. The materials are exemplary used as catalysts or support materials. When selecting mesoporous silica materials for appropriate applications, knowledge about material properties is of enormous importance, because only with this knowledge it is possible to select the right mesoporous silica material for the application. In the literature, many methods are described to characterize the different properties of mesoporous silica materials. In this work, the lattice parameter and pore size were considered as important characteristic properties for mesoporous silica materials used as catalysts and support materials for catalysts, respectively. SAXS measurements were performed as well as TEM investigations and nitrogen physisorption measurements for MCM and SBA materials. A proof of principle for the determination of pore sizes with probe particles was also presented. The comparison of the results obtained for the lattice parameters and the pore size shows that the values determined are in good agreement. Nevertheless, it is useful to use several methods for the determination of lattice parameter or pore size to complement and verify the obtained results. The studies using Au-NPs as probe particles brought first successes showing that the pores of SBA-15 are accessible. However, it became clear that there is still a need for optimization in order to develop an equivalent characterization method. The selection of probe molecules or particles that may not interact with the surface groups plays a major role. In addition, there are challenges in the preparation of the probe molecules or particles. Firstly, the probe molecules or particles must be monodisperse, and secondly, the size difference between the probe molecules or particles used must not be too large, because the larger the difference, the more likely it is to under- or overestimate the pore size range.

Physisorption measurements have great potential for the investigation of porous silica materials since there is little literature using argon as adsorptive, especially for mesoporous silica materials with larger pore sizes. Similar physisorption investigations should also be done for other structural geometries like the hexagonal structure of MCM and SBA materials to receive an overview about the property of characterization methods for mesoporous silica materials with other geometries.

In addition to knowledge of the material properties, it is also possible to modify or adapt the meso-

porous materials depending on the area of application. On the one hand, this is possible via the reaction conditions during the manufacturing process. Another way to change the characteristic properties of the mesoporous silica materials is to introduce catalytically active components post-synthesicelly. If the mesoporous silica material should be used as a support material for stereoselective catalysts, it is particularly important to selectively functionalize the pore walls. This guarantees that the catalytically active components are located exclusively in the pores enabling shape selectivity. Several methods for the functionalization of mesoporous silica are described in the literature. However, usually it is only assumed that it is actually a selective functionalization of the pores. In the present work, a method was developed to investigate and show that selective pore functionalization is indeed present. By performing an independent control step prior to opening the pores of SBA-15, it was shown that the external surface is completely functionalized. At the same time, it was shown that the functionalization of the external surface with HMDS is stable with respect to all subsequent reaction steps. This ultimately ensures that the catalytically active components are located exclusively in the pores and that the reactions carried out are subject to confinement effects of the pore geometry.

A major benefit to research would be the development of characterization methods that could easily and quickly determine where the catalytically active sites are located in the mesoporous support material. Approaches to this include NMR spectroscopic studies in the current literature.[259] In order to be able to produce a broad portfolio of catalysts, it will be important to treat a wide variety of mesoporous silica materials with different functionalization reagents and to investigate the resulting changes in the material properties.

In addition to the investigation of mesoporous silica materials, whose advantageous properties could possibly be further improved by introducing metallic groups into the lattice structure, current research is also working at alternative support materials such as covalent or metal organic frameworks. The advantage of covalent organic frameworks is the atomically precise assembly of the support matrix structure and thus the introduction of the catalytically active sites. The flexibility of metal organic frameworks as soft crystals promises catalysts which can adapt their porous confinement by molecular recognition in a fast-reacting manner.

In addition, there is a large area of research in which the previously known shape-selective catalysts are introduced into the pores of the support material. Click chemistry used in this work is an example reaction. Literature shows that soluble catalysts, which have been successfully used, cannot be introduced into pores of the support material to give equally good results under confinement. For example, for attaching them to the pore wall a functional group has to be added that may influence the catalytically active site. Therefore, there is potential for future research in this area as well.

Once a mesoporous silica material has been found and its properties adapted to the application - selection of the material in terms of pore size, surface properties, etc. - it is possible to use the material in larger batches, in the best case on an industrial scale. For this, large quantities of the catalyst have to be produced and large reactors filled. As a result, large mechanical forces act on

the catalyst. Thus, this work investigated whether the type of pore opening has an influence on the mechanical stability against pressure. Background is that there are other approaches to functionalize mesoporous silica materials besides the one described in this work. The most common method for opening the pores is calcination. On this basis, the mechanical stability of calcined SBA-15 was first considered following the studies known from the literature. Then, various intermediates used in the production of functionalized mesoporous silica materials were tested for their mechanical stability by subjecting them to pressure treatment. The results showed that additional thermal treatment of SBA-15 in nitrogen after the synthesis process and the extraction of the template with ethanol significantly increased its mechanical stability in a way comparable to calcination in air.

In order to make mesoporous silica materials even more suitable for industrial applications in the future, it would be useful to complement similar investigations for mesoporous silica materials with other pore structures. In addition, it should be investigated whether the change in material properties due to the functional groups of the mesoporous silica materials, resulting from the efficient and spatially functionalization, influences the mechanical stability.

Bibliography

[1] BEURER, A.-K.; DIETERICH, S.; SOLODENKO, H.; KAYA, E.; MERDANOGLU, N.; SCHMITZ, G.; TRAA, Y.; BRUCKNER, J. R.: Comparative study of lattice parameter and pore size of ordered mesoporous silica materials using physisorption, SAXS measurements and transmission electron microscopy, *Microporous and Mesoporous Materials*, **2023**, *354*, 112508, DOI: `10.1016/j.micromeso.2023.112508`.

[2] BEURER, A.-K.; KIRCHHOF, M.; BRUCKNER, J. R.; FREY, W.; BARO, A.; DYBALLA, M.; GIESSELMANN, F.; LASCHAT, S.; TRAA, Y.: Efficient and Spatially Controlled Functionalization of SBA–15 and Initial Results in Asymmetric Rh–Catalyzed 1,2–Additions under Confinement, *ChemCatChem*, **2021**, *13* (10), 2407–2419, DOI: `10.1002/cctc.202100229`.

[3] BEURER, A.-K.; BRUCKNER, J. R.; TRAA, Y.: Influence of the Template Removal Method on the Mechanical Stability of SBA-15, *ChemistryOpen*, **2021**, *10* (11), 1123–1128, DOI: `10.1002/open.202100225`.

[4] ROUQUEROL, J.; BARON, G.; DENOYEL, R.; GIESCHE, H.; GROEN, J.; KLOBES, P.; LEVITZ, P.; NEIMARK, A. V.; RIGBY, S.; SKUDAS, R.; SING, K.; THOMMES, M.; UNGER, K.: Liquid intrusion and alternative methods for the characterization of macroporous materials (IUPAC Technical Report), *Pure and Applied Chemistry*, **2012**, *84* (1), 107–136, DOI: `10.1351/PAC-REP-10-11-19`.

[5] ROUQUEROL, F.: *Adsorption by powders and porous solids: Principles, methodology and applications*, second edn., **2014**, Elsevier/Academic Press, Amsterdam, ISBN 978-0-08-097035-6, `https://search.ebscohost.com/login.aspx?direct=true&scope=site&db=nlebk&db=nlabk&AN=485026`.

[6] WANG, G.; WANG, C.; ZHAO, J.; WANG, G.; PARK, C. B.; ZHAO, G.: Modelling of thermal transport through a nanocellular polymer foam: toward the generation of a new superinsulating material, *Nanoscale*, **2017**, *9* (18), 5996–6009, DOI: `10.1039/C7NR00327G`.

[7] GONG, P.; BUAHOM, P.; TRAN, M.-P.; SANIEI, M.; PARK, C. B.; PÖTSCHKE, P.: Heat transfer in microcellular polystyrene/multi-walled carbon nanotube nanocomposite foams, *Carbon*, **2015**, *93*, 819–829, DOI: `10.1016/j.carbon.2015.06.003`.

[8] GAMA, N. V.; FERREIRA, A.; BARROS-TIMMONS, A.: Polyurethane Foams: Past, Present, and Future, *Materials (Basel, Switzerland)*, **2018**, *11* (10), DOI: `10.3390/ma11101841`.

[9] GOHLKE, D. J.; TANNER, J. C.: Gore-Tex® Waterproof Breathable Laminates, *Journal of Coated Fabrics*, **1976**, *6* (1), 28–38, DOI: `10.1177/152808377600600104`.

[10] SCHÜTH, F.: Poröse Materialien im Überblick, *Chemie Ingenieur Technik*, **2010**, *82* (6), 769–777, DOI: `10.1002/cite.201000063`.

[11] KLEITZ, F.; SCHMIDT, W.; SCHÜTH, F.: Calcination behavior of different surfactant-templated mesostructured silica materials, *Microporous and Mesoporous Materials*, **2003**, *65* (1), 1–29, DOI: `10.1016/S1387-1811(03)00506-7`.

[12] MBARAKA, I.; SHANKS, B.: Design of multifunctionalized mesoporous silicas for esterification of fatty acid, *Journal of Catalysis*, **2005**, *229* (2), 365–373, DOI: `10.1016/j.jcat.2004.11.008`.

[13] COLELLA, C.: Ion exchange equilibria in zeolite minerals, *Mineralium Deposita*, **1996**, *31* (6), 554–562, DOI: `10.1007/BF00196136`.

[14] THOMMES, M.; KANEKO, K.; NEIMARK, A. V.; OLIVIER, J. P.; RODRIGUEZ-REINOSO, F.; ROUQUEROL, J.; SING, K. S.: Physisorption of gases, with special reference to the evaluation of surface area and pore size distribution (IUPAC Technical Report), *Pure and Applied Chemistry*, **2015**, *87* (9-10), 160, DOI: `10.1515/pac-2014-1117`.

[15] CHIOLA, V.; RITSKO, J. E.; VANDERPOOL, C. D.; TOWANDA, PA., ASSIGNORS TO SYLVANIA ELECTRIC PRODUCTS INC., A CORPORATION OF DELAWARE: *Process for producing low-bulk density silica: US-Patent 3 556 725*, **1971**.

[16] DI RENZO, F.; CAMBON, H.; DUTARTRE, R.: A 28-year-old synthesis of micelle-templated mesoporous silica, *Microporous Materials*, **1997**, *10* (4-6), 283–286, DOI: `10.1016/S0927-6513(97)00028-X`.

[17] TAGUCHI, A.; SCHÜTH, F.: Ordered mesoporous materials in catalysis, *Microporous and Mesoporous Materials*, **2005**, *77* (1), 1–45, DOI: `10.1016/j.micromeso.2004.06.030`.

[18] MEYNEN, V.; COOL, P.; VANSANT, E. F.: Verified syntheses of mesoporous materials, *Microporous and Mesoporous Materials*, **2009**, *125* (3), 170–223, DOI: `10.1016/j.micromeso.2009.03.046`.

[19] ZHAO, D.: Triblock Copolymer Syntheses of Mesoporous Silica with Periodic 50 to 300 Angstrom Pores, *Science*, **1998**, *279* (5350), 548–552, DOI: `10.1126/science.279.5350.548`.

[20] KRESGE, C. T.; LEONOWICZ, M. E.; ROTH, W. J.; VARTULI, J. C.; BECK, J. S.: Ordered mesoporous molecular sieves synthesized by a liquid-crystal template mechanism, *Nature*, **1992**, *359* (6397), 710–712, DOI: `10.1038/359710a0`.

[21] BECK, J. S.; VARTULI, J. C.; ROTH, W. J.; LEONOWICZ, M. E.; KRESGE, C. T.; SCHMITT, K. D.; CHU, C. T. W.; OLSON, D. H.; SHEPPARD, E. W.; MCCULLEN, S. B.; HIGGINS, J. B.; SCHLENKER, J. L.: A new family of mesoporous molecular sieves prepared with liquid crystal templates, *Journal of the American Chemical Society*, **1992**, *114* (27), 10834–10843, DOI: `10.1021/ja00053a020`.

[22] CIESLA, U.; SCHÜTH, F.: Ordered mesoporous materials, *Microporous and Mesoporous Materials*, **1999**, *27* (2-3), 131–149, DOI: `10.1016/S1387-1811(98)00249-2`.

[23] NISHIYAMA, N.: A mesoporous silica (MCM-48) membrane: preparation and characterization, *Journal of Membrane Science*, **2001**, *182* (1-2), 235–244, DOI: `10.1016/S0376-7388(00)00570-6`.

[24] SEEBACHER, C.; HELLRIEGEL, C.; DEEG, F.-W.; BRÄUCHLE, C.; ALTMAIER, S.; BEHRENS, P.; MÜLLEN, K.: Observation of Translational Diffusion of Single Terrylenediimide Molecules in a Mesostructured Molecular Sieve, *The Journal of Physical Chemistry B*, **2002**, *106* (22), 5591–5595, DOI: `10.1021/jp013198y`.

[25] SCHMIDT, R.; HANSEN, E. W.; STOECKER, M.; AKPORIAYE, D.; ELLESTAD, O. H.: Pore Size Determination of MCM-51 Mesoporous Materials by means of 1H NMR Spectroscopy, N2 adsorption, and HREM. A Preliminary Study, *Journal of the American Chemical Society*, **1995**, *117* (14), 4049–4056, DOI: `10.1021/ja00119a021`.

[26] SCHMIDT, R.; STÖCKER, M.; HENRIK ELLESTAD, O.: Characterization of a cubic mesoporous MCM-48 compared to a hexagonal MCM-41 in: *Zeolites: A Refined Tool for Designing Catalytic Sites, Proceedings of the International Zeolite Symposium*, vol. 97 of *Studies in Surface Science and Catalysis*, **1995**, Elsevier, ISBN 9780444821300, pp. 149–156, DOI: `10.1016/S0167-2991(06)81884-7`.

[27] SCHMIDT, R.; STÖCKER, M.; HANSEN, E.; AKPORIAYE, D.; ELLESTAD, O. H.: MCM-41: a model system for adsorption studies on mesoporous materials, *Microporous Materials*, **1995**, *3* (4-5), 443–448, DOI: `10.1016/0927-6513(94)00055-Z`.

[28] HUNGER, M.; SCHENK, U.; BREUNINGER, M.; GLÄSER, R.; WEITKAMP, J.: Characterization of the acid sites in MCM-41-type materials by spectroscopic and catalytic tech-

niques, *Microporous and Mesoporous Materials*, **1999**, *27* (2-3), 261–271, DOI: `10.1016/S1387-1811(98)00260-1`.

[29] LIU, Y.; FENG, W.; LI, T.; HE, H.; DAI, W.; HUANG, W.; CAO, Y.; FAN, K.: Structure and catalytic properties of vanadium oxide supported on mesocellulous silica foams (MCF) for the oxidative dehydrogenation of propane to propylene, *Journal of Catalysis*, **2006**, *239* (1), 125–136, DOI: `10.1016/j.jcat.2005.12.028`.

[30] VAN DER VOORT, P.; MATHIEU, M.; MEES, F.; VANSANT, E. F.: Synthesis of High-Quality MCM-48 and MCM-41 by Means of the GEMINI Surfactant Method, *The Journal of Physical Chemistry B*, **1998**, *102* (44), 8847–8851, DOI: `10.1021/jp982653w`.

[31] CORMA, A.: From Microporous to Mesoporous Molecular Sieve Materials and Their Use in Catalysis, *Chemical reviews*, **1997**, *97* (6), 2373–2420, DOI: `10.1021/cr960406n`.

[32] COLLART, O.; COOL, P.; VAN DER VOORT, P.; MEYNEN, V.; VANSANT, E. F.; HOUTHOOFD, K.; GROBET, P. J.; LEBEDEV, O. I.; VAN TENDELOO, G.: Aluminum Incorporation into MCM-48 toward the Creation of Brønsted Acidity, *The Journal of Physical Chemistry B*, **2004**, *108* (37), 13905–13912, DOI: `10.1021/jp049837x`.

[33] COLLART, O.; VAN DER VOORT, P.; VANSANT, E. F.; DESPLANTIER, D.; GALARNEAU, A.; DI RENZO, F.; FAJULA, F.: A High-Yield Reproducible Synthesis of MCM-48 Starting from Fumed Silica, *The Journal of Physical Chemistry B*, **2001**, *105* (51), 12771–12777, DOI: `10.1021/jp013037u`.

[34] BENJELLOUN, M.; VAN DER VOORT, P.; COOL, P.; COLLART, O.; VANSANT, E. F.: Reproducible synthesis of high quality MCM-48 by extraction and recuperation of the gemini surfactant, *Phys. Chem. Chem. Phys.*, **2001**, *3* (1), 127–131, DOI: `10.1039/B007022J`.

[35] HUO, Q.; MARGOLESE, D. I.; STUCKY, G. D.: Surfactant Control of Phases in the Synthesis of Mesoporous Silica-Based Materials, *Chemistry of Materials*, **1996**, *8* (5), 1147–1160, DOI: `10.1021/cm960137h`.

[36] ZHANG, J.; LUZ, Z.; GOLDFARB, D.: EPR Studies of the Formation Mechanism of the Mesoporous Materials MCM-41 and MCM-50, *The Journal of Physical Chemistry B*, **1997**, *101* (36), 7087–7094, DOI: `10.1021/jp9709621`.

[37] BOBONICH, F. M.; KOVALENKO, A. S.; VOLOSHINA, Y.; KORCHEV, A. S.; SOLOMAKHA, V. N.; PHILIPPOV, A. P.; IL'IN, V. G.: Adsorptive Properties of Template-Containing Silica-Based MCM-41 and MCM-50 Materials, *Adsorption Science & Technology*, **2002**, *20* (6), 595–605, DOI: `10.1260/026361702321039528`.

[38] SELVAM, P.; BHATIA, S. K.; SONWANE, C. G.: Recent Advances in Processing and Characterization of Periodic Mesoporous MCM-41 Silicate Molecular Sieves, *Industrial & Engineering Chemistry Research*, **2001**, *40* (15), 3237–3261, DOI: `10.1021/ie0010666`.

[39] CASSIERS, K.; LINSSEN, T.; MATHIEU, M.; BENJELLOUN, M.; SCHRIJNEMAKERS, K.; VAN DER VOORT, P.; COOL, P.; VANSANT, E. F.: A Detailed Study of Thermal, Hydrothermal, and Mechanical Stabilities of a Wide Range of Surfactant Assembled Mesoporous Silicas, *Chemistry of Materials*, **2002**, *14* (5), 2317–2324, DOI: `10.1021/cm0112892`.

[40] ALEXANDRIDIS, P.; ALAN HATTON, T.: Poly(ethylene oxide)-poly(propylene oxide)-poly(ethylene oxide) block copolymer surfactants in aqueous solutions and at interfaces: thermodynamics, structure, dynamics, and modeling, *Colloids and Surfaces A: Physicochemical and Engineering Aspects*, **1995**, *96* (1-2), 1–46, DOI: `10.1016/0927-7757(94)03028-X`.

[41] ZHAO, D.; YANG, P.; MELOSH, N.; FENG, J.; CHMELKA, B. F.; STUCKY, G. D.: Continuous Mesoporous Silica Films with Highly Ordered Large Pore Structures, *Advanced Materials*, **1998**, *10* (16), 1380–1385, DOI: `10.1002/(SICI)1521-4095(199811)10:16<1380`.

[42] LIU, Z.; TERASAKI, O.; OHSUNA, T.; HIRAGA, K.; SHIN, H. J.; RYOO, R.: An HREM Study of Channel Structures in Mesoporous Silica SBA-15 and Platinum Wires Produced in the Channels, *ChemPhysChem*, **2001**, *2* (4), 229–231, DOI: `10.1002/1439-7641(20010417)2:4<229`.

[43] GAI, L.; CHEN, Z.; JIANG, H.; TIAN, Y.; WANG, Q.; CUI, D.: Hydroxyl-promoted synthesis of GaN nanorods on SBA-15 surface, *Journal of Crystal Growth*, **2006**, *291* (2), 527–532, DOI: `10.1016/j.jcrysgro.2006.03.048`.

[44] GAO, F.; LU, Q.; LIU, X.; YAN, Y.; ZHAO, D.: Controlled Synthesis of Semiconductor PbS Nanocrystals and Nanowires Inside Mesoporous Silica SBA-15 Phase, *Nano Letters*, **2001**, *1* (12), 743–748, DOI: `10.1021/nl0156383`.

[45] HAN, Y.-J.; KIM, J. M.; STUCKY, G. D.: Preparation of Noble Metal Nanowires Using Hexagonal Mesoporous Silica SBA-15, *Chemistry of Materials*, **2000**, *12* (8), 2068–2069, DOI: `10.1021/cm0010553`.

[46] GU, J.; SHI, J.; XIONG, L.; CHEN, H.; LI, L.; RUAN, M.: A new strategy to incorporate high density gold nanowires into the channels of mesoporous silica thin films by electroless deposition, *Solid State Sciences*, **2004**, *6* (7), 747–752, DOI: `10.1016/j.solidstatesciences.2004.03.034`.

[47] LI, Z.; ZHANG, J.; LI, Y.; GUAN, Y.; FENG, Z.; LI, C.: Preparation and characterization of ordered mesoporous carbons on SBA-15 template, *Journal of Materials Chemistry*, **2006**, *16* (14), 1350, DOI: 10.1039/b512697e.

[48] SHIN, H. J.; RYOO, R.; KRUK, M.; JARONIEC, M.: Modification of SBA-15 pore connectivity by high-temperature calcination investigated by carbon inverse replication, *Chemical Communications*, **2001**, (4), 349–350, DOI: 10.1039/b009762o.

[49] KIM, T.-W.; RYOO, R.; GIERSZAL, K. P.; JARONIEC, M.; SOLOVYOV, L. A.; SAKAMOTO, Y.; TERASAKI, O.: Characterization of mesoporous carbons synthesized with SBA-16 silica template, *Journal of Materials Chemistry*, **2005**, *15* (15), 1560, DOI: 10.1039/b417804a.

[50] DIBANDJO, P.; CHASSAGNEUX, F.; BOIS, L.; SIGALA, C.; MIELE, P.: Comparison between SBA-15 silica and CMK-3 carbon nanocasting for mesoporous boron nitride synthesis, *Journal of Materials Chemistry*, **2005**, *15* (19), 1917, DOI: 10.1039/b417891b.

[51] KRUK, M.; JARONIEC, M.; JOO, S. H.; RYOO, R.: Characterization of Regular and Plugged SBA-15 Silicas by Using Adsorption and Inverse Carbon Replication and Explanation of the Plug Formation Mechanism, *The Journal of Physical Chemistry B*, **2003**, *107* (10), 2205–2213, DOI: 10.1021/jp0271514.

[52] MIYAHARA, M.; VINU, A.; HOSSAIN, K. Z.; NAKANISHI, T.; ARIGA, K.: Adsorption study of heme proteins on SBA-15 mesoporous silica with pore-filling models, *Thin Solid Films*, **2006**, *499* (1-2), 13–18, DOI: 10.1016/j.tsf.2005.07.046.

[53] FAN, J.; LEI, J.; WANG, L.; YU, C.; TU, B.; ZHAO, D.: Rapid and high-capacity immobilization of enzymes based on mesoporous silicas with controlled morphologies - Electronic supplementary information (ESI) available: XRD and nitrogen sorption isotherms for MPSs used in bioimmobilization. See http://www.rsc.org/suppdata/cc/b3/b304391f, *Chem. Commun.*, **2003**, (17), 2140, DOI: 10.1039/b304391f.

[54] XI, J.; QIU, X.; MA, X.; CUI, M.; YANG, J.; TANG, X.; ZHU, W.; CHEN, L.: Composite polymer electrolyte doped with mesoporous silica SBA-15 for lithium polymer battery, *Solid State Ionics*, **2005**, *176* (13-14), 1249–1260, DOI: 10.1016/j.ssi.2005.02.016.

[55] SEGURA, Y.; COOL, P.; KUSTROWSKI, P.; CHMIELARZ, L.; DZIEMBAJ, R.; VANSANT, E. F.: Characterization of vanadium and titanium oxide supported SBA-15, *The Journal of Physical Chemistry B*, **2005**, *109* (24), 12071–12079, DOI: 10.1021/jp0507750.

[56] LIU, Y.-M.; CAO, Y.; YI, N.; FENG, W.-L.; DAI, W.-L.; YAN, S.-R.; HE, H.-Y.; FAN, K.-N.: Vanadium oxide supported on mesoporous SBA-15 as highly selective catalysts in the oxidative dehydrogenation of propane, *Journal of Catalysis*, **2004**, *224* (2), 417–428, DOI: 10.1016/j.jcat.2004.03.010.

[57] Zhu, K.; Ma, Z.; Zou, Y.; Zhou, W.; Chen, T.; He, H.: *Chemical Communications*, **2001**, (24), 2552–2553, DOI: `10.1039/b107487n`.

[58] Morey, M. S.; O'Brien, S.; Schwarz, S.; Stucky, G. D.: Hydrothermal and Post-synthesis Surface Modification of Cubic, MCM-48, and Ultralarge Pore SBA-15 Mesoporous Silica with Titanium, *Chemistry of Materials*, **2000**, *12* (4), 898–911, DOI: `10.1021/cm9901663`.

[59] Tuel, A.; Hubert-Pfalzgraf, L. G.: Nanometric monodispersed titanium oxide particles on mesoporous silica: synthesis, characterization, and catalytic activity in oxidation reactions in the liquid phase, *Journal of Catalysis*, **2003**, *217* (2), 343–353, DOI: `10.1016/S0021-9517(03)00078-2`.

[60] Sumiya, S.; Oumi, Y.; Uozumi, T.; Sano, T.: Characterization of AlSBA-15 prepared by post-synthesis alumination with trimethylaluminium, *Journal of Materials Chemistry*, **2001**, *11* (4), 1111–1115, DOI: `10.1039/b008168j`.

[61] Yue, Y.; Gédéon, A.; Bonardet, J.-L.; D'Espinose, J.-B.; Fraissard, J.; Melosh, N.: Direct synthesis of AlSBA mesoporous molecular sieves: characterization and catalytic activities, *Chemical Communications*, **1999**, (19), 1967–1968, DOI: `10.1039/a904467a`.

[62] Luan, Z.; Hartmann, M.; Zhao, D.; Zhou, W.; Kevan, L.: Alumination and Ion Exchange of Mesoporous SBA-15 Molecular Sieves, *Chemistry of Materials*, **1999**, *11* (6), 1621–1627, DOI: `10.1021/cm9900756`.

[63] Landau, M. V.; Vradman, L.; Wolfson, A.; Rao, P. M.; Herskowitz, M.: Dispersions of transition-metal-based phases in mesostructured silica matrixes: preparation of high-performance catalytic materials, *Comptes Rendus Chimie*, **2005**, *8* (3-4), 679–691, DOI: `10.1016/j.crci.2005.01.011`.

[64] Kumar, M. S.; Pérez-Ramírez, J.; Debbagh, M. N.; Smarsly, B.; Bentrup, U.; Brückner, A.: Evidence of the vital role of the pore network on various catalytic conversions of N2O over Fe-silicalite and Fe-SBA-15 with the same iron constitution, *Applied Catalysis B: Environmental*, **2006**, *62* (3-4), 244–254, DOI: `10.1016/j.apcatb.2005.07.012`.

[65] Balas, F.; Manzano, M.; Horcajada, P.; Vallet-Regí, M.: Confinement and controlled release of bisphosphonates on ordered mesoporous silica-based materials, *Journal of the American Chemical Society*, **2006**, *128* (25), 8116–8117, DOI: `10.1021/ja062286z`.

[66] Qu, F.; Zhu, G.; Huang, S.; Li, S.; Sun, J.; Zhang, D.; Qiu, S.: Controlled release of Captopril by regulating the pore size and morphology of ordered mesoporous silica, *Microporous and Mesoporous Materials*, **2006**, *92* (1-3), 1–9, DOI: `10.1016/j.micromeso.2005.12.004`.

[67] LIU, A. M.; HIDAJAT, K.; KAWI, S.; ZHAO, D. Y.: A new class of hybrid mesoporous materials with functionalized organic monolayers for selective adsorption of heavy metal ions, *Chemical Communications*, **2000**, (13), 1145–1146, DOI: `10.1039/b002661l`.

[68] KRUK, M.; JARONIEC, M.; SAKAMOTO, Y.; TERASAKI, O.; RYOO, R.; KO, C. H.: Determination of Pore Size and Pore Wall Structure of MCM-41 by Using Nitrogen Adsorption, Transmission Electron Microscopy, and X-ray Diffraction, *The Journal of Physical Chemistry B*, **2000**, *104* (2), 292–301, DOI: `10.1021/jp992718a`.

[69] KIPKEMBOI, P.; FOGDEN, A.; ALFREDSSON, V.; FLODSTRÖM, K.: Triblock Copolymers as Templates in Mesoporous Silica Formation: Structural Dependence on Polymer Chain Length and Synthesis Temperature, *Langmuir*, **2001**, *17* (17), 5398–5402, DOI: `10.1021/la001715i`.

[70] IMPÉROR-CLERC, M.; DAVIDSON, P.; DAVIDSON, A.: Existence of a Microporous Corona around the Mesopores of Silica-Based SBA-15 Materials Templated by Triblock Copolymers, *Journal of the American Chemical Society*, **2000**, *122* (48), 11925–11933, DOI: `10.1021/ja002245h`.

[71] BENNADJA, Y.; BEAUNIER, P.; MARGOLESE, D.; DAVIDSON, A.: Fine tuning of the interaction between Pluronic surfactants and silica walls in SBA-15 nanostructured materials, *Microporous and Mesoporous Materials*, **2001**, *44-45*, 147–152, DOI: `10.1016/S1387-1811(01)00178-0`.

[72] RUTHSTEIN, S.; FRYDMAN, V.; KABABYA, S.; LANDAU, M.; GOLDFARB, D.: Study of the Formation of the Mesoporous Material SBA-15 by EPR Spectroscopy, *The Journal of Physical Chemistry B*, **2003**, *107* (8), 1739–1748, DOI: `10.1021/jp021964a`.

[73] RYOO, R.; KO, C. H.; KRUK, M.; ANTOCHSHUK, V.; JARONIEC, M.: Block-Copolymer-Templated Ordered Mesoporous Silica: Array of Uniform Mesopores or Mesopore−Micropore Network?, *The Journal of Physical Chemistry B*, **2000**, *104* (48), 11465–11471, DOI: `10.1021/jp002597a`.

[74] ZHENG, Y.; WON, Y.-Y.; BATES, F. S.; DAVIS, H. T.; SCRIVEN, L. E.; TALMON, Y.: Directly Resolved Core-Corona Structure of Block Copolymer Micelles by Cryo-Transmission Electron Microscopy, *The Journal of Physical Chemistry B*, **1999**, *103* (47), 10331–10334, DOI: `10.1021/jp9923264`.

[75] FULVIO, P. F.; PIKUS, S.; JARONIEC, M.: Tailoring properties of SBA-15 materials by controlling conditions of hydrothermal synthesis, *Journal of Materials Chemistry*, **2005**, *15* (47), 5049, DOI: `10.1039/b511346f`.

[76] CUI, X.; ZIN, W.-C.; CHO, W.-J.; HA, C.-S.: Nonionic triblock copolymer synthesis of SBA-15 above the isoelectric point of silica (pH=2–5), *Materials Letters*, **2005**, *59* (18), 2257–2261, DOI: `10.1016/j.matlet.2005.02.073`.

[77] ANTOCHSHUK, V.; JARONIEC, M.: Functionalized Mesoporous Materials Obtained via Interfacial Reactions in Self-Assembled Silica−Surfactant Systems, *Chemistry of Materials*, **2000**, *12* (8), 2496–2501, DOI: `10.1021/cm000268p`.

[78] NAMBA, S.; MOCHIZUKI, A.: Effect of auxiliary chemicals on preparation of silica MCM-41, *Research on Chemical Intermediates*, **1998**, *24* (5), 561–570, DOI: `10.1163/156856798X00087`.

[79] BLIN, J. L.; SU, B. L.: Tailoring Pore Size of Ordered Mesoporous Silicas Using One or Two Organic Auxiliaries as Expanders, *Langmuir*, **2002**, *18* (13), 5303–5308, DOI: `10.1021/la020042w`.

[80] ZHAO, D.; SUN, J.; LI, Q.; STUCKY, G. D.: Morphological Control of Highly Ordered Mesoporous Silica SBA-15, *Chemistry of Materials*, **2000**, *12* (2), 275–279, DOI: `10.1021/cm9911363`.

[81] JANA, S. K.; NISHIDA, R.; SHINDO, K.; KUGITA, T.; NAMBA, S.: Pore size control of mesoporous molecular sieves using different organic auxiliary chemicals, *Microporous and Mesoporous Materials*, **2004**, *68* (1-3), 133–142, DOI: `10.1016/j.micromeso.2003.12.010`.

[82] ZHANG, H.; SUN, J.; MA, D.; BAO, X.; KLEIN-HOFFMANN, A.; WEINBERG, G.; SU, D.; SCHLÖGL, R.: Unusual mesoporous SBA-15 with parallel channels running along the short axis, *Journal of the American Chemical Society*, **2004**, *126* (24), 7440–7441, DOI: `10.1021/ja048630e`.

[83] ZHANG, Y.; ZHAO, L.; LEE, S. S.; YING, J. Y.: Enantioselective Catalysis over Chiral Imidazolidin-4-one Immobilized on Siliceous and Polymer-Coated Mesocellular Foams, *Advanced Synthesis & Catalysis*, **2006**, *348* (15), 2027–2032, DOI: `10.1002/adsc.200600240`.

[84] DENKOVA, A. G.; MENDES, E.; COPPENS, M.-O.: Effects of salts and ethanol on the population and morphology of triblock copolymer micelles in solution, *The Journal of Physical Chemistry B*, **2008**, *112* (3), 793–801, DOI: `10.1021/jp075114c`.

[85] ULAGAPPAN, N.; RAO, C. N. R.: Evidence for supramolecular organization of alkane and surfactant molecules in the process of forming mesoporous silica, *Chem. Commun.*, **1996**, (24), 2759, DOI: `10.1039/CC9960002759`.

[86] RODRÍGUEZ, C.; UDDIN, M. H.; WATANABE, K.; FURUKAWA, H.; HARASHIMA, A.; KUNIEDA, H.: Self-Organization, Phase Behavior, and Microstructure of Poly(oxyethylene) Poly(dimethylsiloxane) Surfactants in Nonpolar Oil, *The Journal of Physical Chemistry B*, **2002**, *106* (1), 22–29, DOI: 10.1021/jp0121264.

[87] ZHAO, D.; HUO, Q.; FENG, J.; CHMELKA, B. F.; STUCKY, G. D.: Nonionic Triblock and Star Diblock Copolymer and Oligomeric Surfactant Syntheses of Highly Ordered, Hydrothermally Stable, Mesoporous Silica Structures, *Journal of the American Chemical Society*, **1998**, *120* (24), 6024–6036, DOI: 10.1021/ja974025i.

[88] VAN DER VOORT, P.; BENJELLOUN, M.; VANSANT, E. F.: Rationalization of the Synthesis of SBA-16: Controlling the Micro- and Mesoporosity, *The Journal of Physical Chemistry B*, **2002**, *106* (35), 9027–9032, DOI: 10.1021/jp0261152.

[89] MORISHIGE, K.; TATEISHI, N.: Adsorption hysteresis in ink-bottle pore, *The Journal of Chemical Physics*, **2003**, *119* (4), 2301–2306, DOI: 10.1063/1.1585014.

[90] LIN, C.-L.; PANG, Y.-S.; CHAO, M.-C.; CHEN, B.-C.; LIN, H.-P.; TANG, C.-Y.; LIN, C.-Y.: Synthesis of SBA-16 and SBA-15 mesoporous silica crystals templated with neutral block copolymer surfactants, *Journal of Physics and Chemistry of Solids*, **2008**, *69* (2-3), 415–419, DOI: 10.1016/j.jpcs.2007.07.006.

[91] JIN, H.; WU, Q.; CHEN, C.; ZHANG, D.; PANG, W.: Facile synthesis of crystal like shape mesoporous silica SBA-16, *Microporous and Mesoporous Materials*, **2006**, *97* (1-3), 141–144, DOI: 10.1016/j.micromeso.2006.08.008.

[92] MESA, M.; SIERRA, L.; PATARIN, J.; GUTH, J.-L.: Morphology and porosity characteristics control of SBA-16 mesoporous silica. Effect of the triblock surfactant Pluronic F127 degradation during the synthesis, *Solid State Sciences*, **2005**, *7* (8), 990–997, DOI: 10.1016/j.solidstatesciences.2005.04.006.

[93] HWANG, Y. K.; CHANG, J.-S.; KWON, Y.-U.; PARK, S.-E.: Microwave synthesis of cubic mesoporous silica SBA-16, *Microporous and Mesoporous Materials*, **2004**, *68* (1-3), 21–27, DOI: 10.1016/j.micromeso.2003.12.004.

[94] GOBIN, O. C.; WAN, Y.; ZHAO, D.; KLEITZ, F.; KALIAGUINE, S.: Mesostructured Silica SBA-16 with Tailored Intrawall Porosity Part 1: Synthesis and Characterization, *The Journal of Physical Chemistry C*, **2007**, *111* (7), 3053–3058, DOI: 10.1021/jp0635765.

[95] HWANG, Y. K.; CHANG, J.-S.; KWON, Y.-U.; PARK, S.-E.: Morphology control of mesoporous SBA-16 using microwave irradiation in: PARK, S.-E. (Ed.), *Nanotechnology in*

mesostructured materials: Proceedings of the 3rd International Mesostructured Materials Symposium, Jeju, Korea, July 8-11, 2002. - "C books"–Cover, vol. 146 of *Studies in Surface Science and Catalysis*, **2003**, Elsevier, Amsterdam, ISBN 9780444514349, pp. 101–104, DOI: `10.1016/S0167-2991(03)80337-3`.

[96] STEVENS, W. J.; MERTENS, M.; MULLENS, S.; THIJS, I.; VAN TENDELOO, G.; COOL, P.; VANSANT, E. F.: Formation mechanism of SBA-16 spheres and control of their dimensions, *Microporous and Mesoporous Materials*, **2006**, *93* (1-3), 119–124, DOI: `10.1016/j.micromeso.2006.02.015`.

[97] STEVENS, W. J. J.; LEBEAU, K.; MERTENS, M.; VAN TENDELOO, G.; COOL, P.; VANSANT, E. F.: Investigation of the morphology of the mesoporous SBA-16 and SBA-15 materials, *The Journal of Physical Chemistry B*, **2006**, *110* (18), 9183–9187, DOI: `10.1021/jp0548725`.

[98] JANSSEN, A. H.; VAN DER VOORT, P.; KOSTER, A. J.; DE JONG, K. P.: A 3D-TEM study of the shape of mesopores in SBA-15 and modified SBA-15 materials, *Chemical Communications*, **2002**, (15), 1632–1633, DOI: `10.1039/b204943k`.

[99] VAN BAVEL, E.; COOL, P.; AERTS, K.; VANSANT, E. F.: Plugged Hexagonal Templated Silica (PHTS): An In-Depth Study of the Structural Characteristics, *The Journal of Physical Chemistry B*, **2004**, *108* (17), 5263–5268, DOI: `10.1021/jp049815a`.

[100] VAN BAVEL, E.; COOL, P.; AERTS, K.; VANSANT, E. F.: Morphology Variations of Plugged Hexagonal Templated Silica, *Journal of Porous Materials*, **2005**, *12* (1), 65–69, DOI: `10.1007/s10934-005-5235-y`.

[101] VAN DER VOORT, P.; RAVIKOVITCH, P. I.; DE JONG, K. P.; NEIMARK, A. V.; JANSSEN, A. H.; BENJELLOUN, M.; VAN BAVEL, E.; COOL, P.; WECKHUYSEN, B. M.; VANSANT, E. F.: Plugged hexagonal templated silica: a unique micro- and mesoporous composite material with internal silica nanocapsules, *Chemical Communications*, **2002**, (9), 1010–1011, DOI: `10.1039/b201424f`.

[102] VAN DER VOORT, P.; RAVIKOVITCH, P. I.; NEIMARK, A. V.; BENJELLOUN, M.; VAN BAVEL, E.; DE JONG, K. P.; WECKHUYSEN, B. M.; VANSANT, E. F.: Plugged Hexagonal Mesoporous Templated Silica : A unique micro- and mesoporous material with internal silica nanocapsules in: *Nanoporous Materials III, Proceedings of the 3rdInternational Symposium on Nanoporous Materials*, vol. 141 of *Studies in Surface Science and Catalysis*, **2002**, Elsevier, ISBN 9780444511133, pp. 45–52, DOI: `10.1016/S0167-2991(02)80523-7`.

[103] KRUK, M.; JARONIEC, M.; KO, C. H.; RYOO, R.: Characterization of the Porous Structure of SBA-15, *Chemistry of Materials*, **2000**, *12* (7), 1961–1968, DOI: `10.1021/cm000164e`.

[104] MEYNEN, V.; COOL, P.; VANSANT, E. F.: Synthesis of siliceous materials with micro- and mesoporosity, *Microporous and Mesoporous Materials*, **2007**, *104* (1-3), 26–38, DOI: `10.1016/j.micromeso.2006.12.003`.

[105] CELER, E. B.; KRUK, M.; ZUZEK, Y.; JARONIEC, M.: Hydrothermal stability of SBA-15 and related ordered mesoporous silicas with plugged pores, *J. Mater. Chem.*, **2006**, *16* (27), 2824, DOI: `10.1039/B603723B`.

[106] SCHMIDT-WINKEL, P.; LUKENS, W. W.; ZHAO, D.; YANG, P.; CHMELKA, B. F.; STUCKY, G. D.: Mesocellular Siliceous Foams with Uniformly Sized Cells and Windows, *Journal of the American Chemical Society*, **1999**, *121* (1), 254–255, DOI: `10.1021/ja983218i`.

[107] SCHMIDT-WINKEL, P.; LUKENS, W. W.; YANG, P.; MARGOLESE, D. I.; LETTOW, J. S.; YING, J. Y.; STUCKY, G. D.: Microemulsion Templating of Siliceous Mesostructured Cellular Foams with Well-Defined Ultralarge Mesopores, *Chemistry of Materials*, **2000**, *12* (3), 686–696, DOI: `10.1021/cm991097v`.

[108] DE WITTE, K.; MEYNEN, V.; MERTENS, M.; LEBEDEV, O. I.; VAN TENDELOO, G.; SEPÚLVEDA-ESCRIBANO, A.; RODRÍGUEZ-REINOSO, F.; VANSANT, E. F.; COOL, P.: Multi-step loading of titania on mesoporous silica: Influence of the morphology and the porosity on the catalytic degradation of aqueous pollutants and VOCs, *Applied Catalysis B: Environmental*, **2008**, *84* (1-2), 125–132, DOI: `10.1016/j.apcatb.2008.03.015`.

[109] TRONG-ON, D.; UNGUREANU, A.; KALIAGUINE, S.: TS-1 coated mesocellular titanosilica foams as new catalysts for oxidation of bulky molecules, *Phys. Chem. Chem. Phys.*, **2003**, *5* (16), 3534, DOI: `10.1039/B304834A`.

[110] LEE, S. S.; HADINOTO, S.; YING, J. Y.: Improved Enantioselectivity of Immobilized Chiral Bisoxazolines by Partial Precapping of the Siliceous Mesocellular Foam Support with Trimethylsilyl Groups, *Advanced Synthesis & Catalysis*, **2006**, *348* (10-11), 1248–1254, DOI: `10.1002/adsc.200606027`.

[111] LIU, S.; LU, L.; YANG, Z.; COOL, P.; VANSANT, E. F.: Further investigations on the modified Stöber method for spherical MCM-41, *Materials Chemistry and Physics*, **2006**, *97* (2-3), 203–206, DOI: `10.1016/j.matchemphys.2005.09.003`.

[112] LETTOW, J. S.; HAN, Y. J.; SCHMIDT-WINKEL, P.; YANG, P.; ZHAO, D.; STUCKY, G. D.; YING, J. Y.: Hexagonal to Mesocellular Foam Phase Transition in Polymer-Templated Mesoporous Silicas, *Langmuir*, **2000**, *16* (22), 8291–8295, DOI: `10.1021/la000660h`.

[113] ZHU, W.; HAN, Y.; AN, L.: SBS as template to synthesize 3D siliceous mesostructured cellular foams, *Microporous and Mesoporous Materials*, **2004**, *72* (1-3), 137–141, DOI: `10.1016/j.micromeso.2004.04.005`.

[114] CHEN, S.-Y.; CHENG, S.: Acid-Free Synthesis of Mesoporous Silica Using Triblock Copolymer as Template with the Aid of Salt and Alcohol, *Chemistry of Materials*, **2007**, *19* (12), 3041–3051, DOI: `10.1021/cm070232y`.

[115] LIU, J.; LI, C.; YANG, Q.; YANG, J.; LI, C.: Morphological and structural evolution of mesoporous silicas in a mild buffer solution and lysozyme adsorption, *Langmuir*, **2007**, *23* (13), 7255–7262, DOI: `10.1021/la7003134`.

[116] HAN, Y.; LEE, S. S.; YING, J. Y.: Spherical Siliceous Mesocellular Foam Particles for High-Speed Size Exclusion Chromatography, *Chemistry of Materials*, **2007**, *19* (9), 2292–2298, DOI: `10.1021/cm063050x`.

[117] ROZIÈRE, J.; BRANDHORST, M.; DUTARTRE, R.; JACQUIN, M.; JONES, D. J.; VITSE, P.; ZAJAC, J.: Effect of surfactant type, substitution by aluminium and additives on direct liquid crystal templated monolithic silica, *J. Mater. Chem.*, **2001**, *11* (12), 3264–3275, DOI: `10.1039/B105276B`.

[118] LEVENTIS, N.; MULIK, S.; WANG, X.; DASS, A.; PATIL, V. U.; SOTIRIOU-LEVENTIS, C.; LU, H.; CHURU, G.; CAPECELATRO, A.: Polymer nano-encapsulation of templated mesoporous silica monoliths with improved mechanical properties, *Journal of Non-Crystalline Solids*, **2008**, *354* (2-9), 632–644, DOI: `10.1016/j.jnoncrysol.2007.06.094`.

[119] NAKANISHI, K.; KOBAYASHI, Y.; AMATANI, T.; HIRAO, K.; KODAIRA, T.: Spontaneous Formation of Hierarchical Macro−Mesoporous Ethane−Silica Monolith, *Chemistry of Materials*, **2004**, *16* (19), 3652–3658, DOI: `10.1021/cm049320y`.

[120] GAO, R.; DAI, W.-L.; YANG, X.; LI, H.; FAN, K.: Highly efficient tungsten trioxide containing mesocellular silica foam catalyst in the O-heterocyclization of cycloocta-1,5-diene with aqueous H2O2, *Applied Catalysis A: General*, **2007**, *332* (1), 138–145, DOI: `10.1016/j.apcata.2007.08.012`.

[121] CHMIELARZ, L.; KUŚTROWSKI, P.; DZIEMBAJ, R.; COOL, P.; VANSANT, E. F.: Catalytic performance of various mesoporous silicas modified with copper or iron oxides introduced by different ways in the selective reduction of NO by ammonia, *Applied Catalysis B: Environmental*, **2006**, *62* (3-4), 369–380, DOI: `10.1016/j.apcatb.2005.09.004`.

[122] KIM, H.; JUNG, J. C.; KIM, P.; YEOM, S. H.; LEE, K.-Y.; SONG, I. K.: Preparation of H3PMo12O40 catalyst immobilized on surface modified mesostructured cellular foam (SM-MCF) silica and its application to the ethanol conversion reaction, *Journal of Molecular Catalysis A: Chemical*, **2006**, *259* (1-2), 150–155, DOI: `10.1016/j.molcata.2006.06.032`.

[123] SU, Y.; LIU, Y.-M.; WANG, L.-C.; CHEN, M.; CAO, Y.; DAI, W.-L.; HE, H.-Y.; FAN, K.-N.: Tungsten-containing MCF silica as active and recyclable catalysts for liquid-phase ox-

idation of 1,3-butanediol to 4-hydroxy-2-butanone, *Applied Catalysis A: General*, **2006**, *315*, 91–100, DOI: `10.1016/j.apcata.2006.09.002`.

[124] KIM, H.; JUNG, J. C.; YEOM, S. H.; LEE, K.-Y.; YI, J.; SONG, I. K.: Immobilization of a heteropolyacid catalyst on the aminopropyl-functionalized mesostructured cellular foam (MCF) silica, *Materials Research Bulletin*, **2007**, *42* (12), 2132–2142, DOI: `10.1016/j.materresbull.2007.01.010`.

[125] KRÄMER, E.; FÖRSTER, S.; GÖLTNER, C.; ANTONIETTI, M.: Synthesis of Nanoporous Silica with New Pore Morphologies by Templating the Assemblies of Ionic Block Copolymers, *Langmuir*, **1998**, *14* (8), 2027–2031, DOI: `10.1021/la9712505`.

[126] GÖLTNER, C. G.; BERTON, B.; KRÄMER, E.; ANTONIETTI, M.: Nanoporous silica from amphiphilic block copolymer (ABC) aggregates: control over correlation and architecture of cylindrical pores, *Chemical Communications*, **1998**, (21), 2287–2288, DOI: `10.1039/a806701e`.

[127] GÖLTNER, C. G.; BERTON, B.; KRÄMER, E.; ANTONIETTI, M.: Nanoporous Silicas by Casting the Aggregates of Amphiphilic Block Copolymers: The Transition from Cylinders to Lamellae and Vesicles, *Advanced Materials*, **1999**, *11* (5), 395–398, DOI: `10.1002/(SICI)1521-4095(199903)11:5<395`.

[128] YANG, P.; ZHAO, D.; CHMELKA, B. F.; STUCKY, G. D.: Triblock-Copolymer-Directed Syntheses of Large-Pore Mesoporous Silica Fibers, *Chemistry of Materials*, **1998**, *10* (8), 2033–2036, DOI: `10.1021/cm980201q`.

[129] SCHMIDT-WINKEL, P.; YANG, P.; MARGOLESE, D. I.; CHMELKA, B. F.; STUCKY, G. D.: Fluoride-Induced Hierarchical Ordering of Mesoporous Silica in Aqueous Acid-Syntheses, *Advanced Materials*, **1999**, *11* (4), 303–307, DOI: `10.1002/(SICI)1521-4095(199903)11:4<303`.

[130] ZHAO, D.; YANG, P.; CHMELKA, B. F.; STUCKY, G. D.: Multiphase Assembly of Mesoporous−Macroporous Membranes, *Chemistry of Materials*, **1999**, *11* (5), 1174–1178, DOI: `10.1021/cm980782j`.

[131] HOFFMANN, F.; CORNELIUS, M.; MORELL, J.; FRÖBA, M.: Mesoporöse organisch-anorganische Hybridmaterialien auf Silicabasis, *Angewandte Chemie*, **2006**, *118* (20), 3290–3328, DOI: `10.1002/ange.200503075`.

[132] SOLER-ILLIA, GALO J. DE A. A.; SANCHEZ, C.; LEBEAU, B.; PATARIN, J.: Chemical Strategies To Design Textured Materials: from Microporous and Mesoporous Oxides to Nanonetworks and Hierarchical Structures, *Chemical reviews*, **2002**, *102* (11), 4093–4138, DOI: `10.1021/cr0200062`.

[133] MONNIER, A.; SCHÜTH, F.; HUO, Q.; KUMAR, D.; MARGOLESE, D.; MAXWELL, R. S.; STUCKY, G. D.; KRISHNAMURTY, M.; PETROFF, P.; FIROUZI, A.; JANICKE, M.; CHMELKA, B. F.: Cooperative formation of inorganic-organic interfaces in the synthesis of silicate mesostructures, *Science*, **1993**, *261* (5126), 1299–1303, DOI: `10.1126/science.261.5126.1299`.

[134] HUO, Q.; MARGOLESE, D. I.; CIESLA, U.; FENG, P.; GIER, T. E.; SIEGER, P.; LEON, R.; PETROFF, P. M.; SCHÜTH, F.; STUCKY, G. D.: Generalized synthesis of periodic surfactant/inorganic composite materials, *Nature*, **1994**, *368* (6469), 317–321, DOI: `10.1038/368317a0`.

[135] HUO, Q.; MARGOLESE, D. I.; CIESLA, U.; DEMUTH, D. G.; FENG, P.; GIER, T. E.; SIEGER, P.; FIROUZI, A.; CHMELKA, B. F.: Organization of Organic Molecules with Inorganic Molecular Species into Nanocomposite Biphase Arrays, *Chemistry of Materials*, **1994**, *6* (8), 1176–1191, DOI: `10.1021/cm00044a016`.

[136] ATTARD, G. S.; GLYDE, J. C.; GÖLTNER, C. G.: Liquid-crystalline phases as templates for the synthesis of mesoporous silica, *Nature*, **1995**, *378* (6555), 366–368, DOI: `10.1038/378366a0`.

[137] TIAN, B.; LIU, X.; YU, C.; GAO, F.; LUO, Q.; XIE, S.; TU, B.; ZHAO, D.: Microwave assisted template removal of siliceous porous materials, *Chem. Commun.*, **2002**, (11), 1186–1187, DOI: `10.1039/b202180c`.

[138] VAN GRIEKEN, R.; CALLEJA, G.; STUCKY, G. D.; MELERO, J. A.; GARCÍA, R. A.; IGLESIAS, J.: Supercritical Fluid Extraction of a Nonionic Surfactant Template from SBA-15 Materials and Consequences on the Porous Structure, *Langmuir*, **2003**, *19* (9), 3966–3973, DOI: `10.1021/la026970c`.

[139] YANG, C.-M.; WANG, Y.; ZIBROWIUS, B.; SCHÜTH, F.: Formation of cyanide-functionalized SBA-15 and its transformation to carboxylate-functionalized SBA-15, *Phys. Chem. Chem. Phys.*, **2004**, *6* (9), 2461–2467, DOI: `10.1039/b314538g`.

[140] ZHAO, X. S.; LU, G. Q.; WHITTAKER, A. K.; MILLAR, G. J.; ZHU, H. Y.: Comprehensive Study of Surface Chemistry of MCM-41 Using 29Si CP/MAS NMR, FTIR, Pyridine-TPD, and TGA, *The Journal of Physical Chemistry B*, **1997**, *101* (33), 6525–6531, DOI: `10.1021/jp971366+`.

[141] KLEITZ, F.; SCHMIDT, W.; SCHÜTH, F.: Evolution of mesoporous materials during the calcination process: structural and chemical behavior, *Microporous and Mesoporous Materials*, **2001**, *44-45*, 95–109, DOI: `10.1016/S1387-1811(01)00173-1`.

[142] BLANCHARD, J.; SCHÜTH, F.; TRENS, P.; HUDSON, M.: Synthesis of hexagonally packed porous titanium oxo-phosphate, *Microporous and Mesoporous Materials*, **2000**, *39* (1-2), 163–170, DOI: `10.1016/S1387-1811(00)00192-X`.

[143] SCHÜTH, F.; CIESLA, U.; SCHACHT, S.; THIEME, M.; HUO, Q.; STUCKY, G.: Ordered mesoporous silicas and zirconias: control on length scales between nanometer and micrometer, *Materials Research Bulletin*, **1999**, *34* (3), 483–494, DOI: `10.1016/S0025-5408(99)00032-X`.

[144] HITZ, S.; PRINS, R.: Influence of Template Extraction on Structure, Activity, and Stability of MCM-41 Catalysts, *Journal of Catalysis*, **1997**, *168* (2), 194–206, DOI: `10.1006/jcat.1997.1659`.

[145] CHEN, C.-Y.; LI, H.-X.; DAVIS, M. E.: Studies on mesoporous materials, *Microporous Materials*, **1993**, *2* (1), 17–26, DOI: `10.1016/0927-6513(93)80058-3`.

[146] WANG, Z.; LIU, Q.; YU, J.; WU, T.; WANG, G.: Surface structure and catalytic behavior of silica-supported copper catalysts prepared by impregnation and sol–gel methods, *Applied Catalysis A: General*, **2003**, *239* (1-2), 87–94, DOI: `10.1016/S0926-860X(02)00421-0`.

[147] YANG, C.-M.; ZIBROWIUS, B.; SCHÜTH, F.: A novel synthetic route for negatively charged ordered mesoporous silica SBA-15, *Chem. Commun.*, **2003**, *359* (14), 1772–1773, DOI: `10.1039/b304626e`.

[148] GALLIS, K. W.; LANDRY, C. C.: Rapid Calcination of Nanostructured Silicate Composites by Microwave Irradiation, *Advanced Materials*, **2001**, *13* (1), 23–26, DOI: `10.1002/1521-4095(200101)13:1<23`.

[149] IDE, M.; EL-ROZ, M.; DE CANCK, E.; VICENTE, A.; PLANCKAERT, T.; BOGAERTS, T.; VAN DRIESSCHE, I.; LYNEN, F.; VAN SPEYBROECK, V.; THYBAULT-STARZYK, F.; VAN DER VOORT, P.: Quantification of silanol sites for the most common mesoporous ordered silicas and organosilicas: total versus accessible silanols, *Physical chemistry chemical physics : PCCP*, **2013**, *15* (2), 642–650, DOI: `10.1039/c2cp42811c`.

[150] RAMÍREZ, A.; LOPEZ, B. L.; SIERRA, L.: Study of the Acidic Sites and Their Modifications in Mesoporous Silica Synthesized in Acidic Medium under Quiescent Conditions, *The Journal of Physical Chemistry B*, **2003**, *107* (35), 9275–9280, DOI: `10.1021/jp0351472`.

[151] ROSENHOLM, J. M.; CZURYSZKIEWICZ, T.; KLEITZ, F.; ROSENHOLM, J. B.; LINDÉN, M.: On the nature of the Brønsted acidic groups on native and functionalized mesoporous siliceous SBA-15 as studied by benzylamine adsorption from solution, *Langmuir*, **2007**, *23* (8), 4315–4323, DOI: `10.1021/la062450w`.

[152] BRINKER, C. J.; SCHERER, G. W.: Surface Chemistry and Chemical Modification in: *Sol-Gel Science*, **1990**, Elsevier, ISBN 9780080571034, pp. 616–672, DOI: `10.1016/B978-0-08-057103-4.50015-5`.

[153] LANDMESSER, H.: Interior surface hydroxyl groups in ordered mesoporous silicates, *Solid State Ionics*, **1997**, *101-103*, 271–277, DOI: `10.1016/S0167-2738(97)84042-8`.

[154] STEEL, A.; CARR, S. W.; ANDERSON, M. W.: 29Si solid-state NMR study of mesoporous M41S materials, *Chemistry of Materials*, **1995**, *7* (10), 1829–1832, DOI: `10.1021/cm00058a012`.

[155] VAN DER MEER, J.; BARDEZ-GIBOIRE, I.; MERCIER, C.; REVEL, B.; DAVIDSON, A.; DENOYEL, R.: Mechanism of Metal Oxide Nanoparticle Loading in SBA-15 by the Double Solvent Technique, *The Journal of Physical Chemistry C*, **2010**, *114* (8), 3507–3515, DOI: `10.1021/jp907002y`.

[156] SHENDEROVICH, I. G.; MAUDER, D.; AKCAKAYIRAN, D.; BUNTKOWSKY, G.; LIMBACH, H.-H.; FINDENEGG, G. H.: NMR provides checklist of generic properties for atomic-scale models of periodic mesoporous silicas, *The Journal of Physical Chemistry B*, **2007**, *111* (42), 12088–12096, DOI: `10.1021/jp073682m`.

[157] NAWROCKI, J.: The silanol group and its role in liquid chromatography, *Journal of Chromatography A*, **1997**, *779* (1-2), 29–71, DOI: `10.1016/S0021-9673(97)00479-2`.

[158] KOZLOVA, S. A.; KIRIK, S. D.: Post-synthetic activation of silanol covering in the mesostructured silicate materials MCM-41 and SBA-15, *Microporous and Mesoporous Materials*, **2010**, *133* (1-3), 124–133, DOI: `10.1016/j.micromeso.2010.04.024`.

[159] Chapter 2 Physical characterization of the silica surface in: VANSANT, E. F.; VAN DER VOORT, P.; VRANCKEN, K. C. (Eds.), *Characterization and Chemical Modification of the Silica Surface*, vol. 93 of *Studies in Surface Science and Catalysis*, **1995**, Elsevier, ISBN 9780444819284, pp. 31–58, DOI: `10.1016/S0167-2991(06)81510-7`.

[160] GALLAS, J.-P.; GOUPIL, J.-M.; VIMONT, A.; LAVALLEY, J.-C.; GIL, B.; GILSON, J.-P.; MISERQUE, O.: Quantification of water and silanol species on various silicas by coupling IR spectroscopy and in-situ thermogravimetry, *Langmuir*, **2009**, *25* (10), 5825–5834, DOI: `10.1021/la802688w`.

[161] JENTYS, A.; KLEESTORFER, K.; VINEK, H.: Concentration of surface hydroxyl groups on MCM-41, *Microporous and Mesoporous Materials*, **1999**, *27* (2-3), 321–328, DOI: `10.1016/S1387-1811(98)00265-0`.

[162] GILLIS-D'HAMERS, I.; CORNELISSENS, I.; VRANCKEN, K. C.; VAN DER VOORT, P.; VANSANT, E. F.; DAELEMANS, F.: Modelling of the hydroxyl group population using an energetic analysis of the temperature-programmed desorption of pyridine from silica gel, *Journal of the Chemical Society, Faraday Transactions*, **1992**, *88* (5), 723, DOI: `10.1039/ft9928800723`.

[163] SMEULDERS, G.; MEYNEN, V.; SILVESTRE-ALBERO, A.; HOUTHOOFD, K.; MERTENS, M.; SILVESTRE-ALBERO, J.; MARTENS, J. A.; COOL, P.: The impact of framework organic functional groups on the hydrophobicity and overall stability of mesoporous silica materials, *Materials Chemistry and Physics*, **2012**, *132* (2-3), 1077–1088, DOI: `10.1016/j.matchemphys.2011.12.072`.

[164] KOMARNENI, S.; MENON, V. C.; PIDUGU, R.; GOWOREK, J.; STEFANIAK, W.: Temperature-programmed desorption vs. N2 desorption in determining pore-size distribution of mesoporous silica molecular sieves, *Journal of Porous Materials*, **1996**, *3* (2), 115–119, DOI: `10.1007/BF01186041`.

[165] THOMMES, M.; KÖHN, R.; FRÖBA, M.: Sorption and pore condensation behavior of pure fluids in mesoporous MCM-48 silica, MCM-41 silica, SBA-15 silica and controlled-pore glass at temperatures above and below the bulk triple point, *Applied Surface Science*, **2002**, *196* (1-4), 239–249, DOI: `10.1016/S0169-4332(02)00062-4`.

[166] THOMMES, M.; CYCHOSZ, K. A.: Physical adsorption characterization of nanoporous materials: progress and challenges, *Adsorption*, **2014**, *20* (2-3), 233–250, DOI: `10.1007/s10450-014-9606-z`.

[167] SCARLETT, B.; LOWELL, S.; SHIELDS, J. E.; THOMAS, M. A.; THOMMES, M.: *Characterization of Porous Solids and Powders: Surface Area, Pore Size and Density*, vol. 16, **2004**, Springer Netherlands, Dordrecht, ISBN 978-90-481-6633-6, DOI: `10.1007/978-1-4020-2303-3`.

[168] CYCHOSZ, K. A.; GUILLET-NICOLAS, R.; GARCÍA-MARTÍNEZ, J.; THOMMES, M.: Recent advances in the textural characterization of hierarchically structured nanoporous materials, *Chemical Society reviews*, **2017**, *46* (2), 389–414, DOI: `10.1039/c6cs00391e`.

[169] RAVIKOVITCH, P. I.; NEIMARK, A. V.: Density Functional Theory of Adsorption in Spherical Cavities and Pore Size Characterization of Templated Nanoporous Silicas with Cubic and Three-Dimensional Hexagonal Structures, *Langmuir*, **2002**, *18* (5), 1550–1560, DOI: `10.1021/la0107594`.

[170] KRUK, M.; JARONIEC, M.; SAYARI, A.: Relations between Pore Structure Parameters and Their Implications for Characterization of MCM-41 Using Gas Adsorption and X-ray Diffraction, *Chemistry of Materials*, **1999**, *11* (2), 492–500, DOI: `10.1021/cm981006e`.

[171] LEÓN Y LEÓN, C. A.: New perspectives in mercury porosimetry, *Advances in Colloid and Interface Science*, **1998**, *76-77*, 341–372, DOI: `10.1016/S0001-8686(98)00052-9`.

[172] GIESCHE, H.: Mercury Porosimetry in: *Schüth, Sing et al. (Hg.) 2002 – Handbook of Porous Solids*, pp. 309–351, DOI: `10.1002/9783527618286.ch9`.

[173] GIESCHE, H.: Mercury Porosimetry: A General (Practical) Overview, *Particle & Particle Systems Characterization*, **2006**, *23* (1), 9–19, DOI: `10.1002/ppsc.200601009`.

[174] GOWOREK, J.; STEFANIAK, W.: Application of thermogravimetric analysis to the estimation of the porosity of silica gels, *Colloids and Surfaces*, **1991**, *60*, 341–349, DOI: `10.1016/0166-6622(91)80286-W`.

[175] GOWOREK, J.; STEFANIAK, W.: Characterization of the porosity of silica gels by thermogravimetric analysis, *Colloids and Surfaces*, **1991**, *57* (1), 161–165, DOI: `10.1016/0166-6622(91)80188-T`.

[176] GOWOREK, J.; STEFANIAK, W.: Porosity of silica gels by thermogravimetric analysis, *Colloids and Surfaces*, **1992**, *62* (1-2), 135–140, DOI: `10.1016/0166-6622(92)80045-4`.

[177] GOWOREK, J.; STEFANIAK, W.: Porosity of silica gels by thermal desorption of liquids, *Colloids and Surfaces*, **1992**, *69* (1), 23–29, DOI: `10.1016/0166-6622(92)80234-S`.

[178] GOWOREK, J.; STEFANIAK, W.: Investigation on the porosity of silica gel by thermal desorption of liquids, *Materials Chemistry and Physics*, **1992**, *32* (3), 244–248, DOI: `10.1016/0254-0584(92)90206-N`.

[179] GLAVES, C. L.; BRINKER, C. J.; SMITH, D. M.; DAVIS, P. J.: In situ pore structure studies of xerogel drying, *Chemistry of Materials*, **1989**, *1* (1), 34–40, DOI: `10.1021/cm00001a011`.

[180] GALLEGOS, D. P.; MUNN, K.; SMITH, D. M.; STERMER, D. L.: A NMR technique for the analysis of pore structure: Application to materials with well-defined pore structure, *Journal of Colloid and Interface Science*, **1987**, *119* (1), 127–140, DOI: `10.1016/0021-9797(87)90251-7`.

[181] BHATTACHARJA, S.; D'ORAZIO, F.; TARCZON, J. C.; HALPERIN, W. P.; GERHARDT, R.: Internal Structure of Porous Silica: A Model System for Characterization by Nuclear Magnetic Resonance, *Journal of the American Ceramic Society*, **1989**, *72* (11), 2126–2130, DOI: `10.1111/j.1151-2916.1989.tb06043.x`.

[182] ZELEŇÁK, V.; BADANIČOVÁ, M.; HALAMOVÁ, D.; ČEJKA, J.; ZUKAL, A.; MURAFA, N.; GOERIGK, G.: Amine-modified ordered mesoporous silica: Effect of pore size on carbon

dioxide capture, *Chemical Engineering Journal*, **2008**, *144* (2), 336–342, DOI: `10.1016/j.cej.2008.07.025`.

[183] HALÁSZ, I.; MARTIN, K.: Pore Sizes of Solids, *Angewandte Chemie International Edition in English*, **1978**, *17* (12), 901–908, DOI: `10.1002/anie.197809011`.

[184] KNOX, J. H.; RITCHIE, H. J.: Determination of pore size distribution curves by size-exclusion chromatography, *Journal of Chromatography A*, **1987**, *387*, 65–84, DOI: `10.1016/S0021-9673(01)94514-5`.

[185] MAZSAROFF, I.; E. REGNIER, F.: Phase ratio determination in an ion-exchange column having pores partially accessible to proteins, *Journal of Chromatography A*, **1988**, *442*, 15–28, DOI: `10.1016/s0021-9673(00)94454-6`.

[186] GUAN, H.; GUIOCHON, G.: Study of physico-chemical properties of some packing materials, *Journal of Chromatography A*, **1996**, *731* (1-2), 27–40, DOI: `10.1016/0021-9673(95)01197-8`.

[187] DEPHILLIPS, P.; LENHOFF, A. M.: Pore size distributions of cation-exchange adsorbents determined by inverse size-exclusion chromatography, *Journal of Chromatography A*, **2000**, *883* (1-2), 39–54, DOI: `10.1016/S0021-9673(00)00420-9`.

[188] BARTH, H. G.; BOYES, B. E.; JACKSON, C.: Size Exclusion Chromatography, *Analytical chemistry*, **1996**, *68* (12), 445–466, DOI: `10.1021/a19600193`.

[189] AL-BOKARI, M.; CHERRAK, D.; GUIOCHON, G.: Determination of the porosities of monolithic columns by inverse size-exclusion chromatography, *Journal of Chromatography A*, **2002**, *975* (2), 275–284, DOI: `10.1016/S0021-9673(02)01271-2`.

[190] JERABEK, K.; REVILLON, A.; PUCCILLI, E.: Pore structure characterization of organic-inorganic materials by inverse size exclusion chromatography, *Chromatographia*, **1993**, *36* (1), 259–262, DOI: `10.1007/BF02263874`.

[191] GOTO, M.; MCCOY, B. J.: Inverse size-exclusion chromatography for distributed pore and solute sizes, *Chemical Engineering Science*, **2000**, *55* (4), 723–732, DOI: `10.1016/S0009-2509(99)00352-8`.

[192] WEBB, J. D.; SEKI, T.; GOLDSTON, J. F.; PRUSKI, M.; CRUDDEN, C. M.: Selective functionalization of the mesopores of SBA-15, *Microporous and Mesoporous Materials*, **2015**, *203*, 123–131, DOI: `10.1016/j.micromeso.2014.10.032`.

[193] SHEPHARD, D. S.; ZHOU, W.; MASCHMEYER, T.; MATTERS, J. M.; ROPER, C. L.; PARSONS, S.; JOHNSON, B. F. G.; DUER, M. J.: Site-Directed Surface Derivatization of

MCM-41: Use of High-Resolution Transmission Electron Microscopy and Molecular Recognition for Determining the Position of Functionality within Mesoporous Materials, *Angewandte Chemie International Edition in English*, **1998**, *37* (19), 2719–2723, DOI: `10.1002/(SICI)1521-3773(19981016)37:19<2719`.

[194] HARTMANN, M.; VINU, A.: Mechanical Stability and Porosity Analysis of Large-Pore SBA-15 Mesoporous Molecular Sieves by Mercury Porosimetry and Organics Adsorption, *Langmuir*, **2002**, *18* (21), 8010–8016, DOI: `10.1021/la025782j`.

[195] CHYTIL, S.; HAUGLAND, L.; BLEKKAN, E. A.: On the mechanical stability of mesoporous silica SBA-15, *Microporous and Mesoporous Materials*, **2008**, *111* (1-3), 134–142, DOI: `10.1016/j.micromeso.2007.07.020`.

[196] TATSUMI, T.; KOYANO, K. A.; TANAKA, Y.; NAKATA, S.: *Journal of Porous Materials*, **1999**, *6* (1), 13–17, DOI: `10.1023/A:1009682915127`.

[197] GALARNEAU, A.; DESPLANTIER-GISCARD, D.; DI RENZO, F.; FAJULA, F.: Thermal and mechanical stability of micelle-templated silica supports for catalysis, *Catalysis Today*, **2001**, *68* (1-3), 191–200, DOI: `10.1016/S0920-5861(01)00300-5`.

[198] VAN DER VOORT, P.; RAVIKOVITCH, P. I.; DE JONG, K. P.; BENJELLOUN, M.; VAN BAVEL, E.; JANSSEN, A. H.; NEIMARK, A. V.; WECKHUYSEN, B. M.; VANSANT, E. F.: A New Templated Ordered Structure with Combined Micro- and Mesopores and Internal Silica Nanocapsules, *The Journal of Physical Chemistry B*, **2002**, *106* (23), 5873–5877, DOI: `10.1021/jp025642i`.

[199] BRANDHUBER, D.; PETERLIK, H.; HÜSING, N.: Simultaneous drying and chemical modification of hierarchically organized silica monoliths with organofunctional silanes, *Journal of Materials Chemistry*, **2005**, *15* (35-36), 3896, DOI: `10.1039/B505976C`.

[200] LIN, H.-P.; YANG, L.-Y.; MOU, C.-Y.; LIU, S.-B.; LEE, H.-K.: A direct surface silyl modification of acid-synthesized mesoporous silica, *New Journal of Chemistry*, **2000**, *24* (5), 253–255, DOI: `10.1039/b001858i`.

[201] ANDRADE, G. F.; SOARES, D. C. F.; ALMEIDA, R. K.; SOUSA, E. M. B.: Mesoporous Silica SBA-16 Functionalized with Alkoxysilane Groups: Preparation, Characterization, and Release Profile Study, *Journal of Nanomaterials*, **2012**, *2012* (1), 1–10, DOI: `10.1155/2012/816496`.

[202] CATTOËN, X.; NOUREDDINE, A.; CROISSANT, J.; MOITRA, N.; BÜRGLOVÁ, K.; HODAČOVÁ, J.; DE LOS COBOS, O.; LEJEUNE, M.; ROSSIGNOL, F.; TOULEMON, D.; BÉGIN-COLIN, S.; PICHON, B. P.; RAEHM, L.; DURAND, J.-O.; WONG CHI MAN, M.: Click approaches in sol–gel chemistry, *Journal of Sol-Gel Science and Technology*, **2013**, *22* (29), 3208, DOI: `10.1007/s10971-013-3155-x`.

[203] STAWICKA, K.; DRAZKIEWICZ, K.; ZIOLEK, M.: The effect of structure of mesoporous silica and niobiosilicate on incorporation and stability of modifiers introduced by the click reaction catalyzed by different copper salts, *Microporous and Mesoporous Materials*, **2018**, *258*, 41–54, DOI: `10.1016/j.micromeso.2017.09.005`.

[204] MALVI, B.; SARKAR, B. R.; PATI, D.; MATHEW, R.; AJITHKUMAR, T. G.; SEN GUPTA, S.: "Clickable" SBA-15 mesoporous materials: synthesis, characterization and their reaction with alkynes, *Journal of Materials Chemistry*, **2009**, *19* (10), 1409, DOI: `10.1039/b815350g`.

[205] LINARES, N.; SERRANO, E.; RICO, M.; BALU, A. M.; LOSADA, E.; LUQUE, R.; GARCÍA-MARTÍNEZ, J.: Incorporation of chemical functionalities in the framework of mesoporous silica, *Chem. Commun.*, **2011**, *47* (32), 9024–9035, DOI: `10.1039/C1CC11016K`.

[206] MACQUARRIE, D. J.: Direct preparation of organically modified MCM-type materials. Preparation and characterization of aminopropyl–MCM and 2-cyanoethyl–MCM, *Chem. Commun.*, **1996**, *114* (16), 1961–1962, DOI: `10.1039/CC9960001961`.

[207] JUNGES, U.; JACOBS, W.; VOIGT-MARTIN, I.; KRUTZSCH, B.; SCHÜTH, F.: MCM-41 as a support for small platinum particles: a catalyst for low-temperature carbon monoxide oxidation, *The Journal of Chemical Physics*, **1995**, (22), 2283–2284, DOI: `10.1039/C39950002283`.

[208] ÁNGELES ARAMENDÍA, M.; BORAU, V.; JIMÉNEZ, C.; MARINAS, J. M.; ROMERO, F. J.: Supramolecular templated synthesis of platinum-supported silica, *Chem. Commun.*, **1999**, (10), 873–874, DOI: `10.1039/A901924C`.

[209] XIANG, L.; ROYER, S.; ZHANG, H.; TATIBOUËT, J.-M.; BARRAULT, J.; VALANGE, S.: Properties of iron-based mesoporous silica for the CWPO of phenol: a comparison between impregnation and co-condensation routes, *Journal of hazardous materials*, **2009**, *172* (2-3), 1175–1184, DOI: `10.1016/j.jhazmat.2009.07.121`.

[210] GARCIA-MARTINEZ, J.; LINARES, N.; SINIBALDI, S.; CORONADO, E.; RIBERA, A.: Incorporation of Pd nanoparticles in mesostructured silica, *Microporous and Mesoporous Materials*, **2009**, *117* (1-2), 170–177, DOI: `10.1016/j.micromeso.2008.06.038`.

[211] APRILE, C.; ABAD, A.; GARCÍA, H.; CORMA, A.: Synthesis and catalytic activity of periodic mesoporous materials incorporating gold nanoparticles, *J. Mater. Chem.*, **2005**, *15* (41), 4408, DOI: `10.1039/B507418E`.

[212] MILLER, J.: A fundamental study of platinum tetraammine impregnation of silica: 2. The effect of method of preparation, loading, and calcination temperature on (reduced) particle size, *Journal of Catalysis*, **2004**, *225* (1), 203–212, DOI: `10.1016/j.jcat.2004.04.007`.

[213] Ho, S.-W.; Su, Y.-S.: Effects of Ethanol Impregnation on the Properties of Silica-Supported Cobalt Catalysts, *Journal of Catalysis*, **1997**, *168* (1), 51–59, DOI: `10.1006/jcat.1997.1614`.

[214] Sietsma, J. R. A.; Meeldijk, J. D.; Versluijs-Helder, M.; Broersma, A.; van Dillen, A. J.; de Jongh, P. E.; de Jong, K. P.: Ordered Mesoporous Silica to Study the Preparation of Ni/SiO2 ex Nitrate Catalysts: Impregnation, Drying, and Thermal Treatments, *Chemistry of Materials*, **2008**, *20* (9), 2921–2931, DOI: `10.1021/cm702610h`.

[215] Roucoux, A.; Schulz, J.; Patin, H.: Reduced transition metal colloids: a novel family of reusable catalysts?, *Chemical reviews*, **2002**, *102* (10), 3757–3778, DOI: `10.1021/cr010350j`.

[216] Krijnen, S.; Abbenhuis, H. C. L.; Hanssen, Rob W. J. M.; van Hooff, J. H. C.; van Santen, R. A.: Solid-Phase Immobilization of a New Epoxidation Catalyst, *Angewandte Chemie International Edition*, **1998**, *37* (3), 356–358, DOI: `10.1002/(SICI)1521-3773(19980216)37:3<356`.

[217] Wagner, H. H.; Hausmann, H.; Hölderich, W. F.: Immobilization of Rhodium Diphosphine Complexes on Mesoporous Al-MCM-41 Materials: Catalysts for Enantioselective Hydrogenation, *Journal of Catalysis*, **2001**, *203* (1), 150–156, DOI: `10.1006/jcat.2001.3296`.

[218] Raynor, S. A.; Thomas, J. M.; Raja, R.; Johnson, B. F. G.; Bell, R. G.; d. Mantle, M.: A one-step, enantioselective reduction of ethyl nicotinate to ethyl nipecotinate using a constrained, chiral, heterogeneous catalyst, *Chemical Communications*, **2000**, (19), 1925–1926, DOI: `10.1039/b005689h`.

[219] Derouet, D.; Forgeard, S.; Brosse, J.-C.; Emery, J.; Buzare, J.-Y.: Application of solid-state NMR (13C and29Si CP/MAS NMR) spectroscopy to the characterization of alkenyltrialkoxysilane and trialkoxysilyl-terminated polyisoprene grafting onto silica microparticles, *Journal of Polymer Science Part A: Polymer Chemistry*, **1998**, *36* (3), 437–453, DOI: `10.1002/(SICI)1099-0518(199802)36:3<437`.

[220] Mohammadi Ziarani, G.; Hassanzadeh, Z.; Gholamzadeh, P.; Asadi, S.; Badiei, A.: Advances in click chemistry for silica-based material construction, *RSC Advances*, **2016**, *6* (26), 21979–22006, DOI: `10.1039/C5RA26034E`.

[221] Hoffmann, F.; Fröba, M.: Vitalising porous inorganic silica networks with organic functions–PMOs and related hybrid materials, *Chemical Society reviews*, **2011**, *40* (2), 608–620, DOI: `10.1039/c0cs00076k`.

[222] ZAMBOULIS, A.; MOITRA, N.; MOREAU, J. J. E.; CATTOËN, X.; WONG CHI MAN, M.: Hybrid materials: versatile matrices for supporting homogeneous catalysts, *Journal of Materials Chemistry*, **2010**, *20* (42), 9322, DOI: `10.1039/c000334d`.

[223] MOITRA, N.; TRENS, P.; RAEHM, L.; DURAND, J.-O.; CATTOËN, X.; CHI MAN, M. W.: Facile route to functionalized mesoporous silica nanoparticles by click chemistry, *Journal of Materials Chemistry*, **2011**, *21* (35), 13476, DOI: `10.1039/c1jm12066b`.

[224] LU, A.-H.; LI, W.-C.; KIEFER, A.; SCHMIDT, W.; BILL, E.; FINK, G.; SCHÜTH, F.: Fabrication of magnetically separable mesostructured silica with an open pore system, *Journal of the American Chemical Society*, **2004**, *126* (28), 8616–8617, DOI: `10.1021/ja0486521`.

[225] YANG, C.-M.; ZIBROWIUS, B.; SCHMIDT, W.; SCHÜTH, F.: Consecutive Generation of Mesopores and Micropores in SBA-15, *Chemistry of Materials*, **2003**, *15* (20), 3739–3741, DOI: `10.1021/cm031109j`.

[226] CAUDA, V.; SCHLOSSBAUER, A.; KECHT, J.; ZÜRNER, A.; BEIN, T.: Multiple core-shell functionalized colloidal mesoporous silica nanoparticles, *Journal of the American Chemical Society*, **2009**, *131* (32), 11361–11370, DOI: `10.1021/ja809346n`.

[227] ASEFA, T.; LENNOX, R. B.: Synthesis of Gold Nanoparticles via Electroless Deposition in SBA-15, *Chemistry of Materials*, **2005**, *17* (10), 2481–2483, DOI: `10.1021/cm047800j`.

[228] DE JUAN, F.; RUIZ-HITZKY, E.: Selective Functionalization of Mesoporous Silica, *Advanced Materials*, **2000**, *12* (6), 430–432, DOI: `10.1002/(SICI)1521-4095(200003)12:6<430`.

[229] LIU, F.; WANG, J.; HUANG, P.; ZHANG, Q.; DENG, J.; CAO, Q.; JIA, J.; CHENG, J.; FANG, Y.; DENG, D. Y. B.; ZHOU, W.: Outside-in stepwise functionalization of mesoporous silica nanocarriers for matrix type sustained release of fluoroquinolone drugs, *Journal of Materials Chemistry B*, **2015**, *3* (10), 2206–2214, DOI: `10.1039/c4tb02073a`.

[230] YANG, C.-M.; LIN, H.-A.; ZIBROWIUS, B.; SPLIETHOFF, B.; SCHÜTH, F.; LIOU, S.-C.; CHU, M.-W.; CHEN, C.-H.: Selective Surface Functionalization and Metal Deposition in the Micropores of Mesoporous Silica SBA-15, *Chemistry of Materials*, **2007**, *19* (13), 3205–3211, DOI: `10.1021/cm070036r`.

[231] ZIEGLER, F.; TESKE, J.; ELSER, I.; DYBALLA, M.; FREY, W.; KRAUS, H.; HANSEN, N.; RYBKA, J.; TALLAREK, U.; BUCHMEISER, M. R.: Olefin Metathesis in Confined Geometries: A Biomimetic Approach toward Selective Macrocyclization, *Journal of the American Chemical Society*, **2019**, *141* (48), 19014–19022, DOI: `10.1021/jacs.9b08776`.

[232] LANDERS, J.; GOR, G. Y.; NEIMARK, A. V.: Density functional theory methods for characterization of porous materials, *Colloids and Surfaces A: Physicochemical and Engineering Aspects*, **2013**, *437*, 3–32, DOI: `10.1016/j.colsurfa.2013.01.007`.

[233] MONSON, P. A.: Understanding adsorption/desorption hysteresis for fluids in mesoporous materials using simple molecular models and classical density functional theory, *Microporous and Mesoporous Materials*, **2012**, *160*, 47–66, DOI: `10.1016/j.micromeso.2012.04.043`.

[234] GOMMES, C. J.; PRIETO, G.; DE JONGH, P. E.: Small-Angle Scattering Analysis of Empty or Loaded Hierarchical Porous Materials, *The Journal of Physical Chemistry C*, **2016**, *120* (3), 1488–1506, DOI: `10.1021/acs.jpcc.5b09556`.

[235] FÖRSTER, S.; TIMMANN, A.; KONRAD, M.; SCHELLBACH, C.; MEYER, A.; FUNARI, S. S.; MULVANEY, P.; KNOTT, R.: Scattering curves of ordered mesoscopic materials, *The Journal of Physical Chemistry B*, **2005**, *109* (4), 1347–1360, DOI: `10.1021/jp0467494`.

[236] ANTOCHSHUK, V.; ARAUJO, A. S.; JARONIEC, M.: Functionalized MCM-41 and CeMCM-41 Materials Synthesized via Interfacial Reactions, *The Journal of Physical Chemistry B*, **2000**, *104* (41), 9713–9719, DOI: `10.1021/jp0021648`.

[237] GARTMANN, N.; BRÜHWILER, D.: Controlling and imaging the functional-group distribution on mesoporous silica, *Angewandte Chemie International Edition in English*, **2009**, *48* (34), 6354–6356, DOI: `10.1002/anie.200902436`.

[238] ALEXANDRIDIS, P.; IVANOVA, R.; LINDMAN, B.: Effect of Glycols on the Self-Assembly of Amphiphilic Block Copolymers in Water. 2. Glycol Location in the Microstructure, *Langmuir*, **2000**, *16* (8), 3676–3689, DOI: `10.1021/la9912343`.

[239] HERZBERGER, J.; NIEDERER, K.; POHLIT, H.; SEIWERT, J.; WORM, M.; WURM, F. R.; FREY, H.: Polymerization of Ethylene Oxide, Propylene Oxide, and Other Alkylene Oxides: Synthesis, Novel Polymer Architectures, and Bioconjugation, *Chemical reviews*, **2016**, *116* (4), 2170–2243, DOI: `10.1021/acs.chemrev.5b00441`.

[240] MORTENSEN, K.; PEDERSEN, J. S.: Structural study on the micelle formation of poly(ethylene oxide)-poly(propylene oxide)-poly(ethylene oxide) triblock copolymer in aqueous solution, *Macromolecules*, **1993**, *26* (4), 805–812, DOI: `10.1021/ma00056a035`.

[241] LIU, D.; LEI, J.-H.; GUO, L.-P.; DU, X.-D.; ZENG, K.: Ordered thiol-functionalized mesoporous silica with macrostructure by true liquid crystal templating route, *Microporous and Mesoporous Materials*, **2009**, *117* (1-2), 67–74, DOI: `10.1016/j.micromeso.2008.06.008`.

[242] OUHENIA-OUADAHI, K.; LAURENT, G.; BARREZ, E.; YU, P.; MÉTIVIER, R.; DÉBARRE, A.: Spectroscopic Investigation of Diarylethene Photochromes Linked to Silica Nanoparticles, *The Journal of Physical Chemistry C*, **2018**, *122* (12), 6984–6995, DOI: `10.1021/acs.jpcc.8b00396`.

[243] DEL HIERRO, I.; PÉREZ, Y.; CRUZ, P.; JUÁREZ, R.: Pt and Ti Complexes Immobilized onto Mesoporous Silica Microspheres and Their Interaction with Molecules of Biological Interest, *European Journal of Inorganic Chemistry*, **2017**, *2017* (24), 3030–3039, DOI: `10.1002/ejic.201700235`.

[244] NAKAZAWA, J.; SMITH, B. J.; STACK, T. D. P.: Discrete complexes immobilized onto click-SBA-15 silica: controllable loadings and the impact of surface coverage on catalysis, *Journal of the American Chemical Society*, **2012**, *134* (5), 2750–2759, DOI: `10.1021/ja210400u`.

[245] SHINDE, P.; GUPTA, S. S.; SINGH, B.; POLSHETTIWAR, V.; PRASAD, B. L. V.: Amphifunctional mesoporous silica nanoparticles for dye separation, *Journal of Materials Chemistry A*, **2017**, *5* (28), 14914–14921, DOI: `10.1039/C7TA03904B`.

[246] FELICZAK-GUZIK, A.; JADACH, B.; PIOTROWSKA, H.; MURIAS, M.; LULEK, J.; NOWAK, I.: Synthesis and characterization of SBA-16 type mesoporous materials containing amine groups, *Microporous and Mesoporous Materials*, **2016**, *220*, 231–238, DOI: `10.1016/j.micromeso.2015.09.006`.

[247] KOLODZIEJSKI, W.; KLINOWSKI, J.: Kinetics of cross-polarization in solid-state NMR: a guide for chemists, *Chemical reviews*, **2002**, *102* (3), 613–628, DOI: `10.1021/cr000060n`.

[248] OJEDA-LÓPEZ, R.; PÉREZ-HERMOSILLO, I. J.; MARCOS ESPARZA-SCHULZ, J.; CERVANTES-URIBE, A.; DOMÍNGUEZ-ORTIZ, A.: SBA-15 materials: calcination temperature influence on textural properties and total silanol ratio, *Adsorption*, **2015**, *21* (8), 659–669, DOI: `10.1007/s10450-015-9716-2`.

[249] BÉRUBÉ, F.; KALIAGUINE, S.: Calcination and thermal degradation mechanisms of triblock copolymer template in SBA-15 materials, *Microporous and Mesoporous Materials*, **2008**, *115* (3), 469–479, DOI: `10.1016/j.micromeso.2008.02.028`.

[250] HOSEMANN, R.: Der ideale Parakristall und die von ihm gestreute kohrente Röntgenstrahlung, *Z. Physik (Zeitschrift für Physik)*, **1950**, *128* (4), 465–492, DOI: `10.1007/BF01330029`.

[251] HOSEMANN, R.; BAGCHI, S. N.: Diffraction Effects of Crystals with Deformation Faults, *Physical Review*, **1954**, *94* (1), 71–74, DOI: `10.1103/PhysRev.94.71`.

[252] LINDENMEYER, P. H.; HOSEMANN, R.: Application of the Theory of Paracrystals to the Crystal Structure Analysis of Polyacrylonitrile, *Journal of Applied Physics*, **1963**, *34* (1), 42–45, DOI: `10.1063/1.1729086`.

[253] ALI, I.; AL-OTHMAN, Z. A.; NAGAE, N.; GAITONDE, V. D.; DUTTA, K. K.: Recent trends in ultra-fast HPLC: new generation superficially porous silica columns, *Journal of separation science*, **2012**, *35* (23), 3235–3249, DOI: `10.1002/jssc.201200454`.

[254] CABRERA, K.: Applications of silica-based monolithic HPLC columns, *Journal of separation science*, **2004**, *27* (10-11), 843–852, DOI: `10.1002/jssc.200401827`.

[255] SONG, J.-R.; WEN, L.-X.; SHAO, L.; CHEN, J.-F.: Preparation and characterization of novel Pd/SiO2 and Ca–Pd/SiO2 egg-shell catalysts with porous hollow silica, *Applied Surface Science*, **2006**, *253* (5), 2678–2684, DOI: `10.1016/j.apsusc.2006.05.035`.

[256] BAUER, T.; HAASE, S.: Comparison of structured trickle-bed and monolithic reactors in Pd-catalyzed hydrogenation of alpha-methylstyrene, *Chemical Engineering Journal*, **2011**, *169* (1-3), 263–269, DOI: `10.1016/j.cej.2011.02.033`.

[257] RODRIGUEZ, P.; SIMESCU-LAZAR, F.; MEILLE, V.; BAH, T.; PALLIER, S.; FOURNEL, I.: Carbon-coated structured supports. Preparation and use for nitrobenzene hydrogenation, *Applied Catalysis A: General*, **2012**, *427-428*, 66–72, DOI: `10.1016/j.apcata.2012.03.031`.

[258] CAI, X.; HONG, R. Y.; WANG, L. S.; WANG, X. Y.; LI, H. Z.; ZHENG, Y.; WEI, D. G.: Synthesis of silica powders by pressured carbonation, *Chemical Engineering Journal*, **2009**, *151* (1-3), 380–386, DOI: `10.1016/j.cej.2009.03.060`.

[259] RIEG, C.; KIRCHHOF, M.; GUGELER, K.; BEURER, A.-K.; STEIN, L.; DIRNBERGER, K.; FREY, W.; BRUCKNER, J. R.; TRAA, Y.; KÄSTNER, J.; LUDWIGS, S.; LASCHAT, S.; DYBALLA, M.: Determination of accessibility and spatial distribution of chiral Rh diene complexes immobilized on SBA-15 via phosphine-based solid-state NMR probe molecules, *Catalysis Science & Technology*, **2023**, *13* (2), 410–425, DOI: `10.1039/D2CY01578A`.

Appendix

Publication 1: A.-K. Beurer, M. Kirchhof, J. R. Bruckner, W. Frey, A. Baro, M. Dyballa, F. Giesselmann, S. Laschat, and Y. Traa, "Efficient and spatially controlled functionlization of SBA-15 and initial results in asymmetric Rh-catalyzed 1,2-additions under confinement", *ChemCatChem* **2021**, *13*, 2407-2419, DOI 10.1002/cctc.202100229.

Publication 2: A.-K. Beurer, J. R. Bruckner, and Y. Traa, "Influence of the template removal method on the mechanical stability of SBA-15", *Chemistry Open* **2021**, *10*, 1123-1128, DOI 10.1002/open.202100225.

Publication 3: A.-K. Beurer, S. Dieterich, H. Solodenko, E. Kaya, N. Merdanoğlu, G. Schmitz, Y. Traa, and J. R. Bruckner, "Comparative Study of Lattice Parameter and Pore Size of Ordered Mesoporous Silica Materials Using Physisorption, SAXS Measurements and Transmission Electron Microscopy", *Micro Meso Mater* **2023**, *354*, 1387-1811, DOI 10.1016/j.micromeso.2023.112508.

Chemistry
Europe
European Chemical
Societies Publishing

Efficient and Spatially Controlled Functionalization of SBA-15 and Initial Results in Asymmetric Rh-Catalyzed 1,2-Additions under Confinement

Ann-Katrin Beurer,[a] Manuel Kirchhof,[b] Johanna R. Bruckner,[c] Wolfgang Frey,[b] Angelika Baro,[b] Michael Dyballa,[a] Frank Giesselmann,[c] Sabine Laschat,[b] and Yvonne Traa*[a]

Selectively functionalized mesoporous silica may considerably advance heterogeneous catalysis through the controlled immobilization of highly selective complex catalysts inside the mesopores. However, spatially controlled functionalization and the precise analytical verification are still a challenge. In this publication, we report a method, which ensures a selective functionalization of the mesopore surface with a clickable linker and thus makes it possible to study confinement effects during catalyzed reactions. First, we passivate the silanol groups on the particle surface and in the pore entrances of the mesoporous silica material SBA-15 with 1,1,1-trimethyl-*N*-(trimethylsilyl)silanamine. Then we remove the template by solvent extraction and functionalize the pore walls with 3-azidopropyltriethoxysilane before we click the catalyst. In initial experiments of asymmetric Rh-catalyzed 1,2-addition, we investigate the performance of a catalyst clicked selectively in the mesopores and compare it to the dissolved catalyst as well as to the catalyst immobilized exclusively on the external surface of SBA-15.

Introduction

Since their discovery in 1992,[1] ordered mesoporous silica materials (MSMs) have received substantial scientific interest and set the benchmark for all mesoporous materials. In general, the production of most inorganic mesoporous materials is based on the use of organic template molecules. They are brought into solution before the inorganic precursor molecules are added. The precursor molecules deposit around the micelle-like structure of the template and condense into a mesoporous material whose pores are filled with the template.[2] After the mesoporous material is produced, the pores are closed and must be opened after the synthesis.[3] MSMs can easily be synthesized with adjustable pore diameter, a narrow pore size

distribution, surfaces of more than 700 m²g⁻¹ and a high thermal stability. As a result, they became indispensable in present applications. MSMs are mainly used in heterogeneous catalysis,[4] in separation processes,[5] as sensors,[5] or in biomedicine, for example, as drug delivery system.[6] A method to even increase the application range of MSMs is to modify their surface, e.g., by grafting, immobilization and ion exchange.[7,8] During grafting, the functional groups of the reagent are bound to the surface silanol groups by a condensation reaction after the synthesis of the MSMs. However, it cannot be controlled if the functionalization takes place on the particle surface or the internal surface.[7] Therefore, it must be taken into account that MSMs have two different surfaces. Firstly, there is the particle surface, which is typically smaller, but easily accessible. Secondly, there is the internal surface, which represents the larger proportion, but is more difficult to access.[7] Regarding the application of silica, it is often necessary to functionalize the different surfaces selectively in order to determine the location of the modification and to use confinement effects. For the selective functionalization of the particle surface and the internal surface of the MSMs, two methods are feasible – the diffusion-controlled method and the pore protection process.[7] During the diffusion-controlled method, the particle surface of calcined or extracted MSMs is functionalized in the first step. Afterwards, the pore walls are modified. The diffusion-controlled method is only suitable for porous materials with small pores (2–3 nm). The reason for this is that very large, bulky organosilanes, which are not able to enter the pores, must be employed to functionalize the particle surface.[5,9,10] By contrast, the pore protection process is suitable for functionalizing porous materials for all pore diameters.[9,11] The pore protection process uses either as-synthesized silica, the pores of which are blocked by

[a] A.-K. Beurer, Dr. M. Dyballa, Apl. Prof. Y. Traa
     Institute of Technical Chemistry
     University of Stuttgart
     70569 Stuttgart (Germany)
     E-mail: yvonne.traa@itc.uni-stuttgart.de
[b] M. Kirchhof, Dr. W. Frey, Dr. A. Baro, Prof. S. Laschat
     Institute of Organic Chemistry
     University of Stuttgart
     70569 Stuttgart (Germany)
[c] Dr. J. R. Bruckner, Prof. F. Giesselmann
     Institute of Physical Chemistry
   University of Stuttgart
     70569 Stuttgart (Germany)

template used during the synthesis,[7,12] or calcined silica, whose pores are refilled with template or another polymer (e.g., methyl methacrylates).[13] Thus, only the silanol groups of the particle surface are accessible for the functionalization reagent. It should be noted that the modification does not only functionalize the particle surface of the as-synthesized silica, but also parts of the pore walls. This is due to the fact that a small proportion of pores in the as-synthesized SBA-15 is not blocked with template. As a result, the functionalizing reagent can also penetrate into these pores and functionalize the silanol groups there.[11] Furthermore, previous work shows that organosilanes with chloro or ethoxy groups extract template from the pore entrances due to the amphiphilic character of the triblock copolymer P123, which is used as template.[7,13–16] Nevertheless, chloro-, methoxy- or ethoxysilanes are often used to functionalize the particle surface.[13] After functionalizing the particle surface and removing the template from the pores by extraction or calcination, the internal surface can be modified.[7,12]

The functionalization of the porous materials is of great importance to obtain catalysts for further applications. Many different reactions have been described, which are performed on metal-supported silica. For example, Dixit et al. investigated the dehydrogenation of benzyl alcohol on silica-supported copper catalysts.[17] Another field of application is the catalytic reduction of NO on copper oxide supported on silica done by Patel et al.[18] In addition, the literature is very much concerned with cross-coupling reactions performed on palladium-supported silica.[19] Furthermore, oxidation reactions were performed on supported silica, e.g., the selective oxidation of alcohols[20] or sulfides[21] on mesoporous silica with grafted oxovanadium Schiff bases.

The efficient and spatially controlled functionalization of porous materials could also be of great importance for the formation of stereoselective products similar to the functionality of enzymes. The porous properties of the support should help to form the desired configuration of the product. In order to take advantage of the porous structure of the support for the formation of stereoselective products, it is important to ensure that the catalytically active sites are located exclusively in the mesopores after the inertization of the particle surface of the support. However, a proven method to achieve this goal is not available yet. In the literature, several approaches for the selective functionalization of silica have been reported. For example, Yang et al. functionalized the micropores of mesoporous SBA-15 with Pd and assumed that all accessible silanol groups on the particle surface and the mesoporous walls are not able to bind the metal.[22] Liu et al. functionalized MCM-41 via a stepwise procedure by treatment of the external surface with mercaptopropyltrimethoxysilane, extraction of the template with an acidic ethanol solution and functionalization of the pore walls with 3-azidopropyltriethoxysilane.[23] Webb et al. described the stepwise functionalization of SBA-15 and refilled the pores before the functionalization procedure to be sure that only the particle surface is functionalized and not the pore entrances as well. After the refill step, they functionalized the particle surface with hexamethyl disilazane, removed the

template with Soxhlet extraction and modified the pore walls with mercaptopropyltrimethoxysilane.[24] However, these reports did not unequivocally demonstrate that selective functionalization of the inner pore walls was achieved while the particle surface was left inert. In order to obtain unambiguously only the functionalization of the inner mesopore walls, we implemented a control step (see Results and Discussion). In addition, by combining several characterization techniques, we could prove that the final catalyst was immobilized exclusively on the mesopore walls.

In greater detail, the selective functionalization of SBA-15 proposed in this work is based on the pore protection process (Scheme 1). The functionalization of the particle surface of as-synthesized SBA-15 is carried out with 1,1,1-trimethyl-*N*-(trimethylsilyl)silanamine (HMDS) as a functionalization reagent (Scheme 1, Step 1). The inertization of the external surface is checked by a separate, independent control step (see Results and Discussion). Afterwards, the structure-directing template is removed by Soxhlet extraction after the complete functionalization of the particle surface (Scheme 1, Step 2). The pore walls of the mesopores are then functionalized with 3-azidopropyltriethoxysilane (AzPTES) (Scheme 1, Step 3). Subsequent click anchor-
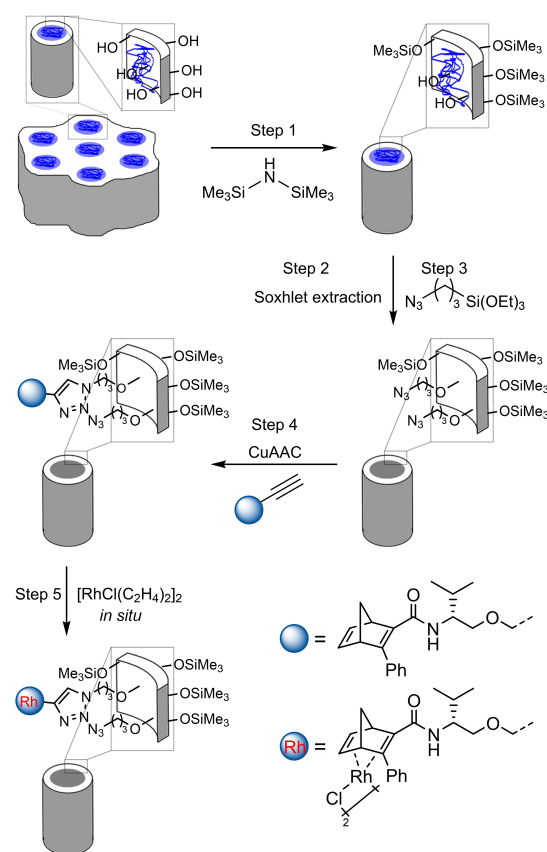
Scheme 1. Procedure for the controlled and selective functionalization of mesoporous materials, followed by immobilization of the diene ligand and final in situ Rh complexation to obtain the immobilized Rh catalyst.

ChemCatChem

Full Papers
doi.org/10.1002/cctc.202100229

Chemistry Europe
European Chemical
Societies Publishing

ing of the alkynyl-functionalized diene ligand via Cu-catalyzed azide-alkyne cycloaddition (CuAAC) (Scheme 1, Step 4) gives the immobilized ligand, followed by *in situ* complexation with the Rh precursor complex $[RhCl(C_2H_4)_2]_2$ to give the immobilized Rh catalyst (Scheme 1, Step 5). CuAAC has been successfully employed for the immobilization of various complex catalysts.[21,25,26] However, there are no examples for the immobilization of Rh diene complexes on silica through CuAAC in the literature. Finally, in order to probe confinement effects of the functionalized SBA-15 on the enantioselective catalysis, the asymmetric 1,2-addition of triphenylboroxine to *N*-tosylimines catalyzed by chiral Rh diene complexes was chosen as a model reaction. The corresponding homogeneously Rh-catalyzed 1,2-addition has been extensively studied and various diene ligands have been developed.[27–29] However, until now the influence of a solid confinement provided by tailored mesoporous silica on the catalytic activity and enantioselectivity of Rh diene complexes has not been investigated. Thus, the aim of the present study was to show that the chiral Rh-containing complexes are located *exclusively* in the mesopores of SBA-15 and can effectively control the enantioselectivity in the 1,2-addition of triphenylboroxine to *N*-tosylimines.

Table 1. Total surface determined by the BET method (S_{BET}), external surface ($S_{external}$) and micropore surface (S_{micro}) of as-synthesized, calcined and selectively functionalized SBA-15. Furthermore, the pore diameter determined by the DFT method ($d_{pore,DFT}$) and the lattice parameter a determined from the X-ray measurements are listed. The azide concentration c_{N3} was determined by elemental analysis.

SBA-15[a]	S_{BET} [m²g⁻¹]	$S_{external}$[b] [m²g⁻¹]	S_{micro} [m²g⁻¹]	$d_{pore,DFT}$ [nm]	a [nm]	c_{N3} [mmol g⁻¹]
as-synthe-sized	80	80	0	7.03	12.4	–
calcined	926	614	311	7.03	11.4	–
-ex	281	281	0	7.56	12.6	–
-ex-control	504	504	0	7.59	12.6	–
-ex-E	518	518	0	7.59	12.6	–
-ex-E-p	788	509	279	7.31	11.7	–
-ex-E-in6	611	611	0	7.56	12.6	–
-ex-E-p-in6	625	472	152	7.31	11.7	3.41·10⁻²
-ex-E-p-in24	826	614	212	7.31	11.7	8.96·10⁻²
-ex-E-p-in72	723	562	162	7.31	11.7	1.23·10⁻¹

[a] The sample names include the following abbreviations: -ex denotes HMDS functionalization on the external particle surface; -control denotes the control step with AzPTES; -E denotes extraction with EtOH; -p denotes pretreatment in N_2; in6, in24 and in72 denote the functionalization time of the internal mesopores with AzPTES, [b] The so-called external surface determined from the N_2 physisorption measurements consists of the particle surface and of the surface of all pores larger than micropores.

Results and Discussion

Synthesis of SBA-15

The starting material for the efficient and spatially controlled functionalization was as-synthesized SBA-15. The as-synthesized SBA-15 shows the characteristic reflexes d_{100}, d_{110} and d_{200}, (Figure S21) which confirm the hexagonal structure (*p6mm*) of SBA-15.[2] The N_2 physisorption measurement of the calcined SBA-15 shows the isotherm typical for SBA-15 (Figure S1) from which the surface area and pore volume as well as the pore diameter were determined and which are listed in Table 1 and Table S1. The results correspond to the characteristic values found in literature.[2]

Explanation of the nomenclature

For a better understanding of the present work, the nomenclature of the different samples is introduced at this point. In Scheme 2, the sample designations are assigned to the corresponding materials. If SBA-15 is mentioned directly after the synthesis, it is called *as-synthesized SBA-15*. The pores of the as-synthesized SBA-15 are sealed with the triblock copolymer P123 and silanol groups are located on the particle surface. As a reference material, SBA-15 with opened pores is used in this paper. It is called *calcined SBA-15* and its pores were opened by the calcination step. To obtain the selectively functionalized catalyst, the external surface of the as-synthesized SBA-15 is functionalized in a first step. The material with functionalized particle surface is named *SBA-15-ex*. In the next step, the triblock copolymer P123 used as a template is removed from the pores of the as-synthesized SBA-15 by Soxhlet extraction

(abbreviated with an "E"). In a pretreatment step, the silanol groups on the pore walls are converted into freely accessible silanol groups (abbreviated with a "p"). This results in the sample designation *SBA-15-ex-E-p* for SBA-15 with functionalized particle surface and open pores. To fix the metal complexes in the pores of SBA-15, the pore walls are modified. This step is abbreviated with "in" in the sample description. Since the concentration of the functional groups on the pore walls is adjusted by the reaction time, the reaction time is also listed. SBA-15, which has a functionalized external surface, opened pores and whose pore walls have been functionalized for 72 h is named *SBA-15-ex-E-p-in72*. Afterwards, linkers are attached to the functional groups on the pore walls to fix the metal complex for catalysis. The sample names with inserted linker carry the abbreviation of the alkyne. This results in *SBA-15-ex-E-p-in72-2c*, for example. Finally, the Rh complex is added which leads to the designation *SBA-15-ex-E-p-in72-2c, [RhCl(C₂H₄)₂]*. As reference materials, SBA-15 with metal complex exclusively on the external surface and with closed pores as well as SBA-15 with the metal complex attached on the particle surface and on the pore walls are used. They are called *SBA-15-ex-2c, [RhCl(C₂H₄)₂]* and *SBA-15-ex+in-2c, [RhCl(C₂H₄)₂]*. The precursor of *SBA-15-ex-2c* is SBA-15 with azido groups exclusively on the external surface (*SBA-15-exN₃*).

Stepwise functionalization and characterization of SBA-15

Functionalization of the particle surface and the pore mouths. The functionalization of the particle surface is important to ensure that the azide groups required for anchoring the catalyst complexes are located exclusively on the mesopore walls. The fact that the functionalization of the particle surface also
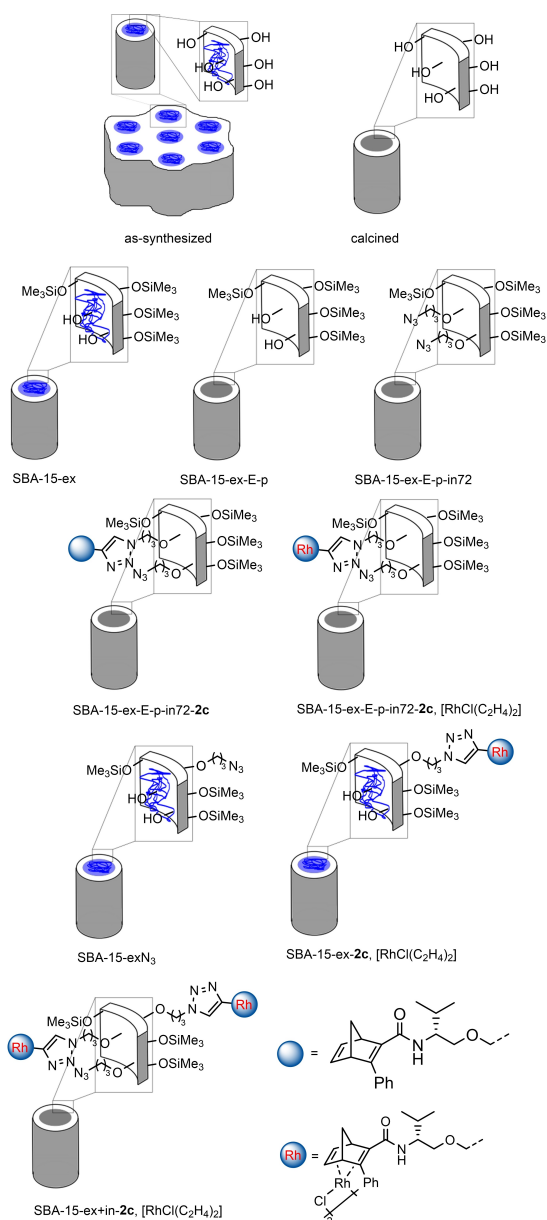
Scheme 2. Assignment of the sample names to a schematic representation of the corresponding material.

alization step, we developed a method, which is shown schematically in Scheme 3. First, the particle surface as well as the pore mouths are functionalized (Scheme 3, (a) functionalization step). The as-synthesized SBA-15 with supposedly fully inert particle surface is then modified with AzPTES to control the inertization of the particle surface (Scheme 3, (b) control step). If the particle surface is inert or, more specifically, there are no accessible silanol groups left on the particle surface and the pore mouths, it will be impossible for AzPTES molecules to bind to the surface. This leads to the conclusion that the accessible silanol groups of the as-synthesized SBA-15 are completely modified or rather inert (Scheme 3, solid box). If the particle surface is not completely inert, there are still accessible silanol groups on the particle surface before the control step. These silanol groups are consequently functionalized in the control step with AzPTES. The attached azide groups can be

modifies the pore entrances and parts of the pore walls does not cause problems and is even desirable for the application described here, because an unambiguous confinement effect can only be studied if the catalyst is not located in close proximity of the pore entrance. Thus, it is more important to localize the azide groups, which are introduced in the functionalization step (Scheme 1, Step 3). To ensure that the particle surface and the pore mouths of the SBA-15 are fully functionalized and chemically inert during the second function-

Scheme 3. Schematic description of the inertization of the particle surface and the pore mouths consisting of (a) a functionalization step and (b) a control step.

ChemCatChem

Full Papers
doi.org/10.1002/cctc.202100229

Chemistry Europe
European Chemical
Societies Publishing

detected spectroscopically or by elemental analysis. The presence of azide groups on the particle surface would allow for the conclusion that the inertization of the particle surface was incomplete before the control step (Scheme 3, dashed box).

To verify if there are accessible silanol groups left on the particle surface or not, all compounds shown in Scheme 3 were investigated by means of IR spectroscopy. The IR spectrum of SBA-15 functionalized with HMDS (SBA-15-ex) in Figure 1 shows the characteristic bands of the silica between 1100 and 1000 cm^{-1} as well as between 800 and 729 cm^{-1}.[30,31] Additionally, the characteristic bands of the silanol groups on the surface of SBA-15 are visible between 3550 and 2700 cm^{-1} and between 1010 and 832 cm^{-1}.[30,31] However, it should be noted that the bands of the silanol groups are reinforced by adsorbed water molecules on the surface. The bands in the range between 2970 and 2850 cm^{-1}, at 1475 cm^{-1} and at 1375 cm^{-1} are due to CH$_3$ and CH oscillations.[30–33] They are assigned to the structure-directing triblock copolymer P123 and the CH$_3$ groups on the particle surface which were introduced by functionalizing the particle surface with HMDS. Based on the IR spectrum, it is therefore impossible to make a statement as to whether the particle surface has been completely inertized in the functionalization step (Scheme 3(a)). Thus, the supposedly fully inertized SBA-15 (SBA-15-ex) was subjected to the control step with AzPTES (SBA-15-ex-control) (Scheme 3(b)). The IR spectrum of SBA-15 after the control step shows no differences to the IR spectrum of SBA-15-ex. This means that the usually intense band at 2100 cm^{-1} which is characteristic for azide groups is not visible.[34] Because of this, it can be concluded that the silanol groups on the particle surface and in the pore entrances were completely functionalized with HMDS in the functionalization step (Scheme 3(a)). The binding of a surplus aza functionality is not possible, which is the prerequisite for the unambiguous binding of a complex to the inner mesopore wall (Scheme 1, Steps 3–5). Thus, the particle surface is inert
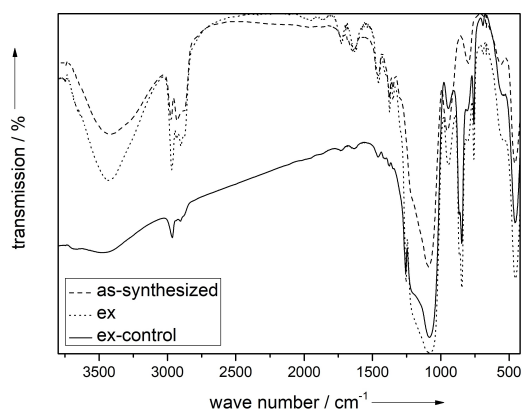
with respect to the functionalization of the pore walls. The results of the elemental analysis confirm the fact that the particle surface of SBA-15-ex is inert, since no nitrogen was detected in the sample SBA-15-ex-control (Table S2). The results from N$_2$ physisorption show that the functionalization with HMDS increases the BET surface and the pore diameter as compared to the as-synthesized material (Table 1). The HMDS treatment removes P123 from the particle surface and the pore mouths. The measurement gives not the real, cylindrical pore diameter (the pores are still filled with P123), but the larger diameter of the spherical or elliptical pore mouth.

Functionalization of the pore walls. After the inertization of the particle surface of the SBA-15 but before the functionalization of the pore walls, it is necessary to remove the structure-directing triblock copolymer P123 by Soxhlet extraction with ethanol (SBA-15-ex-E). The results from the N$_2$ physisorption measurements show that the treatment with ethanol removed a large part of the triblock copolymer P123 and leads to an increase of the total surface and pore volume compared to the SBA-15 with functionalized particle surface (SBA-15-ex) (Tables 1 and S1). Nevertheless, compared to the calcined SBA-15, the total surface and the pore volume remain smaller. The reason for this is that extraction with ethanol does not completely remove the triblock copolymer from the pores. By contrast, the pore diameter of extracted SBA-15 (SBA-15-ex-E) obtained from N$_2$ physisorption measurements is larger compared to the calcined SBA-15 (additional information in Table S1; isotherms of N$_2$ physisorption measurements and pore size distributions are shown in Figures S5 and S6). The difference can be explained by the fact that extraction of the triblock copolymer P123 with ethanol prevents the pores from shrinking. This effect of the shrinkage of the pores due to the calcination is described in the common literature.[5] After the removal of the triblock copolymer P123 from the pores, the extracted SBA-15 was heated in a N$_2$ stream at 400°C for 6 h (SBA-15-ex-E-p). This pretreatment leads to a shrinkage of the lattice parameter from 12.6 nm for SBA-15-ex to 11.7 nm for SBA-15-ex-E-p as shown by X-ray analysis (Table 1). The results are confirmed by N$_2$ physisorption measurements. The calculated pore diameter based on the physisorption isotherm is reduced by 0.28 nm to 7.31 nm due to the pretreatment in N$_2$ (Table 1). It was demonstrated with thermogravimetry and dynamic differential calorimetric studies that the N$_2$ pretreatment removed the last parts of the template remaining after Soxhlet extraction (SI, chapter 2). In addition, it could be shown that the functionalization of the external surface was stable during N$_2$ pretreatment at 400°C (SI, chapter 2). The pretreatment ensured also that the silanol groups on the pore walls are in the more reactive geminal or single state and do not interact with each other via hydrogen bonds.[35]

The influence of the type of silanol groups present on the surface on the functionalization was investigated with experiments performed on pretreated SBA-15 with only easily accessible (single and geminal) silanol groups (SBA-15-ex-E-p-in6) and on SBA-15 without pretreatment which had also interacting silanol groups (SBA-15-ex-E-in6). IR spectroscopic investigations of SBA-15-ex-E-in6 show no characteristic band in

Figure 1. IR spectra of as-synthesized SBA-15 (dash), of SBA-15 after the functionalization step with HMDS (SBA-15-ex; dot) and of SBA-15 with functionalized particle surface after the control step (SBA-15-ex-control; solid) to check if the particle surface of the SBA-15 is completely inertized after the functionalization step of Scheme 3.

ChemCatChem

Full Papers
doi.org/10.1002/cctc.202100229

Chemistry
Europe
European Chemical
Societies Publishing

the range of the expected band of the azide groups. By contrast, the IR spectrum of SBA-15, which was pretreated and subsequently functionalized with AzPTES (SBA-15-ex-E-p-in6), shows the band typical for azide groups at 2100 cm^{-1} (Figure 2). Consequently, the silanol species on the surface have an influence on whether azide groups can be attached to the surface or not. These results are confirmed by the results of the elemental analysis, which are listed in Table 1. The pore walls of the not pretreated sample (SBA-15-ex-E-in6) were not function-alized within 6 h, while the pretreated SBA-15-ex E-p-in6 has an azide concentration of $3.41 \cdot 10^{-2}$ mmol g^{-1} (Table 1). These results make clear that N$_2$ pretreatment of SBA-15 is necessary. It must also be considered that heating in N$_2$ leads to the opening of further pores of the SBA-15. The results of the N$_2$ physisorption measurements of SBA-15-ex-E-in6 and SBA-15-ex-E-p-in6 listed in Table 1 (additional information in Table S1; isotherms of N$_2$ physisorption measurements and pore size distributions are shown in Figures S5–S10) show that the non-pretreated SBA-15 has no micropores, whereas the SBA-15 (SBA-15-ex-E-p-in6) heated to 400 °C in a N$_2$ stream has micro-pores. Generally, micropores lead to an increased BET surface and a decreased average pore diameter.

For varying the concentration of azide groups on the pore walls, the pretreated SBA-15-ex-E-p was functionalized with AzPTES at 80 °C for a time period between 6 h and 72 h. The IR spectra of the SBA-15 with inert particle surface and with azide groups on the pore walls show the characteristic bands of the silica, the CH$_3$ groups on the particle surface and the oscillation band of the azide groups at 2100 cm^{-1} independent of the reaction time (Figure S50). A statement about the influence of the reaction time of the functionalization with AzPTES on the concentration of the azide groups attached to the pore walls cannot be made from IR spectroscopy since this is a qualitative method. For the investigation of the influence of the reaction time on the concentration of azide groups attached to the pore walls, the results of the elemental analysis were used (Table S2).
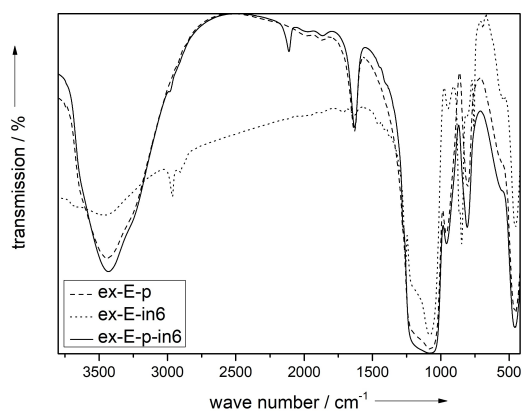
Based on these results, the concentrations of the azide groups of the individual samples present on the pore walls per gram sample were calculated. The calculations give after a reaction time of 6 h $3.41 \cdot 10^{-2}$ mmol g^{-1} azide groups, after 24 h $8.96 \cdot 10^{-2}$ mmol g^{-1} and after 72 h $1.23 \cdot 10^{-1}$ mmol g^{-1} (Table 1). The calculated concentrations show that with increasing reaction time more azide groups are present on the pore walls. Since the same amount of AzPTES was used for all experiments, it can be assumed that the influence of the reaction time on the concentration of the azide groups is due to the diffusion of AzPTES into the pores.

Further investigations concerning the amount of azide groups were performed by ^{13}C cross polarization (CP) MAS NMR spectroscopy with SBA-15-ex-E-p-in6 and SBA-15 whose exter-nal particle and internal mesopore surface was functionalized with AzPTES (SBA-15-ex + in). SBA-15-ex-E-p-in6 contains an azide concentration of $3.41 \cdot 10^{-2}$ mmol g^{-1} while SBA-15-ex + in has an azide concentration of $2.03 \cdot 10^{-1}$ mmol g^{-1}. The two obtained ^{13}C spectra are shown in Figure 3. In both spectra, the signals of the azidopropyl moiety at 9 ppm, 22 ppm and 54 ppm can be observed. In addition, signals at a chemical shift $\delta_{13C} = 16$ ppm and 59 ppm can be seen. They can be assigned to the ethoxy silane moieties that did not react with silanol groups on the surface.[35,36] In principle, it is possible that AzPTES can react with up to three free silanol groups on the surface. If only one or two of the ethoxy groups react, the unreacted ethoxysilane moieties are visible in the ^{13}C CP MAS NMR spectrum. Furthermore, the spectrum of SBA-15-ex-E-p-in6 shows a strong signal at a chemical shift of $\delta_{13C} = -3$ ppm. It can be assigned to the (CH$_3$)$_3$–Si moiety on the particle surface of the SBA-15.[32] Overall, it is found that the intensities of all signals are relatively low which can be explained by the low concentration of functional groups on the surface and the absence of ^{13}C enrichment. A reason for the different signals observed are primarily the different functional groups present. On SBA-15-ex + in, only the azidopropyl moiety is found, while

Figure 2. IR spectrum of SBA-15 with mesopores functionalized with AzPTES without N$_2$ pretreatment (SBA-15-ex-E-in6; dot) and with N$_2$ pretreatment (SBA-15-ex-E-p-in6; solid). As reference, the IR spectrum of SBA-15 after N$_2$ pretreatment without mesopore functionalization (SBA-15-ex-E-p; dash) is inserted.
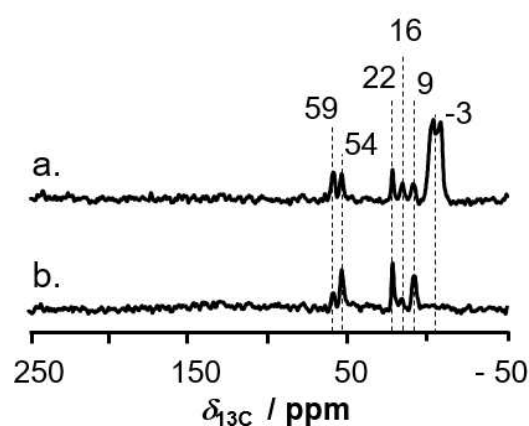

Figure 3. ^{13}C CP MAS NMR spectra of SBA-15, which only has azide groups in the mesopores (SBA-15-ex-E-p-in6; a.) and of SBA-15 which has azide groups on the external particle surface and on the walls of the mesopores (SBA-15-ex + in; b.).

ChemCatChem

Full Papers
doi.org/10.1002/cctc.202100229

Chemistry
Europe
European Chemical
Societies Publishing

on the surface of SBA-15-ex-E-p-in6, there are also (CH₃)₃–Si moieties. Another reason is that the functional groups are present in different conformations on the surface. It is possible that the azidopropyl moiety protrudes into the pore at an angle of 90° to the pore wall. On the other hand, it is also conceivable that the azidopropyl moiety interacts with the pore walls and thus "rests" on them. Since the cross polarization intensity depends on the number of ¹H in close proximity to ¹³C atoms, dynamics of the complexes and distances in between nuclei and the different conformations on the surface might result in different intensities of signals in the CP spectra.[37] It can be summarized that the presence of the functional groups can be detected by ¹³C CP MAS NMR spectroscopy. For reasons indicated above, a quantitative statement regarding the concentration of the functional groups is not possible. Furthermore, no statement can be made with this characterization method regarding the location of the functional groups. However, due to the applied functionalization procedure, the results show that the passivation of the particle surface stays intact after extraction and pretreatment. The location of the attached Rh complex is studied in a later section of this publication.

Besides the influence of the reaction time on the amount of azide groups, it was investigated whether the functionalization of the pore walls with azide groups influences the structure of the SBA-15. The total surface areas S_{BET} of the selectively functionalized SBA-15, determined from the isotherms of the N₂ physisorption measurements, are in a similar range as the total surface area of SBA-15 whose pore walls are not functionalized (SBA-15-ex-E-p) (Table 1). The same applies to the external and micropore surfaces. However, the observation of the pore volumes shows that the total pore volume increases with increasing azide concentration at the pore walls. The proportion of micropore volume does not show any dependence on the azide concentration (Table S1). A change of the pore diameter is not observed due to the functionalization of the pore walls with AzPTES (additional information in Table S1; isotherms of N₂ physisorption measurements and pore size distribution are shown in Figures S9 and S10). It can be concluded that the functionalization of the pore walls with AzPTES has no influence on the structure of the SBA-15, and the hexagonal arrangement of the pores is preserved. In addition to the N₂ physisorption measurements, TEM images were made of the intermediate stages of the SBA-15. The TEM images are shown in the supporting information and show no difference due to the functionalization (Figure S17–S20). Based on the TEM images, it is not possible to make a statement regarding the functionalization of the SBA-15. However, they show that the functionalization of the particle surface and the pore entrances, the removal of the template and the pretreatment, as well as the functionalization of the pore walls with AzPTES and the application of the metal complexes have no influence on the hexagonal structure.

Synthesis of chiral diene ligands and their immobilization on SBA-15

In order to test the influence of the linker between diene ligand and mesoporous materials, three different chiral norbornadienes 2a–c with terminal alkyne suitable for click immobilization were envisioned. As outlined in Scheme 4, the synthesis of norbornadienes 2 commenced with the treatment of known oxazolidinone-substituted 3-phenylnorbornadiene ligands 1a, b[38] with ethynyl magnesium bromide. Depending on the substitution pattern at C 5 of the oxazolidinone auxiliary (CMe₂ vs CH₂), either the propargylic ketone 2a was obtained by exocyclic cleavage from 1a or the tethered amide 2b was isolated from 1b. Saponification of 2b to alcohol 4 and subsequent Williamson etherification[39] with propargylic bromide yielded the respective propargylic ether 2c in 89% yield (Scheme 4, path B). Alternatively, starting diene ligand 1b was directly treated with KOH in dioxane to give alcohol 4, which was etherified to 2c (Scheme 4, path A).

For comparison of immobilized ligands 2 in heterogeneous catalysis with homogeneous catalysis, soluble triazole-containing ligands 3 were then prepared by reaction of 2a–c with benzylazide in the presence of 10 mol% CuSO₄·5 H₂O, 20 mol% Na ascorbate in CH₂Cl₂ and H₂O following a literature procedure.[40] The click reaction of 2a, b gave the respective triazoles 3a–c in 57–62% yield.

With the ethynyl-tethered norbornadienes 2a–c in hand, conditions for the click immobilization on SBA-15-ex+in were screened. After some optimization, it was found that CuSO₄/Na ascorbate in CH₂Cl/H₂O gave better results than CuI/iPr₂NEt in THF (Table S4) and that repetitive suspending/evaporation cycles improved the yield, presumably by overcoming diffusion problems. Under the optimized conditions, click immobilization of 2a on various SBA-15 samples with different azide functionalization and azide loading was studied (Table 2).

As seen from Table 2, decreasing the azide concentration/loading in the mesopores significantly increased the conversion up to >99%. This result might be due to decreased steric
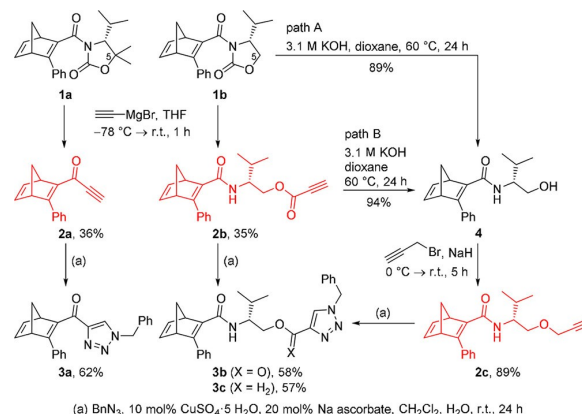
Scheme 4. Synthesis of alkyne-substituted norbornadienes 2a–c and benchmark click reaction with benzylazide.

ChemCatChem

Full Papers
doi.org/10.1002/cctc.202100229

Chemistry
Europe
European Chemical
Societies Publishing

Table 2. Dependence of the conversion of the alkyne dienes **2a** and **2c** on the used SBA-15.[a]

Entry	Alkyne	Azide functionalization[b]	Conc. N_3 [mmol g^{-1}]	t [d]	Conv. [%][d]
1	**2a**	particle surface[c]	0.75	5	55
2	**2a**	particle surface + mesopores	0.75	3	46
3	**2a**	mesopores	0.19	3	78
4	**2a**	mesopores	0.17	3	72
5	**2a**	mesopores	0.10	3	>99
6	**2a**	mesopores	0.06	3	>99
7	**2c**	particle surface	0.085	3	80
8	**2c**	particle surface + mesopores	0.424	3	>99
9	**2c**	mesopores	0.034	3	>99
10	**2c**	mesopores	0.090	3	>99
11	**2c**	mesopores	0.123	3	>99

[a] Conditions: 1.5 eq. $CuSO_4 \cdot 5 H_2O$, 3 eq. Na ascorbate, CH_2Cl_2, H_2O, r.t., [b] Materials dried under vacuum, [c] Without drying under vacuum, [d] Conversion of the alkyne determined from the ^1H NMR of the supernatant using mesitylene as the external standard.

hindrance of the azide groups inside the mesopores with decreasing concentration. When norbornadiene ligand **2c** with a more flexible tether between diene and propargylic ether was employed in the click immobilization, 80% up to quantitative conversion to the silica materials SBA-15 was obtained (Entries 7–11). The immobilization was monitored by ^{13}C CP MAS NMR spectroscopy, IR spectroscopy and ICP-OES measurements.

For the immobilizations of **2a** on the particle surface as well as on the particle surface and on the walls of the mesopores (Entries 1,2), the azide band almost completely disappeared after the click reaction, while only 46–55% conversion of the alkyne **2a** was observed in the ^1H NMR spectra of the supernatants (Figures S46, S51, S52). Since the azide concentration of these materials was determined from the amount of azide used in the post-functionalization, it was assumed that the azide loadings were overestimated. In literature, elemental analysis is a common method to determine the amount of azide groups on the surface of silica.[41] Therefore, the azide concentrations were determined by elemental analysis (Entries 3–9) to use only the effectively required amount of alkyne for the click reaction in the present work. Nevertheless, the azide bands were still strongly visible in the IR spectra, while the ^1H NMRs of the supernatants showed up to >99% conversion of the alkynes **2a**, **c**, when the linkers were clicked inside the mesopores (Figure S47, S48, S53-S56, S53–S56, S59–S62). It is assumed that there are further azide groups on the pore walls. Despite the excess of azide groups, it was possible to perform catalytic experiments with the correct catalyst loadings because the concentration of norbornadienes on the support could be calculated directly from the conversion of alkynes **2a**, **c** in the click reaction. Due to the characteristic bands of the azide groups in the IR spectra of the clicked materials, it is not possible to say whether the click reaction actually took place or whether the ligands are adsorbed on the pore walls. Therefore, the materials were additionally examined by ^{13}C CP MAS spectroscopy. The spectra of both samples are shown in Figure 4. Both show the signals of the azidopropyl moiety at 9 ppm, 22 ppm and 54 ppm. Additionally, the ^{13}C spectrum of the unclicked SBA-15 (Figure 4 a.) shows the signals of the ethoxysilane moieties at $\delta_{13C} = 16$ ppm and 59 ppm that did not react with silanol groups on the surface during the functional-
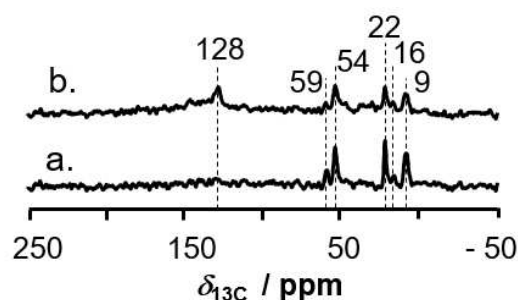

Figure 4. ^{13}C CP MAS NMR spectra of SBA-15 which has azide groups on the external particle surface and in the internal mesopores (SBA-15-ex + in; a.) and of SBA-15 after the click reaction (SBA-15-ex + in-**2a**, b.).

ization step.[23,32] Compared to the spectrum of the unclicked SBA-15 (SBA-15-ex + in), the ^{13}C spectrum of the clicked SBA-15 (SBA-15-ex + in-**2a**) shows a signal at 128 ppm. It can be assigned to aromatic carbon atoms, for example in the triazole ring, which has a bond to a nitrogen atom and a double bond to another carbon atom.[42] The presence of this signal suggests, that the click reaction was successful.

In the next step, Rh was immobilized on the materials. The amount of Rh applied was determined by ICP-OES analysis. The results show on the one hand that after the immobilization there is still Cu on the materials (Table S7). The Cu was needed for the click reaction. On the other hand, the results from elemental analysis show that around 60–80% of the Rh used in the immobilization interacts with the applied ligands (Table S7).

Investigation of the functionalization by scattering experiments

In addition to the verification of the hexagonal structure and the determination of the lattice parameters, we used small angle X-ray scattering (SAXS) to study the variation of the periodic electron density distribution due to the individual functionalization steps. This is possible as the square root of the scattered X-ray intensity I is proportional to the modulus of the

ChemCatChem

Full Papers
doi.org/10.1002/cctc.202100229

Chemistry Europe
European Chemical
Societies Publishing

scattered wave $F(\mathbf{q})$, which is equal to the Fourier transform of the electron density $\rho(r)$ according to Equation (1):

$$\sqrt{I} \propto F(\mathbf{q}) = \int_V \rho(r) \cdot \exp(2\pi i \mathbf{q} \cdot \mathbf{r}) d\mathbf{r} \qquad (1)$$

with $\mathbf{r}$ the spatial vector in real space and $\mathbf{q}$ in reciprocal space, integrated over the probed volume V.[43]

In Figure 5, the diffractograms of as-synthesized SBA-15 and solvent-extracted, pretreated SBA-15 (SBA-15-ex-E-p) are pictured. The peak positions shift to slightly larger q-values after the treatment with N_2 at 400 °C, which causes a full condensation of the silica and thus a compacting of the structure. Additionally, a difference in the scattering intensities relative to the (100)-peak occurs, which is especially noticeable in the decrease of the intensity at q-values below 0.4 nm^{-1} and an increase above 0.8 nm^{-1}. This reflects the increased electron
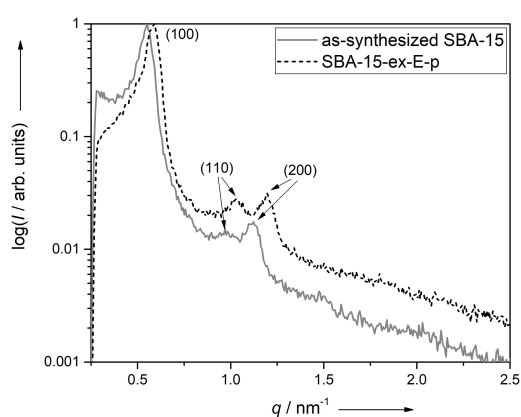

Figure 5. SAXS curves of the as-synthesized SBA-15 (solid) and the solvent-extracted and pretreated SBA-15 (SBA-15-ex-E-p; dash). The maximum scattering intensities, i.e., the (100)-peaks, are normalized to a value of 1 for better comparison.
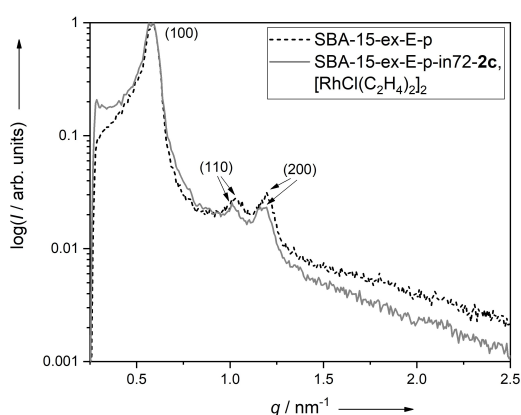

Figure 6. SAXS curves of SBA-15 functionalized with a Rh catalyst (SBA-15-ex-E-p-in72-**2c**, [RhCl(C$_2$H$_4$)$_2$]$_2$; solid) together with the one of the solvent-extracted SBA-15 (SBA-15-ex-E-p; dash).

density contrast between the empty (air filled) pores and the silica walls compared to the pores filled with the template P123 and silica. Before extraction of the template but after the HDMS treatment, the relative intensity of the scattering curve can be found in between the two (Figure S21), which suggests that already during the HMDS treatment a part of the template is removed. It seems very unlikely that this change is due to the functionalization of the particle surface, considering that the average diameter of the particles is well above 0.1 μm and thus not accessible by SAXS measurements.
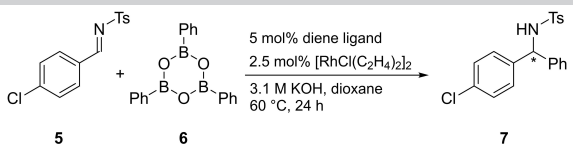
The subsequent functionalization steps all lead to gradual changes in the relative scattering intensity (Figures S22–S25) which is most prominent after the attachment of the electron-rich Rh catalyst. The scattering curve of the SBA-15 with the highest catalyst loading (SBA-15-ex-E-p-in72-**2c**, [RhCl(C$_2$H$_4$)$_2$]$_2$ 0.123 mmol g^{-1}) is depicted in Figure 6 together with the one of the ethanol-extracted SBA-15 (SBA-15-E-p). Compared to the extracted material, the diffractogram of the catalyst-containing material exhibits increased relative scattering intensities for small q-values and decreased ones above $q=1$ nm^{-1}. This makes it look more similar to the scattering curve of the as-synthesized SBA-15 and suggests that the electron density within the pores has increased again. It clearly shows that the electron density distribution of SBA-15-ex-E-p-in72-**2c**, [RhCl(C$_2$H$_4$)$_2$]$_2$ has been altered in a periodic manner, considering that non-periodic changes would cause no q-depended changes of the scattered intensity. Additionally, by comparing the different catalyst loadings, it is also obvious that the change of the scattered intensity correlates with the concentration of the catalyst (Figure S24).

Thus, the decreasing electron density contrast after selective functionalization, identified by the similarities between the SAXS curves of complex-bearing SBA-15 and template-bearing as-synthesized SBA-15, indicates a functionalization in the pores. Combined with the absence of binding sites on the surface, as proven by IR spectroscopy, we conclude that the ligand was unambiguously immobilized to the mesopore wall.

Initial results in asymmetric Rh-catalyzed 1,2-additions under confinement

A first series of catalytic reactions was performed with SBA-15 functionalized with rigid triazolyl tether SBA-15-**2a** differing in their internal and particle surface functionalization and diene content (Table 3). For example, the addition of 2.5 mol% [RhCl(C$_2$H$_4$)$_2$]$_2$ to a suspension of SBA-15-ex-**2a** in dioxane in the presence of 3.1 M KOH to immobilize the Rh on the functionalized SBA-15 followed by addition of N-tosylimine **5** and triphenylboroxine **6** and heating at 60 °C for 24 h gave the addition product N-tosylamine **7** in an isolated yield of 11% and enantioselectivity of 73:27 in favor of the (R) enantiomer (Entry 1). With SBA-15-ex+in-**2a** containing dienes at the internal mesopore surface and the particle surface (0.35 mmol g^{-1} of **3** on SBA-15), the NMR yield of **7** was disappointingly low (1%) (Entry 2). Upon use of SBA-15-ex-E-in24-**2a**, SBA-15-ex-E-in72-**2a**, SBA-15-ex-E-p-in24-**2a** or SBA-

ChemCatChem

Full Papers
doi.org/10.1002/cctc.202100229

Chemistry Europe
European Chemical
Societies Publishing

Table 3. Comparison of Rh-catalyzed 1,2-addition of phenylboroxine **6** to *N*-tosylimine **5** with immobilized catalysts and catalysts in solution.

Entry	Catalyst	Conc. of **3** on SBA-15 [mmol g⁻¹]	Yield of **7** [%] NMR	Yield of **7** [%] isol.	E.r. *R:S*
1[a]	SBA-15-ex-**2a**, [RhCl(C₂H₄)₂]₂	0.41	16	11	73:27
2[a]	SBA-15-ex + in-**2a**, [RhCl(C₂H₄)₂]₂	0.35	1	n.d.	n.d.
3[a]	SBA-15-ex-E-p-in72-**2a**, [RhCl(C₂H₄)₂]₂	0.19	1	n.d.	n.d.
4[a]	SBA-15-ex-E-p-in24-**2a**, [RhCl(C₂H₄)₂]₂	0.15	1	n.d.	n.d.
5[a]	SBA-15-ex-E-in72-**2a**, [RhCl(C₂H₄)₂]₂	0.12	traces	n.d.	n.d.
6[a]	SBA-15-ex-E-in24-**2a**, [RhCl(C₂H₄)₂]₂	0.06	0	n.d.	n.d.
7[a]	SBA-15-ex-**2c**, [RhCl(C₂H₄)₂]₂	0.068	8	n.d.	n.d.
8[a]	SBA-15-ex + in-**2c**, [RhCl(C₂H₄)₂]₂	0.424	75	70	14:86
9[a]	SBA-15-ex-E-p-in6-**2c**, [RhCl(C₂H₄)₂]₂	0.034	29	16	15:85
10[a]	SBA-15-ex-E-p-in24-**2c**, [RhCl(C₂H₄)₂]₂	0.090	31	28	18:82
11[a]	SBA-15-ex-E-p-in72-**2c**, [RhCl(C₂H₄)₂]₂	0.123	47	47	17:83
12[b]	**2a**, [RhCl(C₂H₄)₂]₂	–	58	40	82:18
13[b]	**3a**, [RhCl(C₂H₄)₂]₂	–	5	n.d.	n.d.
14[b]	**2c**, [RhCl(C₂H₄)₂]₂	–	91	81	20:80
15[b]	**2b**, [RhCl(C₂H₄)₂]₂	–	61	52	23:77
16[b]	**3b**, [RhCl(C₂H₄)₂]₂	–	80	69	15:85
17[b]	**3c**, [RhCl(C₂H₄)₂]₂	–	62	58	19:81
18	[RhCl(C₂H₄)₂]₂	–	5	n. d.	n. d.

[a] The catalysts for heterogeneous catalysis were prepared by addition of 2.5 mol% [RhCl(C₂H₄)₂]₂ to a suspension of 5 mol% immobilized diene ligand in dioxane, subsequent stirring for 30 min at room temperature and addition of 3.1 M KOH, [b] The catalysts for homogeneous catalysis were prepared by addition of 2.5 mol% [RhCl(C₂H₄)₂]₂ to a solution of 5 mol% diene ligand in dioxane subsequent stirring for 15 min at room temperature and addition of 3.1 M KOH.

15-ex-E-p-in72-**2a** and decreasing the diene content, the yields could not be improved (Entries 3–6). Homogeneous catalysis with alkyne- (**2a**) and triazolyl-containing **3a** was performed for comparison. Diene **2a** led to **7** in 40% isolated yield with a slightly higher enantiomeric (*R*):(*S*) ratio of 82:18 (Entry 12). By contrast, diene **3a** gave only 5% NMR conversion. These results suggest that the triazole in close proximity to the diene unit suppresses the Rh catalysis, presumably due to electronic interference of the triazolyl moiety with the Rh center and steric hindrance exerted inside the mesopore.

We surmised that the ligand **3c** with a more flexible tether between diene and triazole unit might be better suited for heterogeneous catalysis. As shown in Table 3, Rh-catalyzed 1,2-addition using externally functionalized SBA-15-ex-**2c** (0.068 mmol g⁻¹ of **3** on SBA-15) only yielded 8% *N*-tosylamine **7** (Entry 7). When the immobilized diene SBA-15-ex + in-**2c** with additional functionalization inside the mesopores and the highest diene content (0.424 mmol g⁻¹ of **3** on SBA-15) was used the yield was significantly increased to 75% and an (*R*):(*S*) ratio of 14:86 was obtained (Entry 8). Internally functionalized SBA-15-ex-E-p-in6-**2c** (0.034 mmol g⁻¹ of **3** on SBA-15) yielded 16% *N*-tosylamine **7** with an (*R*):(*S*) ratio of 15:85 (Entry 9). Higher diene content slightly decreased the enantiomeric ratio to 17:83, but improved the yield (47%, Entry 11). It should be noted that the material SBA-15-ex-**2c** carrying diene ligands only at the external surface gave only a very poor yield (8%, Entry 7). Thus, despite the better steric accessibility of the external surface-bound ligands, a higher catalytic activity was determined inside the mesopores. For comparison, the addition

reaction was run with soluble dienes. Norbornadienes **2b** and **2c** gave higher yields but slightly lower enantioselectivities, whereas **3b** with acyltriazolyl moiety gave **7** in 69% yield with an enantiomeric ratio of 15:85 (Entries 14–17). When **3c** was applied, the *N*-tosylamine **7** was obtained in 58% yield with an enantiomeric ratio of 19:81 (Entry 17). This is in good agreement with the results obtained for the immobilized ligand (Entries 7–11). The results indicate that the triazole unit in the spacer does not disturb the Rh catalysis as long as it is kept at distance and the spacer has some conformational flexibility. To investigate whether background catalysis of the rhodium precursor takes place, an experiment with only [RhCl(C₂H₄)₂]₂ and no diene ligand was carried out (Entry 18). Only 5% yield of *N*-tosylamine **7** was observed and therefore it can be concluded that background catalysis of the precursor is insignificant.

Since high concentrations of copper were detected on the immobilized systems via ICP-OES, a series of experiments with addition of CuSO₄·5 H₂O was done to secure that copper species do not disturb the 1,2-addition (Tables S8 and S9). We found that copper neither in homogeneous nor in heterogeneous catalysis had a significant impact on yield and enantioselectivity. Furthermore, SBA-15-ex-E-p-in72-**2c** was washed several times with EDTA solution and then applied in catalysis for comparison (Table S9). The results were similar to the results obtained with the non-washed supported catalyst.

In addition to the investigations on catalysis, investigations on the leaching of the Rh from the SBA-15 were carried out. For this purpose, the SBA-15, which was recovered after catalysis, and the supernatant of the catalysis were investigated by ICP-

ChemCatChem

Full Papers
doi.org/10.1002/cctc.202100229

Chemistry
Europe
European Chemical
Societies Publishing

OES. The results show that small amounts of Rh are present in the supernatant (Table S6). However, small amounts of Si of SBA-15 are also found (Table S5). It is assumed that the Rh is still present on the SBA-15. An explanation for the small amounts of catalyst in the supernatant is that during the reaction, due to the reaction conditions (e.g., strong stirring), tiny particles of the mesoporous support material are removed by abrasion together with the catalyst immobilized on it. Due to their small particle size, they cannot be recovered by centrifugation during separation. This means that no leaching occurred during the experiments (Table S5 and S6).

Furthermore, it was tested whether the immobilized diene ligand leaches into solution under the basic conditions of the catalysis. Thus, the supernatant from the catalysis with SBA-15-ex-E-p-in72-**2c** was filtered through a filter paper and the filtrate measured via ESI-MS (Figure S62). Since no peak in the mass spectrum could be assigned to the diene ligand or any hydrolysis fragment, it was assumed that no leaching of the ligand occurs. Finally, the recyclability of the immobilized system SBA-15-ex-E-p-in72-**2c** was tested (Table S10). For the first and the second cycle, similar yields and enantioselectivities were observed. After the third cycle, the yield significantly decreased. Therefore, fresh [RhCl(C_2H_4)$_2$]$_2$ was added to the catalyst and a fourth cycle was tested. Unfortunately, the yield could not be improved and thus it was assumed that the catalyst irreversibly deactivated in agreement with results by Yang and Xu on A–B type sterically regular polymeric 2,4-diphenylbicyclo[3.3.0]octadienes.[44]

Conclusions

In this work, we present a method for the efficient and spatially controlled functionalization of SBA-15. First, the silanol groups on the particle surface and in the pore entrances were passivated with 1,1,1-trimethyl-*N*-(trimethylsilyl)silanamine. After extraction of the structure-directing agent Pluronic® P123 with ethanol, a pretreatment step at 400°C in N_2 converted the silanol groups to the single and geminal state. Afterwards, the azide functionality was introduced *exclusively* into the mesopores. This could be shown by use of a control step and characterization by SAXS. Therefore, the Rh-containing catalyst could be immobilized *unambiguously* in the mesopores. Initial catalytic asymmetric Rh-catalyzed 1,2-additions revealed that the linker between catalyst and pore wall played an important role in the heterogeneous catalysis. While short rigid triazole-containing linkers completely suppressed the conversion of *N*-tosylimines to the corresponding amines, longer and more flexible linkers did not interfere with the catalysis. Comparison with the corresponding soluble catalysts under homogeneous conditions revealed that the triazole unit is an innocent ligand as long as it is sufficiently far away positioned from the Rh catalyst, resulting in good yields and enantioselectivities. Thus, future experiments need to investigate confinement effects resulting from the interplay of pore size, pore geometry and linker lengths on the enantioselective heterogeneous catalysis.

Work along these lines is currently in progress in our laboratories.

Experimental Section

Synthesis of SBA-15. For the synthesis of SBA-15, 16 g of triblock copolymer Pluronic P123 (average molar mass ~5800 g mol^{-1}, Sigma Aldrich) was dissolved in a mixture of 520 ml demineralized water and 80 ml 37 wt% hydrochloric acid at room temperature and a stirring speed of 100 rpm overnight. The solution was heated to 45°C before adding 37 ml tetraethyl orthosilicate (TEOS, 98%, reagent grade, Sigma Aldrich). The mixture was stirred for 7.5 h at 45°C with a stirring speed of 150 rpm. A hydrothermal treatment under static conditions at 80°C followed. Afterwards, the as-synthesized SBA-15 was separated under vacuum, washed with demineralized water and dried in an oven at 80°C. To open the pores, the as-synthesized SBA-15 was calcined at 550°C in an air flow of 150 l h^{-1}. The heating rate was 1 K min^{-1}.

Functionalization of the particle surface and the pore mouths. The functionalization of the particle surface of as-synthesized SBA-15 was performed in pure 1,1,1-trimethyl-*N*-(trimethylsilyl)silanamine (HMDS, ≥98% (for GC), Carl Roth GmbH+Co. KG). The suspension of HMDS and as-synthesized SBA-15 was stirred at room temperature for 6 h. The functionalized material (SBA-15-ex) was separated under vacuum, washed with demineralized water and dried in an oven at 80°C.

Removal of P123. The triblock copolymer P123 was removed from the pores of the SBA-15-ex by Soxhlet extraction over 112 h using ethanol as extracting agent. The extracted material (SBA-15-ex-E) was dried in an oven at 80°C.

Pretreatment before the functionalization of the internal surface. Before the functionalization of the pore walls took place, SBA-15-ex-E was treated in an oven at 400°C for 6 h in N_2. The treatment was performed with a heating rate of 2 K min^{-1} and a nitrogen flow of 58 l h^{-1}. The product obtained was named SBA-15-ex-E-p.

Functionalization of the internal surface. A suspension of 15 ml toluene and 9.5·10^{-4} mol 3-azidopropyltriethoxysilane (AzPTES, prepared after Nakazawa et al.[45]) per gram SBA-15-ex-E-p was prepared to functionalize the pore walls. The reaction mixture was stirred at room temperature. The reaction time was between 6 h and 72 h to vary the concentration of the azide moieties on the pore walls. The functionalized SBA-15 (SBA-15-ex-E-p-in) was separated under vacuum, washed with ethanol and dried in the oven at 80°C.

Copper-catalyzed azide-alkyne cycloadditions with SBA-15. To a suspension of the azide-functionalized SBA-15 (e.g., 0.60 g, 54.0 μmol azide, c_{N3}=0.09 mmol g^{-1}) in CH_2Cl_2 (5 mL), a solution of the alkyne **2c** (18.1 mg, 54.0 μmol) in CH_2Cl_2 (181 μL) was added. The solvent was evaporated under reduced pressure, and CH_2Cl_2 (6 mL) was added. This step was repeated twice. Degassed water (6 mL), sodium ascorbate (31.7 mg, 0.16 mmol) and $CuSO_4 \cdot 5 \, H_2O$ (10.1 mg, 40.5 μmol) were added, and the reaction mixture was stirred for 2 d at room temperature in the dark. $CuSO_4 \cdot 5 \, H_2O$ (10.1 mg, 40.5 μmol) was added, and the reaction mixture was stirred for another 24 h at room temperature. The dispersion was centrifuged with 4000 rpm, the sediment was washed with CH_2Cl_2 (4 mL) and the suspension was centrifuged again. The sediment was washed with water (4 mL), centrifuged and washed with EtOAc (4 mL). After an additional centrifugation step, the sediment was dried under vacuum, and the diene-functionalized material was obtained as a colorless solid (0.44 g, ≥99% alkyne conversion, 0.09 mmol/g **3c**). For the determination of the conversion of **2c**,

the combined supernatants were extracted with CH_2Cl_2 (3×10 mL), the combined organic layers were dried over $MgSO_4$, and the solvent was removed under reduced pressure. The residue was taken up in $CDCl_3$ (0.4 mL) and the conversion of **2c** was determined from the ^1H NMR spectrum using mesitylene (7.46 μL, 6.49 mg, 54.0 μmol) as the external standard.

Catalytic 1,2-additions with diene-functionalized SBA-15. [$RhCl(C_2H_4)_2$]$_2$ (e.g., 1.94 mg, 5.00 μmol) was added under a N_2 atmosphere to a suspension of the diene-functionalized material SBA-15-ex-E-p-in72-**2c** (81.3 mg, 10.0 μmol diene, c(diene) = 0.123 mmol g^{-1}) in degassed dioxane (2.0 mL). The suspension was stirred for 30 min at room temperature, 3.1 M KOH (12.9 μL, 40.0 μmol) was added and the suspension was stirred for another 5 min at room temperature. The reaction mixture was heated to 60 °C, triphenylboroxine **6** (74.8 mg, 0.24 mmol) and N-tosylimine **5** (58.8 mg, 0.20 mmol) were added, and the reaction mixture was stirred for 24 h at 60 °C. EtOAc (2 mL) was added, the suspension was centrifuged with 4000 rpm and the solvent of the supernatant was removed under reduced pressure. The crude product was purified by column chromatography on silica (PE/EtOAc = 10:1), and the N-tosylamine **7** was obtained as a colorless solid (34.0 mg, 91.4 μmol, 47%).

Characterization methods

SAXS. The powdery samples were filled into mark capillaries with a diameter of 1 mm (Hilgenberg, glass no. 14) and flame-sealed. For measurements, a SAXSess mc^2 diffractometer (Anton Paar) in the line collimation geometry was used for which the sample to detector distance was calibrated with cholesteryl palmitate. X-ray radiation with a wavelength of λ(Cu—Kα) = 0.1542 nm was generated by an ID 3003 X-ray generator (Seifert) operated at 40 kV and 40 mA. To ensure a uniform irradiation of all lattice planes, samples were rotated during the measurement using a RotorCell placed in a TCS 120 hot stage (both Anton Paar). The sample housing was evacuated prior to measurements, which were carried out at 25 °C and averaged over 60 individual measurements. The scattered X-ray intensity was detected with a one-dimensional CMOS Mython 2 K detector (Dectris). Using the software SAXSquant^{TM}, the measured scattering profiles were background corrected with a measurement of an empty mark capillary and deconvoluted. The obtained Bragg-like diffraction maxima were fitted with Lorentzian functions to extract the exact peak positions.

N_2 physisorption. The surface area as well as the pore size of the SBA-15 samples were analyzed by N_2 physisorption measurements. The adsorption and desorption isotherms were recorded using Autosorb 3B from Quantachrome Instruments. Before the measurements, the samples were outgassed under vacuum at 200 °C for 16 h. After the pretreatment, the nitrogen physisorption measurements were performed in a liquid nitrogen bath at -196 °C. From the adsorption isotherms, the surfaces were calculated using the BET method, whereas the pore sizes and pore size distributions were determined with the DFT method, taking into account the hexagonal structure.

FTIR. To characterize the functional groups on the surface of SBA-15, the samples were examined by IR spectroscopy. The spectrometer Nicolet 6700 from Thermo Scientific was used. The spectra were examined in the range from 3800 cm^{-1} to 420 cm^{-1} with 16 scans and a resolution of 4 cm^{-1}. For the measurements, tablets of potassium bromide (KBr for IR spectroscopy, Uvasol®, Sigma Aldrich) and the sample were prepared. The mass ratio of KBr to the sample was 200.

Elemental analysis. The amount of carbon, hydrogen and nitrogen was measured with an Elemental Analizer 1106 from the company Carlo Erba Strumentazione. To determine the copper and rhodium content, the clicked samples and the samples after catalysis were analyzed by plasma-induced optical electron emission spectroscopy (ICP-OES). The analysis was performed on an Avio 200 of Perkin Elmer. In preparation for the measurement, the samples were digested with 3 ml 10% hydrofluoric acid and 3 ml aqua regia in a microwave oven up to 200 °C and diluted with 3 ml aqua regia and demineralized water before the measurement.

Solid state NMR. ^1H-^{13}C CP MAS NMR experiments were performed on an Avance III 400WB spectrometer at a resonance frequency of 100.6 MHz, at a spin rate of 8 kHz (in 4 mm rotors with Kel-F cap), using a contact time of 3 ms, a 70–100 ramp during the Hartmann-Hahn contact period and spinal64 decoupling during acquisition. A delay of 5 s between the scans was applied, at least 35000 scans accumulated (measurement time > 2 d) and the background subtracted. Spectra were referenced to adamantane at 38.48 ppm.

Acknowledgements

Conflict of Interest

The authors declare no conflict of interest.

[1] C. T. Kresge, M. E. Leonowicz, W. J. Roth, J. C. Vartuli, J. S. Beck, *Nature* **1992**, *359*, 710–712.
[2] V. Meynen, P. Cool, E. F. Vansant, *Microporous Mesoporous Mater.* **2009**, *125*, 170–223.
[3] P. Alexandridis, T. Alan Hatton, *Colloids Surf. A* **1995**, 96 (1–2), 1–46.
[4] D. E. de Vos, M. Dams, B. F. Sels, P. A. Jacobs, *Chem. Rev.* **2002**, *102*, 3615–3640.
[5] a) F. Kleitz, W. Schmidt, F. Schüth, *Microporous Mesoporous Mater.* **2003**, *65*, 1–29; b) I. Mbaraka, B. Shanks, *J. Catal.* **2005**, *229*, 365–373.
[6] M. Liong, S. Angelos, E. Choi, K. Patel, J. F. Stoddart, J. I. Zink, *J. Mater. Chem.* **2009**, *19*, 6251.
[7] J. D. Webb, T. Seki, J. F. Goldston, M. Pruski, C. M. Crudden, *Microporous Mesoporous Mater.* **2015**, *203*, 123–131.
[8] D. S. Shephard, W. Zhou, T. Maschmeyer, J. M. Matters, C. L. Roper, S. Parsons, B. F. G. Johnson, M. J. Duer, *Angew. Chem. Int. Ed. Engl.* **1998**, *37*, 2719–2723.
[9] N. Linares, E. Serrano, M. Rico, A. M. Balu, E. Losada, R. Luque, J. García-Martínez, *Chem. Commun.* **2011**, *47*, 9024–9035.
[10] V. Cauda, A. Schlossbauer, J. Kecht, A. Zürner, T. Bein, *J. Am. Chem. Soc.* **2009**, *131*, 11361–11370.
[11] a) T. Asefa, R. B. Lennox, *Chem. Mater.* **2005**, *17*, 2481–2483; b) F. de Juan, E. Ruiz-Hitzky, *Adv. Mater.* **2000**, *12*, 430–432.
[12] F. Liu, J. Wang, P. Huang, Q. Zhang, J. Deng, Q. Cao, J. Jia, J. Cheng, Y. Fang, D. Y. B. Deng, W. Zhou, *J. Mater. Chem. B* **2015**, *3*, 2206–2214.
[13] A.-H. Lu, W.-C. Li, A. Kiefer, W. Schmidt, E. Bill, G. Fink, F. Schüth, *J. Am. Chem. Soc.* **2004**, *126*, 8616–8617.

[14] a) V. Antochshuk, A. S. Araujo, M. Jaroniec, *J. Phys. Chem. B* **2000**, *104*, 9713–9719; b) V. Antochshuk, M. Jaroniec, *Chem. Mater.* **2000**, *12*, 2496–2501.

[15] N. Gartmann, D. Brühwiler, *Angew. Chem. Int. Ed. Engl.* **2009**, *48*, 6354–6356.

[16] a) P. Alexandridis, R. Ivanova, B. Lindman, *Langmuir* **2000**, *16*, 3676–3689; b) J. Herzberger, K. Niederer, H. Pohlit, J. Seiwert, M. Worm, F. Wurm, H. Frey, *Chem. Rev.* **2016**, *116*, 2170–2243; c) K. Mortensen, J. S. Pederson, *Macromolecules* **1993**, *26*, 805–812.

[17] M. Dixit, M. Manish, P. A. Joshi, D. O. Shah, *Procedia Eng.* **2013**, *51*, 467–472.

[18] A. Patel, P. Shukla, T. Rufford, S. Wang, J. Chen, V. Rudolph, Z. Zhu, *Appl. Catal. A* **2011**, *409–410*, 55–65.

[19] a) C. M. Crudden, M. Sateesh, R. Lewis, *JACS* **2005**, *127*, 10045–10050; b) V. Polshettiwar, C. Len, A. Fihri, *Coord. Chem. Rev.* **2009**, *253*, 2599–2626.

[20] S. Verma, M. Nandi, M. Mahasweta, J. Arindam, L. Suman, A. Bhaumik, *Adv. Synth. Catal.* **2011**, *353*, 1897–1902.

[21] S. L. Jain, B. S. Rana, B. Singh, A. K. Sinha, A. Bhaumik, M. Nandi, B. Sain, *Green Chem.* **2010**, *12*, 374–377.

[22] C.-M. Yang, H.-A. Lin, B. Zibrowius, B. Spliethoff, F. Schüth, S.-C. Liou, M.-W. Chu, C.-H. Chen, *Chem. Mater.* **2007**, *19*, 3205–3211.

[23] F. Liu, J. Wang, P. Huang, Q. Zhang, J. Deng, Q. Cao, J. Jia, J. Cheng, Y. Fang, D. Y. B. Deng, W. Zhou, *J. Mater. Chem. B* **2015**, *3*, 2206–2214.

[24] J. D. Webb, T. Seki, J. F. Goldston, M. Pruski, C. M. Crudden, *Micro- and Mesoporous Materials* **2015**, *203*, 123–131.

[25] a) A. E. Fernandez, A. M. Jonas, O. Riant, *Tetrahedron* **2014**, *70*, 1709–1731; b) Y. Li, C. Cai, *Chem. Asian J.* **2011**, *6*, 2592–2605.

[26] a) H. Ying, C. Cai, *Chem. Commun.* **2011**, *47*, 12319–12321; b) A. R. Mc Donald, N. Franssen, G. P. M. van Klink, G. van Koten, *J. Org. Chem.* **2009**, *694*, 2153–2162.

[27] a) C. Defieber, H. Grützmacher, E. M. Carreira, *Angew. Chem. Int. Ed.* **2008**, *47*, 4482–4502; *Angew. Chem.* **2008**, *120*, 4558–4579; b) J. B. Johnson, T. Rovis, *Angew. Chem. Int. Ed.* **2008**, *47*, 840–871; *Angew. Chem.* **2008**, *120*, 852–884; c) C.-G. Feng, M.-H. Xu, G.-Q. Lin, *Synlett* **2011**, *1345–1356*; d) X. Feng, H. Du, *Asian J. Org. Chem.* **2012**, *1*, 204–213.

[28] a) T. Mühlhäuser, A. Savin, W. Frey, A. Baro, A. J. Schneider, H.-G. Döteberg, F. Bauer, A. Köhn, S. Laschat, *J. Org. Chem.* **2017**, *82*, 13468–13480; b) N. Sieffert, J. Boisson, S. Py, *Chem. Eur. J.* **2015**, *21*, 9753–9768; c) T. Yasukawa, T. Kuremoto, H. Miyamura, S. Kobayashi, *Org. Lett.* **2016**, *18*, 2716–2718; d) C. C. Chen, B. Gopula, J.-F. Syu, J.-H. Pan, T.-S. Kuo, P.-Y. Wu, J. P. Henschke, H.-L. Wu, *J. Org. Chem.* **2014**, *79*, 8077–8085; e) Y. Luo, H. B. Hepburn, N. Chotsaeng, H. W. Lam, *Angew. Chem. Int. Ed.* **2012**, *51*, 8309–8313; *Angew. Chem.* **2012**, *124*, 8434–8438; f) T. Nishimura, T. Nagai, R. Takechi, Y. Ebe, *Synthesis* **2016**, *48*, 2612–2618; g) F. Xue, Q. Liu, Y. Zhu, Y. Qing, B. Wan, *RSC Adv.* **2019**, *9*, 25377–25381.

[29] M. Deimling, M. Kirchhof, B. Schwager, Y. Qawasmi, A. Savin, T. Mühlhäuser, W. Frey, B. Claasen, T. Sottmann, S. Laschat, *Chem. Eur. J.* **2019**, *25*, 9464–9476.

[30] G. F. Andrade, D. C. Soares, R. Almeida, E. Sousa, *J. Nanomater.* **2012**, *1*, 1–10.

[31] D. Liu, J.-H. Lei, L.-P. Guo, K. Zeng, *Microporous Mesoporous Mater.* **2009**, *117*, 67–74.

[32] A. Feliczek-Guzik, B. Jadach, H. Piotrowska, M. Murias, J. Lulek, I. Nowak, *Microporous Mesoporous Mater.* **2016**, *220*, 231–238.

[33] M. Hesse, H. Meier, B. Zeeh in *Spektroskopische Methoden in der organischen Chemie, 7. Überarb. Aufl.*, Georg Thieme Verlag KG, Stuttgart, **2005**, pp. 40–56.

[34] B. Malvi, B. R. Sarkar, D. Pat, R. Mathew, T. G. Ajithkumar, S. Sen Gupta, *J. Mater. Chem.* **2009**, *19*, 1409.

[35] X. S. Zhao, G. Q. Lu, A. K. Whittaker, G. J. Millar, H. Y. Zhu, *J. Phys. Chem.* **1997**, *101*, 6525–6531.

[36] P. Shinde, S. S. Gupta, B. Singh, V. Polshettiwar, B. L. V. Bhagavatula, *J. Mater. Chem. A* **2017**, *5*, 14914–14921.

[37] W. Kolodziejski, J. Klinowski, *Chem. Rev.* **2002**, *102*, 613–628.

[38] M. Kirchhof, K. Gugeler, F. R. Fischer, M. Nowakowski, A. Bauer, S. Alvarez-Barcia, K. Abitaev, M. Schnierle, Y. Qawasmi, W. Frey, A. Baro, D. P. Estes, T. Sottmann, M. R. Ringenberg, B. Plietker, M. Bauer, J. Kästner, S. Laschat, *Organometallics* **2020**, *39*, 3131–3145.

[39] G. Broggini, G. Poli, E. M. Beccalli, F. Brusa, S. Gazzola, J. Oble, *Adv. Synth. Catal.* **2015**, *357*, 677–682.

[40] F. Himo, T. Lovell, R. Hilgraf, V. V. Rostovtsev, L. Noodleman, K. B. Sharpless, V. V. Fokin, *J. Am. Chem. Soc.* **2005**, *127*, 210–216.

[41] a) K. Stawicka, K. Drazkiewicz, M. Ziolek, *Microporous Mesoporous Mater.* **2018**, *258*, 41–54; b) K. Ouhenia-Ouadahi, G. Laurent, E. Barrez, P. Yu R Métivier, A. Déberre, *J. Phys. Chem. C* **2018**, *122*, 6984–6995; c) I. del Hierro, Y. Pérez, P. Cruz, R. Juárez, *Eur. J. Inorg. Chem.* **2017**, *24*, 3030–3039.

[42] G. E. Negrón-Silva, R. González-Olvera, D. Angeles-Beltrán, N. Maldonado-Carmona, A. Espinoza-Váquez, M. E. Palomar-Pardavé, M. A. Romero-Romo, R. Santillan, *Molecules* **2013**, *18*, 4613–4627.

[43] C. Giacovazzo in *Fundaments of Crystallography*, Third Edition (Ed.: C. Giacovazzo), Oxford University Press, Oxford, **2011**, pp. 161162.

[44] H. Yang, M. Xu, *Chin. J. Chem.* **2013**, *31*, 119–122.

[45] J. Nakazawa, B. J. Smith, T. D. P. Stack, *J. Am. Chem. Soc.* **2012**, *134*, 2750–2759.

ChemistryOpen

Communications
doi.org/10.1002/open.202100225

Check for updates

Chemistry
Europe
European Chemical
Societies Publishing

Influence of the Template Removal Method on the Mechanical Stability of SBA-15

Ann-Katrin Beurer,[a] Johanna R. Bruckner,*[b] and Yvonne Traa*[a]

Removing the template from the pores after the polycondensation of the silica precursor is a necessary step in the synthesis of mesoporous silica materials. In our previous work, we developed a method for the efficient and spatially controlled functionalization of SBA-15. First, the silanol groups on the particle surface and in the pore entrances were passivated. After extraction of the template, a pretreatment step in N_2 converted the silanol groups to the single and geminal state. Afterwards, an azide functionality was introduced exclusively into the mesopores. This ensured that the catalyst could afterwards be immobilized unambiguously in the mesopores. The mechanical stability of a material functionalized in such a spatially controlled manner is studied and compared to other template removal methods. Even though several studies investigated the influence of the calcination temperature, the presence or the absence of oxygen during the template removal, the specific conditions used during the herein reported selective functionalization procedure have not been covered yet.

Mesoporous silica materials modified with different functionalities can be used in heterogeneous catalysis.[1,2] Spatially controlled functionalization of porous materials is necessary for the study of confinement effects in catalytic applications. For this reason, it is important that the developed catalysts can be used in larger reactors and synthesized on a larger scale. Therefore, the catalysts, which are often prepared in powder form, must be formed, for example, by tableting or extrusion. On that account, the mechanical stability of the catalysts is of interest. In the various approaches to the selective functionalization of mesoporous materials, different template removal methods are used.[3–6] However, the question if the template removal method affects the mechanical stability of the meso-

[a] A.-K. Beurer, Prof. Dr. Y. Traa
Institute of Technical Chemistry
University of Stuttgart
70550 Stuttgart (Germany)
E-mail: yvonne.traa@itc.uni-stuttgart.de

[b] Dr. J. R. Bruckner
Institute of Physical Chemistry
University of Stuttgart
70550 Stuttgart (Germany)
E-mail: johanna.bruckner@ipc.uni-stuttgart.de

porous support material has not been addressed so far. One method for the selective functionalization starts with calcined mesoporous silica material, which is commercially available. In this case, it is necessary to refill the pores with template before the functionalization of the particle surface. Soxhlet extraction with ethanol reopens the pores after the functionalization. In the last step, the pore walls can be modified.[7] Another method, which we disclosed in a previous report,[8] is more time- and material-efficient, as the particle surface of mesoporous silica is functionalized prior to the removal of the template. In a second step, Soxhlet extraction with ethanol and thermal treatment in N_2 open the pores and activate the silanol groups. The pretreatment is carried out in N_2 to protect the organic groups on the particle surface. If the thermal treatment is carried out in air, the organic groups would burn and thus no longer ensure that the catalytically active component would only be present in the pores of the support material after the functionalization step.[9,10] Additionally, this manufacturing process also opens the possibility to recycle the structure-directing template. Subsequently, the pore walls can be functionalized. The conditions during the functionalization steps are comparatively gentle compared to the ones during the template removal and should not affect the mechanical stability of the mesoporous material.

Up to now, studies reported in the literature have dealt with the influence of the calcination temperature,[11,12] the presence or absence of oxygen during the template removal,[13,14] and with the comparison of different porous silica materials with regard to their mechanical stability.[15–17] Furthermore, the mechanical stability of calcined SBA-15 as a function of pressures between 16 and 260 MPa has been considered.[17,18] The XRD diffractograms showed a loss of intensity of the characteristic reflections (100), (110) and (200) for the calcined and pressed SBA-15. The decrease of the intensities was attributed to a loss of the long-range order. The lattice parameters and the main pore size of the different samples did not change compared to the unpressed material. However, the pore size distribution widened with increasing pressure. The authors explained this by a deformation of the pores during pressing. Due to the change of the pores, the surface area and the mesopore volume decreased, too.[17,18] As preliminary investigations for this communication, we determined the mechanical stability of calcined SBA-15 (**SBA-15-calc**; for an explanation of the nomenclature, see Supporting Information chapter 1) against pressures similar to what has been reported in the literature (see Supporting Information, chapter 2). Our results concerning small angle X-ray scattering (SAXS) and N_2 physisorption measurements are in agreement with the literature.[17,18]

ChemistryOpen

Communications
doi.org/10.1002/open.202100225

Chemistry Europe
European Chemical
Societies Publishing

Based on the insights from these investigations, we considered the influence of the template removal method. For this purpose, we investigated and compared the intermediates of the selective functionalization process with each other. The selective functionalization of the surfaces of SBA-15 was omitted (see Supporting Information, chapter 3), because it occurs in every method and is known to further increase the mechanical stability.[15] The materials under study encompass **SBA-15-calc**, which was calcined in air, and calcined SBA-15 whose pores were first refilled with the template (Pluronic® P-123) and then reopened by Soxhlet extraction with ethanol (**SBA-15-calc-re-E**). In addition, SBA-15 whose pores were opened by Soxhlet extraction with ethanol (**SBA-15-as-E**) and SBA-15 heated to 400 °C or 550 °C in N_2 after Soxhlet extraction (**SBA-15-as-E-p400** and **SBA-15-as-E-p550**) were considered. All SBA-15 samples were then pressed into a tablet for 10 min with a pressure of 156 MPa and carefully crushed for further investigations (appended with "156 MPa").
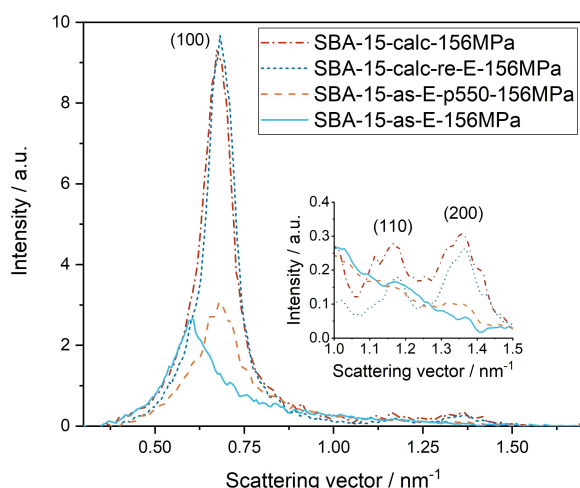
The SAXS experiments show that the hexagonal lattice parameter (Figure 1, Table 1) does not change significantly upon pressing compared to the unpressed materials (see Supporting Information, Figures S5–S8). The SAXS curves of **SBA-15-calc-156MPa** and **SBA-15-calc-re-E-156MPa** are almost identical. This can be explained by the fact that the calcination conditions are much harsher than those during Soxhlet extraction with ethanol. Therefore, calcination is expected to have a greater effect on the structure. To prove this assumption, the SAXS curves of **SBA-15-as**, **SBA-15-calc** and **SBA-15-as-E** must be considered (Supporting Information, Figures S4, S5, S8). The reflexes in the SAXS curves of **SBA-15-calc** show a shift to smaller values of the scattering vector, resulting in a smaller lattice parameter compared to the lattice parameter of **SBA-15-as** (Tables 1, S4). This indicates that the distance from pore center to pore center is smaller for **SBA-15-calc**. The described effect is not observable for **SBA-15-as-E**. Therefore, it can be assumed that calcination has a greater effect on the structure of **SBA-15** than Soxhlet extraction with ethanol. In the synthesis of **SBA-15-calc-re-E**, a combination of both methods is used to remove the template. However, since calcination is performed first and then ethanol extraction is performed after refilling the pores with P-123, it can be assumed that the influence of calcination is much larger and the structure as well as the mechanical stability properties of **SBA-15-calc-re-E** are more similar to those of **SBA-15-calc**. Accordingly, it is also expected that the intensities of the SAXS curves of **SBA-15-calc-re-E-156MPa** and **SBA-15-calc-156MPa** are identical or very similar. **SBA-15-as-E** and **SBA-15-as-E-156MPa** exhibit a lattice parameter value of $a = 12.2$ nm, while the lattice parameters of the samples treated at 550 °C in N_2 are significantly smaller, suggesting a degree of silica condensation similar to the one after calcination.

Looking at the diffractograms in Figure 1, it however becomes obvious that the similar lattice parameter is not a good indicator for the stability of the materials. While the pressure has only a minor effect on the two calcined samples, both **SBA-15-as-E-156MPa** and **SBA-15-as-E-p550-156MPa** show a partial corruption of the nanostructure as revealed by

Figure 1. SAXS curves of the samples **SBA-15-calc**, **SBA-15-calc-re-E**, **SBA-15-as-E** and **SBA-15-as-E-p550**, which were all pressed with 156 MPa for 10 min.

Table 1. Total surface determined by the BET method (S_{BET}), micropore surface (S_{micro}) as well as the total volume (V_{tot}), the mesopore volume (V_{meso}) and the micropore volume (V_{micro}) of differently treated SBA-15 samples and their analogues pressed with 39 MPa or 156 MPa. Furthermore, the pore diameters determined by the DFT method ($d_{pore,DFT}$), the lattice parameter (a) from the SAXS measurements and the percentage of removed template (Δ) calculated (for details see Supporting Information, chapter 4) from results of the elemental analysis are listed.

Sample name	S_{BET} [m^2 g^{-1}]	S_{micro} [m^2 g^{-1}]	V_{tot} [cm^3 g^{-1}]	V_{meso} [cm^3 g^{-1}]	V_{micro} [cm^3 g^{-1}]	$d_{pore,DFT}$ [nm]	a [nm]	Δ [%]
SBA-15-calc	897	222	1.128	1.033	0.095	7.0	10.9	97
SBA-15-calc-39MPa	772	193	0.976	0.897	0.079	7.0	10.9	n.d.[a]
SBA-15-calc-156MPa	670	125	0.948	0.899	0.049	6.8	10.9	n.d.[a]
SBA-15-calc-re-E	510	0	1.345	1.345	0	6.8	10.7	62
SBA-15-calc-re-E-156MPa	409	7	0.699	0.699	0	6.6	10.8	n.d.[a]
SBA-15-as-E	727	134	1.094	1.042	0.052	7.6	12.2	15
SBA-15-as-E-156MPa	460	170	0.371	0.299	0.072	2.6	12.2	n.d.[a]
SBA-15-as-E-p550	869	236	1.148	1.053	0.095	7.0	11.1	99
SBA-15-as-E-p550-39MPa	819	222	0.995	0.902	0.093	6.8	11.0	n.d.[a]
SBA-15-as-E-p550-156MPa	720	209	0.697	0.610	0.087	6.8	10.8	n.d.[a]

[a] The pressed samples were not investigated by elemental analysis. It can be assumed that no change in the carbon content has occurred as a result of pressing. Accordingly, the amount of removed Pluronic® P-123 corresponds to that of the unpressed material.

ChemistryOpen

Communications
doi.org/10.1002/open.202100225

Chemistry
Europe
European Chemical
Societies Publishing

the intensity decrease and the broadening of the scattering peaks. A direct connection between the intensity decrease and the structural integrity cannot be drawn easily, as discussed in detail in the Supporting Information. The widths of the scattering maxima, though, correlate with the degree of order in the two-dimensional hexagonal lattice as described by the paracrystal model.[19] Comparing the width increase of the (100) peaks of these two samples before and after applying pressure (Figures S7, S8) suggests that the corruption of the structure is stronger for **SBA-15-as-E-156MPa** (+190%) than for **SBA-15-as-E-p550-156MPa** (+72%).

Furthermore, N_2 physisorption measurements were performed (Figure 2). **SBA-15-calc** shows a type IV isotherm with the H1 hysteresis typical for mesoporous materials (Figure 2(a)).[21] After pressing at 156 MPa, a type IV isotherm is still present, but the H1 hysteresis is weakened. This change suggests that the uniformity of the pores is lost due to the pressure.[11] This assumption of the corrupted structure is confirmed by the pore size distributions. While **SBA-15-calc** shows a sharp pore size distribution with a main pore diameter of 7.0 nm and only few pores in the microporous region, **SBA-15-calc-156MPa** shows a broadening of the pore size distribution and a loss of pores with the original main pore diameter. This is also confirmed by the surface areas and pore volumes listed in Table 1. For **SBA-15-calc-re-E**, similar results were found (Figure 2(b), Table 1). However, the BET surface areas are significantly lower compared to the solely calcined samples, and no micropores seem to be present. The minimal increase in micropore surface area for samples whose last treatment step was the removal of the template by extraction is due to the error of the measurement method. Furthermore, elemental analysis showed that Pluronic® P-123 cannot be removed by Soxhlet extraction with ethanol alone (Tables 1, S3). Accordingly, parts of the pore system, especially the micropores, remain closed and are thus inaccessible to N_2 during the physisorption measurement, causing an underestimation of the micropore surface area. Most likely, upon pressing, parts of these micropores are freed from the template or micropores become accessible by breaking the pore walls, which leads to an apparent increase of the micropore surface area. Even though there is residual template in the pores of **SBA-15-calc-re-E-156MPa**, the broadening of the pore size distribution illustrates that it has no supporting and thus no positive influence on the mechanical stability of the material against pressure.

Knowing that calcination might repair imperfections in the lattice of **SBA-15-as**,[11] we anticipated that the silica lattice of **SBA-15-calc** should be more stable than the one of **SBA-15-as-E**. **SBA-15-as-E** also shows a typical type IV isotherm with H1 hysteresis (Figure 2(c)). Pressing at 156 MPa changes the hysteresis to a H4 hysteresis, indicating a complex pore structure.[21] The pore size distributions, the surface areas and pore volumes calculated from the N_2 physisorption isotherms confirm the destructive effect of the pressure (Table 1). For **SBA-15-as-E-p550-156MPa**, we found that the isotherm, the pore size distribution, the calculated surface areas and pore volumes are similar to those of **SBA-15-calc** and **SBA-15-calc-re-E** (Figure 2, Table 1). The hysteresis of **SBA-15-as-E-p550-156MPa** is very similar to that of **SBA-15-calc-156MPa** and is much more pronounced than for **SBA-15-as-E-156MPa**. This behavior can be explained by the elevated temperature during the pretreatment step in N_2 which leads to further condensation reactions in the SiO_2 lattice.[11] This is expected to be accompanied by an increase in stability of the pore walls of **SBA-15-as-E-p550** in comparison to **SBA-15-as-E**. Furthermore, it leads to reduction of the lattice parameter to a similar value as found for **SBA-15-calc** (Table 1). While the pore size distributions of **SBA-15-as-E-p550** and **SBA-15-calc** are almost identical, pressing of **SBA-15-as-E-p550** at 156 MPa results in a greater loss of pores with the main pore diameter than in the case of **SBA-15-calc**, indicating that calcination in air leads to slightly more stable materials.

In a continuative experiment, we investigated the influence of the temperature during the thermal treatment and found that the increase in stability correlates with the absolute value of the temperature, that is, the materials treated in N_2 at 550 °C are more stable than the ones treated in N_2 at 400 °C (see Supporting Information, chapter 6). Additionally, the thermal treatment in N_2 has the benefit of removing remnants of the template. Due to this, 99% of the Pluronic® P-123 are removed from the pores of **SBA-15-as-E-p550**, whereas only a 62% removal is found for **SBA-15-calc-re-E** (Tables 1, S3). The residual template in **SBA-15-calc-re-E** blocks parts of the pores, leaving less accessible surface area, and might even interfere with catalyzed reactions. In this aspect, **SBA-15-as-E-p550** is clearly superior.

In laboratory-scale reactors and ultra-fast HPLC setups, much lower pressures of up to 40 MPa are used.[22-27] Thus, we decided to additionally investigate the mechanical stability of **SBA-15-calc** and **SBA-15-as-E-p550** under similar conditions, for which we pressed the samples for 10 min with 39 MPa. The SAXS measurements of **SBA-15-calc-39MPa** and **SBA-15-as-E-p550-39MPa** still exhibit the three characteristic (100), (110) and (200) peaks (Figure 3). In both cases, the full width at half maximum of the (100) peaks increases by only 6% compared to the respective unpressed samples, showing that the damage caused by the applied pressure is the same for both materials and only minor. The intensity changes are due to two conflicting effects, that is, the formation of silica without any nanostructure and an increasing degradation of the hexagonal lattice in the nanostructured parts (see Supporting Information, chapter 2), thus forbidding to draw a direct conclusion from them. The N_2 physisorption isotherms and pore size distributions of **SBA-15-calc-39MPa** and **SBA-15-as-E-p550-39MPa** show only minor changes (Figure 4). The similarity is also reflected in the surface area and pore volume values listed in Table 1. The comparison between the unpressed (Figure 2) and the pressed samples (Figure 4) shows deviations within the range of error. This also applies to the comparison of **SBA-15-calc-39MPa** and **SBA-15-as-E-p550-39MPa**. Since the pore size distributions shown in Figure 4 as well as the SAXS curves in Figure 3 are very similar, we assume that the two template removal methods lead to the same mechanical stability of SBA-15 against a pressure of 39 MPa.
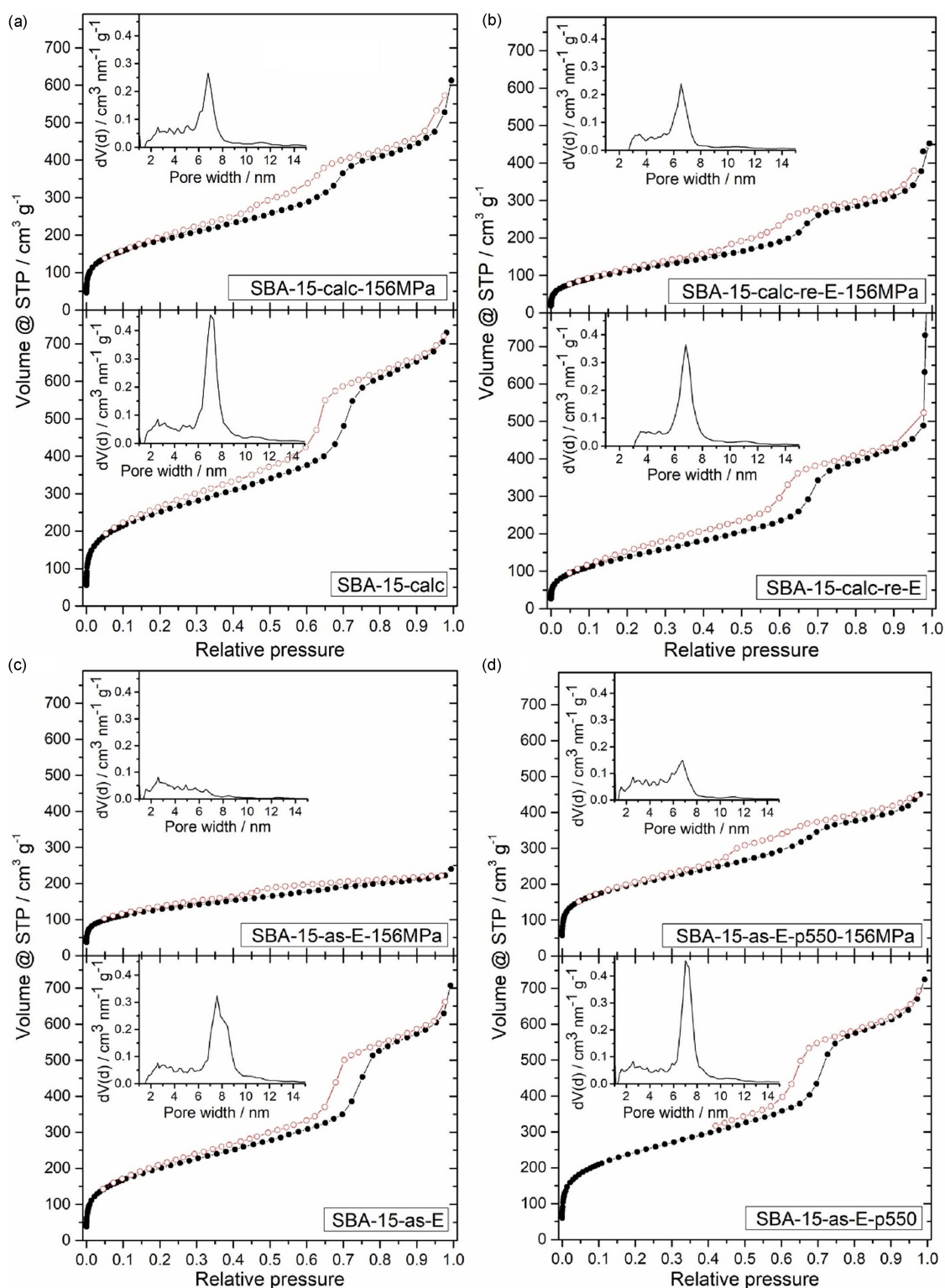
ChemistryOpen

Communications
doi.org/10.1002/open.202100225

Chemistry
Europe
European Chemical
Societies Publishing

Figure 2. N$_2$ adsorption (●) and desorption (○) isotherms and pore size distributions of (a) **SBA-15-calc**, (b) **SBA-15-calc-re-E**, (c) **SBA-15-as-E** and (d) **SBA-15-as-E-p550** and their analogues pressed with 156 MPa for 10 min.
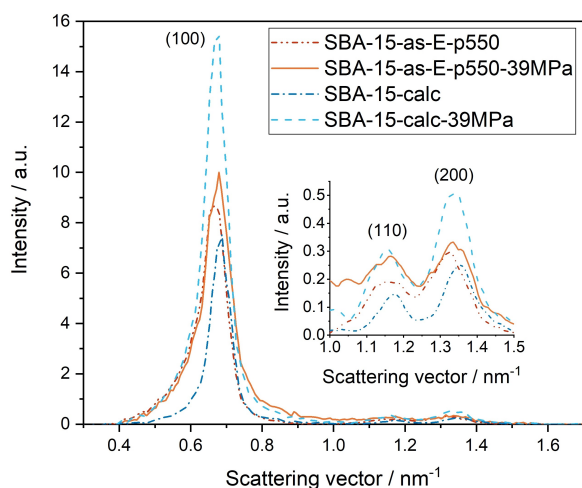
ChemistryOpen

Communications
doi.org/10.1002/open.202100225

Chemistry
Europe
European Chemical
Societies Publishing

Figure 3. SAXS curves of **SBA-15-calc** and **SBA-15-as-E-p550** and their analogues pressed with 39 MPa for 10 min.
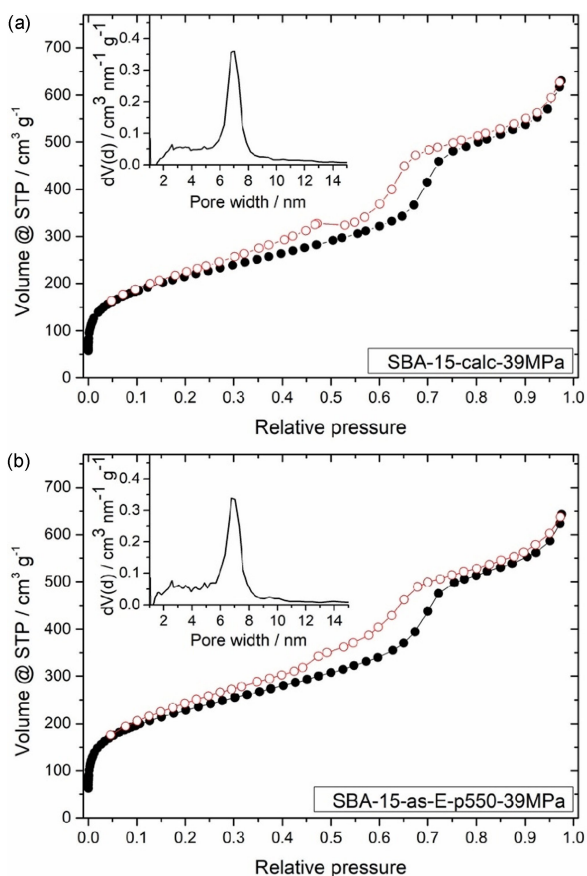
Figure 4. N_2 adsorption (●) and desorption (○) isotherms as well as pore size distributions of (a) **SBA-15-calc-39MPa** and (b) **SBA-15-as-E-p550-39MPa**. The isotherms and the pore size distributions of the unpressed samples are depicted in Figure 2.

In conclusion, it is apparent that the specific template removal method influences the mechanical stability of SBA-15. The comparison of the different methods shows that the thermal treatment of SBA-15 has a positive influence on the mechanical stability of SBA-15 against pressure. When the thermal treatment is performed in the presence of oxygen during the calcination, the mesoporous silica material is more stable against very high pressures, indicating that oxygen catalyzes the rearrangement of the silica network into a more stable conformation. However, if moderate pressures of up to 39 MPa are applied, SBA-15, which was thermally treated in the presence of N_2 at 550 °C, is just as stable as **SBA-15-calc**. Accordingly, solid catalysts from both routes of selective functionalization can be used for laboratory-scale applications, with **SBA-15-as-E-p550** having the advantage of being 99% template-free and allowing for a more time- and material-efficient selective functionalization.

Conflict of Interest

The authors declare no conflict of interest.

[1] J. D. Webb, T. Seki, J. F. Goldston, M. Pruski, C. M. Crudden, *Microporous Mesoporous Mater.* **2015**, *203*, 123–131.
[2] D. S. Shephard, W. Zhou, T. Maschmeyer, J. M. Matters, C. L. Roper, S. Parsons, B. F. G. Johnson, M. J. Duer, *Angew. Chem. Int. Ed. Engl.* **1998**, *37*, 2719–2723.
[3] M. Kruk, M. Jaroniec, *Chem. Mater.* **2000**, *12*, 1961–1968.
[4] B. Tian, YX. Liu, C. Yu, F. Gao, Q. Luo, S. Xie, B. Tu, D. Zhao, *Chem. Commun.* **2002**, *11*, 1186–1187.
[5] R. van Grieken, G. Calleja, G. D. Stucky, J. A. Melero, R. A. García, J. Iglesias, *Langmuir* **2003**, *19*, 3966–3973.
[6] D. Zhao, J. Feng, Q. Huo, N. Melosh, G. H. Fredrickson, B. F. Chmelka, G. D. Stucky, *Science* **1998**, *279*, 548–552.
[7] F. Ziegler, J. Teske, I. Elser, M. Dyballa, W. Frey, H. Kraus, N. Hansen, J. Rybka, U. Tallarek, M. R. Buchmeiser, *J. Am. Chem. Soc.* **2019**, *141*, 19014–19022.
[8] A.-K. Beurer, M. Kirchhof, J. R. Bruckner, W. Frey, A. Baro, M. Dyballa, F. Giesselmann, S. Laschat, Y. Traa, *ChemCatChem* **2021**, *13*, 2407–2419.
[9] S. Li, Z. Li, D. Medina, C. Lew, Y. Yan, *Chem. Mater.* **2005**, *17*, 1851–1854.
[10] P. M. Shewale, A. Venkateswara Rao, A. Rao, *Appl. Surf. Sci.* **2008**, *245*, 6902–6097.
[11] F. Kleitz, W. Schmidt, F. Schüth, *Microporous Mesoporous Mater.* **2003**, *65*, 1–29.
[12] R. Ojeda-López, I. J. Pérez-Hermosillo, J. M. Esparza-Schulz, A. Cervantes-Uribe, A. Domínguez-Ortiz, *Adsorption* **2015**, *21*, 659–669.
[13] P. F. Fulvio, S. Pikus, M. Jaroniec, *J. Mater. Chem.* **2005**, *15*, 5049–5053.
[14] F. Bérbué, S. Kaliaguine, *Microporous Mesoporous Mater.* **2008**, *115*, 469–479.

[15] T. Tatsumi, K. A. Koyani, Y. Tanaka, S. Nakata, *J. Porous Mater.* **1999**, *6*, 13–17.

[16] A. Galarneau, D. Desplantier-Giscard, F. Di Renzo, F. Fajula, *Catal. Today* **2001**, *68*, 191–200.

[17] M. Hartmann, A. Vinu, *Langmuir* **2002**, *18*, 8010–8016.

[18] S. Chytil, L. Haugland, E. A. Blekkan, *Microporous Mesoporous Mater.* **2008**, *111*, 134–142.

[19] a) R. Hosemann, *Z. Phys.* **1950**, *128*, 465–492; b) R. Hosemann, S. N. Bacchi, *Phys. Rev.* **1954**, *94*, 71–74; c) R. Hosemann, P. H. Lindenmeyer, *J. Appl. Phys.* **1963**, *34*, 42–45.

[20] V. Meynen, P. Cool, E. F. Vansant, *Microporous Mesoporous Mater.* **2009**, *125*, 170–223.

[21] M. Thommes, K. Kaneko, A. V. Neimark, J. P. Olivier, F. Rodriguez-Reinoso, J. Rouquerol, K. S. W. Sing, *Pure Appl. Chem.* **2015**, *87*, 1051–1069.

[22] I. Ali, Z. A. Al-Othman, N. Nagae, V. D. Gaitonde, K. K. Dutta, *J. Sep. Sci.* **2012**, *35*, 3235–3249.

[23] K. Cabrera, *J. Sep. Sci.* **2004**, *27*, 843–852.

[24] J.-R. Song, L.-X. Wen, L. Shao, J.-F. Chen, *Appl. Surf. Sci.* **2006**, *253*, 2678–2684.

[25] T. Bauer, S. Haase, *Chem. Eng. J.* **2011**, *169*, 263–269.

[26] P. Rodriguez, F. Simescu-Lazar, V. Meille, T. Bah, S. Pallier, *Appl. Catal. A* **2012**, *427–428*, 66–72.

[27] X. Cai, R. Y. Hong, L. S. Wang, X. Y. Wang, H. Z. Li, Y. Zheng, D. G. Wie, *Chem. Eng. J.* **2009**, *151*, 380–386.

ChemistryOpen

Supporting Information

Influence of the Template Removal Method on the Mechanical Stability of SBA-15

Ann-Katrin Beurer, Johanna R. Bruckner,* and Yvonne Traa*

Table of Contents

1   Explanation of the Nomenclature

For a better understanding of the present work, the nomenclature of the different samples is introduced in Table S1.

Table S1. Explanation of the sample nomenclature.

SBA-15-as	directly after the synthesis; called as-synthesized SBA-15
SBA-15-calc	pores were opened by calcination in air
SBA-15-calc-XMPA	pores were opened by calcination, and the sample was pressed with 8 to 156 MPa; abbreviated with "XMPa" depending on the pressure X
SBA-15-calc-re	pores were refilled with Pluronic® P-123; abbreviated with "re"
SBA-15-calc-re-E	pores were reopened with Soxhlet extraction with ethanol; abbreviated with an "E"
SBA-15-as-E	pores were opened with Soxhlet extraction with ethanol
SBA-15-as-E-p400	SBA-15-as-E pretreated in N_2 at 400°C; abbreviated with "p400"
SBA-15-as-E-p550	SBA-15-as-E pretreated in N_2 at 550°C; abbreviated with "p500"

2   Mechanical Stability of SBA-15-calc

To better understand if there is an influence of the template removal method on the mechanical stability of SBA-15 against pressure, the mechanical stability of SBA-15-calc was investigated first. Therefore, SBA-15-calc was pressed with pressures between 8 and 156 MPa. Afterwards, the different samples were investigated with SAXS and N_2 physisorption measurements.

The SAXS curves of the calcined and the pressed samples are pictured in Figure S1. All diffractograms shown have been normalized to the same intensity of the attenuated primary beam. Considering that the sample preparation and the measurement set-up were the same for every sample, this relative value depends on the X-ray absorption of the sample and the amount of scattered X-rays only.[1] The intensity of the attenuated beam I follows the equation

$$I = I_0 e^{-\mu x}, \tag{E1}$$

with I_0 the intensity of the unattenuated primary beam, x the sample thickness and μ the linear attenuation coefficient. The latter relates to the total cross section σ_{tot} via

$$\sigma_{\text{tot}} = \mu/N_a, \tag{E2}$$

with N_a the number of attenuating centers, i.e., atoms, per volume. This total cross section may be further divided into contributions from the photoelectric absorption (σ_{pe}), pair production (σ_{pp}), Compton (σ_{inel}) and Thomoson (σ_{el}) cross sections. Except for the Thomoson scattering, which arises due to the form or structure factor of the investigated sample, all of these contributions to the total cross section solely depend on the type and density of the atoms within the sample as well as the energy of the X-ray beam used. Taking into account that all samples consist of the same atoms, i.e., silicon and oxygen in a ratio of 1:2, differences in the scattering intensities after normalization to the attenuated primary beam may thus directly be attributed to a variation in the ratio of total silica to nanostructured silica.
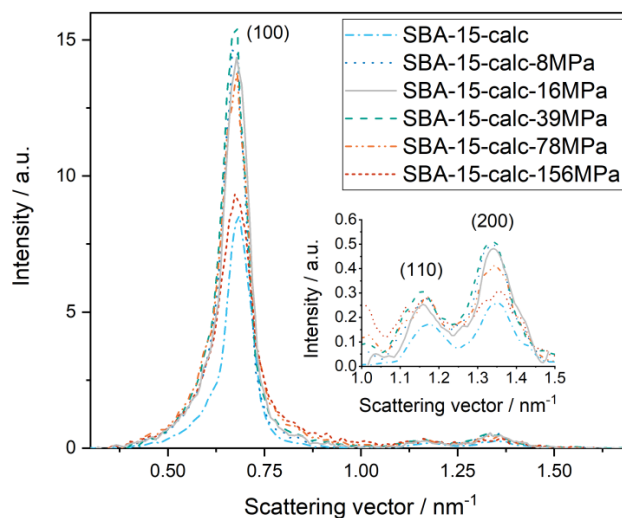
Figure S1. SAXS curves of SBA-15-calc and of SBA-15-calc-XMPa. The pressure was variated between 8 and 156 MPa.

As seen from Figure S1, the scattering intensity of SBA-15-calc-8MPa increases compared to the unpressed sample. This intensity increase indicates that the amount of unstructured silica is larger after applying pressure, which shows that a part of the SBA-15 is destroyed by this rather small pressure, already. At the same time, the full width at half maximum of the scattering peaks, which is plotted in Figure S2 for the example of the (100) reflection, stays constant, revealing that the properties of the nanostructured part of the sample stay unchanged. When increasing the pressure, the scattering intensities of the three characteristic peaks as well as their width stay almost constant up to a value of 39 MPa. When increasing the pressure to 78 MPa, the scattering intensity, especially of the (200) peak, starts to decrease, and the width of the peaks increases, a trend which continues for even higher pressures. This broadening of the scattering maxima was previously attributed to a reduction of the average diameter of the crystallites within the pressed sample.[2] However, if this was the case, the relative intensity of the individual peaks should not decrease,[3,4] but rather increase as the amount of unstructured silica rises further. Thus, it seems more likely to us that the observed broadening is due to an increasing disorder of the second kind, which means that the positions of the hexagonally arranged pores become more and more "blurred".[5] Such blurring may arise, if parts of the pores collapse, leading to plugged or partially filled pores. Chytil et al.[6] came to the same conclusion in their work.
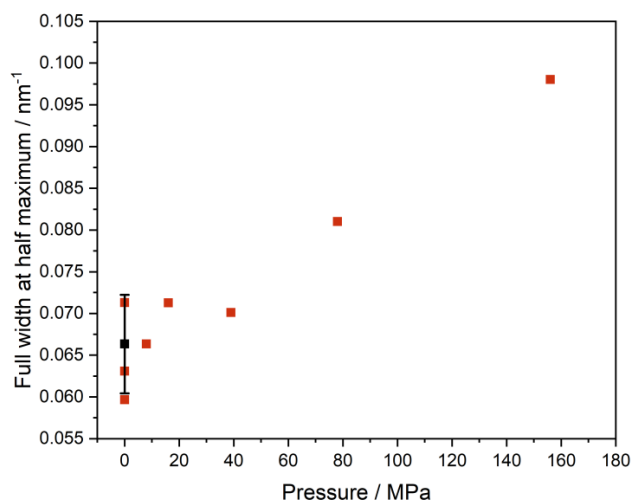
4

Figure S2. Full width at half-maximum *w* of the (100) peak from the SAXS curves of calcined SBA-15 plotted against the applied pressure. The black data point at 0 MPa depicts the average over four individual measurements, indicating the accuracy of the method.

In addition to the SAXS measurements, N_2 physisorption measurements were performed. The resulting isotherms are shown in Figure S3(a). Unpressed SBA-15-calc shows the typical type IV isotherm.[7] With increasing pressure, the type of the isotherms changes, and the hysteresis gets smaller. This is an indication for a loss of mesoporosity within SBA-15-calc.[8] The results evaluated from the N_2 physisorption measurements are listed in Table S2. The decrease in surface area and pore volume, as described in the literature and expected from the change in isotherms of the N_2 physisorption measurements, are not so pronounced. The comparison of the pore size distribution of the different samples shows a change with increasing pressure (Figure S3(b)). It can be seen that the amount of pores with the main pore diameter decreases with increasing pressure.[6,7] This leads to the conclusion that SBA-15-calc is mechanically stable against pressures up to 39 MPa. At higher pressures, there is an increasing loss of the hexagonal structure of SBA-15.
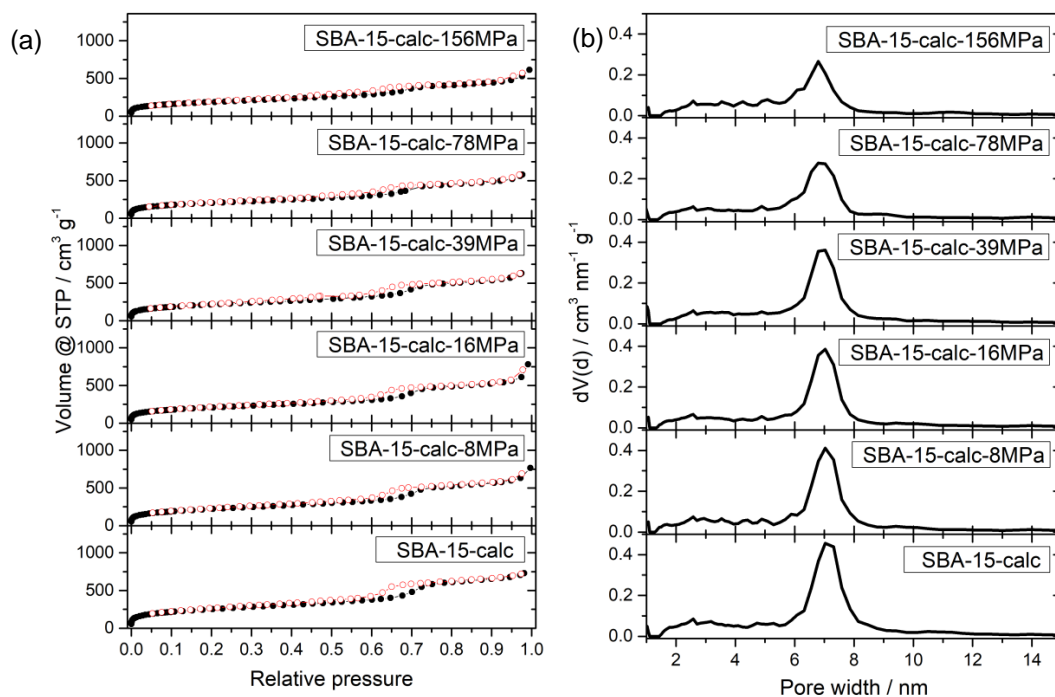
Figure S3. (a) Adsorption (●) and desorption (○) isotherms and (b) pore size distributions of SBA-15-calc and of SBA-15-calc-XMPa. The pressure was variated between 8 and 156 MPa.

Table S2. The total surface determined by the BET method (S_{BET}) and micropore surface (S_{micro}) as well as the total pore volume (V_{tot}) and the micropore volume (V_{micro}) of SBA-15-calc and of SBA-15-calc-XMPa samples are listed. The pressure was variated between 8 and 156 MPa. Furthermore, the pore diameters determined by the DFT method ($d_{pore,DFT}$) are given.

Sample name	S_{BET} / m^2 g^{-1}	S_{micro} / m^2 g^{-1}	V_{tot} / cm^3 g^{-1}	V_{micro} / cm^3 g^{-1}	$d_{pore,DFT}$ / nm
SBA-15-calc	897	222	1.128	0.095	7.0
SBA-15-calc-8MPa	800	195	1.186	0.076	7.0
SBA-15-calc-16MPa	750	208	1.209	0.085	7.1
SBA-15-calc-39MPa	878	258	1.101	0.106	6.8
SBA-15-calc-78MPa	723	208	0.897	0.089	6.8
SBA-15-calc-156MPa	670	125	0.948	0.049	6.8

3   Experimental Section

Synthesis of SBA-15

For the synthesis of SBA-15, 16 g of triblock copolymer Pluronic® P-123 (average molar mass ~ 5800 g mol^{-1}, Sigma Aldrich) was dissolved in a mixture of 520 ml demineralized water and 80 ml 37 wt% hydrochloric acid at room temperature at a stirring speed of 100 rpm overnight in a 1 l teflon-coated autoclave (Berghof Products + Instruments GmbH). The solution was heated to 45°C before adding 37 ml tetraethyl orthosilicate (TEOS, 98 %, reagent grade, Sigma Aldrich). The mixture was stirred for 7.5 h at 45°C with a stirring speed of 150 rpm. A hydrothermal treatment under static conditions at 80°C followed. Afterwards, the SBA-15-as was separated under vacuum, washed with demineralized water and dried in an oven at 80°C. The SBA-15-as of one batch was used as starting material for all experiments in this work.

Removal of Pluronic® P-123 – Calcination

To open the pores, SBA-15-as was calcined for 6 h at 550°C in an air flow of 150 l h^{-1}. The heating rate was 1 K min^{-1}.

Refilling of the Pores

To refill the pores with template, Pluronic® P-123 was dissolved in ethanol overnight. SBA-15-calc was added to the solution, and the suspension was stirred for 42 h at room temperature. The solution used to refill the pores was 4 g Pluronic® P-123 in 60 ml ethanol per gram calcined SBA-15. Subsequently, the SBA-15 with refilled pores (SBA-15-calc-re) was separated under vacuum, washed with 500 ml of demineralized water and dried in an oven at 80°C.

Removal of Pluronic® P-123 – Soxhlet Extraction

The triblock copolymer Pluronic® P-123 was removed from the pores of SBA-15-as or SBA-15-calc-re by Soxhlet extraction for 112 h using ethanol as extracting agent. The extracted materials (SBA-15-as-E and SBA-15-calc-re-E) were dried in an oven at 80°C.

Pretreatment in N$_2$

SBA-15-as-E was treated in an oven at 400°C or 550°C for 6 h in N$_2$. The treatment was performed with a heating rate of 2°C min^{-1} and a N$_2$ flow of 58 l h^{-1}. The product obtained was named SBA-15-as-E-p400 or SBA-15-as-E-p550 depending on the temperature during the pretreatment.

7

Investigation of the Mechanical Stability

For the investigation of the mechanical stability, the press FluXana (Vaneox® Pressing Technology) was used. For each experiment, 150 mg of the respective sample was pressed with different pressures. The pressed tablets were then carefully crushed again in a mortar in order to be able to characterize the samples.

4   Characterization Methods

Small angle X-ray scattering (SAXS)

The powdery samples were filled into mark capillaries with a diameter of 1 mm (Hilgenberg, glass no. 14) and flame-sealed. For measurements, a SAXSess mc^2 diffractometer (Anton Paar) in the line collimation geometry was used for which the sample to detector distance was calibrated with cholesteryl palmitate. X-ray radiation with a wavelength of λ(Cu-Kα) = 0.1542 nm was generated by an ID 3003 X-ray generator (Seifert) operated at 40 kV and 40 mA. The sample housing was evacuated prior to measurements, which were carried out at 25°C with the help of a TCS 120 hot stage (Anton Paar) and averaged over 60 individual measurements. The scattered X-ray intensity was detected with a one-dimensional CMOS Mythen 2K detector (Dectris). The semi-transparent beam-stop allowed for an additional measurement of the transmitted primary X-ray beam. Using the software SAXSquant^{TM}, the measured scattering profiles were normalized to the same intensity of the attenuated primary beam, background-corrected and deconvoluted. Subsequently, the scattering curves were Lorentz- and polarization-corrected. The scattering associated to the form factor of the mesopores as well as further incoherent scattering was removed by fitting and subtracting a double exponential decay, leaving only the part of the scattering, which originates from the hexagonal structure. The obtained Bragg-like diffraction maxima were fitted with Lorentzian functions to extract the exact peak positions and full widths at half maximum.

N_2 physisorption

The surface area as well as the pore size of the SBA-15 samples were analyzed by N_2 physisorption measurements. The adsorption and desorption isotherms were recorded using Autosorb 3B from Quantachrome Instruments. Before the measurements, the samples were outgassed under vacuum at 200°C for 16 h. After the pretreatment, the N_2 physisorption measurements were performed in a liquid N_2 bath at −196°C. From the adsorption isotherms, the surfaces were calculated using the BET method, whereas the pore sizes and pore size distributions were determined with the DFT method, taking into account the hexagonal structure.

Elemental analysis

The amount of carbon and hydrogen was measured with an Elemental Analizer 1106 from the company Carlo Erba Strumentazione.

The results of the elemental analysis (Table S3) show how much of the structure-directing template was removed from the pores during the pore opening. With these results, it is possible

to calculate the percentage of removed Pluronic® P-123 *(Δ)* for the different samples. The calculation for SBA-15-calc follows the equation

$$\Delta = 100 \cdot \left(1 - \frac{w(\text{C in SBA}-15-\text{calc})}{w(\text{C in SBA}-15-\text{as})}\right) = 100 \cdot \left(1 - \frac{0.26\ wt.\%}{8.90\ wt.\%}\right) = 97\ \% \qquad \text{(E3)}$$

Depending on the template removal method of the structure-directing template Pluronic® P-123, the corresponding starting material is used for the calculation. For the calculation of the removed amount of template of SBA-15-as-E, SBA-15-as-E-p400 and SBA-15-as-E-p550, the carbon amount of SBA-15-as is used as starting material. The amount of removed Pluronic® P-123 for SBA-15-calc-re-E was calculated from the carbon amount of SBA-15-calc-re. The calculated results are listed in Table S3.

Table S3. Results of the elemental analysis and the calculated percentage of the removed structure-directing template (Δ). The percentage of the removed template was calculated from the value of the starting material of the respective method for removing the template.

Sample name	w(C) / wt.%	w(H) / wt.%	Δ / %
SBA-15-as	8.90	2.50	-
SBA-15-calc	0.26	0.89	97
SBA-15-calc-re	21.37	3.52	-
SBA-15-calc-re-E	8.03	1.86	62
SBA-15-as-E	7.60	2.80	15
SBA-15-as-E-p400	0.10	1.00	99
SBA-15-as-E-p550	0.09	1.02	99

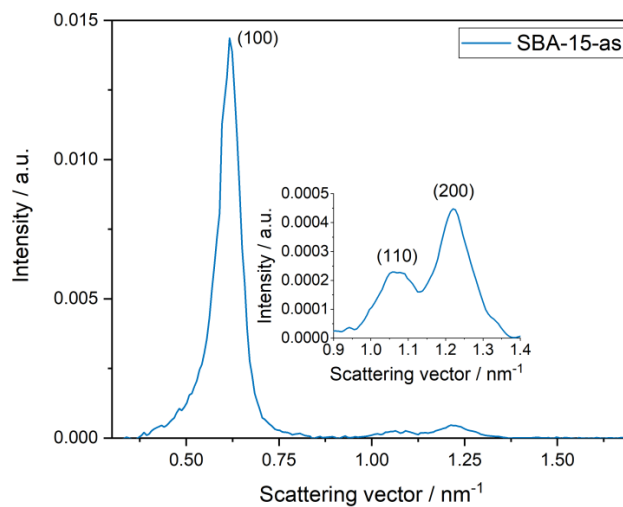## 5   SAXS Measurements

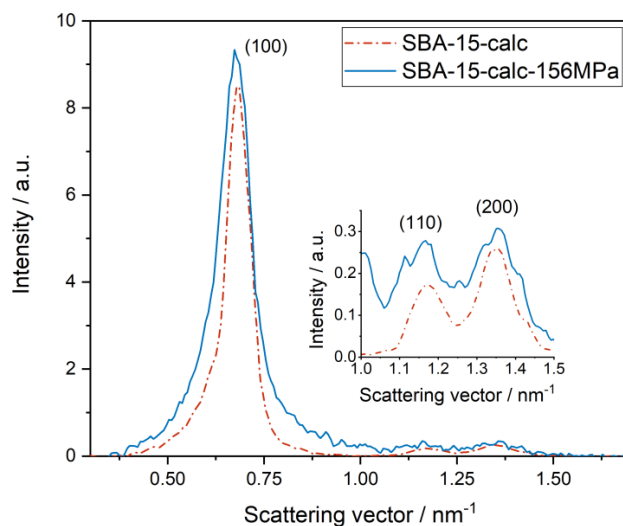**Figure S4.** SAXS curve of SBA-15-as.

Figure S5. SAXS curves of SBA-15-calc prior and after applying a pressure of 156 MPa for 10 min. The increase of the full width at half maximum is 48 %.
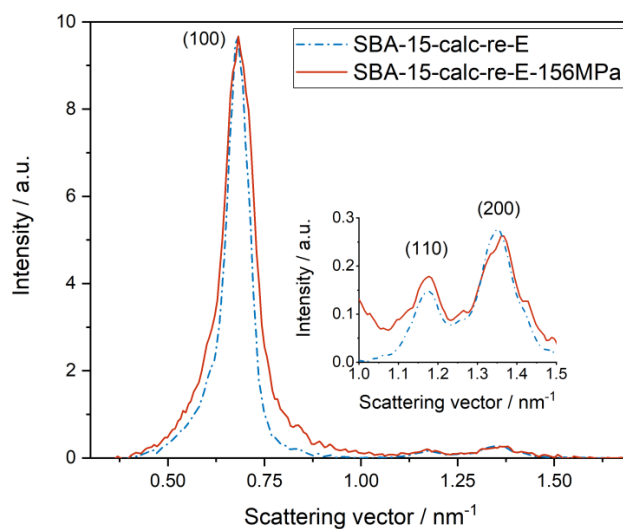
Figure S6. SAXS curves of SBA-15-calc-re-E prior and after applying a pressure of 156 MPa for 10 min. The increase of the full width at half maximum is 38 %.
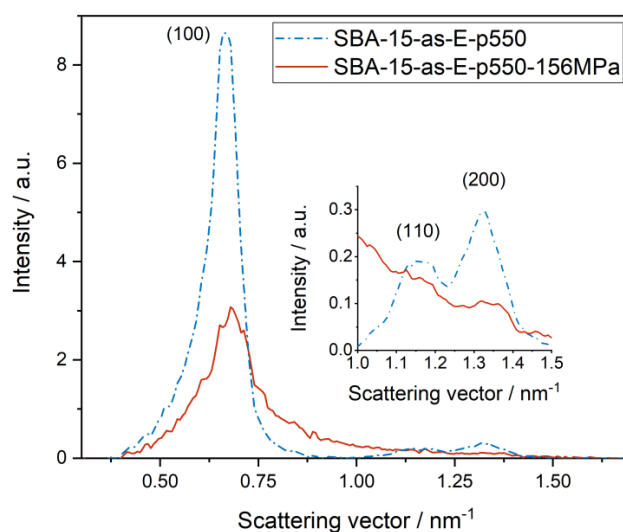

Figure S7. SAXS curves of SBA-15-as-E-p550 prior and after applying a pressure of 156 MPa for 10 min. The increase of the full width at half maximum is 72 %.
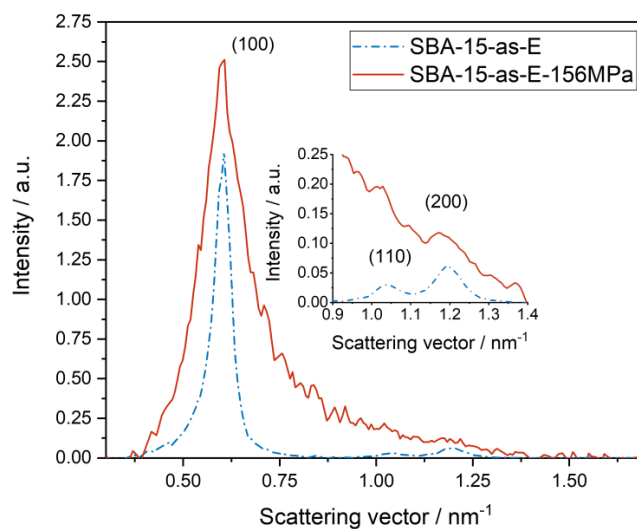
Figure S8. SAXS curves of SBA-15-as-E prior and after applying a pressure of 156 MPa for 10 min. The increase of the full width at half maximum is 190 %.
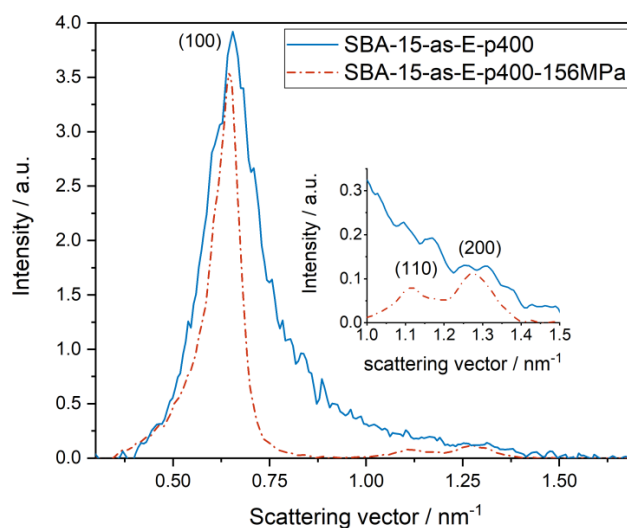

Figure S9. SAXS curves of SBA-15-as-E-p400 prior and after applying a pressure of 156 MPa for 10 min. The increase of the full width at half maximum is 94 %.
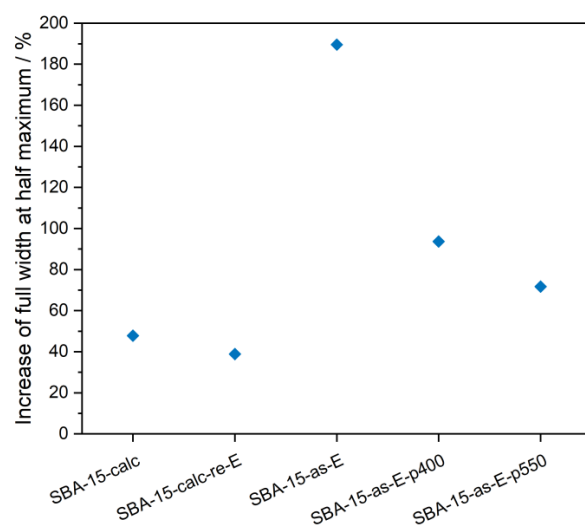
Figure S10. Percentage increase of the full width at half maximum (FWHM) of Lorentzian function fitted to the (100) peak upon pressing.

6   Influence of the Temperature during the Pretreatment in N$_2$

As described in the main article, SBA-15-as-E was pretreated at 400°C and 550°C in N$_2$ and subsequently analyzed by elemental analysis, SAXS measurements, and N$_2$ physisorption measurements.

Observation of the calculated fractions of removed Pluronic® P-123 (Table S3) shows that after thermal treatment at 400°C and 550°C, the remaining template was removed from the pores and all pores were accessible.

The SAXS curves of SBA-15-as-E-p400 in Figure S9 and of SBA-15-as-E-p550 in Figure S7 are almost identical and show the characteristic reflections (100), (110) and (200). However, the comparison to the SAXS curves of the pressed samples SBA-15-as-E-p400-156MPa (Figure S9) and SBA-15-as-E-p550-156MPa (Figure S7) show some differences. In particular, while reflections (100) and (200) are not visible in the SAXS curve of SBA-15-as-E-p400-156MPa, the reflections in the SAXS curve of SBA-15-as-E-p550-156MPa can be adumbrated. Therefore, it can be assumed that SBA-15-as-E-p550 was not damaged to the same extent as SBA-15-as-E-p400 and, thus, higher temperatures during pretreatment in N$_2$ have a positive effect on the mechanical stability of SBA-15 against pressure. Furthermore, a decrease of the lattice parameter with increasing temperature can be observed compared to SBA-15-as, due to the pretreatment in N$_2$ (Table S4). This shrinkage is accompanied by a shrinkage of the pores (Table S4).

These results are confirmed by the N$_2$ physisorption measurements. While the shapes of the N$_2$ physisorption isotherms and their relatively narrow pore size distribution of the two unpressed samples are very similar, the samples pressed at 156 MPa differ significantly from the unpressed materials (Figure S11). Looking at the different surface areas, pore volumes and pore sizes determined from the N$_2$ physisorption measurements for SBA-15-as-E-p400 and SBA-15-as-E-p550 in Table S4, smaller differences are seen. This can be explained by the stronger shrinkage of the pores at higher temperatures. It is known from the literature that the unit cell shrinks at higher temperatures in air due to further condensation of the silica framework.[9] It seems that the oxygen in the air as well as from desorbed water molecules acts as catalyst for reordering the silica bonds in the lattice.[10] However, it is also known, that the temperature range in which the strongest shrinkage is observable is between 300°C and 500°C.[9] Accordingly, it can be assumed that a similar effect is also obtained when heating in N$_2$, so that further condensation reactions make the pore walls more ordered and thus more stable to pressure. In this work, the pretreatment is done in N$_2$ at 400°C and at 550°C, and the shrinkage is more pronounced for SBA-15-as-E-p550. This leads to the assumption that the higher temperature is necessary to overcome the binding energies to reorder the silica lattice.

15

This leads to a more ordered silica lattice and results in more stable pore walls for SBA-15-as-E-p550 compared to SBA-15-as-E-p400.

A comparison of the unpressed materials with those pressed at 156 MPa shows large differences between the N_2 physisorption isotherms and pore size distributions. The analysis shows the expected decrease in surface areas and pore volumes due to pressing at 156 MPa. In addition, the comparison of SBA-15-as-E-p400-156MPa and SBA-15-as-E-p550-156MPa shows further differences. Although the two N_2 physisorption isotherms look similar, large differences between the pore size distributions are evident. While the amount of the original main pores has almost completely disappeared for SBA-15-as-E-p400-156MPa, it has also decreased for SBA-15-as-E-p550-156MPa, but is still perceived as the main fraction. Accordingly, the pore structure of SBA-15-as-E-p550-156MPa was less damaged. This confirms the assumptions of the SAXS studies and shows that a higher temperature during the pretreatment has a positive effect on the mechanical stability of SBA-15 against pressure.
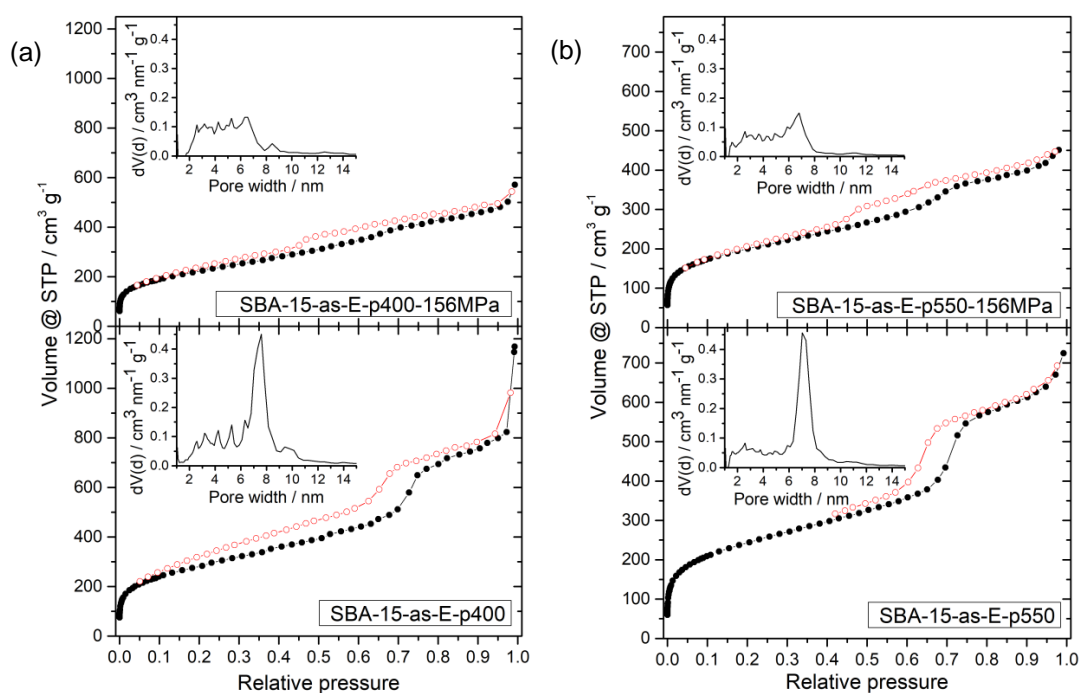

Figure S11. Adsorption (●) and desorption (○) isotherms and pore size distributions of (a) SBA-15-as-E-p400 and (b) SBA-15-as-E-p550 and their analogues pressed with 156 MPa for 10 min.

Table S4. Total surface determined by the BET method (S_{BET}), micropore surface (S_{micro}) as well as the total (V_{tot}), the mesopore (V_{meso}) and the micropore volume (V_{micro}) of SBA-15-as-E-p400, SBA-15-as-E-p550 and their analogues pressed with 39 or 156 MPa. Furthermore, the pore diameters determined by the DFT method ($d_{pore,DFT}$) and the lattice parameter (a) determined from SAXS are listed.

| SBA-15-	S_{BET} / m^2 g^{-1}	S_{micro} / m^2 g^{-1}	V_{tot} / cm^3 g^{-1}	V_{meso} / cm^3 g^{-1}	V_{micro} / cm^3 g^{-1}	$d_{pore,DFT}$ / nm	a / nm
as	-	-	-	-	-	-	11.9
as-E-p400	1016	140	1.807	1.751	0.056	7.6	11.4
as-E-p400-156MPa	798	132	0.884	0.830	0.054	6.6	11.3
as-E-p550	869	236	1.148	1.053	0.095	7.0	11.1
as-E-p550-39MPa	819	222	0.995	0.902	0.093	6.8	11.0
as-E-p550-156MPa	720	209	0.697	0.610	0.087	6.8	10.8

7   Literature

[1]   J. H. Hubbell, S. M. Seltzer, "Tables of X-Ray Mass Attenuation Coefficients and Mass Energy-Absorption Coefficients". National Institute of Standards and Technology (NIST). Retrieved 14 July 2021.

[2]   M. Hartmann, A. Vinu, *Langmuir* **2002**, *18*, 8010-8016.

[3]   P. Scherrer, *Nachrichten von der Gesellschaft der Wissenschaften zu Göttingen, Mathematisch-Physikalische Klasse* **1918**, 98-100.

[4]   C. F. Holder, R. E. Schaak, *ACS nano* **2019**, *13(7)*, 7359-7365.

[5]   R. Hosemann, *Z. Physik* **1950**, *128(4)*, 465-492; R. Hosemann, S. N. Bacchi, *Phys. Rev.* **1954**, *94(1)*, 71-74; R. Hosemann, P. H. Lindenmeyer*, J. Appl. Phys.* **1963**, *34(1)*, 42-45.

[6]   S. Chytil, L. Haugland, E. A. Blekkan, *Microporous Mesoporous Mater.* **2008**, *111*, 134-142.

[7]   V. Meynen, P. Cool, E. F. Vansant, *Microporous Mesoporous Mater.* **2009**, *125*, 170-223.

[8]   M. Thommes, K. Kaneko, A. V. Neimark, J. P. Olivier, F. Rodriguez-Reinoso, J. Rouquerol, K. S. W. Sing, *Pure Appl. Chem.* **2015**, *87(9-10)*, 1051-1069.

[9]   F. Kleitz, W. Schmidt, F. Schüth, *Microporous Mesoporous Mater.* **2003**, *65*, 1–29.

[10]   T. Tatsumi, K. A. Koyani, Y. Tanaka, S. Nakata, *J. Porous Mater.* **1999**, *6*, 13-17.
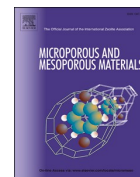
Comparative study of lattice parameter and pore size of ordered mesoporous silica materials using physisorption, SAXS measurements and transmission electron microscopy

Ann-Katrin Beurer [a], Sonja Dieterich [b], Helena Solodenko [c], Elif Kaya [a], Nağme Merdanoğlu [a], Guido Schmitz [c], Yvonne Traa [a,**], Johanna R. Bruckner [b,*]

[a] Institute of Technical Chemistry, University of Stuttgart, 70550, Stuttgart, Germany
[b] Institute of Physical Chemistry, University of Stuttgart, 70550, Stuttgart, Germany
[c] Institute for Materials Science, University of Stuttgart, 70550, Stuttgart, Germany

ARTICLE INFO

ABSTRACT

A precise knowledge of the structural properties of ordered mesoporous materials is essential for their use in almost every application. Researchers use various methods, based on transmission electron microscopy, physisorption and scattering experiments to obtain this data. Here, we evaluate and compare the different methods for four different mesoporous silica materials with pore sizes ranging from 3 to 11 nm. We use the commonly applied methods of physisorption to measure the pore size, fitting of small-angle X-ray scattering data to obtain both the pore size and the lattice parameter, and estimate the lattice parameter from transmission electron micrographs. Besides this, we extract information about the pore sizes from electron density maps. We perform a comparative analysis of the different methods as well as discuss their advantages and disadvantages. We find that all methods deliver comparable results over the investigated pore size range and thus are interchangeable. The only exception is the evaluation of physisorption data of very small mesopores with the BJH method, which does not provide meaningful results.

1. Introduction

Since their discovery in 1992 [1], ordered mesoporous silica materials (OMSMs) have attracted great scientific interest and have become the benchmark for all mesoporous materials. For the preparation of most inorganic mesoporous materials, dissolved organic template molecules are used. In solution, the amphiphilic template molecules form micelles depending on their composition and concentration [2]. The added inorganic precursor molecules accumulate around these micelles. Due to condensation reactions, a mesoporous material forms, whose pores are filled with the structure-directing template [3]. In addition to various synthesis methods, including the direct or true liquid crystal templating (TLCT) [4,5] and the cooperative self-assembly mechanism [6], there exist different methods [3] to open the pores and thus obtain the mesoporous material [7–10]. Since OMSMs with adjustable pore size, narrow pore size distribution, surface areas of more than 700 m^2g^{-1} and high thermal stability can be easily synthesized, they have become

indispensable for many applications. OMSMs are mainly used in heterogeneous catalysis [11], in separation processes [12], as sensors [13] or in biomedicine, e.g., as drug delivery systems [14]. In order to make OMSMs applicable, knowledge of their characteristic structural properties is of great importance. The most important characteristic quantities include the lattice parameter and the pore size of the materials. To the present date, different groups of researchers utilize various characterization methods to obtain this information, which may lead to deviating results for the same material. There has been some work on the comparison of certain methods for specific materials. Kruk et al. investigated the pore size and especially the pore wall thickness of MCM-41, which was synthesized with different templates with nitrogen physisorption measurements, transmission electron microscopy (TEM), and X-ray diffraction [15]. They have shown that the pore wall thickness of the individual materials determined by different methods are in a similar range. An increase in pore wall thickness with increasing pore size was observed. It was also shown that non-thermally treated materials have a thick surfactant layer on the particle surface. Komarneni

---

* Corresponding author.
** Corresponding author.
E-mail addresses: yvonne.traa@itc.uni-stuttgart.de (Y. Traa), johanna.bruckner@ipc.uni-stuttgart.de (J.R. Bruckner).

List of acronyms and abbreviations

BJH	Barrett, Joyner, and Halenda
DFT	density functional theory
FFT	fast Fourier transform
ISEC	inverse size exclusion chromatography
MCM	mobil composition of matter
NLDFT	non-local-density functional theory
OMSM	ordered mesoporous silica material
OMS_TLCT	ordered mesoporous silica synthesized via true liquid crystal templating
sa	swelling agent
SAXS	small-angle X-ray scattering
SBA	Santa Barbara Amorphous
SI	supporting information
TEM	transmission electron microscopy
TLCT	true liquid crystal templating

---

et al. [16] considered the pore size distribution of mesoporous silica molecular sieves using temperature-programmed desorption and nitrogen physisorption measurements. They showed that for their materials, the temperature-programmed desorption method using thermogravimetric analysis is an alternative to nitrogen physisorption measurements for determining the pore size distribution [16]. Galarneau et al. [17] published a comparative study to determine the characteristic properties of hierarchical MFI zeolites with different sorption studies [17]. Furthermore, there is one study that determines the surface area of porous materials using small-angle X-ray scattering (SAXS) measurements and gas physisorption measurements [18]. To the best of our knowledge, there is no study, which compares and evaluates the most frequently used methods for the determination of lattice parameter and pore size over a larger range of OMSMs and pore sizes. Thus, clarification is needed concerning the general interchangeability of the different methods.

In the present work, we tackle this issue by studying the structural properties of four different literature-known OMSMs with hexagonally arranged mesopores ranging from small, i.e., ca. 3 nm, to larger mesopores, i.e., ca. 11 nm, by using TEM, SAXS, as well as nitrogen physisorption measurements. We apply different methods to analyze the obtained data and thereby extract information about the pore size and the lattice parameter. Furthermore, we will present a modified version of a rarely used method [19,20] based on the calculation of electron density maps to obtain information about the pore size. We believe that this work will help other researchers to critically evaluate data published in the field of OMSM research and to choose the best possible characterization method for their purpose.

The structure of this manuscript is as follows: We will start by giving some background information about the most important methods to characterize the structure of OMSMs and lay the necessary basis for the calculation of electron density maps. Afterwards we will detail the results of our investigations, starting with the determination of the lattice parameter, followed by the pore size. Finally, we will discuss and compare the results obtained by the different methods.

2. Background

2.1. Transmission electron microscopy (TEM)

TEM is an ideal method to directly visualize the structure of OMSMs. The easy sample preparation, the high resistance of the silica to the electron beam and the high contrast between the empty pores and silica walls make OMSMs perfect specimens for the method. Typical lab-scale transmission electron microscopes have resolutions of about 200 pm,

newer electron microscopes with aberration-correction may even go beyond this limit, down to 50 pm [21]. Extended imaging series even enable a tomography of the specimen and thus yield 3D images of the sample [22,23]. However, as limitations in the numerical volume reconstruction tend to reduce the resolution, we will focus on the classical 2D transmission electron micrographs in this work. This method is already described for the determination of the lattice parameter and for the pore size, but the procedure itself is scarcely explained in literature [24,25]. Another important aspect is that with TEM only a small section of the whole material is observed, which means that there is a large dependence on statistical sampling.

2.2. Small-angle X-ray scattering (SAXS)

SAXS can give rise to both, information about the lattice parameter a, which equals the nearest pore-to-pore distance in case of hexagonal OMSMs, and the pore size d. In contrast to TEM, SAXS probes a macroscopic sample volume, which leads to statistically averaged and thus more representative values. On the other hand, SAXS requires a more complex data analysis, because it does not provide a direct image of the structure, but a representation of the structure in inverse space. Due to the profound differences among the typical (crystal or colloid) samples investigated in different scientific communities, there are different approaches to said data analysis.

In crystallography, highly ordered crystalline materials are investigated, which lead to sharp Bragg reflections in X-ray scattering experiments if the reflection conditions are met. The corresponding intensities I are thus specified in terms of their individual Miller indices (hkl) [26]. Since we limit our discussion to OMSMs with two-dimensional hexagonal structure, we may omit the third Miller indices (l), resulting in:

$$I(hk) \propto |F_A(hk)|^2 \tag{1}$$

$F_A(hk)$ is the complex scattering amplitude. Performing an inverse Fourier transformation of it results in the electron density distribution

$$\rho(r) = \frac{1}{V} \sum_{hk} F_A(hk) \cdot \exp\left[-2\pi \cdot i \cdot (h \cdot r_x + k \cdot r_y)\right] \tag{2}$$

of the investigated sample with r_x and r_y being the components of the position vector r in x- and y-direction. Thus, we can calculate the electron density distribution of the sample from the square root of the intensity $I(hk)$, if we make certain assumptions about the complex part of the scattering amplitude $F_A(hk)$. The so obtained electron density map represents an indirect visualization of the mesoporous structure, similar to the direct image obtained by transmission electron microscopy. Further details concerning data handling, the assumptions made and the practical calculation of the electron density maps can be found in section 3.2.2 of the supporting information (SI).

In colloidal science, less ordered materials are investigated, which often lead to more diffuse scattering maxima of various shapes. Next to the two-dimensional hexagonal arrangement of the mesopores, we here also consider a contribution to the scattered intensity by the shape of the rod-like mesopores, the micropores within the silica walls and the surface of the silica grains. Hence, we can write the scattered intensity I in dependency of the absolute value q of the scattering vector as

$$I(q) = c_\mu \cdot I_\mu(q) + c_m \cdot I_m(q) + c_g \cdot I_g(q) \tag{3}$$

with c_μ, c_m and c_g being scaling factors for the scattering intensities originating from the micropores ($I_\mu(q)$), the mesopores ($I_m(q)$) or grains ($I_g(q)$), respectively [27]. According to

$$I_m(q) = \theta_m \left\{ |\langle F(q) \rangle|^2 (Z'(q) - 1) + \langle |F(q)|^2 \rangle \right\} \tag{4}$$

the scattering from the mesopores contains information about both the form factor $F(q)$ of the cylindrical pores and the lattice parameter $Z'(q)$,

with θ_m specifying the number density of the mesopores in the plane orthogonal to the pore direction. Hence, fitting equation (3) to the measured SAXS curves provides information about the lattice parameter *a* as well as the pore size *d*. Further information about the theoretical and practical aspects of the fitting procedure are provided in chapter 3.2.1 in the SI.

2.3. Physisorption

Physisorption isotherms allow the detection and the characterization of micropores and mesopores in terms of pore shape and dimension [28]. For sorption studies, gases such as nitrogen, carbon monoxide, and argon, as well as vapors such as water vapor are used [16]. Nitrogen is the most commonly used adsorptive when it comes to the investigation of mesoporous materials, regardless of its quadrupole moment, which leads to specific interactions with polar surfaces and might thus lead to potential errors [28–30].

Independent from the adsorptive, information about surfaces and pore sizes can be determined from the adsorption and desorption isotherms. The pore size of the primary mesopores is generally defined as the maximum of the pore size distribution [4]. For the analysis of mesopores, the Kelvin equation has been used for many years [28]. In order to ascertain the surface areas and pore sizes as accurately as possible, the Kelvin equation has been modified over time. One of the best known methods was proposed by Barrett, Joyner, and Halenda (BJH) [31,32]. However, when using the BJH method, it should be noted that the pore size is significantly underestimated for small mesopores (<20 nm) [30,33]. The inaccuracies can be compensated by methods based on molecular simulations or density functional theory (DFT) (e.g., non-local-density functional theory - NLDFT). Using this method, the essential properties of micropores and mesopores are taken into account [33,34]. This leads to a more accurate determination of pore sizes in the microporous and mesoporous regions [30,33]. However, when using a DFT method, it should be noted that not all material types and pore shapes are available in the commercial DFT software [28].

2.4. Further methods for the determination of the pore size

In addition, several other characterization methods are proposed in the literature to determine pore sizes. These include mercury porosimetry for the characterization of macropores and larger mesopores. In addition, mercury porosimetry can be used to collect further information on pore shape, network effects, etc. [35–37]. Due to the toxicity of mercury, this characterization method is rarely used nowadays and thus was not considered in this work. As an alternative technique for determining pore size distributions, Goworek and Stefaniak [38] described thermogravimetric analysis in the early 1990s. In this method, porous materials are loaded with an adsorbate and the mass loss during thermogravimetric desorption is determined. From the mass loss during the measurement, the total pore volume and the pore size can be provided [38]. Since for each material the experiments have to be adapted and optimized [39–42], we have refrained from investigations of this kind.

A further method for the determination of the pore size is the inverse size exclusion chromatography (ISEC) [43]. The method has been used for various materials to determine pore sizes and their distribution [44–47]. In ISEC, the material to be characterized is often packed into a column as a monolith, but it is although possible to fill the column with a powder. Afterwards, the material in the column is treated with solutes with different particle sizes [48–50]. It is important that the mobile phase and solvent do not interact with the stationary phase, i.e., the material under investigation. If the solute is chosen correctly, the corresponding chemical interactions between stationary and mobile phases are suppressed, so that the exclusion is based on a physical sieving process. From the resulting retention time, information about the pore size as well as its distribution can subsequently be obtained [49,50]. ISEC is usually performed with monodisperse standard solutions.

However, there are also studies showing that the same information about pore structure can be obtained with polydisperse suspensions. In this case, care must be taken to minimize dispersive mass transfer effects [51]. Since the selection of standards with particles in the range of the required pore size is difficult, and the effects of particle gaps can lead to erroneous determination of the pore size, we did not include this method in our study.

3. Experimental

All chemicals used within this study are listed in chapter 1 of the SI together with information about manufacturer and purity.

3.1. Ordered mesoporous silica materials (OMSMs)

The synthesis of OMS_TLCT (ordered mesoporous silica synthesized via true liquid crystal templating) was already described elsewhere [52]. In brief, 30.5 g of tetramethyl orthosilicate were added to 21.8 g 0.1 N hydrochloric acid and stirred at room temperature for approximately 10 min while an underpressure of 120 mbar was applied to remove most of the forming methanol. This colloidal silica mixture was added to 15.0 g of dodecylethyldimethylammonium bromide and homogenized. The clear liquid was poured into a polytetrafluoroethylene dish and was left at 353 K for 48 h to complete the polycondensation process. The then solid material was milled for 1 min with a ball mill (Spex 8000 Mixer/Mill, vial and balls made from stainless steel). Afterwards the as-synthesized material was calcined at 823 K in an air flow of 150 l h^{-1} with a heating rate of 1 K min^{-1}.

The procedure of the synthesis of MCM-41 ((Mobil Composition of Matter 41) was already described elsewhere [3]. 5.2 g of cetyltrimethylammonium bromide were dissolved in 800 ml of demineralized water at 303 K in a 1 l polypropylene flask. 5.4 g sodium metasilicate were added and completely dissolved while stirring. To the mixture, 8.0 ml ethyl acetate were added dropwise under vigorous stirring. Stirring was stopped after 15 s. The reaction mixture stayed for 24 h at room temperature under static conditions. A hydrothermal treatment under static conditions at 373 K followed for 48 h. Afterwards, the as-synthesized MCM-41 was separated under vacuum, washed with demineralized water and dried at room temperature. To open the pores, as-synthesized MCM-41 was calcined at 823 K in an air flow of 150 l h^{-1} with a heating rate of 1 K min^{-1} [3].

SBA-15 (Santa Barbara Amorpous 15) was prepared according to an approach known in the literature [53]. Therefore, 16 g of triblock copolymer Pluronic P123 were dissolved in a mixture of 520 ml demineralized water and 80 ml 37 wt% hydrochloric acid at room temperature and a stirring speed of 100 rpm overnight in a 1 l teflon-lined autoclave. The solution was heated to 318 K before adding 37 ml tetraethyl orthosilicate. The mixture was stirred for 7.5 h at 318 K with a stirring speed of 150 rpm. A hydrothermal treatment under static conditions at 353 K for a time period of 15 h followed. Afterwards, the as-synthesized SBA-15 was separated under vacuum, washed with demineralized water and dried in an oven at 353 K. To open the pores, as-synthesized SBA-15 was calcined at 823 K in an air flow of 150 l h^{-1} with a heating rate of 1 K min^{-1}

For the synthesis of SBA-15 with bigger pores (SBA-15_sa) compared to the standard SBA-15 described above, we used a similar method and the swelling agent (sa) *n*-decane [54]. At first, 2.5 g of triblock copolymer Pluronic P123 was dissolved in 65 ml demineralized water in a round-bottom flask. During the solution process, the mixture was heated to 323 K. After the Pluronic P123 was completely solved, 18.2 g *n*-decane were added. The turbid mixture was stirred at 323 K for 5 min and then cooled to room temperature. In the next step, 8.9 g tetraethyl orthosilicate and afterwards 8.5 ml 37 wt% hydrochloric acid were added under stirring. Care had to be taken to ensure that the reaction mixture was well mixed, as two phases initially formed. A stirring period followed for 20 h after cooling down the reaction mixture to 308 K. For the hydrothermal treatment at 373 K under static conditions, the

reaction mixture was transferred to a 250 ml polypropylene bottle. After 24 h, the as-synthesized SBA-15_sa was separated under vacuum, washed with demineralized water and dried in an oven at 373 K. To open the pores, as-synthesized SBA-15_sa was calcined at 823 K in an air flow of 150 l h^{-1}. The heating rate was 1 K min^{-1}.

3.2. Characterization

After the preparation and before the characterization, all four materials were carefully ground into a powder using a mortar and pestle. The powder was then mixed very well with a glass rod and by shaking to avoid inhomogeneity. The different materials were stored in a well-sealed small glass vial at room temperature in the laboratory. Before each sampling, the respective material was mixed again.

For SAXS measurements, the SAXSess mc^2 diffractometer from Anton Paar in the line collimation geometry was used. The sample to detector distance was calibrated with cholesteryl palmitate. X-ray radiation with a wavelength of λ(Cu-K$_\alpha$) = 0.1542 nm was generated by an ID 3003 X-ray generator (Seifert) operated at 40 kV and 40 mA. Samples were filled into single-use capillaries (article no. 24897, Anton Paar). To ensure a uniform irradiation of all lattice planes, samples were rotated during the measurement using a RotorCell placed in a TCS 120 hot stage (both Anton Paar). The sample housing was evacuated prior to measurements, which were carried out at 298 K and averaged over 60 individual measurements. The scattered X-ray intensity was detected with a one-dimensional CMOS Mythen 1K detector (Dectris). The measured scattering profiles were deconvoluted with the beam profile using the software SAXSquant™.

The surface area as well as the pore size of all samples were analyzed by nitrogen physisorption measurements. The adsorption and desorption isotherms were recorded using Autosorb iQ from Quantachrome Instruments. Before the measurements, the samples were degassed under vacuum at 473 K for 8 h. After the degassing, the physisorption measurements were performed in a liquid nitrogen bath at 77 K. Two aliquots of each material were analyzed to investigate the reproducibility of the nitrogen physisorption measurements. For the analysis of the isotherms the software Quantachrome® ASiQwin Version 3.01 was used. From the isotherms, the surfaces were calculated using the BET (Brunauer, Emmett, Teller) method. The "Micropore BET Assistant" of the ASiQwin software was used to determine the investigated pressure range. The pore sizes and pore size distributions were determined with the BJH (Barett, Joyner, Halanda) method as well as with the NLDFT method [28]. For the NLDFT calculations, the kernel for silica materials with cylindrical pores was chosen, taking into account the hexagonal structure. The mean pore size is defined as the maximum of the pore size distribution. For the determination of the total pore volume, the last point of the adsorption branch was used whenever possible. Unfortunately, not all measurements reached a plateau after hysteresis. In these cases, the last point before the uncontrolled (second) increase of the isotherm was used (see for example Fig. S15).

All materials were investigated by a transmission electron microscope (Phillips, FEG CM200) to determine the lattice parameters. Suspensions of each of the well homogenized materials in ethanol were prepared and mixed in an ultrasonic bath. The suspensions were then dropped onto Formvar/carbon foil coated copper grids (Plano, 300 mesh, d = 3.05 mm). Once the ethanol was evaporated at room temperature, the dripping of the suspensions was repeated for two more times. All images were recorded at a slight under-focus to enhance the contrast between pores and pore walls. This will have an effect on the actual magnification and therefore the measured distances in the TEM. The development of a method to determine the lattice parameter from TEM images was performed on calcined SBA-15. The ImageJ 1.53e software was used to evaluate the TEM images. The various procedures are explained in detail in the SI in chapter 2.2.1.

All raw data obtained for the characterization of the materials can be found in the data repository of the University of Stuttgart (DaRUS) and are accessible via https://doi.org/10.18419/darus-3348.

4. Results and discussion

4.1. Determination of the lattice parameter

The most commonly used method for the determination of the lattice parameter of porous materials is to calculate it from the position of the scattering maxima obtained by SAXS experiments via equation S1 (a_{SAXS}, cf. SI, chapter 2.1 for further details). The scattering curves of OMS_TLCT, MCM-41, SBA-15 and SBA-15_sa samples show at least the three characteristic reflexes d_{10}, d_{11} and d_{20} (Fig. S1), which confirm a hexagonal structure (*p6mm*) [3,53]. The lattice parameters a_{SAXS} for each OMSMs are listed in Table 1. Standard deviations were calculated based on the averaging over all observed reflection maxima, because this led to the biggest errors compared to, e.g., fitting errors or repeated experiments.

Unsurprisingly, the values $a_{lattice\ factor}$, which are extracted from the SAXS curves by fitting equation (3), differ only marginally from a_{SAXS}, by a maximum of ±0.13 nm, which almost equals the fixed Debye-Weller factor (cf. SI, chapter 3.2.1). As an alternative method, we evaluated TEM images and compared the results with the lattice parameters obtained from the SAXS data. In order to obtain a representative value of the lattice parameter for each material, we investigated different approaches for the evaluation of the TEM images to find a method, which enables the evaluation of as many pores as possible with little effort and high reproducibility (cf. SI, chapter 2.2.1). The method, which meets these requirements the best, depends upon TEM images, which show the pores in the top and side view. Plotting the gray tones along specific lines of a TEM image with the side view of the pore channels results in recurring periodic sequences (Fig. 1), for which the distance between the maxima corresponds to the (10) distance. Using equation S2 gives $a_{TEM,line}$ (cf. SI, chapter 2.2.1). Since the lattice parameter $a_{TEM,line}$ is determined for each pore channel, it is possible to show a distribution of the lattice parameter (Figures S9, S11, S12, S14) and specify a standard deviation. The pores in the top view are considered with the fast Fourier transform (FFT) method (Fig. 1), leading to the (10) distance, which gives rise to the lattice parameter $a_{TEM,FFT}$ by applying equation S2 (cf. SI, chapter 2.2.1). This method has the advantage that a very large number of pores can be considered with little effort. However, the top view orientation of the pore entrances is less frequent than the side view orientation.

Following the different approaches for pores in the top or side view, the lattice parameter was determined for several particles and a large number of pores for all four samples. The resulting lattice parameters are listed in Table 1. Exemplary used TEM images can be found in the SI in the chapter 2.2 accompanied by a more detailed discussion of the results. In general, the lattice parameter $a_{TEM,line}$ differs by a maximum of

Table 1
The mean lattice parameters and standard deviations calculated directly from SAXS data (a_{SAXS}), extracted from the SAXS curves by fitting equation (3) ($a_{lattice\ factor}$), as well as from TEM images with top view of the pores ($a_{TEM,FFT}$) and with the side view of the pore channels ($a_{TEM,line}$). In addition, the number of investigated particles and pores are given in parentheses (investigated particles/ estimated number of pores).

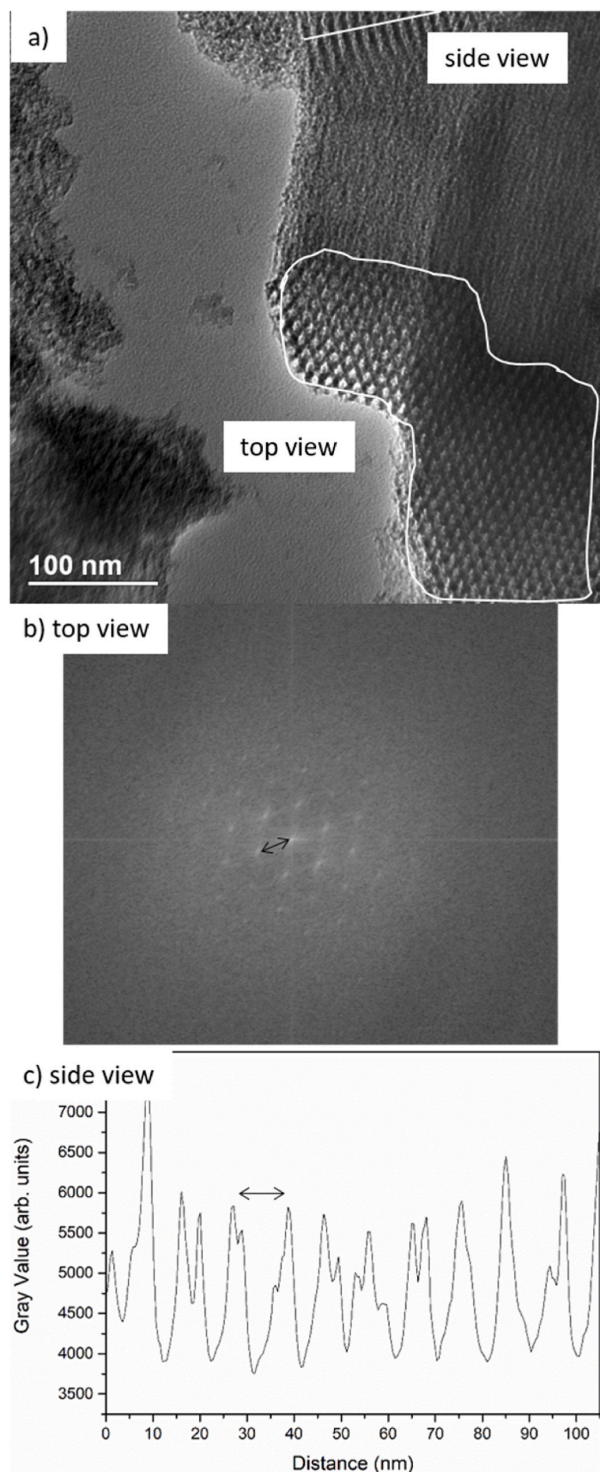| Sample	a_{SAXS} [nm]	$a_{lattice\ factor}$ [nm]	$a_{TEM,FFT}$ [nm]	$a_{TEM,line}$ [nm]
OMS_TLCT	3.567 ± 0.008	3.5 ± 0.1	4.3 ± 0.1 (2/ 292)	3.4.3 ± 0.4 (5/ 542)
MCM-41	4.502 ± 0.004	4.5 ± 0.1	4.2 ± 0.2 (5/ 3320)	4.3 ± 0.9 (5/ 265)
SBA-15	10.37 ± 0.05	10.5 ± 0.1	9.9 ± 0.3 (4/ 570)	9.7 ± 0.9 (7/ 241)
SBA-15_sa	13.74 ± 0.07	13.7 ± 0.1	13.3 ± 0.3 (6/ 5870)	13.3 ± 2.5 (6/ 220)

Fig. 1. Exemplary TEM image of SBA-15 (a) with pores in the side and top view. The marked area of the pores in the top view are transformed by the fast Fourier transform method resulting in the (10) distance (b). The gray tones are plotted along the drawn white line for the pore channels in the side view (c). The distance between the maxima gives the (10) distance as well. Equation S2 allows the calculation of the lattice parameters $a_{\text{TEM,FFT}}$ and $a_{\text{TEM,line}}$.

2% from $a_{\text{TEM,FFT}}$. The comparison with the lattice parameters obtained by SAXS measurements a_{SAXS} and $a_{\text{lattice factor}}$ shows that all determined lattice parameters are in the same range. This result can be rationalized by considering the prerequisites for an accurate identification of the lattice parameters from the transmission electron micrographs (for details see SI p. 9). When viewed from top, the pores need to be aligned parallel to the viewing direction; otherwise, the hexagonal arrangement of the pores will appear to be distorted, leading to false values. Fortunately, bigger distortions of this kind can easily be detected by the naked eye and the corresponding particles may be omitted in the measurements. When viewed from the side, things become more complicated. Although deviations from a proper alignment along the (10) direction are usually difficult to detect, it is possible to obtain consistent values, if enough particles and pores are considered. It is obvious that the biggest relative deviations between lattice parameters obtained from SAXS and from TEM measurements occur for OMS_TLCT, which points at increasing resolution limitations of the TEM measurements for smaller structures.

In summary, it can be concluded that the evaluation of TEM images for the determination of the lattice parameters is definitely an alternative characterization method, however, a quite time-consuming one. Moreover, due to the orientation of the pores, there is a risk of obtaining larger errors. It must be considered that despite the observation of several different particles, only a small section of the investigated sample is characterized, whereas in SAXS investigations a macroscopic sample volume is examined. Accordingly, TEM images reveal heterogeneities in the sample and deliver a good approximation of the lattice parameter, but do not provide a statistically averaged value as SAXS measurements do.

4.2. Determination of the pore size

In the next step, OMS_TLCT, MCM-41, SBA-15 and SBA-15_sa were used to study different methods for determining the pore size. First, nitrogen physisorption measurements were carried out for all materials. The corresponding isotherms are shown in Fig. S15 in the SI. The shape of the adsorption and desorption isotherm of the calcined OMS_TLCT corresponds to a type IV(a) isotherm. Therefore, it can be assumed that this is a material with very small mesopores [28]. The adsorption and desorption isotherms for MCM-41 allow the conclusion that the mesopores are in the range of 4 nm [3,28,55,56]. SBA-15 shows the, for mesoporous materials with pore sizes >4 nm, typical type IV isotherm with an H1 hysteresis [3,28]. The same is true for SBA-15_sa.

The surface areas, pore volumes and pore sizes determined from the physisorption isotherms are listed in Table 2 and S6. The measurements of further aliquots of the same samples, shows that the determination of the pore size is reproducible (Table S6). At this point it should be noted that the comparison of the surface areas determined by the BET method with the values from the literature is difficult. It is known that the values for S_{BET} are in a wide range, depending on the laboratory equipment used for the measurement [57]. For the determination of the pore size distribution, the thermodynamic equilibrium process must be considered. Since most of the materials investigated for this manuscript exhibit H1 hysteresis, which closes at relative pressures >0.4, the desorption isotherms describe the thermodynamic equilibrium process. Therefore, the desorption branches of the different materials were used to determine the pore size [33,34]. Only OMS_TLCT does not exhibit an H1 hysteresis. In this case, the pore sizes determined from the adsorption or desorption branch differ only slightly (cf. Table S6). Nevertheless, we use the pore sizes from the desorption branch for consistent comparison with the other materials. However, there are some conclusions about the network and structure effects, which can be drawn from the shift of the pore size distributions determined from both the adsorption branch and the desorption branch [58]. For this reason, the pore size distributions from both branches of the nitrogen physisorption measurements were determined for this work (Fig. S16). A similar relative range of the pore

size distributions determined from the adsorption and desorption branches can be observed for all samples. According to the literature, this indicates that there are no network effects such as pore blocking or cavitation [58].

Two methods are typically used to obtain the pore size distribution from either the adsorption or desorption branch. For historical reasons, the pore size in literature is usually determined with the BJH method. The determined pore sizes calculated with the BJH method from the desorption branch are listed in Table 2. In addition, the pore size distributions are shown in Fig. 2. For OMS_TLCT, no pore size could be determined with the BJH method from the nitrogen physisorption measurement (Fig. 2 a). We suspect that the pores of the OMS_TLCT are so small that they cannot be depicted by the BJH method used for the mesoporous region. In contrast, the DFT method provides more accurate results by considering the pore structure and the conditions during the physisorption measurement [30,33,34]. However, it should be kept in mind that it is not possible to determine the pore size for all pore structures using the DFT method. There are kernels for cylindrical, spherical or slit-like pores [28]. For all materials investigated in this work, the NLDFT kernel for silica materials with cylindrical pores provides this possibility. A double peak occurs in the pore size distribution of MCM-41 determined by the NLDFT method from the desorption branch (Fig. 2 b) which is caused by a forced hysteresis closure leading to a second step in the isotherm at higher relative pressures (Fig. S15) [3]. Therefore the maximum around 3.8 nm describes the actual pore size distribution within the sample. When evaluating the desorption branch with the BJH method only one maximum is visible, which is due to the forced hysteresis closure, however. Thus the actual pore size of MCM-41 is still too small to be evaluated by the BJH method (for details see SI, chapter 3.1). The pore size distributions of the larger pored SBA-15 (Fig. 2 c) and SBA-15_sa (Fig. 2 d) do not suffer from this problem, but show nearly monomodal maxima for the evaluation by both the NLDFT and the BJH method. The comparison of the mean pore sizes determined with the BJH and the NLDFT method shows deviations of up to 23% for the nitrogen physisorption measurements. This is consistent with other findings in the literature that the pore size of mesopores with a diameter of less than 10 nm is underestimated by up to 30% using the BJH method [28].

In the following, alternative methods for the characterization of the pore size are studied. We have chosen not to determine the pore size from TEM images. The reason for this is that despite extensive efforts to evaluate the images, it is not possible to determine the boundary of the pore from the graphical representation due to the gradual increase of the gray tones.

Extracting the pore sizes form SAXS measurements is a well-established alternative to the more frequently used physisorption measurements, as shown in literature by several working groups [27,59,60]. Fig. 3 depicts the SAXS curves obtained from measuring the four OMSMs together with the fitted graph of equation (3). It is obvious, that the measured data is described quite well by the theory. There are only some

slight deviations at smaller values of the scattering vector q, which are especially visible in Fig. 3a), and at higher values, detectable for Fig. 3c) and d). At small q-values, the fit is dominated by the shape and surface of the grains, which make up the OMSM powder (cf. equation S6). At high q-values, the scattering is dominated by the micropores (cf. equation S7). Considering that we are mainly interested in the mesopore shape and diameter as well as the pore-to-pore distances, these slight deviations do not affect our data evaluation. Therefore, the most relevant part of the fit comprises the region around the Bragg-like reflexes. Detailed graphs, which show the separate contributions to the overall-fit $I_{full}(q)$ can be found in Figs. S18 and S19 in the SI. As equation (4) states, the two contributions of the mesopores, i.e., the form factor of the cylindrical pores and the lattice factor of the hexagonal ordering, do not simply add up but have to be multiplied. Hence, small variations of the pore size lead to pronounced changes in the relative intensities of the Bragg-like reflexes. In the consequence, the extraction of pore sizes from SAXS data results in rather distinct results.

The lattice parameters obtained by fitting the scattering curves according to equation (3) ($a_{lattice\ factor}$), result in almost identical values as obtained for solely fitting the Bragg-like reflections (a_{SAXS}) (Table 1). Thus, there seems to be no advantage in determining the lattice parameter with the more time-consuming fitting of equation (3), if information about the pore size is not required. The values obtained by this method for the pore sizes $d_{form\ factor}$ are listed in Table 2. Comparing the values with the ones determined by physisorption measurements, we find the best agreement with the pore sizes extracted from the nitrogen physisorption measurements by the NLDFT method ($d_{DFT,des}$). For the smaller pore sizes, the values of $d_{form\ factor}$ are somewhat smaller, i.e., 4% for OMS_TLCT and 8% for MCM-41, than the data from physisorption, while they are each 6% larger for SBA-15 and SBA-15_sa, respectively. The biggest deviation arises when comparing the values with the pore sizes obtained from the nitrogen physisorption measurements by the BJH method. This is especially significant for larger pore sizes, which leads to a maximum deviation of −33% for SBA-15.

For the two established methods, i.e., physisorption measurements and fitting of SAXS data, we also looked into the width of the pore size distribution. Therefore, we determined the standard deviations by assuming a normal distribution of the pore size (cf. SI, chapter 3.1). The obtained values are given in Table 2. It is obvious that in all cases there is a trend of wider pore size distributions with increasing mean pore sizes. In most cases, there is a quite reasonable agreement between standard deviations determined for the different methods.

Next to the more commonly used method of fitting equation (3) to the SAXS curves, we here suggest a method to determine the pore size from SAXS experiments, which is based on the reconstruction of the electron density distribution of the OMSMs according to equation (2). This method is a modification of the continuous density function technique introduced by Solovyov and coworkers [61]. While the technique of Solovyov and coworkers assumes a certain electron density distribution based on a sophisticated model and checks its validity by comparison with the SAXS curves, our method uses the scattering intensities directly to yield an electron density map without relying on any structure models. Even though the suggested method might result in slightly less accurate electron density distributions, it is easier to implement and holds the benefit of being model independent.

Fig. 4 shows the electron densities calculated with the suggested method, whereby regions of high electron density, i.e., the pore walls, are depicted in yellow and regions of low electron density, i.e., the mesopores, are visualized in blue. The determined pore size is indicated as white circles in the respective images. For a direct comparison, TEM images of the corresponding OMSMs are shown on the right side of Fig. 4. We find a quite good agreement between the distinct features visible in the two visualizations, e.g., larger wall-to-pore ratios of SBA-15 compared to SBA-15_sa. Note that the scale bar is the same for each of the electron density maps as well as each of the TEM images, but differs between the two.

Table 2
Mean pore sizes determined by the BJH (d_{BJH}) and the NLDFT (d_{DFT}) method from the desorption (des) branches of the nitrogen physisorption measurements of OMS_TLCT, MCM-41, SBA-15 and SBA-15_sa. In addition, the mean pore sizes determined from the SAXS data ($d_{form\ factor}$, $d_{electron\ density}$) are listed. If available, the standard deviations of the individual values are given.

	$d_{DFT,des}$ [nm]	$d_{BJH,des}$ [nm]	$d_{form\ factor}$ [nm]	$d_{electron\ density}$ [nm]
OMS_TLCT	2.7 ± 0.6	-[a]	2.6 ± 0.5	2.6
MCM-41	3.9 ± 0.6	-[a]	3.6 ± 0.4	3.3
SBA-15	7.0 ± 1.0	5.4 ± 0.7	7.4 ± 0.7	7.1
SBA-15_sa	10.1 ± 1.1	8.3 ± 0.8	10.7 ± 0.8	10.1

[a] The pore size cannot be determined due to the settings in the software, which is used for the evaluation with the BJH method (cf. SI, chapter 3.1 for further details).
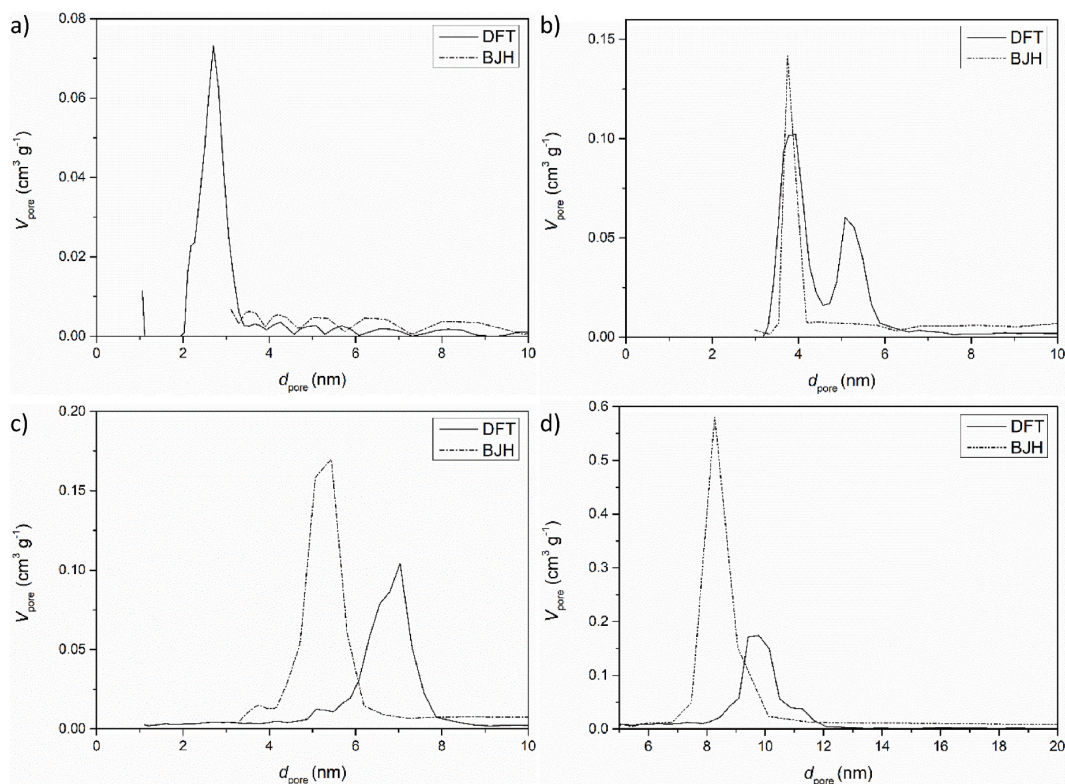
Fig. 2. Pore size distributions resulting from the desorption branch of the nitrogen physisorption measurements determined with the BJH and the NLDFT method for a) OMS_TLCT, b) MCM-41, c) SBA-15 and d) SBA-15_sa.

Due to the inverse Fourier synthesis used for constructing the electron density maps, the decrease of the electron density representing the mesopores does not follow a rectangular but a sinusoidal function. This might even be the more realistic description, considering that OMSMs prepared with Pluronic-type surfactants typically contain a corona of gradually decreasing silica and thus electron density around the mesopores [62–64]. Nonetheless, this raises the problem which value of the electron density should be set as the cut-off value indicating the wall-mesopore interface. In order to make this method broadly applicable, we wanted to keep the rule for obtaining the cut-off value as simple as possible. In general, we can treat our OMSMs as two-component systems with low electron densities at the mesopores positions and high electron densities at the position of the silica walls. As the method gives rise to periodic relative deviations of the actual electron density from the over-all electron density of the OMSMs only, the average electron density of the calculated distributions is set to zero. If we do not want to fall back on information from further measurements, e.g. about the pore volume or mass density of the pore walls, the most sensible approach is to assume that the wall-mesopores interface is characterized by the most rapid increase of the electron density distribution. We thus determined the vertical turning points of the electron density distribution by calculating the second derivatives and measure the distance between the two turning points which are the furthest apart (Fig. S20). With this method, we obtain the values listed in Table 2 for $d_{\text{electron density}}$, which are surprisingly close to the values obtained from fitting the SAXS curves, i.e., $d_{\text{form factor}}$. Taking into account that the same raw data was used for fitting the form factor as well as calculating the electron density maps, the excellent agreement of the obtained pore sizes for all four OMSMs investigated suggests the validity of the method. It would be highly interesting to investigate if this method of determining the pore size can also be transferred to other ordered

mesoporous materials, e.g., made up from carbon [65] or ZnO [66].

Summing up, comparison of the pore sizes determined by different methods listed in Table 2 shows a quite good agreement between all methods. Solely, the evaluation of the physisorption data with the BJH method is problematic for smaller mesopores, since it does not give access to pore sizes <3 nm with the applied software. For OMSMs with larger mesopores, i.e. SBA-15 and SBA-15_as, we found a good agreement between the pore sizes determined by nitrogen physisorption measurements evaluated by the NLDFT method, by fitting the form factor and by calculating the electron density distribution. When evaluating nitrogen physisorption measurements with the BJH method, we find that the determined pore size is up to 23% smaller, which is in accordance with literature reports, stating that the BJH method underestimates the pore size [28].

Due to the very similar pore sizes obtained for many of the considered methods, it is difficult to rank them. However, every method has its advantages and disadvantages: Physisorption measurements are the state of the art for determining the pore size. The amount of sample used for the measurement is rather small and can be reused after the measurement. Additionally, further information about the pore structure, the surface area and the mesopores can be determined. Nonetheless, the measurement times are often very long and various assumptions are made when analyzing the data (e.g., cross-sectional area for nitrogen), which can affect the accuracy of the results. SAXS measurements, like physisorption measurements, require small amounts of sample, which can be reused after the measurement. As for the physisorption experiments, fitting SAXS data is a well-established method and additional information can be derived. The short measurement times of typically 1–10 min are an additional advantage. However, SAXS instruments are not as broadly available due to their high cost, and beam time at larger facilities is scarce. As we showed, the pore size can also be determined
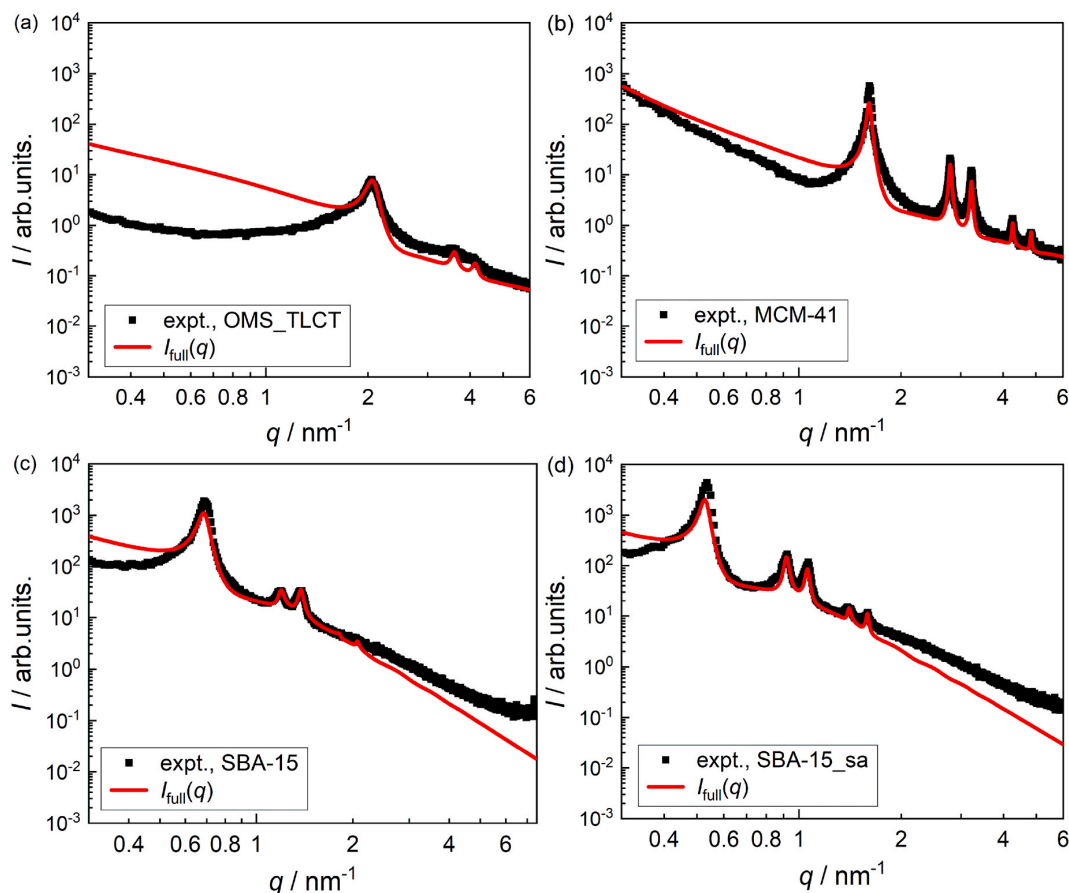
Fig. 3. SAXS curves (black squares) of a) OMS_TLCT, b) MCM-41, c) SBA-15 and d) SBA-15_sa. The scattering intensity is analyzed using equation (3), and the best fits $I_{full}(q)$ are shown as red lines.

from SAXS data by calculating the electron density maps. Even though, we found that this method gave reliable results, it is still in its infancy. Compared to fitting the SAXS curves, the calculations are less complicated due to the relatively basic scattering theory applied. In addition, the results can be visualized well, which allows easy understanding.

5. Conclusion

In the present work, we investigated and evaluated different methods to determine the hexagonal lattice parameter as well as the cross-section size of the cylindrical pores for four different OMSMs with mean pore sizes ranging from approximately 3 to 11 nm. We found that lattice parameters determined from TEM images are in good agreement with the ones determined from the SAXS data if the measured values are averaged over several different particles (Fig. 5 a). While SAXS is still the method of choice, considering that it probes a macroscopic, and thus statistically more significant sample volume and the data evaluation consumes significantly less time, TEM might be seen as a reliable alternative method to determine the lattice parameter if no SAXS device is available. However, more important is that it provides information on heterogeneities and local defects.

We found that measuring the size of small pores from TEM images alone is difficult because the gray level transition from pore wall to pore is blurred. Therefore, it is difficult to obtain reliable and reproducible results. All other investigated methods provide reliable results, which are in good agreement with each other (Fig. 5 b). Only the BJH method is

increasingly limited for smaller pore sizes when using the software Quantachrome® ASiQwin Version 3.01, leading to no or no meaningful pore size distribution for very small mesopores. Furthermore, data evaluated with the BJH method yields smaller pore sizes than data analyzed with the NLDFT method for larger mesopores.

In total, our investigations show that all used methods provide rather similar and reliable results within certain limitations. Based on our comparative analysis, we suggest that physisorption measurements of OMSMs with pore sizes $< \sim 3$ nm should not be evaluated with the BJH method. Outside of these limitations, we suggest that all methods can be used equally, depending on availability. Nonetheless, the silver bullet is to use several methods for mutual verification of the obtained results.

CRediT authorship contribution statement

Ann-Katrin Beurer: Writing – original draft, Visualization, Validation, Methodology, Investigation, Data curation. **Sonja Dieterich:** Writing – review & editing, Visualization, Software, Data curation. **Helena Solodenko:** Writing – review & editing, Visualization, Investigation, Data curation. **Elif Kaya:** Writing – review & editing, Investigation. **Nağme Merdanoğlu:** Writing – review & editing, Investigation. **Guido Schmitz:** Writing – review & editing, Validation, Supervision, Resources, Project administration, Funding acquisition. **Yvonne Traa:** Writing – review & editing, Validation, Supervision, Resources, Project administration, Methodology, Funding acquisition, Data curation, Conceptualization. **Johanna R. Bruckner:** Writing – original draft,
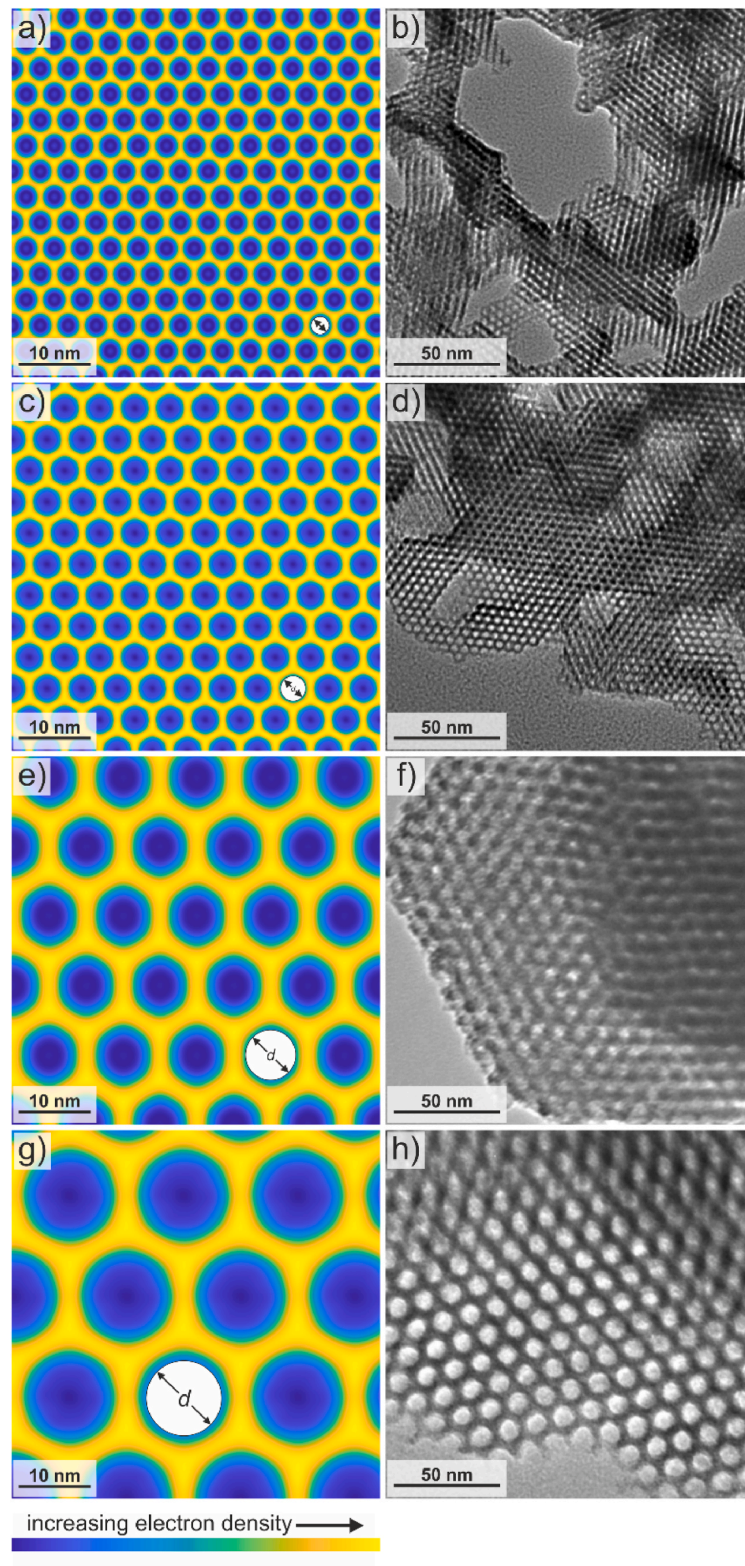
Fig. 4. Calculated electron densities (left) together with transmission electron micrographs (right) of OMS_TLCT (a, b), MCM-41 (c, d), SBA-15 (e, f) and SBA-15_sa (g, h). The pore size determined from the electron density maps is indicated as white circles in the according maps.
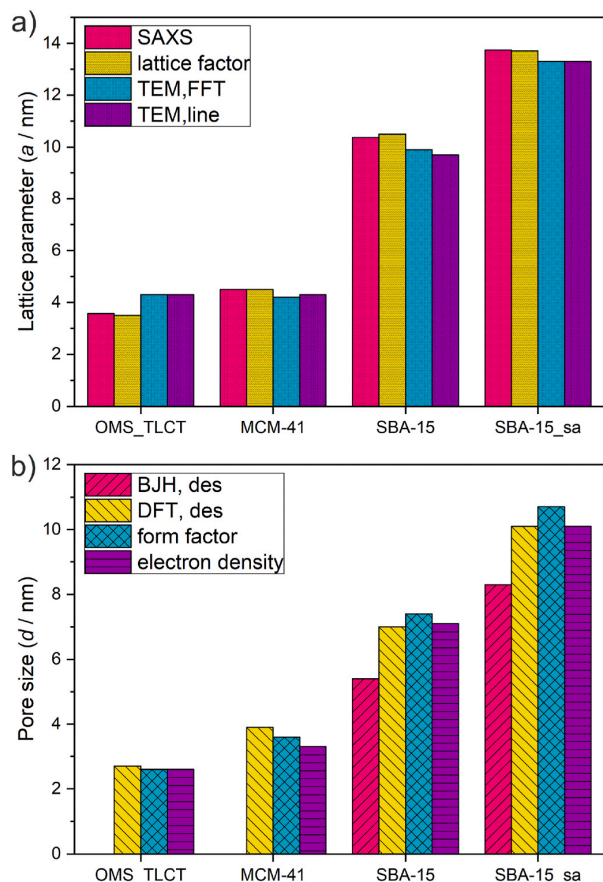
Fig. 5. Column charts of the values obtained from different measurement and/or analysis methods for a) the lattice parameter a and b) the pore size d.

Visualization, Supervision, Software, Project administration, Methodology, Investigation, Funding acquisition, Data curation, Conceptualization.

Declaration of competing interest

The authors declare that they have no known competing financial interests or personal relationships that could have appeared to influence the work reported in this paper.

Data availability

All raw data used in this manuscript is accessible via https://doi.org/10.18419/darus-3348.

Appendix A. Supplementary data

Supplementary data to this article can be found online at https://doi.org/10.1016/j.micromeso.2023.112508.

References

[1] C.T. Kresge, M.E. Leonowicz, W.J. Roth, J.C. Vartuli, J.S. Beck, Nature 359 (1992) 710–712.
[2] P. Alexandridis, T. Alan Hatton, Colloids Surf. A Physicochem. Eng. Asp. 96 (1–2) (1995) 1–46.
[3] V. Meynen, P. Cool, E.F. Vansant, Microporous Mesoporous Mater. 125 (2009) 170–223.
[4] G.S. Attard, J.C. Glyde, C.G. Göltner, Nature 378 (1995) 366–368.
[5] J.R. Bruckner, J. Bauhof, J. Gebhardt, A.-K. Beurer, Y. Traa, F. Giesselmann, J. Phys. Chem. B 125 (2021) 3197–3207.
[6] G.J. de A A Soler-Illia, C. Sanchez, B. Lebeau, J. Patarin, Chem. Rev. 102 (2002) 4093–4138.
[7] M. Kruk, M. Jaroniec, Chem. Mater. 12 (2000) 1961–1968.
[8] B. Tian, Y.X. Liu, C. Yu, F. Gao, Q. Luo, S. Xie, B. Tu, D. Zhao, Chem. Commun. (2002) 1186–1187.
[9] R. van Grieken, G. Calleja, G.D. Stucky, J.A. Melero, R.A. García, J. Iglesias, Langmuir 19 (2003) 3966–3973.
[10] (a) D. Zhao, J. Feng, Q. Huo, N. Melosh, G.H. Fredrickson, B.F. Chmelka, G. D. Stucky, Science 279 (1998) 548–552;
(b) D.E. de Vos, M. Dams, B.F. Sels, P.A. Jacobs, Chem. Rev. 102 (2002) 3615–3640.
[11] (a) J. Liang, Z. Liang, R. Zou, Y. Zhao, Adv. Mater. 29 (2017), 1701139;
(b) W.Y. Perez-Sena, K. Eränen, N. Kumar, L. Estel, S. Leveneur, T. Salmi, J. CO2 Util. 57 (2022) 101879–101889;
(c) N.S. Ali, Z.T. Alismaeel, H. Sh. Majidi, H.G. Salih, M.A. Abdulrahman, N. M. Cata Saady, T.M. Albayati, Heliyon 8 (2022), e09737;
(d) A.A. Sadovnikov, O.V. Arapova, V. Russo, A.L. Mxaimov, D.Y. Murzin, E. R. Naranov, Ind. Eng. Chem. Res. 61 (2022) 1994–2009.
[12] (a) K.-Q. Ma, F. Zhang, H. Yan, C.-F. Zhang, Y. Liu, M. Gu, C.-T. Yang, S. Hu, L. Shi, Chem. Eng. J. 436 (2022), 135213;
(b) G. Castruita-de León, A. de Jesús Montes-Luna, C.Y. Yeverino-Miranda, G. Alvarado-Tenorio, H.I. Meléndez-Ortiz, O. Péres-Camacho, L.A. García-Cerda, Polym. Adv. Technol. 33 (2022) 1412–1426;
(c) S. Giret, Y. Hu, N. Masoumifard, J.-F. Boulanger, E. Juère, F. Kleitz, D. Larivière, ACS Appl. Mater. Interfaces 10 (2018) 448–457.
[13] (a) M.R. de Barros, J.P. Winiarski, F. de Matros Marowski, R.G. Marim, E. S. Chaves, A. Blacha-Grzechnik, C.L. Jost, Microchim. Acta 189 (2022) 269;
(b) S. Chatterjee, J. Qin, X. Li, F. Liang, D.K. Rai, Y.-W. Yang, J. Mater. Chem. B 8 (2020) 2238–2249;
(c) M. Gao, J. Zeng, D. Zhao, B. Kong, Adv. Funct. Mater. 30 (2020), 1906950.
[14] (a) E.D. Mohamed Isa, H. Ahmad, M.B.A. Rahman, M.R. Gill, Pharmaceutics 13 (2021) 152;
(b) M. Manzano, M. Vallet-Regí, Adv. Funct. Mater. 30 (2019), 1902634;
(c) N. Iturrioz-Rodríguez, M.A. Correa-Duarte, M.L. Fanarraga, Int. J. Nanomed. 14 (2019) 3389–3401.
[15] M. Kruk, Y. Sakamoto, O. Terasaki, R. Ryoo, C.H. Ko, M. Jaroniec, J. Phys. Chem. B 104 (2000) 292–301.
[16] S. Komarneni, V.C. Menon, R. Pidugu, J. Goweorek, W. Stefaniak, J. Porous Mater. 3 (1996) 115–119.
[17] A. Galarneau, L. Desmurs, C. Vaulot, H. Nouali, B. Lebeau, T.J. Daou, V. Hulea, C. Cammarano, I. Batonneau-Gerner, A. Sachse, Catal. Res. 2 (2022) 1–29.
[18] C. Schlumberger, C. Scherdel, M. Kriesten, P. Leicht, A. Keilbach, H. Ehmann, P. Kotnik, G. Reichenauer, M. Thommes, Microporous Mesoporous Mater. 329 (2022), 111554.
[19] R. Itri, L.Q. Amaral, P. Mariani, Phys. Rev. 54 (1996) 5211–5216.
[20] M. Prehm, F. Liu, U. Baumeister, X. Zeng, G. Ungar, C. Tschierske, Chem. Int. 46 (2007) 7972–7975.
[21] R. Erni, M.D. Rossell, C. Kisielowski, U. Dahmen, Phys. Rev. Lett. 102 (2009), 96101.
[22] H. Friedrich, P.E. de Jongh, A.J. Verkleij, K.P. de Jong, Chem. Rev. 109 (2009) 1613–1629.
[23] S.-J. Reich, A. Svidrytski, A. Höltzel, J. Florek, F. Kleitz, W. Wang, C. Kübel, D. Hlushkou, U. Tallarek, J. Phys. Chem. C 122 (2018) 12350–12361.
[24] V. Zeleňák, M. Badaničová, D. Halamová, J. Čejka, A. Zukal, N. Murafa, G. Georigk, Chem. Eng. J. 144 (2008) 336–342.
[25] M. Kruk, M. Jaroniec, Y. Sakamoto, O. Terasaki, R. Ryoo, C.H. Ko, Chem. Mater. 12 (2000) 1961–1968.
[26] C. Giacovazzo, in: C. Giacovazzo (Ed.), Fundamentals of Crystallography, third ed., Oxford University Press Inc., New York, 2011, pp. 157–232.
[27] C.J. Gommes, G. Prieto, P.E. de Jongh, J. Phys. Chem. C 120 (2016) 1488–1506.
[28] M. Thommes, K. Kaneko, A.V. Neimark, J.P. Olivier, F. Rodriguez-Reinoso, J. Rouquerol, K.S.W. Sing, Pure Appl. Chem. 87 (2015) 1051–1069.
[29] F. Rouquerol, J. Rouqerol, P. Llewellyn, G. Maurin, Adsorption by Powders and Porous Solids, second ed., Academic Press, London, 2013.
[30] M. Thommes, K.A. Cychosz, Adsorption 20 (2014) 233–250.
[31] J. Rouquerol, F. Rouquerol, K.S.W. Sing, P. Llewellyn, G. Maurin, Adsorption by Powders and Porous Solids: Principles, Methodology and Applications, Academic Press, 2014.
[32] S. Lowell, J. Shields, M.A. Thomas, M. Thommes, Characterization of Porous Solids and Powders: Surface Area. Porosity and Density, Springer, 2004.
[33] J. Landers, G.Y. Gor, A.V. Neimark, Colloid Surfaces: Physicochem. Eng. Aspects 437 (2013) 3–32.

[34] P.A. Monson, Microporous Mesoporous Mater. 160 (2012) 47–66.
[35] H. Giesche, in: F. Schüth, K.S.W. Sing, J. Weitkamp (Eds.), Handbook of Porous Solids, 1, Wiley-VCH, Weinheim, 2002, pp. 309–351.
[36] C. León y León, Adv. Colloid Interface Sci. 76–77 (1998) 341–372.
[37] J. Rouquerol, G. Baron, R. Denoyel, H. Griesche, J. Groen, P. Klobes, P. Levitz, A. V. Neimark, S. Rigby, R. Skudas, K. Sing, M. Thommes, K. Unger, Pure Appl. Chem. 84 (1) (2012) 107–136.
[38] J. Goworek, W. Stefaniak, Colloid. Surface. 60 (1991) 341–349.
[39] J. Goworek, W. Stefaniak, Colloid. Surface. 57 (1991) 161–165.
[40] J. Goworek, W. Stefaniak, Mater. Chem. Phys. 32 (1992) 244–248.
[41] J. Goworek, W. Stefaniak, Colloid. Surface. 62 (1992) 135–140.
[42] J. Goworek, W. Stefaniak, Colloid. Surface. 69 (1992) 23–29.
[43] I. Halász, K. Martin, Angew. Chem., Int. Ed. Engl. 17 (1987) 901–908.
[44] J.H. Knox, H.J. Ritchie, J. Chromatogr. A 387 (1987) 65–84.
[45] I. Mazsaroff, E.E. Regnier, J. Chromatogr. 445 (1988) 15–28.
[46] H. Guan, G. Guiochon, J. Chematogr. 1–2 (1996) 27–40.
[47] P. DePhillips, A.M. Lenhoff, J. Chematogr. A 1–2 (2000) 39–54.
[48] H.G. Barth, B.E. Boyes, C. Jackson, Anal. Chem. 70 (1998) 251–278.
[49] M. Al-Bokari, D. Cherrak, G. Guiochon, J. Chromatogr. A 975 (2002) 275–284.
[50] K. Jerabek, A. Revillon, E. Puccilli, Chromatographia 36 (1993) 259–262.
[51] M. Goto, B.J. McCoy, Chem. Eng. Sci. 55 (2000) 723–732.
[52] F. Ziegler, H. Kraus, M.J. Benedikter, D. Wang, J.R. Bruckner, M. Nowakowski, K. Weißer, H. Solodenko, G. Schmitz, M. Bauer, N. Hansen, M.R. Buchmeiser, ACS Catal. 11 (2021) 11570–11578.
[53] A.-K. Beurer, M. Kirchhof, J.R. Bruckner, W. Frey, A. Baro, M. Dyballa, F. Giesselmann, S. Laschat, Y. Traa, ChemCatChem 13 (2021) 2407–2419.
[54] S.K. Jana, R. Nishida, K. Shindo, T. Kugita, S. Namba, Microporous Mesoporous Mater. 68 (2004) 133–142.
[55] P.J. Branton, P.G. Hall, K.S.W. Sing, J. Chem. Soc. Faraday. Trans. 90 (19) (1994) 2965–2967.
[56] A.V. Neimark, P.I. Ravikovitch, M. Grün, F. Schüth, K.K. Unger, J. Colloid Interface Sci. 207 (1998) 159–169.
[57] J.W.M. Osterrieth, et al., Adv. Mater. 34 (2022), 2201502.
[58] R. Guillet-Nicolas, F. Bérubé, M. Thommes, M.T. Janicke, F. Kleitz, J. Phys. Chem. C 121 (2017) 24505–24526.
[59] S. Förster, A. Timmann, M. Konrad, C. Schellbach, A. Meyer, S.S. Funari, P. Mulvaney, R. Knott, J. Phys. Chem. B 109 (2005) 1347–1360.
[60] M. Impéror-Clerc, P. Davidson, A. Davidson, J. Am. Chem. Soc. 122 (2000), 11925.
[61] a) V.B. Fenelonov, A. Derevyankin, S.D. Kirik, L.A. Solovyov, A.N. Shmakov, J.- L. Bonardet, A. Gedeon, V.N. Romannikov, Microporous Mesoporous Mater. 44–45 (2001) 33–40;
b) L.A. Solovyov, S.D. Kirik, A.N. Shmakov, V.N. Romannikov, Microporous Mesoporous Mater. 44–45 (2001) 17–23;
c) L.A. Solovyov, O.V. Belousov, A.N. Shmakov, V.I. Zaikovskii, S.H. Joo, R. Ryoo, E. Haddad, A. Gedeon, S.D. Kirik, S.-E. Park (Eds.), Nanotechnology in Mesostructured Materials: Proceedings of the 3rd International Mesostructured Materials Symposium, Elsevier, Amsterdam, 2004, pp. 299–302. Jeju, Korea, July 8-11, 2002, 1. ed., 2. impression;
d) L.A. Solovyov, Chem. Soc. Rev. 42 (2013) 3708–3720.
[62] A. Sundblom, C.L.P. Oliveira, A.E.C. Palmqvist, J.S. Pedersen, J. Phys. Chem. C 113 (2009) 7706–7713.
[63] R.A. Pollock, B.R. Walsh, J. Fry, I.T. Ghampson, Y.B. Melnichenko, H. Kaiser, R. Pynn, W.J. DeSisto, M.C. Wheeler, B.G. Frederick, Chem. Mater. 23 (2011) 3828–3840.
[64] W.-S. Chiang, E. Fratini, P. Baglioni, D. Georgi, J.-H. Chen, Y. Liu, J. Phys. Chem. C 120 (2016) 4354–4363.
[65] F. Markus, Ch. Vogler, J.R. Bruckner, S. Naumann, ACS Appl. Nano Mater. 4 (2021) 3486–3492.
[66] S.R. Kousik, D. Sipp, K. Abitaev, Y. Li, T. Sottmann, K. Koynov, P. Atanasova, Nanomaterials 11 (2021) 196.

List of Figures

List of Tables